ABSTRACT

OLDHAM, CHRISTOPHER JOHN. Applications of Atmospheric Plasmas. (Under the direction of Dr. Jerome J. Cuomo).

Surface modification techniques using plasmas have historically been completed in a low pressure environment due to *Pd* (*pressure x gap distance*) considerations influencing the behavior of plasma generation. Generally, plasmas produced in a low pressure environment are of a non-thermal or cold nature. The basic feature of non-thermal plasmas is the majority of electrical energy used to generate the plasma is primarily used to produce energetic electrons for generating chemical species. Low pressure plasmas serve many purposes for materials processing. Since the plasma environment is contained within a closed vessel, the plasma can be controlled very easily. Low pressure plasmas have been used in many industries but the complexity associated with the large pumping stations and limitation to batch processing has motivated new work in the area of atmospheric plasmas. Atmospheric plasmas offer both economic and technical justification for use over low pressure plasmas. Since atmospheric plasmas can be operated at ambient conditions, lower costs associated with continuous processing and a decrease in the complexity of equipment validate atmospheric plasma processing as a next generation plasma-aided manufacturing process. In an effort to advance acceptance of atmospheric plasma processing into industry, a process was developed, the dielectric barrier discharge (DBD), in order to generate a homogeneous and non-thermal plasma discharge at ambient conditions. The discharge was applied to the reduction of known food borne pathogens, deposition of thin film materials, and modification of lignocellulosic biomass.

© Copyright 2009 by Christopher John Oldham
All Rights Reserved

Applications of Atmospheric Plasmas

by
Christopher John Oldham

A dissertation submitted to the Graduate Faculty of
North Carolina State University
in partial fulfillment of the
requirements for the Degree of
Doctor of Philosophy

Materials Science and Engineering

Raleigh, North Carolina

2009

APPROVED BY:

Dr. Mark A.L. Johnson
Associate Professor of Materials Science and Engineering

Dr. J. Michael Rigsbee
Professor of Materials Science and Engineering

Dr. Mohamed A. Bourham
Professor of Nuclear Engineering

Dr. Jerome J. Cuomo
Distinguished Research Professor of Materials Science and Engineering
Chair of Advisory Committee

DEDICATION

This work is dedicated to two people who have always loved and supported me. Their encouragement inspired me to do things I never thought possible, thank you.

My Parents:
John and Sally Oldham

I also dedicate this work to a very special person who has travelled this journey with me. You encouraged and supported me, and throughout, always gave me confidence that I could get to the finish line. Thank you for all of your love and support.

My wife:
Josephine Greenwood Oldham

BIOGRAPHY

Christopher John Oldham was born April 1st, 1979 in Tacoma, WA to John and Sally Oldham. He is the younger brother to Steve and Tereasa Oldham. The family resided in a suburb just between Seattle and Tacoma, WA called Federal Way. During his youth he was actively involved in sports and playing percussion in the school band. In 1994, the family moved to Raleigh-Durham area in a corporate relocation for his father's job. The family settled in Cary, NC. During his high school years at Apex High, he found the world involved other things than sports and music. During this time he discovered he had an interest in the math and science classes he took at Apex High. Encouraged by his parents to pursue more education at NC State University, he enrolled in the First Year College in the fall of 1997. With the help his First Year College advisor, Betsy Alexieff, he made a plan to transfer to the Department of Chemical Engineering at NC State. After drifting through the first year of the Chemical Engineering curriculum, he went to a seminar by Dr. Greg Parsons where a topic entitled "Electronic Materials", peaked his interest. It was at this moment, he realized why he was in engineering. After this seminar, he began working as an undergraduate research assistant at the Analytical Instrumentation Facility (AIF) under Dr. Phil Russell at NC State. Upon graduating in 2002, he began to court a wonderful woman Josephine Greenwood, whom he married in 2007. After graduation, he was persuaded to apply for graduate school in the Department of Materials Science and Engineering at NC State. After a brief semester as a graduate research assistant at AIF, he realized his passion for everything microscopy was not as strong as it was as an undergraduate student. Upon this realization, he began to seek a new mentor to finish his graduate work and on a cold and rainy day in late 2002, Dr. Roger Sanwald spoke to him about a possible opening in the Center for Advanced Manufacturing Processes and Materials (CAMP-M) with Dr. Jerome J. Cuomo. Starting in early 2003, he began working with colleagues at CAMP-M on all things related to plasmas.

It was here at CAMP-M and later in the Institute for Maintenance Science and Technology (IMST) where Dr. Cuomo allowed him to grow and develop into a better student and researcher. Through countless hours in Dr. Cuomo's office, a great friendship was developed. Under Dr. Cuomo's tutelage, he worked on all things related to atmospheric pressure plasmas. After just over six years exploring many ideas developed in Dr. Cuomo's office, the journey through graduate school is completed. The lessons learned during his time working with Dr. Cuomo and others in his group will be preserved as he begins a new chapter in his life. He is very thankful for the great opportunity afforded him to work with such a great mentor.

ACKNOWLEDGEMENTS

I would like to thank all those who helped make this work possible.

- Dr. Cuomo for the opportunity to be a member in your group. I am forever indebted for all that you have done for me during this experience. Thank you for all of the honey that you have shared with me over the past six years.
- Dr. Bourham for teaching me all things related to plasma physics. You are a great teacher and motivator.
- Dr. Rigsbee and Dr. Johnson for your critical comments that ultimately lead to framework for completing this work.
- The various past and present members of CAMP-M and IMST who contributed to this work. This work was not an individual effort and I appreciate everyone who worked to make this research effort come to fruition.
- Dr. Jung Won Cho and Pete Yancey for getting me started in the group.
- Adam Lassister, Josh Grossman, Casey Holder, Kristina Marshall, Jenna Puckett, Victor Prince, Myles Connor, Brian Allen, Kevin Ball, and Brent Thomas for their individual contributions to this work.
- Dr. Roger Sanwald, Sarah Daniel, and Anne Bach for managing the administrative aspects of this project.
- Dr. Dick Guarnieri for teaching me all you could about running equipment, setting up a lab, and how to get data. This work would not have been completed without your critical comments and constant words of encouragement. Thank you for all of the Saturday morning sessions to help me solve problems I was experiencing either with equipment or data.
- Matt King for all the hours spent in the laboratory fixing equipment and conducting experiments. Thank you for your critical comments throughout this

research effort, it would not have been possible without you. You are a great teacher and motivator and I will always remember this as a special time due in no small part to the time we worked together. Thanks for being such a great teammate.

- Brad Hartman who shared the same journey with me through all of the hoops of graduate school. I will miss the daily doses of humor that you shared with me.
- Dr. Bill Kiether for teaching me the hoops of graduate school. You helped guide me through the many landmines that can happen in graduate school and taught me many lessons that allowed me to finish this work, thank you.
- Various friends and colleagues I was able to share this experience with; Dr. Jess Jur, Dr. Jon Ihlefeld, Dr. Mark Losego, Andy Newell, Dr. Brad Busche, Dr. Marcus Hunt, and everyone else whom I may have forgotten but not intentionally. Thank you all the fun and good times.
- Vinay Sakhrani at Tribofilm Research Inc.
- Larry, Rick and Terry at the College of Engineering's Precision Machine Shop.
- Ms. Edna Deas for guiding me through all things academic. You always made sure to keep me in good academic standing and calmed my fears when all seemed lost, thank you for everything.
- The staff at the Analytical Instrumentation Facility (AIF), with special thanks to Roberto Garcia, Fred Stevie, Dr. Dale Batchelor, and Dr. Phil Russell. I would also like to thank Dr. Kristin Bunker and Dr. Mike Salmon for encouraging me to go to graduate school while working at AIF as an undergraduate assistant.
- Dr. Carrier Donley at the Chapel Hill Analytical and Nanofabrication Laboratory (CHANL) at UNC.
- Dr. Simon Lappi at the Laser Spectroscopy Laboratory at NC State.
- Birgit Anderson in the Textiles Characterization Laboratory at NC State.

- The staff at the Shared Materials Instrumentation Facility (SMIF) at Duke University.
- The various funding groups who supported this work; PPG Industries, Air Force Office of Scientific Research, Department of Energy, Dr. John Gilligan and the Office for Research and Graduate Studies at NC State, Dean Louis Martin-Vega of the College of Engineering at NC State, and Dr. Mike Rigsbee of the Department of Materials Science and Engineering of NC State for financial support of this work.
- My wife Josephine for being so supportive of this work. Your love, friendship, and constant words of encouragement helped make all of this possible.
- My parents for teaching me the value of hard work and dedication. You have done so much for me, thank you for all of your love and support.
- My brother Steve and sister Tereasa for all of your love and support along this journey, thank you.
- My in-laws Rick and Lee, for encouraging me along this journey. Thank you both for all that you have done to support Josephine and me.
- The Oldham, Sodden, Greenwood, and Broadley Families for all of their support and encouragement.
- Vann and Leroy for being great study partners and writing buddies.

TABLE OF CONTENTS

LIST OF TABLES xi
LIST OF FIGURES xiii
1. Executive Summary of Dissertation 1
1.1 Background 3
1.2 Statement of Purpose 10
1.3 Specific Questions to this Research Project 12
1.4 Summary 34
2. Literature Review 36
2.1 Plasma Impact 36
2.2 Plasma-Aided Manufacturing 37
2.3 Generation and Collisional Behavior of a Plasma 39
2.4 Plasma Classification 44
2.5 Gas Breakdown 47
2.6 Low-Pressure (Vacuum) versus Atmospheric Plasmas 57
2.7 Non-Equilibrium Atmospheric Plasma Discharges 59
2.8 Barrier Discharge 59
2.9 References 66
3. Equipment and Procedures 67
3.1 Introduction 67
3.2 Dielectric Barrier Discharge (DBD) Reactor 67
3.3 Enclosure 70
3.4 Operation of DBD Reactor 72
3.5 Dielectric Selection 73
3.6 Power Source 75
3.7 Electrical Diagnostics 77
3.8 Optical Diagnostics 77

3.9 Gas Phase Diagnostics 80

4. Reduction of *Listeria innocua* and *Salmonella* spp. using Atmospheric Plasma Processing and Role of Reduction Mechanisms on Pathogen Growth after Plasma Exposure 82

4.1 Abstract 83

4.2 Introduction 84

4.3 Experimental Methods 85

4.4 Results and Discussion 92

4.5 Proposed Reduction Mechanisms in the DBD and Plasma Pen Sources 104

4.6 Conclusions 116

4.7 Acknowledgements 117

4.8 References 118

5. Electrical and Optical Characteristics of a Low-Frequency Atmospheric Plasma Source for Powering a Dielectric Barrier Discharge at Atmospheric Pressure 119

5.1 Abstract 120

5.2 Introduction 121

5.3 Experimental 125

5.4 Results and Discussion 126

5.5 Conclusions 147

5.6 References 148

6. Development of a Pulsed DBD Assisted PE-CVD Process at Atmospheric Pressure for the Deposition of Hybrid Coatings 149

6.1 Abstract 150

6.2 Introduction 151

6.3 Experimental 159

6.4 Results and Discussion 162

6.5 Conclusions 179

6.6 Acknowledgments 180

6.7 References 180

7. Pulsed Plasma-Enhanced Chemical Vapor Deposition (P-PECVD) of Amorphous Silicon Carbon with a Low-Frequency Dielectric Barrier Discharge (DBD) using a Factorial Design of Experiments 181
7.1 Abstract 182
7.2 Introduction 183
7.3 Experimental 189
7.4 Results and Discussion 192
7.5 Conclusions 221
7.6 References 222
8. Experimental Study of a Hybrid Biomass Treatment: Atmospheric Plasma Enhanced Two-Step Acid Hydrolysis Process 223
8.1 Abstract 224
8.2 Introduction 225
8.3 Experimental 226
8.4 Results and Discussion 229
8.5 Conclusions 241
8.6 Acknowledgements 242
8.7 References 242
9. Concluding Remarks and Future Directions 243
9.1 Summary 243
9.2 Future Outlook 247
10. References 248

LIST OF TABLES

Table 2.1: Electric fields for Townsend breakdown of 1 cm size gap at atmospheric pressure. 52

Table 2.2: Numerical constants for parameters A and B for calculation of Townsend coefficient α. 55

Table 2.3: Properties of microdischarges in a DBD. 63

Table 4.1: Exposure time for treating Listeria innocua Salmonella spp. with rotating substrate with the Tepla plasma pen. 92

Table 4.2: Observed number of plates with complete inactivation of the Listeria innocua bacteria at the various gas mixing and treatment configurations from the DBD plasma. 96

Table 4.3: Results from Tepla plasma pen on Salmonella Spp. 98

Table 4.4: Found in the following table is the reaction mechanism and reaction rates for NO_2 production where the reaction rates depend on the relative velocities of collision partners. NO_2 production is dependent on a third body, M = O_2, N_2, the wall, or other third body to form NO_2. 111

Table 4.5: Found in the following table is the reaction mechanism and reaction rates for ozone production where the reaction rates depend on the relative velocities of collision partners. Ozone production is dependent on a third body, M = O_2, N_2, the wall, or other third body to form ozone. 111

Table 6.1: Representative bond energies of hydrogen, silicon, carbon, nitrogen, oxygen, and fluorine with various species. 155

Table 7.1: Definitions and levels of factors used in DOE. 189

Table 7.2: The pseudo t-value and probability for the main factors and interaction effects in the deposition rate discussion. 194

Table 7.3: Bond strengths of H2, SiH4, and CH4 molecules. 202

Table 7.4: The pseudo t-value and probability for the main factors and interaction effects in the optical band gap discussion.. 208
Table 7.5: Atomic concentrations from the Si2p deconvoluted peak. The atomic concentrations are from the experimental DOE with the coded values as shown described in Table 7.1. The peaks are Si-Si/Si-H, Si-C, and SiC_xO_y bonding configurations....... 217

LIST OF FIGURES

Figure 1.1: On the left is an image of the aurora borealis (non-thermal) and on the right is an image of a cloud to ground lighting strike (thermal). 3

Figure 1.2: Electron temperature and gas temperature as a function of pressure [7]. 6

Figure 1.3: Common Dielectric Barrier Discharge configurations in the planar and cylindrical configurations [4]. 8

Figure 2.1: Plasma-aided manufacturing techniques as a function of various pressure regimes (based on [45]). 38

Figure 2.2: Atomic energy level diagram for helium with both the singlet and triplet transition states [47]. 42

Figure 2.3: Schematic of early arc lamp as used by de la Rive and Davy [48]. 45

Figure 2.4: Electron temperature and gas temperature as a function of pressure [7]. 47

Figure 2.5: Capacitive planar discharge gap, separated by distance, d, with electric potential E. 48

Figure 2.6: DC discharge characterization (based on [49]). 49

Figure 2.7: Paschen breakdown voltages for various gases as a function of various pressures and gap distances (Pd) (based on [50]). 51

Figure 2.8: Illustration of the Townsend breakdown mechanism where each primary electron generated near the cathode produces exp(αd) -1 positive ions in the gas gap [2]. 53

Figure 2.9: Streamer propagation head, time evolution of electron avalanche to streamer transition in nanoseconds (based on [2]). 56

Figure 2.10: Common Dielectric Barrier Discharge configurations in the planar and cylindrical configurations [33]. 60

Figure 3.1: DBD reactor shown in Riddick Hall just after completing the enclosure to house the reactor, pump, and high voltage transformers. To the left is the control rack with the

MOD I power supply, function generator, oscilloscopes for monitoring power, and gas monitoring and control system.. 68
Figure 3.2: Updated photograph of the DBD reactor, enclosure, power supply, and other process monitoring controls that were added to the control rack. Additions included a digital oscilloscope, computer to collect data and run the controllers, spectrometers, and substrate heater. Also, new MFC displays in order to accommodate the needs of the different projects in the atmospheric plasma area. Photograph captured in the new Engineering Building 1. 69
Figure 3.3: Original cylindrical DBD reactor used to process gases into renewable fuels. The reactor consisted of six independent chambers where the dielectrics in the reactor were syringes used by the medical industry. 70
Figure 3.4: Shown in the photograph is the AP Solutions AIR-DBD-5000 power module used during the second phase of this research. Module has capability to generate up to 5000W of power. 76
Figure 3.5: Wavelength calibration for UV-VIS spectrometer (200-425 nm)........................ 78
Figure 3.6: Wavelength calibration for VIS spectrometer (400-725 nm)............................... 79
Figure 3.7: Wavelength calibration for VIS-NIR spectrometer (600-900 nm). 79
Figure 3.8: The MKS Instruments residual gas analyzer (RGA), mass range from 1-200..... 81
Figure 4.1: Schematic representation of dielectric barrier discharge (DBD) system used in Listeria innocua experiments. 86
Figure 4.2: Picture of Tepla plasma pen in an experiment to measure temperature of plasma. Tank of dry air hooked up as gas source with Tepla unit plugged directly into 110V outlet. 88
Figure 4.3: Schematic representation of Tepla plasma pen. 89
Figure 4.4: Experimental setup for Tepla plasma pen. 91
Figure 4.5: Growth of Listeria innocua on control plates of 10^4 and 10^6 CFU/ml. 93

Figure 4.6: Centralized growth pattern found after 1.25 and 2.5 minute plasma exposures of 1.5% nitrogen in helium. 95
Figure 4.7: The gram staining process where the gram-negative bacteria E. coli. is stained purple (on the right) and the gram-positive bacteria Staphylococcus aureus is stained pink (on the left) [111]. 103
Figure 4.8: Representative spectra from DBD treatment of Listeria innocua in the 100% helium gas mixture. Emission lines at 501.5 nm, 587.5 nm, 667.8 nm, 706.5 nm, and 728.1 nm from atomic helium peaks [125], emission from the (0-0) band of second positive N_2 system at 337.1 nm along with the OH rotational band at 306.6 nm (R branch) and the 309.2 nm (P branch) [85, 114, 126]. 105
Figure 4.9: Representative spectra from DBD treatment of Listeria innocua in the 1.5% nitrogen in helium gas mixture. Spectral lines indentified in as the nitrogen second positive (337.1 nm), the nitrogen first positive system (550-900nm) along γ-band of NO radiation (213 nm, 224 nm, 234 nm, 245 nm, 257nm, 270 nm, 284 nm) [127, 128]. 106
Figure 4.10: Representative spectra from DBD treatment of Listeria innocua in the 1% oxygen, 4% nitrogen in helium gas mixture. The nitrogen second positive system and an emission line of atomic oxygen at 777.2 was identified [125]. 107
Figure 4.11: Fit profile of the second positive system of the nitrogen ($C^3\pi_u$ (υ'=0)$\rightarrow B^3\pi_g$ (υ'''=2)) rotational band transition at 391.4 nm. A temperature of ~320K$\pm$3.2K was measured by modeling the intensity distribution and fitting a temperature profile with LIFBASE 2.0 software. 108
Figure 4.12: Shown in the figure is a graph describing the dependence of gas temperature on the production of NO_2. At higher temperatures, Reaction (1) consumes NO_2 and is the dominate reaction pathway. At lower temperatures and in the presence of an atomic oxygen source, Reaction (2) produces NO_2. 113

Figure 4.13: Shown in the figure is a graph describing the dependence of gas temperature on the production of ozone. In Reactions (7), the dependence of ozone production on temperature is shown, at higher temperatures more ozone is consumed. At lower gas temperatures, reactions (9) and (11) dominate the reaction pathway. If a source of atomic oxygen is present, ozone formation is favored at the lower temperatures. 114

Figure 4.14: Representative spectra of a 100% air discharge from Tepla plasma pen. Strong emission of the 777.2 nm and 844.6 nm lines associated with atomic oxygen identified [125]. Also found was emission from the nitrogen second positive system [128]. Cutoff of the signal at ~400 nm is from channel cutoff between monochromators in the Ocean Optics S-2000 spectrometer setup. 115

Figure 5.1: Inverter signal of APS AIR-DBD-5000 power source indicating the type of inverter used to power the load is from a true sine wave signal. Top waveform is before plasma ignition and bottom waveform is after plasma ignition. In the figure, the voltage is shown in pink and the current is shown in green. 129

Figure 5.2: A fast Fourier transform of the APS AIR-DBD-5000 power source, taken at the lower resonant mode of operation, 28 kHz. 130

Figure 5.3: Shown in the Figure are the output I-V waveforms before and after ignition at the lower resonant mode of 29 kHz. In the figure, the voltage is shown in pink and the current is shown in green. Also shown in the figure are the I-V characteristics with and without dielectrics in the gas gap. 131

Figure 5.4: A fast Fourier transform of the APS AIR-DBD-5000 power source, taken at the main resonant mode of operation, 81 kHz. 132

Figure 5.5: Shown in the Figure are the output I-V waveforms before and after ignition at the main resonant mode of 81 kHz. In the figure, the voltage is shown in pink and the current is shown in green. Also shown in the figure are the I-V characteristics with and without dielectrics in the gas gap. 133

Figure 5.6: A fast Fourier transform of the APS AIR-DBD-5000 power source, taken at the higher resonant mode of operation, 160 kHz. 134
Figure 5.7: Shown in the Figure are the output I-V waveforms before and after ignition at the higher resonant mode of 160 kHz. In the figure, the voltage is shown in pink and the current is shown in green. Also shown in the figure are the I-V characteristics with and without dielectrics in the gas gap. 135
Figure 5.8: Current-voltage characteristics of the lower resonant mode of operation in 100% helium, 0.5% nitrogen in helium, and 0.5% oxygen in helium. Dielectrics inserted in the gas gap during plasma ignition. 137
Figure 5.9: Current-voltage characteristics of the main resonant mode of operation in 100% helium, 0.5% nitrogen in helium, and 0.5% oxygen in helium. Dielectrics inserted in the gas gap during plasma ignition. 138
Figure 5.10: Current-voltage characteristics of the higher resonant mode of operation in 100% helium, 0.5% nitrogen in helium, and 0.5% oxygen in helium. Dielectrics inserted in the gas gap during plasma ignition. 139
Figure 5.11: Current-voltage characteristics of the lower resonant mode of operation in 100% helium, 0.5% nitrogen in helium, and 0.5% oxygen in helium. No dielectrics inserted in the gas gap during plasma ignition. 140
Figure 5.12: Current-voltage characteristics of the main resonant mode of operation in 100% helium, 0.5% nitrogen in helium, and 0.5% oxygen in helium. No dielectrics inserted in the gas gap during plasma ignition. 141
Figure 5.13: Current-voltage characteristics of the higher resonant mode of operation in 100% helium, 0.5% nitrogen in helium, and 0.5% oxygen in helium. No dielectrics inserted in the gas gap during plasma ignition. 141
Figure 5.14: Photograph of the 100% helium discharge; (a) top photo with dielectrics and (b) bottom photo without dielectrics. 142

Figure 5.15: Photograph of the 0.5% nitrogen in helium discharge; (a) top photo with dielectrics and (b) bottom photo without dielectrics. 143
Figure 5.16: Photograph of the 0.5% oxygen in helium discharge; (a) top photo with dielectrics and (b) bottom photo without dielectrics. 143
Figure 5.17: Spatial profile of the emission intensity between the electrodes for the α-mode of operation from the 100% helium discharge at 28 kHz. 144
Figure 5.18: Optical emission spectra from the three gas mixture with dielectrics inserted in the gas gap. 146
Figure 5.19: Optical emission spectra from the three gas mixture without dielectrics inserted in the gas gap. 147
Figure 6.1: Schematic representation of the DBD used in experiments for this work. 160
Figure 6.2: Schematic representation of plug flow reactor. 162
Figure 6.3: A schematic representation of the concentration gradients expected in the DBD assisted PE-CVD reactor. 164
Figure 6.4: A schematic representation of linear change in concentration, a process that is essentially linear and independent of time. 164
Figure 6.5: Schematic representation showing the formation of a boundary layer in a laminar flow regime. 166
Figure 6.6: Representation of the boundary layer formed in the DBD assisted PE-CVD reactor. Boundary layer calculated to be 0.15 cm. 167
Figure 6.7: Side view of depletion during deposition in the DBD reactor. 171
Figure 6.8: Top view of depletion over dielectric plate during deposition process. 171
Figure 6.9: Example of pulsed plasma process used during depositions. 173
Figure 6.10: Deposition results at varying duty cycles and pulse lengths. 174
Figure 6.11: Deposition results of SiC at varying substrate temperatures while depositing during a 1 sec pulse lengths with a 30% duty cycle. 175

Figure 6.12: XPS spectra of bonding in an as deposited amorphous silicon carbide thin film. 176
Figure 6.13: The pulsed DBD assisted PE-CVD processing window, depicting the dependency of conformal film growth and deposition rate. The process window is depicted with the bolded line where changes in process conditions (substrate temperature) shifts the reaction outside of the window and into a powder growth, desorption, and decomposition mode. 178
Figure 7.1: Geometric illustration of four factor, 2-level factorial DOE used in these experiments. 188
Figure 7.2: Schematic representation of the DBD used in experiments for this work. 191
Figure 7.3: Response surface contours of the deposition rate as a function of silane and hydrogen flow rates at (a) Substrate temperature at 250 C and (b) Substrate temperature at 400 C. 195
Figure 7.4: Response surface contours of the deposition rate (Angs/min) as a function of silane and hydrogen flow rates at (a) Methane flow rate of 2 sccm and (b) Methane flow rate of 10 sccm. 197
Figure 7.5: Response surface contours of the deposition rate (Angs/min) as a function of silane and hydrogen flow rates. 198
Figure 7.6: Response surface contours of the deposition rate (Angs/min) as a function of methane and hydrogen flow rates. 198
Figure 7.7: Response surface contours of the deposition rate (Angs/min) as a function of substrate temperature and hydrogen flow rate. 199
Figure 7.8: Optical emission spectra generated at various experimental conditions. 201
Figure 7.9: Calculation of the activation energies in the DBD assisted pulsed PE-CVD process. Activation energies from 0.02-0.18 were found from the process. 204

Figure 7.10: Relationship between $(\alpha h\upsilon)^{1/2}$ and $h\upsilon$ of the thin films deposited by the process. Each line represents a different sample. The optical band gap is determined by extrapolating the linear region to the x-axis. Optical band gaps between 1.3 and 3.2 eV were observed. 207
Figure 7.11: Response surface contours of the optical gap (eV) as a function of methane and hydrogen flow rates..... 209
Figure 7.12: Response surface contours of the optical gap (eV) as a function of silane and hydrogen flow rates at (a) Methane flow rate of 2 sccm and (b) Methane flow rate of 10 sccm. 211
Figure 7.13: High Resolution XPS scan of Si2p peak at the experimental condition of (+, -, +, +); 0.50 sccm of silane, 2 sccm of methane, 125 sccm of hydrogen, and 400 C. 215
Figure 7.14: High Resolution XPS scan of Si2p peak at the experimental condition of (-, +, -, +); 0.25 sccm of silane, 10 sccm of methane, 0 sccm of hydrogen, and 400 C. 216
Figure 7.15: Depth profile of atomic concentrations of carbon, silicon, and oxygen at the (+, -, -, -) condition; 0.50 sccm of silane, 2 sccm of methane, 0 sccm of hydrogen, and 250 C. 219
Figure 7.16: Depth profile of atomic concentrations of carbon, silicon, and oxygen at the (+, -, -, +) condition; 0.50 sccm of silane, 2 sccm of methane, 0 sccm of hydrogen, and 400 C. 220
Figure 8.1: Schematic representation of dielectric barrier discharge (DBD) used to process biomass substrates..... 226
Figure 8.2: Design of experiments flow diagram. Four sample groups and the treatment conditions are described. Washed samples of the loblolly pine were collected after each hydrolysis step for relating sugar production to the experimental conditions found in the diagram. 228

Figure 8.3: Percent improvement of sugar production over sample group 4 (control) for sample group 1-3 from the 5.6% oxygen in helium plasma exposure. Total sugars were collected and measured after all treatment steps were completed; first acid hydrolysis, plasma exposure, and second acid hydrolysis.. 231

Figure 8.4: Percent improvement of sugar production over sample group 4 (control) for sample group 1-3 from the 5.6% air in helium plasma exposure. Total sugars were collected and measured after all treatment steps were completed, first acid hydrolysis, plasma exposure, and second acid hydrolysis.. 232

Figure 8.5: SEM micrographs: A) Untreated biomass B) Untreated biomass C) After first acid hydrolysis step D) After first acid hydrolysis step. A backscatter electron detector was used to collect the electron signal. The SEM was operated at a pressure of 60 Pa to prevent charging of the biomass substrate. 234

Figure 8.6: SEM micrographs A-D after first acid hydrolysis step and 10-minute plasma treatment in 5.6% air in helium gas mixture. The SEM was operated at 60 Pa with a backscatter electron detector. 235

Figure 8.7: FTIR results from 1450-1100 cm^{-1}. Peak contributions related to cellulose and lignin peaks were collected from representative samples with no treatment, after the first acid hydrolysis step, and the 5% oxygen in helium plasma exposure for 10 minutes. Results from the 5% air spectrum also detected the same degradation of the cellulose peak structure. 236

Figure 8.8: FTIR results from 1800-1450cm^{-1}. Peak contributions related to lignin peaks were collected from representative samples with no treatment, after the first acid hydrolysis step, and 5% oxygen in helium plasma exposure for 10 minutes. Results from the 5% air spectrum also detected the same degradation of the lignin peak structure.... 237

Figure 8.9: A representative emission spectrum recorded from a gas mixture of (5% oxygen in helium). Found in the emission profile were atomic helium, atomic oxygen, and singly

ionized oxygen emission lines. The emission profile was collected at a pressure of 760 torr, plasma current of 100mA, driving frequency of 89-110 kHz, and gas flow rate of 3 L/min. Spectral resolution=0.5 nm. 239

Figure 8.10: A representative emission spectrum recorded from a gas mixture of (5% air in helium). Found in the emission profile were band heads of the NO_γ, N_2 second positive, and N_2 first positive systems. Emission lines from atomic helium were also detected. Marks on the x-axis represent overlay of three spectra from the same experiment at different signal to noise times for presentation of separate bands in emission profile. The emission profile was collected at a pressure of 760 torr, plasma current of 100mA, driving frequency of 89-110 kHz and total gas flow rate of 3 L/min. Spectral resolution=0.5 nm. 240

1. Executive Summary of Dissertation

A plasma is a distinct state of matter, the fourth to be exact and is often referred to as an "ionized gas" [1]. The term "ionized gas" means that at least one electron has been stripped from an atom or molecule resulting in a conversion of that atom or molecule into a positively charged ion. When defining a plasma, it is important to understand the other states of matter. From a fundamental definition, there are three states of matter: solid, liquid, and gas. These states are generally transformed by increases in temperature. Plasmas are generated when energy in the form of electrical, thermal, or magnetic is supplied to a gas. At some point the energy reaches a threshold and the gas is transformed into a plasma. Plasmas are referred to as the fourth state of matter due the following transformation sequence: solid → liquid → gas → plasma. The makeup of a plasma is a unique soup of charged and chemical species. This soup is composed of a collection of electrons, ions, neutral species, photons, metastable and other excited states of the gas. Controlling how these species behave is of great interest to the plasma research community.

Plasma can occur naturally in the form of lightning, solar coronas, and in the earth's ionosphere, but the promise of plasmas generated in laboratories for applied applications is what propels current scientific endeavors in plasma research. Opportunities for man-made plasma applications include nuclear fusion, lighting, combustion, and even electro-surgery, but not all plasmas are created as equal. Both natural and man-made plasmas occur over a wide range of electron temperatures and densities. Plasmas generated for application can range from room temperature to temperatures approaching the energy found in the interior of stars. Electron densities in plasmas can vary over 15 orders of magnitude. Most applied plasmas have electron temperatures (T_e) from 1-20 eV and electron densities (n_e) from 10^8-10^{18} electrons/cm^3 [2]. This wide variation allows for very specific chemistries to be designed into a particular application. This variation also influences the type of plasma generated, thermal or non-thermal. Thermal plasmas are used in applications where the temperature of a substrate is not a consideration, for example high melting point materials.

Thermal plasmas are hot and as such the chemical selectivity is limited. These issues limit practical applicability to perform surface treatments on materials where thermal considerations are a necessity, such as on polymer and biological substrates. This limitation is overcome by working with non-thermal plasma discharges. Non-thermal plasma discharges have traditionally been only generated in a low pressure ($<10^{-3}$ Torr) environment in order to limit energy transfer between electrons and neutrals in the gas [3]. As a consequence, plasma operation at atmospheric pressure is commonly found only in the form of high energy arcs. Recent progress in the field of atmospheric plasma discharges has shown by using an alternating current (AC) power source and isolating the electrodes with a dielectric material, a non-thermal plasma discharge can be generated at atmospheric pressure [1]. Hence, it is the potential to generate a non-thermal plasma at atmospheric pressure and applying the discharge to new applications that motivates this research effort.

1.1 Background

1.1.1 Types of Plasmas

Plasmas are found in two variations, thermal and non-thermal [4]. An example of some naturally occurring plasmas in both a non-thermal and thermal mode operation is found in Figure 1.1 [5].

Figure 1.1: On the left is an image of the aurora borealis (non-thermal) and on the right is an image of a cloud to ground lighting strike (thermal).

Plasma classification depends on how a plasma is generated. Generally, plasmas are generated when an external energy source such an applied electric field, E, is applied across a gas gap. Free electrons in gas gap gain energy from the electric field and lose energy via collisions with neutrals or other third bodies. The parameter which controls this collision frequency is the pressure of operation, p, as the pressure increases, the number of collisions increases. As the collision frequency increases, more energy is transferred from the electrons to the neutrals and as a result a plasmas moves towards an equilibrium or thermal mode of operation. One parameter that governs this transition is the reduced electric field, E/p, which gives an indication to the average electron energy in a plasma system. The higher the value of E/p (higher electric field or lower pressure), the average energy of the electrons and gas molecules is further apart and the plasma system moves far away from equilibrium.

1.1.2 Equilibrium or Thermal Plasmas

As the name implies, thermal plasmas are hot with gas temperatures in excess of 5000 K. Thermal plasmas are referred to as being in a state of local thermodynamic equilibrium (LTE). Due to an equilibrium distribution of energy, the average electron energy (T_e) is approximately equal to the background gas (T_g). Thermal plasmas are usually found in the form of high energy arcs and were extensively developed for use in fusion applications and coating applications for the aeronautics industry. Thermal plasmas have been extensively used where high gas temperatures are not a consideration. Thermal plasmas are usually sustained at high power densities and as result the plasmas have high gas temperatures and limited chemical selectivity to perform basic chemical reactions for practical applications. Typical currents in thermal plasmas can range from 10-1000A and high electron densities of 10^{15}-10^{21} cm^3 are not uncommon [6]. The drawback for use of thermal plasmas in industrial applications is the excitation selectivity, high gas temperature, limited energy efficiency, and high quenching effect of chemical reactions.

1.1.3 Non-Equilibrium or Non-Thermal Plasmas

Alternatively, when the electron temperature and gas temperature differ significantly, a non-equilibrium or non-thermal plasma is formed. In a non-equilibrium plasma, $T_e >> T_g$. The gas temperature can range from room temperature to about 1000 K while the electron temperature can range from 10,000-100,000 K. The basic feature of non-thermal plasmas is the majority of electrical energy used to generate the plasma is primarily used to produce energetic electrons for generating chemical species whereas in thermal plasmas this energy is used to heat the background gas stream.

Non-thermal plasmas are widely used in industrial practice. This is due to some attractive features for generating unique chemistries. The features include: (1) certain components in the plasma offer higher energy density than those by conventional chemistry techniques, (2) the plasma is highly concentrated with charged and chemical species such as electrons, ions, radicals, metastables, and photons of different wavelengths that can be used to lower the activation energy for chemical reaction, and (3) non-thermal plasmas are by

definition far from equilibrium that results in an environment with high concentrations of active species and gas temperatures at or near room temperature [4]. These features result in a chemical environment that is often impossible to duplicate by conventional chemical techniques.

The motivation for working with non-thermal plasmas was largely lead by the birth of the semiconductor industry in the 1960's. Since non-thermal plasmas have a relatively low energy associated with the ions and neutrals, the reaction environment tends to not increase the gas enthalpy. Therefore, materials in contact with the plasma have no thermal damage. The low gas temperature is very powerful and allows for the ability to surface treat thermally sensitive substrates.

1.1.4 Non-Thermal Plasmas Generation at Low and Atmospheric Pressure

Traditionally, non-thermal plasma generation was only found in a low pressure environment. Operation at lower pressure (<10 Torr) was the only controllable method for limiting energy transfer between electrons and neutral species in the plasma. Consequently, non-thermal plasma operation at atmospheric pressure was limited due to the tendency to overheat the gas and transition the plasma into a thermal or equilibrium regime. A schematic representation of the relationship between T_e and T_g is represented in Figure 1.2.

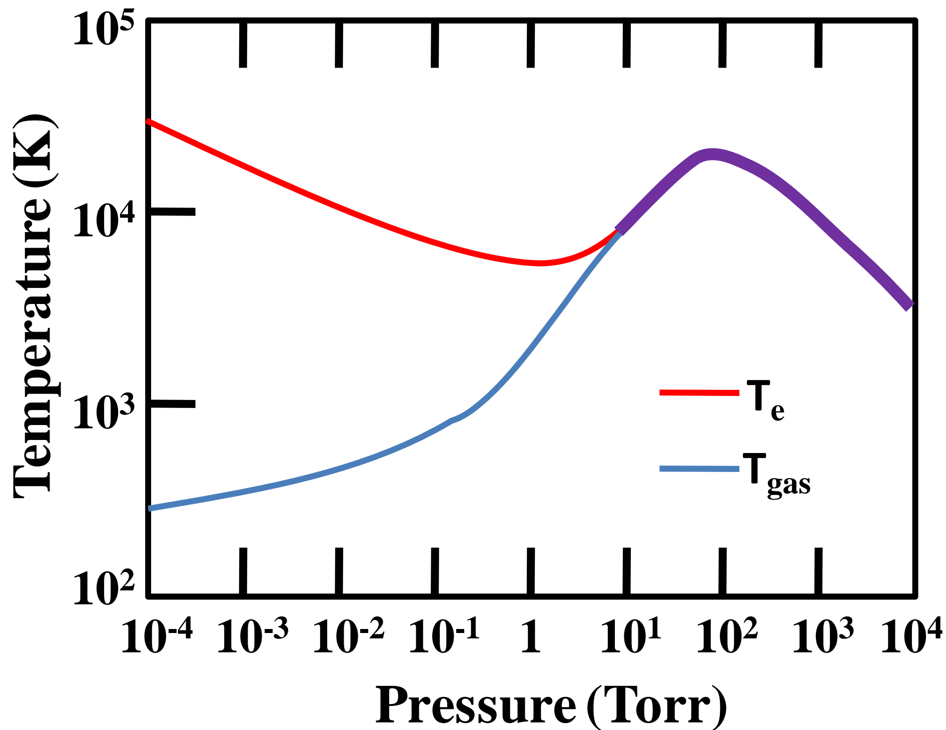

Figure 1.2: Electron temperature and gas temperature as a function of pressure [7].

Although much effort has been invested in developing low pressure plasmas for industrial application, recent efforts have been centered at reproducing a non-thermal discharge at atmospheric pressure. Except for the last 15 years, all plasmas operated at atmospheric pressure were generated in a thermal mode of operation. Atmospheric plasmas in a thermal mode were primarily used in the fields of welding, lamps, circuit breakers, and waste disposal. Recent progress in plasma research has shown the ability to reproduce a low pressure plasma environment (T_e>>T_g) at atmospheric pressure [7]. The motivation for generating non-thermal plasmas at atmospheric pressure is primarily driven by economic considerations but also by interest in reproducing similar plasmas chemistries at ambient conditions. Atmospheric plasma processing offers a continuous manner in which to manufacture parts and reduces floor space on a manufacturing line while speeding production. Additionally, new areas of treatment where large area plasma exposure is

preferred can be realized by atmospheric plasma operation because in theory, an atmospheric plasma based process is not constrained by equipment limitations and the plasma can be scaled to meet the demands of the process requirements.

1.1.5 Atmospheric Plasma Processing

When surface treating thermally sensitive substrates, thermal plasmas are prohibitive. Since the ions and neutrals in non-thermal plasmas remain relatively cold, the benefits to non-thermal plasma operation at atmospheric pressure have led to a number of important applications. These applications are mainly focused towards modifying the surface chemistry via deposition, etching or functionalization of the surface bonds but also include pollution control, volatile organic compound removal, and decontamination [8-12].

Historically, the most common configurations for generating non-thermal plasmas discharge have been operated in a jet or parallel plate configuration [13]. Due to the difficulty in sustaining a discharge at atmospheric pressure, new challenges are presented for stable operation of the plasma. At atmospheric pressure, higher voltages are required for gas breakdown. The higher voltages often lead to arcing between the electrodes and a tendency for the discharge to transition to a thermal mode of operation. To prevent arcing, pointed electrodes or insulating barriers have proven feasible in producing a stable discharge [14-18].

1.1.6 Barrier Discharge

Barrier discharges are a simple way to generate a stable and in some conditions, a uniform discharge. Starting with research by Siemens in 1857, a barrier discharge in a non-thermal mode of operation was found to generate ozone for water purification applications [19]. The barrier discharge is often referred to as the dielectric barrier discharge (DBD) or silent discharge. The silent discharge was used as a description for the low amount of sound emanating from the discharge source. The characteristic feature of the DBD is that insulating barriers are placed in contact with one or both electrodes. Due to the characteristic dielectric barrier, DC operation is not possible so a power source with pulsed DC or alternating current (AC) is used to generate the discharge. The applied frequencies can vary from line frequency to MHz frequencies. The barrier discharge has found a number of

industrial applications including VUV excimer radiation, polymer surface treatment, and more recent advancements in deposition of materials. Typical configurations are found in either a planar or cylindrical geometry as shown in Figure 2.10.

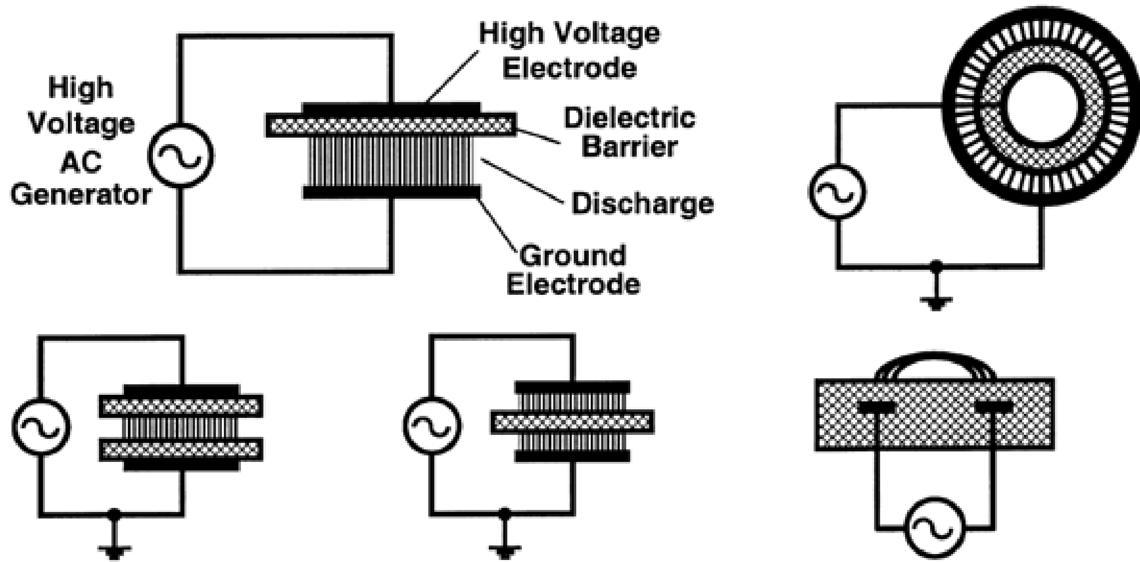

Figure 1.3: Common Dielectric Barrier Discharge configurations in the planar and cylindrical configurations [4].

In both geometries, a dielectric element is present in the current path between the electrodes. Although the dielectric element is present, the discharge still behaves as if the discharge was operated between two metal electrodes. The gas gap in a DBD is typically less than 1mm but discharges in gas gaps as large as several centimeters have been demonstrated [20]. The placement of the dielectric element between the metal electrodes is for good reason. Due to the high collision frequency at atmospheric pressure the electron avalanche develops much faster. The fast ionization generates a number of highly conductive channels that are referred to as microdischarges or streamers. The mutual relationship between the highly conductive channel and resulting microdischarge results in a discharge that is filamentary and appears random. Physically speaking, under an applied electric field, charge carries move rapidly in the gas gap and charges begin to accumulate on

the dielectric surface. The accumulated charges generate an induced electric field opposite to the external field and therefore the flow of current is limited. As a result, the external field is reduced and the electron avalanche decreases. When the applied voltage is reduced to a value below the self-sustaining criterion, the conductive channels are extinguished. During the next half AC cycle, the voltage polarity is reversed and the deposited negative charge accumulates on the opposite dielectric. As a result of the changing polarity and presence of a dielectric element, gas breakdown is easily achieved in a DBD configuration.

Recently, there has been an interest in developing and applying the DBD to applications commonly reserved for low pressure operation. Development of the underlying mechanisms for integrating the DBD in practical application is of critical interest as one end goal of this work is to help acceptance by industry of atmospheric plasmas. Initially, it was thought, by simply using a noble gas and inserting dielectric plates between an AC driven electrode system was all that was needed to fully integrate the DBD for industrial application. However, as research has progressed, it has been found there are specific operating conditions that can enhance the effect of the plasma discharge and modify the desired outcome. Centered in this motivation is the role of operating conditions that affect the behavior and ultimately the chemistry of the discharge. Understanding the role of the plasma chemistry is a core focus of this dissertation.

1.2 Statement of Purpose

The purpose of this research was to investigate and develop the DBD for use in industrial applications. In particular, this research, which was conducted in the Center for Advanced Manufacturing Processes and Materials (CAMP-M) and the Institute for Maintenance Science and Technology (IMST) under the direction of Distinguished Research Professor Jerome J. Cuomo, and was directed towards the decontamination of food borne pathogens, deposition of thin film materials, and modification of lignocellulosic biomass. Through the development of the underlying physical processes leading to successful integration of the DBD in each application, the role of the plasma components was determined.

The dissertation is outlined in the following. In Chapter 2, a complete literature review surrounding plasma generation, classification, and low pressure and atmospheric pressure discharges is discussed. In Chapter 3, the dielectric barrier discharge system and components used in this research is reviewed. In Chapter 4, a description of early work for decontaminating *Listera innocua* and *Salmonella* spp. is presented. In this work, an early experimental power supply was used to power the DBD reactor. A second study with a thermal plasma torch was completed to compare the efficacy of decontaminating with non-thermal and thermal discharge sources. The electrical and optical characteristics of a low-frequency atmospheric plasma power source are presented in Chapter 5. The power source was used for the bulk of the experimental work in this dissertation. In Chapter 6, the development of a pulsed plasma enhanced chemical vapor deposition (P-PECVD) to synthesize materials will be described. In Chapter 7, the deposition of amorphous silicon carbide using the P-PECVD process was examined with a 2^4 factorial design of experiments. And in Chapter 8, a new technique for treating lignocellulosic feedstocks for bioethanol production will be presented. Finally, in Chapter 9, a brief description of ongoing work and future directions will be discussed. Chapters 4-8 have been prepared in manuscript form for publication in a scientific journal. Due to overlap of references between chapters, a single reference chapter was selected to combine all references into a central location, the reference chapter can be found in Chapter 10. Additionally, images were inserted into the body of

each individual chapter to aid in reading and review of the work presented in this dissertation.

1.3 Specific Questions to this Research Project

Specific questions to be answered and answers we found in this project are bulleted in the following section by Chapter where the work is discussed.

1.3.1 Chapter 4

"*Reduction of Listeria innocua and Salmonella spp. using Atmospheric Plasma Processing and Role of Reduction Mechanisms on Pathogen Growth after Plasma Exposure*"

Specific questions to be answered:

- To investigate the use of two atmospheric plasma sources for reduction of *Listeria innocua* and *Salmonella* spp., known food borne pathogens
- To determine the optimum conditions and resulting reduction pathway using a non-thermal plasma source, the dielectric barrier discharge (DBD) configuration.
- To investigate the optimum conditions and resulting reduction pathway using a thermal plasma source, a commercially produced portable atmospheric plasma torch. The torch is produced by PVA Tepla.
- Both plasma sources were considered based on known reduction pathways of chemical species, UV exposure, heat, and charged species.
- The reduction pathways examined in detail and compared to establish a basis for applying to industrial use.

This is what we found:

- This study has shown the gas composition to be an important factor in bacterial reductions of *Listeria innocua* using the DBD configuration.
- The addition of oxygen to a nitrogen and helium plasma greatly reduced the necessary time to achieve a 6-log reduction of *Listeria innocua*, that is reducing the number of *Listeria innocua* cells by 1,000,000 times. The treatment time was reduced by over 10 min.
- A treatment of 1.25 min was found to achieve a full 6-log reduction when oxygen was added to the gas mixture. No reductions were found at this treatment time in a nitrogen and helium gas compositions.

- It was found the chemical species in the plasma were the primary reduction pathway while charged species and heat produced by the plasma acted as secondary mechanisms.
- From analysis by optical emission spectroscopy, the presence of a large amount of nitrogen and oxygen contamination showed emission from the (0-0) band of second positive N_2 system at 337.1 nm along with the OH rotational band at 306.6 nm (R branch) and the 309.2 nm (P branch). Additionally, spectral lines indentified included the nitrogen second positive (337.1 nm), the nitrogen first positive system (550-900nm), and the γ-band of NO radiation (213 nm, 224 nm, 234 nm, 245 nm, 257nm, 270 nm, 284 nm) associated with the production of germicidal UV (λ=220-280 nm) was detected in the emission spectra.
- Using the experimentally generated spectra, the N_2 rotational band (λ=391.4 nm) was fitted to provide a temperature measurement of the gas. Fitting a profile to the N_2 rotational band gives a good indication of the plasma gas temperature and is very useful because the measurement does not perturb the plasma environment during treatment.
- The rotational band is measured from the intensity distributions in the emission spectra of the second positive system of the nitrogen ($C^3\pi_u$ (υ'=0)$\rightarrow B^3\pi_g$ (υ'''=2)) transition at the band head of 391.4 nm. A temperature of 320K$\pm$3.2K was measured by modeling the intensity distribution and fitting a temperature profile with LIFBASE 2.0 software.
- Since the temperature measurements were within or below the temperature for pasteurization (~350K), it was concluded heat produced by the plasma was not a primary factor.
- The role of electrostatic disruption (charged species) from electrostatic stress on the cell membrane is not believed to be a mechanism in this work. The role of charged species in a DBD as a reduction pathway is well supported for gram-

negative bacteria like *Salmonella* spp. and *Bacillus subtilus*, but for gram positive bacteria like *Listeria innocua* the outer cell membrane is very thick and provides resistance to the charged species.

- The outer cell wall is made up a polymer known as peptidoglycan. Peptidoglycan consists of sugars and amino acids which form into a mesh structure outside of the membrane of the cell wall. The peptidoglycan layer varies between 2-8 nm in gram-negative bacteria and can be as much as 80 nm in gram-positive bacteria. It is believed this difference provides the structural strength for *Listeria innocua* to resist electrostatic disruption from charged species in the plasma.
- From these findings it is concluded, the primary reduction pathway of *Listeria innocua* in this DBD plasma is not just from oxidation of the lipid bilayers but also from UV doses inducing dimerization of thymine bases in the *Listeria innocua* DNA. The role of heat and charged species is believed to be a secondary reduction pathway.
- Using the portable plasma pen, 6-log reductions of *Listeria innocua* were achieved in about one second and 3-log reductions of *Salmonella spp.* were found in 0.41 seconds.
- Due to competing reaction pathways, the mechanism is speculated to be chemical species, heat, or some combination of the two.
- The primary reduction pathway from the portable plasma pen was speculated to be heat.
- A gas temperature of ~630 C or ~900 K was measured in just 20 seconds from the active plasma environment.
- As an example of the heat generated by the plasma pen, two substrates, polycarbonate and polyethylene terephthalate (PET), with melting temperatures of 540 K and 533 K respectively, were quickly rastered under the plasma pen for one pass. Both substrates melted, the estimated treatment time was just under 0.5 sec.

- The extreme heat produced by the plasma pen also affected other reductions pathways such as chemical oxidation and UV generation.
- Compounds such as nitrogen oxides and ozone are very sensitive to temperature shifts. Temperatures greater than 500K shift the kinetic reaction pathway and limit the production of these compounds for use as a reduction mechanism.
- Kinetic information produced by King *et. al.* found the temperature of the plasma as measured by portable plasma source (~900 K) greatly effects the production of ozone and NO_2 [21].
- From this, it is concluded chemical species may not have the same role in reduction process as in the DBD discharge.
- The role of charged particles from the plasma pen in reducing the two bacteria strains is unclear. The critical energy needed for electrons in a plasma torch to rupture or tear a cell wall membrane is estimated to be T_e>5 eV. It is expected that a least a portion of the electron energy distribution function could possibly contain a large fraction of electrons in this energy range. At this time the role of charged species has not been fully determined.
- In conclusion, this work discovered the use of thermal plasmas source as reduction source for food borne pathogens is not a preferred technique.
- The high temperature of the plasma presents a problem for treating thermally sensitive substrates such as the food packaging and preparation tools that are often of a polymer matrix. The high temperatures also pose a risk altering the appearance of the food products, which would be detrimental to the sale of products in grocery stores or restaurants.
- Reduction with the DBD discharge demonstrated the source as an effective tool for reducing food borne pathogens. The rich chemical nature produced by the non-thermal plasma source achieved a 99.9999% reduction of *Listeria innocua* in just 1.25 minutes.

- Ultimately, knowledge developed from this research has greatly increased the level of understanding for not only the food industry but also the medical and healthcare industries, government agencies, and other commercial groups interested in designing plasma decontamination sources for protection against various biological hazards. This work will contribute to the design of decontamination sources that easily kill both gram-negative and gram-positive bacteria along with more resistant germs such as *Aspergillus niger* and *Bacillius subtilis* that are currently of great interest due to the threat of possible terrorist attack using these bacteria.

1.3.2 Chapter 5

"Electrical and Optical Characteristics of a Low-Frequency Atmospheric Plasma Dielectric Barrier Discharge"

Specific questions to be answered:

- To examine the conditions for producing a homogeneous glow discharge with a new low frequency power supply design.
- To determine the discharge properties (electrical and optical) based on the operating conditions (gas mixture, gap distance, applied frequency, etc.).
- To evaluate and compare the new power supply for use in industrial applications.

This is what we found:

- It was found the power supply had three characteristic resonant modes of operation at 28 kHz, 81 kHz, and 160 kHz.
- Results from the electrical waveforms show the lower resonant mode at 28 kHz contained some non-linear characteristics. The non-linear characteristics are attributed to contributions from higher resonant modes operating at this resonant point.
- The higher resonant modes at 81 and 160 kHz operated without influence from higher resonant modes and the signal output of both modes was sinusoidal.
- The 100% helium discharge operated similarly to other atmospheric glow discharge plasmas in the field of DBD's.
- Operation with dielectrics in the gas gap resulted in a α-mode of operation, similar to the abnormal glow regime found in low pressure plasma discharges.
- Plasmas generated in the 0.5% nitrogen and 0.5% oxygen in helium gas mixtures resulted in a filamentary discharge.

- A α-γ mode transition was observed as power was increased with dielectrics in the gas gap.
- Without dielectric plates, only a γ-mode of operation could be produced. Large area plasma generation in the γ-mode was not shown with this power source.
- From this work, the power supply has been demonstrated to be a possible solution for industrial applications in need of generating a large area homogenous plasma at atmospheric pressures.
- The power source provides a commercially available solution to current laboratory based power supply designs.
- Potential applications for large area deposition, etching, and surface modification at ambient conditions can now be realized for industrial application. Work towards realizing these potential applications will be discussed in more detail in the results from the next few chapters.

1.3.3 Chapter 6

"Development of a Pulsed DBD Assisted PE-CVD Process at Atmospheric Pressure for the Deposition of Amorphous Silicon Carbide"

Specific questions to be answered:

- To fabricate a hybrid inorganic/organic coating systems of amorphous silicon carbide using a pulsed DBD assisted plasma enhanced chemical vapor deposition (PECVD) system.
- To develop operating conditions leading to conformal thin film growth.
- To study the overriding driving forces leading to conformal film growth at atmospheric pressure.
- To establish a scientific basis for the general observations that pulsed mode PECVD, non continuous mode PECVD is a preferred technique for growth of amorphous silicon carbide at atmospheric pressure.

This is what we found:

- Implementing a pulsed plasma mode into the deposition process, it was shown for the first time that deposition of a hybrid coating system at atmospheric pressure using a DBD process could be achieved.
- A 1-D plug flow analysis was completed to simulate the fluid flow conditions at atmospheric pressure.
- The results of this analysis predicted the process could be operated in either a surface limited or mass transport limited regime.
- From this analysis, deposition of amorphous silicon carbide was attempted in a continuous wave (CW) mode of the plasma discharge from silane (SiH_4) and methane (CH_4) in a carrier gas of helium. Homogenous gas phase nucleation and

gas phase depletion dominated the reactions mechanism in CW mode. The process was limited in range and deposition was not successful.

- Pulse lengths from 0.5-10 sec with varying duty cycles from 10-90% were studied.
- Conformal thin film growth was found at pulse lenths of 1 sec with plasma on periods of 0.25-0.5 sec (25-50% duty cycle).
- Deposition rates from 100-250 angtroms/min were recorded.
- Pulse lengths greater than 2.5 sec and 50% duty cycle, resulted in a deposition process that resembled CW mode.
- Supported by analysis with a 1-D plug fow reactor, large concentration gradients were observed during deposition.
- XPS analysis showed the coatings contained good Si-C bonding. In the C 1s peak, Si-C bonding was on the order of 60% and in the Si 2P peak, Si-C bonding was found to be about 62%.
- Operation of the PECVD reactor in a pulsed wave mode as opposed to a CW mode decreased homogeneous gas phase nucleation and gas phase depletion.
- It is proposed the deposition process proceeds through generation of reactive species during plasma on periods and consumption of these species during plasma off periods through chemisorption and subsequent polymerization on the substrate to produce solid films.
- Further optimization in order to understand the direct mechanisms of the pulsed PECVD process is required. Optimization may include attempts to deposit under an ALD-like condition where both the organic and inorganic material are pulsed in the plasma discharge at separate times, where gas pulses would coincide with plasma on periods.
- It was determined in order for the DBD assisted pulsed PECVD process to be commercially viable and industrially accepted, a high mass flow rate of activated

species to the substrate would be required in order to overcome transport issues through the large boundary layer found at atmospheric pressure. Current results support further development and process refinement in order to meet the needs of a robust, scalable PECVD reactor at atmospheric pressure for deposition and coating applications.

1.3.4 Chapter 7

"Pulsed Plasma-Enhanced Chemical Vapor Deposition (P-PECVD) of Amorphous Silicon Carbon with a Low-Frequency Dielectric Barrier Discharge (DBD)"

Specific questions to be answered:

- To determine the conditions that control the deposition process and study the growth, optical, and chemical composition of the resulting films.
- To compare the growth, optical, and chemical composition of the resulting films through an experimental design methodology. The experimental design of experiment (DOE) used was a 2^4 factorial design of experiment.
- To evaluate what influence, if any, there is on the growth, optical, and chemical composition of the films by the substrate temperature and the silane, methane, and hydrogen flow rates.
- To establish a scientific basis for the parameters and interactions parameters with statistical influence on the growth, optical, and chemical composition properties of the deposited films.

This is what we found:

- Sixteen experimental runs were completed.
- Two of the samples were excluded from the analysis due to powder observed on the substrate. Powder was observed at the following run conditions;
    1) (coded value from DOE:- - + -), 0.25 sccm SiH_4, 2 sccm CH_4, 125 sccm H_2, and 250C,
    2) (coded value from DOE: + + + -), 0.50 sccm SiH_4, 10 sccm CH_4, 125 sccm H_2, and 250C.
- The response variables studied were the growth rate, optical gap energy, and bonding in the Si2p peak from x-ray photoelectron spectroscopy (XPS) chemical analysis.

- Using a model generated in the program SAS JMP 7.0, *pseudo t-values* and *p-values* were calculated for the three response variables studied in this experiment.
- The performance of the data fitting was completed by fitting the data using the bootstrap method. The bootstrap method is used in near saturated or saturated DOE's in order gather statistical data on small sample sets.
- The bootstrap method uses the data produced in the sample population and approximates the distribution by creating a pseudo data set. The pseudo data set is created by sampling the data set many times and replacing each sample within the subpopulation of the data set.
- The process creates a large number of phantom samples known as bootstrap samples in order to test the data set for statistical significance. Statistical significance is determined by computing the *p-values* on the pseudo data set. *Pseudo p-values* are calculated from the *t-value* on the pseudo data-set.
- The *pseudo p-values* of the process parameters were determined significant when $p<0.05$ (95% confidence interval).
- The factors of interest were the substrate temperature (T) and the silane (SF), methane (MF), and hydrogen (HF) flow rates.
- The thickness of the thin films, as measured by profilometry, ranged from 81-345 nm. The deposition rate varied from 1-6 Angstroms/sec.
- The factors and interactions between factors that were found to statistically influence the deposition rate are as follows. The only individual parameter that was found to be significant was the hydrogen flow rate (HF). To lesser extent the silane flow rate (SF) was somewhat significant with a *pseudo p-value* of 0.11, while the methane flow rate (MF) and substrate temperature (T) alone had a trivial effect.
- However, interactions between parameters such as methane flow rate (MF) and substrate temperature (T) were determined statistically significant when combined

with the hydrogen flow rate (HF) and silane flow rate (MF). The higher order parameters with significant influences were SF*HF*T, SF*MF*HF, MF*HF, HF*T, and SF*HF because their *pseudo p-values* were less than 0.05.

- The results of this analysis can be interpreted by the looking at how the decomposition of SiH_4, CH_4, and H_2 proceeds in the plasma environment. Both precursors are decomposed in the gas phase through electron-molecule reactions while hydrogen is dissociated through two-electron impact events or through excitation with metastable species.
- During deposition, SiH_4 and CH_4 are decomposed into SiH_{x-1} (x=2-4), Si, CH_{x-1} (x=2-4), C, and H by the plasma discharge. The plasma produces these species to generate Si-C, $SiCH_n$, Si-Si, and Si-H_n bonds for film formation.
- It was found by increasing the concentration of methane, silane, and hydrogen in the plasmas discharge resulted in faster deposition rate.
- The common significant term between all parameters deemed statistically significant was the hydrogen flow rate.
- It is known carbon incorporation into a film is a result of repeated interaction with SiH species. These results find the role hydrogen is important in creating a concentration of Si and SiH radicals that influences film formation.
- From the optical emission (OES) analysis, it was found the strong presence of atomic hydrogen lines and CH species suggests the CH_4 molecule is effectively decomposed through interaction with atomic hydrogen ($CH_m + H \rightarrow CH_{m+1}$), while the lack of intensity from the SiH radical and Si atoms implies the decomposition of SiH_n species may be preferentially suppressed ($SiH_n + H \rightarrow SiH_{n-1} + H_2$).
- Additionally, the spectral analysis indicates the presence of strong atomic hydrogen lines as a key factor for production of deposition species such as SiH_n and CH_m that ultimately lead to Si-C bond formation.

- Thus, it is concluded the introduction of hydrogen gas, and in turn atomic hydrogen promotes dissociation of the silane and methane molecules.
- Moreover, since the OES analysis did not reveal the presence of SiH, Si, and C_2 species suggests either a gas phase reaction or reaction at the growing film surface is occurring between the deposition precursors and the SiH_n species and Si atoms.
- Supported by the spectral analysis, the growth rate was found to be controlled by reactions at the film growing surface. The intensity of species such as SiH, Si, and C_2 in the spectra is limited, but these species are produced in the plasma environment. It is concluded rapid secondary reactions at the surface incorporate the species into the film matrix.
- The optical band gap, E_{opt}, was determined by measuring the ratio of transmitted light to the incident light (%T) with a UV-VIS spectrophotometer. E_{opt} was calculated with the Tauc formula.
- Optical gap between 1.7-3.2 eV were found. As a comparison, reported material band gaps for silicon, silicon carbide, and carbon thin film are 1.1, 2.9, and 4.0 eV respectively. This data suggests the band gaps produced by this process can be varied from a silicon rich to a more carbon rich chemical structure where the majority of optical band gaps were found between 2.2-2.9 eV.
- Similar to the deposition rate analysis, the hydrogen flow rate had a statistical influence on the optical band gap energy.
- Only two interactions were found to be statistically significant with *pseudo p-value* < 0.05. The two interaction parameters were MF*HF and MF*HF*SF.
- The optical gap was found to vary from carbon rich at lower hydrogen flow rates to silicon rich at higher hydrogen flow rates. This supports the proposed mechanism that Si-C bond formation is greatly influenced by the amount of atomic hydrogen produced in the plasma, where more atomic hydrogen

production induces dissociation events of silane. Any increase in the produce of silane radicals such as SiH_n will in turn promote Si-C bond formation with methane molecules.

- It was also found a much narrower range of optical gaps (2.3-2.7 eV) was predicted when a large methane flow rate was used. This indicates that dissociation of the methane molecule may be in a saturated regime where the number of methane radicals produced dominates bond formation to a Si-C structure or possibly C-C bonding formation in the film matrix.
- It is known, when the carbon ratio increases, the optical gap is greatly influenced by the sp^2 and sp^3 bonding in a C-C bond. Additionally, hydrogen promotes C sp^3 over sp^2 bonding, the preferentially bonding results in large optical gaps, often greater than 3.5 eV, from a lowering of the valence band and leads to a sharper, more abrupt band edge. The sharper band edge is a product of an increase in the disorder of localized states at the band edge is has been attributed to the many bonding configurations that carbon can undergo, sp^3, sp^2, and sp^1 hybridization.
- Chemical analysis was completed x-ray photoelectron analysis. The analysis revealed the presence of distinct bands at binding energies which correspond to Si2p, C1s, O1s, N1s and Na1s core levels.
- The Na1s core level was detected in six of the eight samples deposited at 400 C and 2 of the eight samples deposited at 250 C. The sodium percentage varied from about 0.9-7.7% in the eight samples. The detection of sodium is attributed to diffusion from the glass substrates.
- Si-C bond formation was detected in fourteen samples.
- Additionally, Si-Si/Si-H bond formation was detected in all fourteen samples. The Si-Si/Si-H bonding percentage varied from about 20-52% in the films.
- Detection of the Si-Si/Si-H bond, supports the finding that the growth rate is mainly dependent on a reaction at the growing film surface since both SiH_n species and Si atoms were not readily detected in the OES analysis.

- High resolution scans taken on the Si2p peak reveal variations in the bonding chemistry in the deposited thin films. From the scans, two distinct bonding configurations were found.
- In the first bonding orientation, deconvolution of the peak revealed two peak structures, assigned at 98.0 and 99.4 eV. The peak of 99.0 eV is attributed to Si-Si/Si-H bonds and the peak at 99.4 eV is attributed to Si-C bonds in the film matrix.
- In the second bonding configuration, contributions from oxygen were found to modify the film matrix. Three peaks were deconvoluted and assigned at binding energies of 97.7, 98.8, and 100.5 eV.
- The peaks at 97.7 and 98.8 are assigned to Si-Si/Si-H bonds and Si-C bonds in the film matrix. The peak assigned to 100.5 eV is lower than a bonding peak attributed to SiO_2 (~102.6 eV) and it is likely this peak is from formation of a silicon oxycarbide, such as $SiOC_3$, SiO_2C, and SiO_3C.
- From the statistical analysis, it was determined there were no significant factors or interactions that influenced the bonding configurations. The lowest *pseudo p-value* of 0.15 was found for the interaction between the methane and hydrogen flow rates and was related to the Si-C bonding orientation. All other *pseudo p-values* of the factors and interaction parameters were found to be greater than 0.40 for the three bonding orientations.
- The size and shape of the oxygen peak varied between experiments and its role is contributed to two potential contamination sources. The first may be from etching or desorption of residual water and oxygen species off the quartz chamber walls from atomic hydrogen or other plasma species. The second may arise from reactions with dangling bonds from the atmosphere or moisture present in the chamber that may occur after the film is exposed to the ambient atmosphere.
- Considering the sample volume of XPS analysis is only about 5 nm, it is possible to investigate whether the oxide structure is only found on the surface from

exposure to the ambient atmosphere or whether a constant source of oxygen is responsible for the oxide formation in the deposition environment. To do this, a depth profile analysis was completed on at two experimental conditions in order to get a baseline atomic percentage for silicon, carbon, and oxygen throughout the film matrix.

- Data was collected at the surface and at 10, 30, and 60 nm below the sample surface.
- The analysis revealed the oxide structure was greatest on the sample surface with an atomic oxygen percentage of about 15%. Results below the sample surface showed the oxide layer decreased in atomic percentage, but remained constant to a depth of 60 nm. The resulting atomic concentration of oxygen throughout the film matrix was about 9%.
- This indicated the oxygen formation was most likely due to incorporation of oxygen from either water vapor or oxygen bonded to the chamber walls.
- In summary, it was found, by controlling the methane and hydrogen flow rates, the optical gap could be tuned to desired band gap energies. This control shows promise for applications in optoelectronic devices. For example, in single junction solar cells, Si rich amorphous silicon carbide has been used as transparent doped layers for the window material to increase conversion efficiency while C rich films have shown promise in large area displays due to room temperature photoluminescence (PL). The current results support further work to investigate how amorphous silicon carbide thin films produced by the DBD assisted PECVD process can be used in optoelectronic devices.

1.3.5 Chapter 8

"Experimental Study of Atmospheric Plasma Enhanced Two-Step Acid Hydrolysis Process of Southern Pine"

Specific questions to be answered:

- To evaluate what influence, if any, there is by adding a plasma treatment into a traditional two-step acid hydrolysis process.
- To evaluate the role of plasma treatments on lignocellulosic biomass.
- To determine the conditions that improved production of fermentable sugars.

This is what we found:

- The investigation found the addition of atmospheric plasma processing to a conventional 2-step acid hydrolysis process increased fermentable sugar production from loblolly pine by 50%.
- Conventional acid pretreatments were completed in two steps in order to pre-treat different parts of biomass, the cellulose, hemicellulose, and lignin. In the first step, a weak acid is used in order to release the five carbon sugars from the hemicellulose. In the second step, a stronger acid is used in order to free the six carbon sugars the cellulose component) which is surrounded by a protective binder (lignin).
- The basic premise behind adding a plasma step to the pretreatment process, is to aid the second acid step in removing the lignin component.
- In doing so, a plasma treatment was added in between the two pretreatment steps in order to evaluate the influence of the plasma on the lignin component.
- From the physical and chemical analysis, the biomass substrate was degraded and the lignin capability for protecting the underlying sugars was decreased.

- Plasma treatments were completed at treatment times of 10 seconds and 10 minutes. Additionally, the electrode polarity was varied.
- Two plasma chemistries were studied in order to determine if there was an effect from the radicals in the plasma on the production of fermentable sugars. The two gas mixtures are; 5.6% oxygen in helium and 5.6% air in helium.
- High-performance liquid chromatography (HPLC) was used to measure the xylose and glucose content of the products.
- A negligible difference was found for on sugar production using different electrode polarity.
- Additionally, a negligible difference between the two plasma chemistries was found.
- Overall, the greatest effect was found with changes in plasma exposure times with the biomass.
- High performance liquid chromatography (HPLC) of the 10 min plasma treated samples found for both chemistries, the production of five and six carbon sugars was about 50% greater than without a plasma treatment.
- Additionally, it was determined with both chemistries, the production of five and six carbon sugars was about 8% greater than without a plasma treatment at the 10 sec pretreatment time.
- Analysis with scanning electron microscopy (SEM) revealed the degradation of the biomass after each treatment step. Micrographs from the untreated biomass sample showed the pores and trachea of the biomass sample undisturbed. Little or no evidence of cracking or physical degradation was observed in the micrographs of the untreated biomass samples.
- Micrographs after the first acid hydrolysis step indicate swollen pores after hydrolysis.

- The resulting micrographs from plasma treatments in both plasma chemistries indicate more severe swelling of the pores, cracking and bubbling of the trachea surface.
- Additional shredding and further deterioration of the trachea wall and lignin component after plasma treatment was evident.
- Through analysis with Fourier transform infrared (FT-IR) analysis the specific peak contributions of the three main biomass constituents; cellulose, hemicellulose, and lignin were determined. The analysis found, after treating the biomass with the first acid step and plasma treatment using either chemistry, the lignin and cellulose peak contributions were degraded.
- Peak shifting of cellulose component indicates the underlying chemical makeup was modified after both treatments.
- The peak contribution at 1426 cm^{-1} (cellulose), shifted after the first acid pretreatment step. After treatment with either plasma chemistry, the peak was completely degraded, and not detected in the spectra.
- Similarly, lignin peak contributions at 1595 and 1510 cm^{-1} were not degraded after the first acid treatment. It was determined, the addition of the atmospheric plasma treatment resulted in the characteristic lignin peaks to be shifted or completely removed from the chemical makeup.
- The resulting increase in sugar production after plasma treatment and further analysis with SEM and FT-IR indicates four possible mechanisms for the degradation of the biomass substrate.
    1) Mechanism 1: Etching of the biomass; removal of the surface biomass components including protective inhibitors.
    2) Mechanism 2: Cross-linking or degradation of cellulose, hemicellulose, and lignin polymers.
    3) Mechanism 3: Functionalization of the biomass substrate.

4) Mechanism 4: Degradation of lignin via oxidation in the plasma environment.

- Since the production of five and six carbon sugars was seen with both plasma chemistries, oxidation of the lignin component is the most likely mechanism by which degradation of the biomass occurs.
- Investigation of species in the plasma chemistry was completed via optical emission spectroscopy.
- Emission lines attributed to atomic helium peaks (388.7 nm, 501.5 nm, 587.5 nm, 667.8 nm, 706.5 nm, and 728.1 nm) were both plasma chemistries. In the 5% oxygen mixture, strong radiation from atomic oxygen lines (777.2 nm and 844.6 nm) and first ionization states of oxygen (446.6 nm, 470.3nm, 492.5nm, and 615.3 nm) was observed. In the 5% air mixture, radiation from the nitrogen second positive (337.1 nm) and the nitrogen first positive system (550-900nm) was found along with strong emission of the γ-band of NO radiation (213 nm, 224 nm, 234 nm, 245 nm, 257nm, 270 nm, 284 nm).
- Chemical analysis from FT-IR spectroscopy and plasma chemistry from OES shows both the lignin and crystalline cellulose components were chemically modified after plasma treatment.
- This indicates the chemical radicals produced in the plasma as a key mechanism to the increase in sugar production.
- From the experimental design, the only process parameter which promoted a significant increase in sugar production was treatment time, and despite the two plasma chemistries producing vastly different chemical radicals, similar increases in sugar production were found in both chemistries.
- Two patent applications have been filed to protect the discoveries from this research effort.

1.4 Summary

Throughout this research effort a central theme was the focus, atmospheric plasmas. Although broad, this theme was later targeted to specific applications using the Willie Sutton approach to research. Remember, Willie Sutton is the famous bank robber who when asked by a reporter why he robbed banks, he replied "because that's where the money is", is similar to the approach we took in applying atmospheric plasmas to solve critical issues in industry and as a nation. Throughout this project, questions were presented to our group and we attempted to solve these issues atmospheric plasma processing. At times precipitated by the need to find money but largely motivated by our curiosity to provide answers to these questions, the core issues of answering these questions and applying a scientific basis was a common theme throughout the project. What was found is although atmospheric plasmas can be a solution, critical questions need to be asked in order solve the addressed problem.

From the fundamental questions found in section 1.3, a central theme developed where it was discovered the plasma chemistry is a key factor in applying atmospheric plasmas to a particular application. Starting with work to apply atmospheric plasmas to issues related not only to food borne pathogens but also largely motivated by the terrorist attacks on the mail system in 2001 and SARS outbreak in 2003, led to new needs for a fast decontamination source. What was found is through implementation of non-thermal DBD based plasma discharge; the oxidative nature of the plasma can be an effective agent in reducing both gram positive and gram negative bacteria. Additionally, when gas prices and the supply of oil began to fluctuate in an almost random motion over the year 2007, motivation was developed in order to find alternatives to petroleum based feedstocks. Again, it was found the oxidative nature of the plasma environment could be equally applied to modify lignocellulosic biomass in order to improve production of fermentable sugars from renewable sources for bioethanol production. Moreover, research into determining the stabilizing mechanisms in order to produce a non-thermal plasma discharge at atmospheric pressure is largely based on the types of chemistries used. This work also found that chemistries largely dominated by an inert atmosphere, can be used with a commercially available power supply for large scale

integration of non-thermal atmospheric plasmas in industry. Further, fabrication of novel thin film materials, once only produced in a low pressure environment, were demonstrated by controlling not only the chemistry but also how the chemistry is transported to a desired substrate. The establishment of a basis for solving these questions was completed by asking what chemistry can be generated in order to answer the question, "can an atmospheric plasma be used to ___". This question was asked many times, and our curiosity to push atmospheric plasmas into new applications is the foundation for this research effort. The details of this effort are contained in the following chapters.

2. Literature Review

2.1 Plasma Impact

With the arrival of the industrial revolution in the early 19th century, many nations were forever transformed from agricultural to industrialized nations. Many consider the invention and further improvement of technologies such as the steam engine for providing the catalyst to the age of mass production by large-scale manufacturing techniques [22]. The term manufacturing is from the latin word "*manu facture*" or "making by hand". The word was used to describe a process by which tools and labor produce items that can be consumed, utilized, or sold. In the modern sense, the term manufacturing refers to the practice of taking raw materials and transforming the materials into finished goods on a large scale and in rapid time. In terms of manufacturing techniques, the role of plasmas are not often credited or referenced as a key component in the manufacturing of raw materials into finished parts and goods. However, from the computer chip that allowed this thesis to be produced, to the hardening of cutting tools, to the deposition of specialized coatings on window glass, plasma manufacturing techniques play a quiet role in keeping the world working.

Plasmas have been utilized in manufacturing processes for over forty years. Although this may seem like a very long time, plasmas in manufacturing are still in a sort of infancy as compared to other manufacturing techniques such as casting. Casting technology has long history, which dates back over 6000 years [23]. Initial use of plasmas in manufacturing was in the semiconductor industry to produce integrated chips (IC's). The plasmas associated with semiconductor manufacturing are contained in a closed vessel and under sub-atmospheric conditions. The conditions create an environment that is favorably to fabricate complex circuits.

From this initial birth of using plasmas to manufacture IC's, a wide range of new applications have been pioneered for use in other industries. The applications have continued the long tradition of using plasmas in a closed batch process (i.e. at lower pressures), but newer applications in the past 15-20 years have begun to investigate the role

of plasmas at ambient conditions (i.e. atmospheric plasmas) [3, 6, 24-44]. These applications of plasmas in manufacturing have given birth to a term "Plasmas-Aided Manufacturing" to describe the plasma manufacturing process [45].

2.2 Plasma-Aided Manufacturing

The application of plasmas in manufacturing has grown at an exponential rate [45]. Today, plasma-aided manufacturing impacts many industries. The cross-disciplinary nature of industrial plasma research has resulted in a direct impact on almost every high tech industry. The use of industrial plasmas in high tech markets is worth billions of dollars per year [45]. As such, the range of applications for industrial plasmas continues to expand. The present and future applications of plasmas include:

- Advanced fabrication techniques of IC's
- Anticorrosion coatings on metal surfaces
- Environmental remediation
- Lighting
- Production of new chemicals and material systems
- High performance ceramics
- Actuators for next generation airplanes
- Electro-surgery
- Improved combustion techniques
- Microplasmas for gas sensors, plasma diagnostics, and lab-on-the-chip applications.

Industrial plasmas are often classified by the pressure regime of the plasma process. As an example, Figure 2.1 describes the dependence of many plasma-aided manufacturing techniques as a function of pressure.

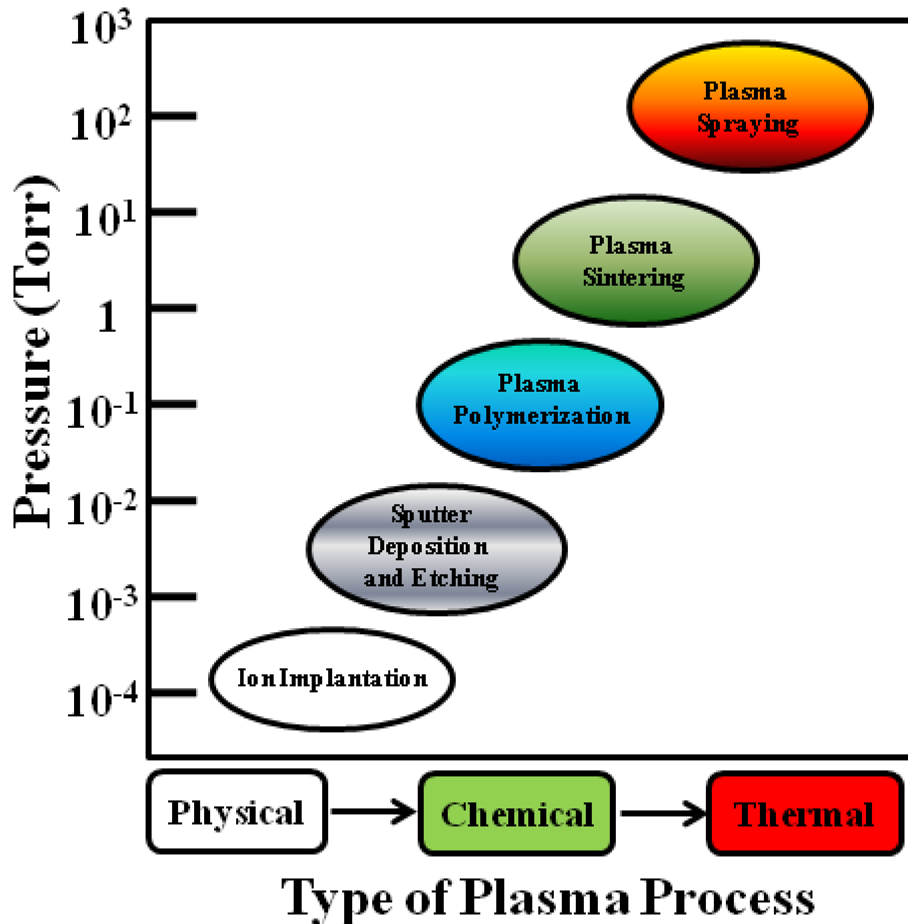

Figure 2.1: Plasma-aided manufacturing techniques as a function of various pressure regimes (based on [45]).

Many operating parameters control a plasma manufacturing process. To name a few, these parameters can include gas composition, flow rates of gases, reactor design, power, and applied frequency (direct current (DC), radio-frequency (RF), microwave, etc.) of the power source. These external process variables control the generation, flux, densities, and energies of the electrons, ions, radicals, and neutrals in the plasma environment and ultimately control the outcome of manufactured product.

The complexity associated with plasma processing has historically resulted in process development coming first from an empirical method with the theoretical understanding

coming after the process is developed. Although this method is not a preferred method for process development, many plasma assisted processes and products have been successfully developed through this methodology. As such, new plasma applications require an understanding of plasma formation, behavior of plasmas, and how the characteristics of plasmas can be tailored to a particular application.

In the following sections, a presentation of the physics and chemistry associated with generation and operation of a plasma will be made. The sections will draw on comparing and contrasting how plasma behavior and impact as a manufacturing process can change at varying pressure regimes. Lastly, the sections will discuss the operating modes of atmospheric plasmas and in particular, the dielectric barrier discharge as a process to be used in next generation plasma-aided manufacturing techniques.

2.3 Generation and Collisional Behavior of a Plasma

Plasmas are ignited by the transfer of energy to a gas by electric currents, electromagnetic radiation or thermal energy. Typically, electrical energy is transferred to a neutral gas through collisional events with electrons. The result is generation of a fluid containing electrons, ions, photons, metastable species, and species in the ground and excited states. From a macroscopic view, a plasma is electrically neutral but free charge carriers allow for the plasma to be conductive. The conductivity of a plasma is dependent on the number of charge carriers in a plasma (n), electron charge (e), the mass of the charge carrier (m), and the collision frequency of the charge carriers (υ_{ei}). Depending on equilibrium conditions of the plasma, the plasma conductivity can vary greatly according to the following relationship where σ is the plasma conductivity, $\sigma = \left[\frac{n_e e^2}{m_e \upsilon_{en}} \right]$. Additionally the plasma conductivity is dependent on temperature according to $\sigma \sim T^{3/2}$, so unlike a metal where conductivity decreases with increasing temperature, the conductivity in a plasma increases with temperature.

When viewed on a microscopic level, the plasma is a fluid, similar to a gas or liquid with an equal number of electrons and ions. When this fluid is viewed in small volumes, the large size difference between electrons and ions (~1:2000) creates a plasma potential. When viewed in large volumes, this fluid is assumed to have an equal number of negative and positive charges. This state of an equal number of positive and negative charge carries is referred to as quasi-neutrality [46].

The type of collisions which can be found in a plasma are 1) elastic collisions where the kinetic energy of the neutral particle and electron is conserved and 2) inelastic collisions where at least some of the kinetic energy of one of the particles is transformed into internal energy for the other particle. Elastic collisions between electrons and background species are the most simple to consider. Due to the large size difference between an electron and background gas molecule, the electron changes direction without changing speed, but the background atom is relatively unaffected by the collision and energy is conserved by the electron but understanding how plasma formation takes place requires a description of the different inelastic collisions.

One of the most common collisional processes in a plasma is electron impact ionization where the primary electron removes an electron from a neutral atom (A). The result of this process is production of a positive ion (A^+) and two electrons.

$$\mathrm{e{+}A \rightarrow 2e{+}A^{+}} \text{ Electron Impact Ionization} \qquad \text{(Reaction 2.1)}$$

The electron ionization process produces two electrons, which in turn multiplies and results in a cascade or avalanche of electron and ion generation. This multiplication process provides the fuel for a plasma discharge to be maintained.

A secondary inelastic collision process is excitation, where the bound electron is excited to a higher energy level within the atom. The excited state is represented by superscript asterisk and can be found in Reaction 2.2 and is referred to as a metastable atom (A^*).

$$e + A \rightarrow e + A^{*} \text{ Electron Impact Excitation} \qquad \text{(Reaction 2.2)}$$

The process occurs by electron impact excitation and is important in producing two other ionization processes, metastable-neutral ionization and electron-metastable ionization. In the metastable-neutral collision process, a metastable atom collides with a neutral atom. The neutral atom can become ionized if the ionization energy of the neutral atom (B) is less than the excitation energy of the metastable (A^*). The metastable-neutral ionization process is known as Penning ionization and can be seen in the following reaction.

$$A^* + B \rightarrow e + B^+ \text{ Penning Ionization} \qquad \text{(Reaction 2.3)}$$

Similar to Penning ionization, a metastable can be ionized by electron impact and is depicted by the following process.

$$e + A^* \rightarrow 2e + A^+ \text{ Electron-Metastable Ionization} \qquad \text{(Reaction 2.4)}$$

In the electron-metastable ionization process, the metastable atom is already excited to a higher energy state and less energy is needed to fully ionize the metastable.

The characteristic glow in a plasma discharge is generated by relaxation of excited atoms and molecules. Relaxation is a result of excited atoms or molecules decaying from unstable excited states. The electron configuration returns to its ground state in one or several transitions. The transition period can last from nanoseconds to seconds depending on the atom and molecule but at each transition a characteristic photon of light is emitted. Found in Figure 2.2 is the energy level diagram for helium [47]. Helium is a two electron system and the energy levels in the electronic states are separated into two multiplet systems, a singlet (1^1S) and triplet (2^3P). Electronic transitions for the singlet system at 501 nm, 667 nm, and 728 nm are shown along with transitions for the triplet state at 388 nm, 501 nm, and 706nm. These transitions have specific energies and each transition can be detected through analytical techniques such as optical emission spectroscopy.

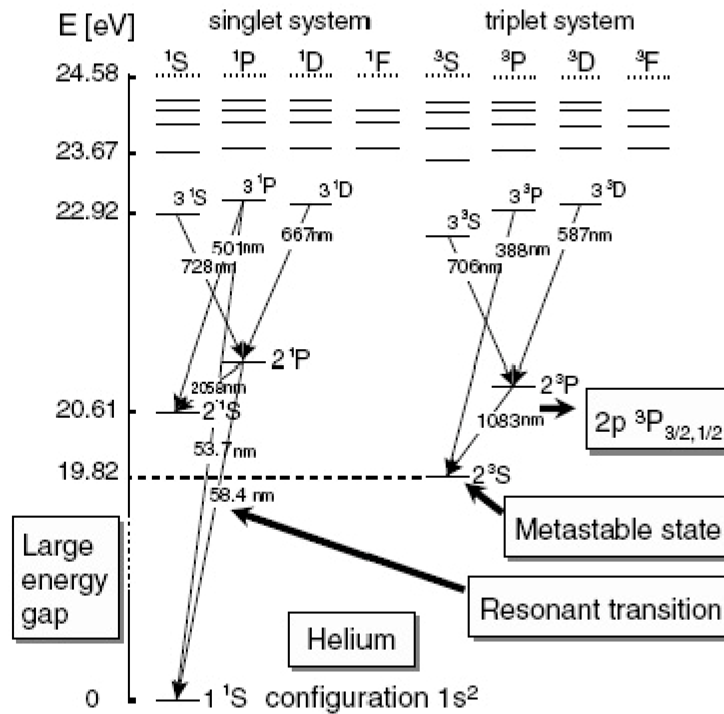

Figure 2.2: Atomic energy level diagram for helium with both the singlet and triplet transition states [47].

The other key collision process in the gas environment is recombination. As relaxation is the opposite of excitation, the opposite of ionization is recombination [46]. Recombination is the process where an electron recombines with an ion to form a neutral atom. Due to the large size difference between an ion and electron there are energy and momentum considerations. The conservation of energy and momentum are satisfied when an electron and ion recombine and collide with a third body, either a wall in the plasma environment or neutral gas atom. At higher pressures, the probability of recombination increases due to the increase in neutral species. The increase results in many new “walls” for recombination to take place. Recombination is also possible in a two body reaction if an electron and neutral combine to form a negative ion. Although not as likely as a three body reaction, it is possible for a negative ion to collide with a positive ion and form one neutral atom.

Ionization of molecular species such as nitrogen, oxygen, and carbon tetrafluoride undergo a process called dissociation. The process of dissociation breaks apart a molecule into two ions. As with ionization, dissociation is a result of electrons with energies over the threshold for dissociation colliding with molecular species, i.e. above the bond energy of the molecule. Typically, dissociation results in a plasma environment with enhanced chemical activity. Two common examples are provided below. Both reactions are used in the semiconductor industry to etch photoresists.

$$e + O_2 \rightarrow e + O^- + O^-$$
$$e + CF_4 \rightarrow e + CF_3^- + F^-$$

Dissociation Equation (2.5)

2.4 Plasma Classification

Once a plasma is initiated, the amount energy supplied to a gas gap controls the temperature of the plasma. "Hot" plasmas are produced in environments where large amounts of energy applied to the gas gap, results in gas heating of the neutral species. The result is a high intensity discharge. A plasma is defined as hot when the electron temperature is at or near the background gas temperature, $T_e=T_{gas}$, where the background gas contains "heavy" particles such as ions, molecules, and neutral species.

From the research community, hot plasmas are referred to as thermal or equilibrium plasmas. This description comes from the definition that when $T_e=T_{gas}$, the plasma is in a state of local thermodynamic equilibrium (LTE). The LTE state implies local areas of the plasma environment have an equilibrium temperature. Hot plasmas approaching the LTE criterion have gas temperatures around 5,000-30,000K and are useful for such applications as welding, plasma spraying of materials, arc lamps, and production of energy from nuclear reactors. Figure 2.3 shows a schematic for an arc-lamp using a thermal discharge as used by Auguste-Arthur de La Rive and Sir Humphry Davy for lighting in the 19th century [48]. Typical currents required for thermal plasma generation can range from 10-1000 A.

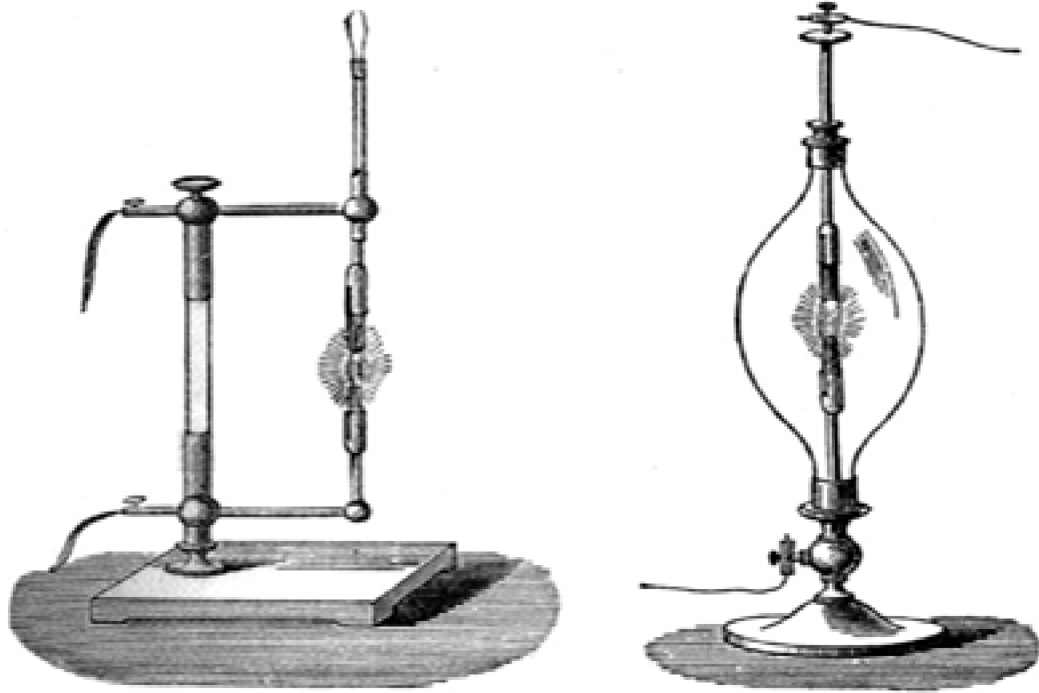

Figure 2.3: Schematic of early arc lamp as used by de la Rive and Davy [48].

From the description of thermal plasmas, the characteristics are not preferred for materials processing. For example, surface treatment of thermally sensitive materials such as polymers and some low melting point metals like aluminum (T_{melt}=660 C), could result in irreversible damage to the substrates. Additionally, uniform materials treatment is not common with thermal plasma treatment since the discharges are normally a collection of micro-arcs and when viewed on the microscopic level create local non-uniform temperature zones. As a result, increasing materials research is focused in working with cold non-equilibrium plasmas (non-LTE).

Alternatively, the applied electrical energy used to generate a “cold” non-equilibrium plasma is used to energize free electrons rather than heat the background gas species. The discharge is characterized by a rather high electron temperature compared to the background gas temperature, $T_e >> T_{gas}$. Electron temperatures can reach above 100,000K while the gas

temperature remains at or near room temperature (~300-1000K). Due to the non-equilibrium characteristics of the discharge, a cold plasma discharge offers a wide range of chemical freedom for industrial applications. The high electron temperature increases inelastic collisions in the plasma. The increase in ineleastic collisions helps to sustain the plasma through electron-impact ionization events that help to enrich the chemical nature of the plasma environment. An added feature of the cold plasma discharges is the wide variety of external controls in the plasma environment for tailoring the cold plasma into particular applications. These controls can be defined as:

- Chemical structure (the working gas defines the structure and nature of the species in the plasma environment);
- Discharge configuration (plasma volume, electrode or electrodeless discharge, and frequency range of operation can influence plasma generation);
- Pressure (0.01 Torr to atmospheric pressure where operation at higher pressures reduces the mean free path and can potentially push the discharge towards to equilibrium or arc like discharge);
- Electromagnetic field structure (electric and magnetic fields can be used to enhance the plasma environment).

Figure 2.4 shows a graph of how electron and gas temperatures behave in a plasma at various pressure regimes. The graph illustrates that at lower pressures, a non-equilibrium regime is found ($T_e >> T_{gas}$). This regime has been heavily implemented in the semiconductor industry for fabricating IC's. The graph also implies plasmas found at higher pressures (atmospheric plasmas) are only found in an equilibrium regime ($T_e = T_{gas}$). In later sections of this dissertation, new techniques for generating atmospheric plasmas in a non-equilibrium regime will be shown along with new application areas for plasmas and materials processing. First, a description of plasma formation (gas breakdown) will be discussed.

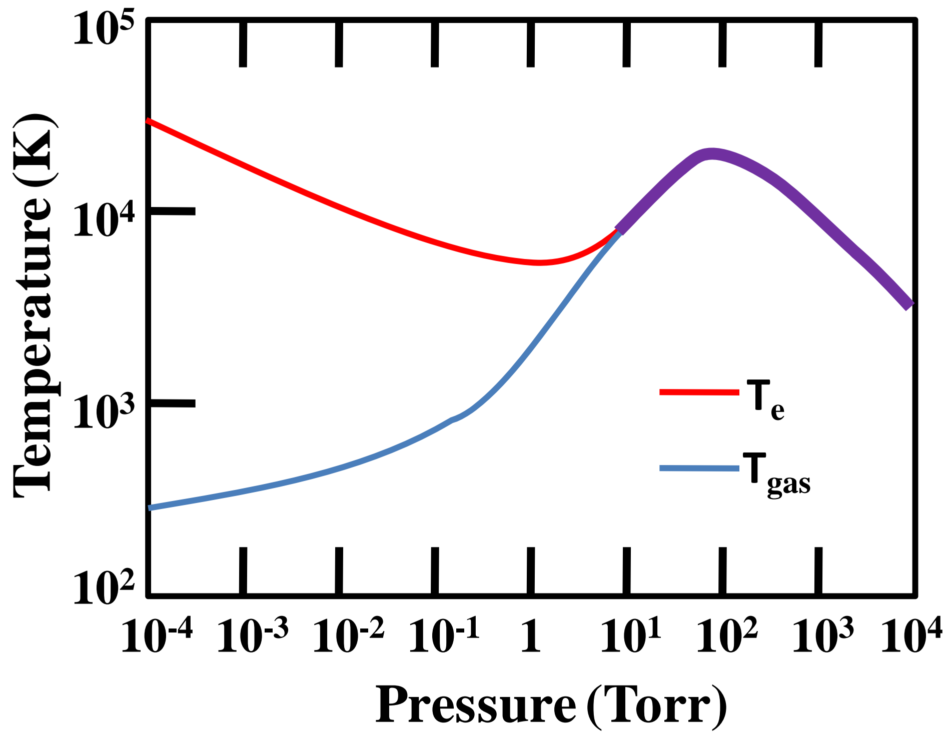

Figure 2.4: Electron temperature and gas temperature as a function of pressure [7].

2.5 Gas Breakdown

To understand gas breakdown conditions, one must consider the physical process of gas breakdown. The simplest breakdown occurs in a planar gas gap of length *d* between two electrodes of opposite polarity as shown in Figure 2.5.

Figure 2.5: Capacitive planar discharge gap, separated by distance, d, with electric potential E.

The physical phenomenon of gas breakdown starts with an applied electric field energizing free electrons in the gas gap. Under the influence of the electric field, the free electrons grow into an electron avalanche. The path of the electron avalanche can take many forms and the resulting plasma discharge can vary greatly. Depending on the voltage applied to the gas gap and gas used in the process, very different breakdown conditions exist. In general, breakdown is a threshold where breakdown only occurs when the electric potential of the gas is above the threshold voltage. Generally, the gas and electrode material determine the threshold voltage. The threshold voltage is referred as the breakdown voltage and is calculated as a function of the product of the pressure p and gap distance d. Understanding the resulting discharge conditions directly impacts the application of plasmas to industrial processes. A short summary of the two gas breakdown mechanisms is provided in the following sub-sections.

2.5.1 Townsend Breakdown

The work leading to a definition for Townsend breakdown was first completed by Druyvesteyn and Penning in 1940 [49]. One of the famous graphs from this work is still used today to characterize plasma discharges, this graph is depicted in Figure 2.6.

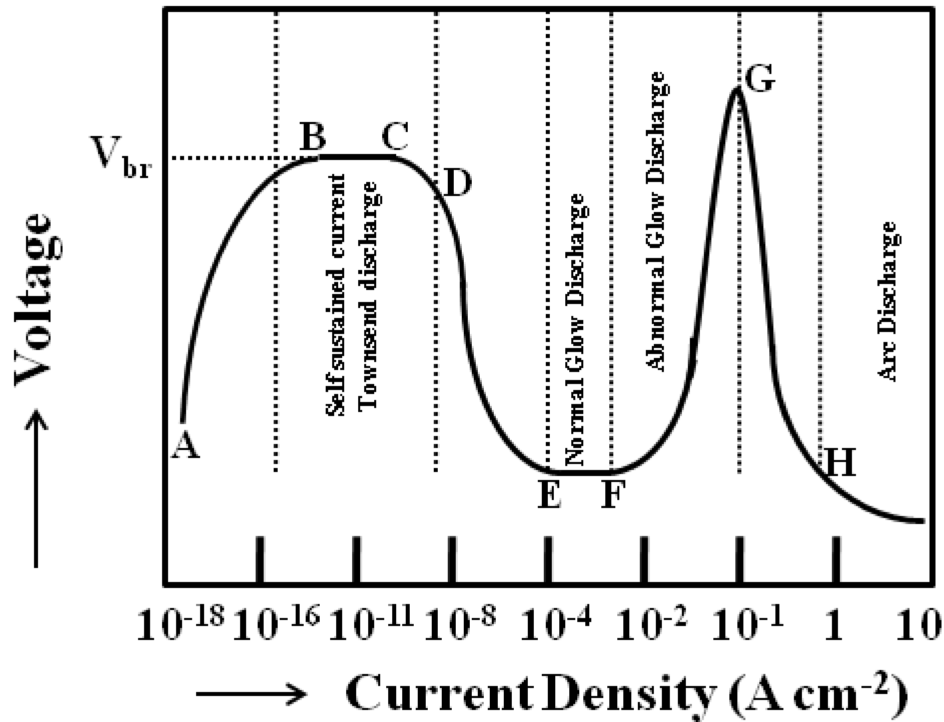

Figure 2.6: DC discharge characterization (based on [49]).

From Figure 2.6, points A→B describe a region where the discharge is non-self-sustained and an external power source is required to sustain the current in the discharge. At the breakdown voltage (V_{br}) for plasma initiation, point B, the discharge transitions into a self-sustained region, it is this region between points B→C, which is defined as a Townsend discharge (dark discharge). In this region, the Townsend or dark discharge is characterized by a low current density. The low charge density in the plasma has little to no influence on the applied electric field and the degree of ionization is so low that little to no light is emitted from the plasma. In the region C→D, the local electric field exceeds the breakdown potential of the neutral background gas and electrical breakdown occurs. A dark discharge occurs from regions D→E due to the discharge not being visible to the eye and finally at point E the discharge transitions to a glow discharge regime. In the region from E→F, the current found in the discharge is enough to sustain the ionization processes of the

background gas and the discharge becomes visible to the eye. As the current is further increased from F→G, the discharge transitions to an abnormal regime and the voltage behaves more as a function of the current in the discharge. At point G, the discharge makes a transition from glow to arc and the plasma becomes very conductive until at point H where the plasma resembles a thermal arc

The breakdown voltage (V_{br}) for every gas (and cathode material) can be found very easily and is only dependent on the product of the pressure (*p*) and electrode gap distance (*d*). This relation is found in Equation 2.1:

$$V_{br} = f(pd) \tag{2.1}$$

the *pd* relationship and role in breakdown voltage for plasma discharges was first determined by Paschen in 1889 . The empirical relationship found by Paschen determined a minimum voltage point for gas breakdown to occur. Figure 2.7 describes the relationship between breakdown voltages as a function of pressure for various inert and molecular gases [50].

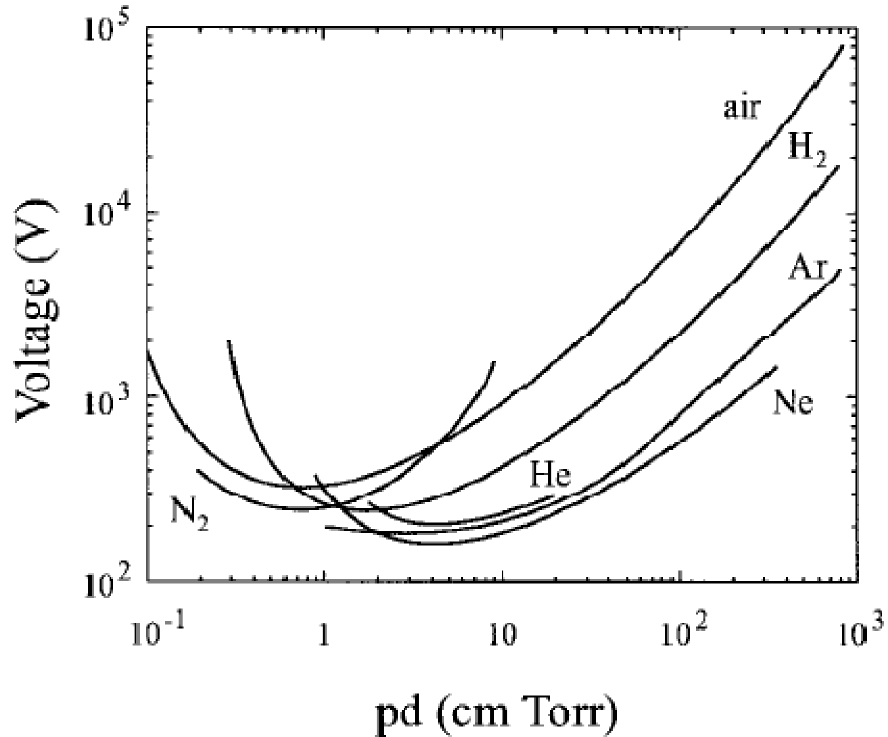

Figure 2.7: Paschen breakdown voltages for various gases as a function of various pressures and gap distances (Pd) (based on [50]).

The relation found in Equation 2.1 can be used to reduce a Paschen curve for any gas. The curve is found by simply obtaining the values for the ionization coefficient α, and coefficient of secondary electron emission γ. The ionization coefficient α is the first Townsend coefficient and is defined by the number of electrons produced in a single electron path of 1 cm in the direction of the electric field. The ionization coefficient is related to the electron drift velocity v_d and ionization rate coefficient ($k_i\left(E/n_o\right)$) as:

$$\alpha = \frac{1}{v_d}(E/n_o)n_o \qquad (2.2)$$

where the first Townsend coefficient α is described by the probable number of ionizing collisions per meter of travel, which is a relationship that is dependent on the pressure and is found by the similarity parameter α/p. The similarity parameter is dependent on the reduced

electric field E/p and is found from $\alpha / p = f(E / p)$, where the dependence is found in units of ion-electron pairs per mTorr. Constants for the reduced electric filed for various inert and molecular gases are listed below in Table 2.1 [2].

Table 2.1: Electric fields for Townsend breakdown of 1 cm size gap at atmospheric pressure.

Gas	E/p, kV/cm
Air	32
Hydrogen	20
Helium	10
Oxygen	30
Chlorine	76
Neon	1.4
Nitrogen	35
Argon	2.7

From the relationship defined in Equation 2.2, when a homogeneous electric field is applied to a gas gap, each primary electron generated near the cathode produces $\exp(\alpha d) - 1$ positive ions in the gas gap [2]. An illustration of the Townsend breakdown mechanism is depicted in Figure 2.8. Positive ions produced in the gas gap per one electron move to the cathode to eliminate $\gamma * [\exp(\alpha d) - 1]$ electrons by secondary electron emission from the cathode. The coefficient of secondary electron emission γ is referred to as the second Townsend coefficient. The coefficient is dependent on the gas, material used for the electrode, and reduced electric field E/p (related to ion energy).

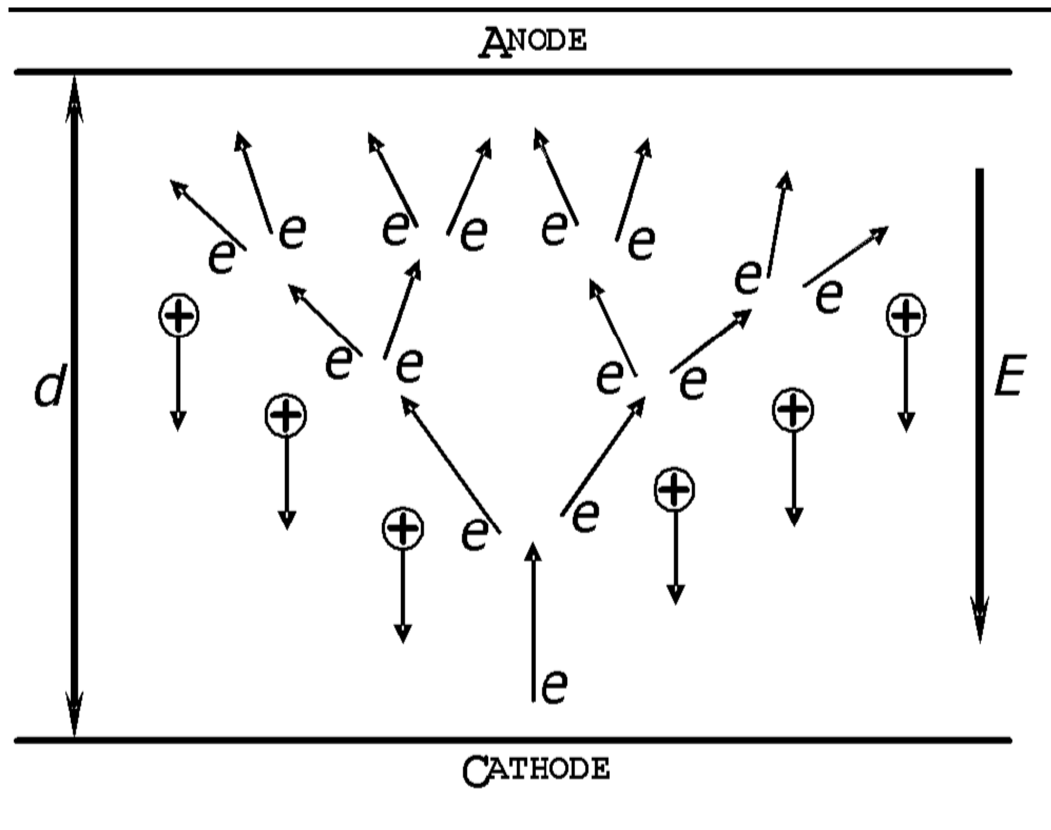

Figure 2.8: Illustration of the Townsend breakdown mechanism where each primary electron generated near the cathode produces exp(αd) -1 positive ions in the gas gap [2].

Using this information, the Townsend mechanism of self-sustained breakdown can be derived by finding the total current at the cathode i_{cath}. By taking the current in the primary electrons i_o and current from secondary electron emission, the total cathode current can be defined as:

$$i_{cath} = i_o + \gamma i_{cath}\left[\exp(\alpha d) - 1\right] \tag{2.3}$$

With the absence of ion current at the anode, the total current in the external circuit is found to be equal to the total current at the anode where the total current can be described as:

$$i = i_{cath}\exp(\alpha d) \tag{2.4}$$

By inserting Equation 2.3 into Equation 2.4, the Townsend current amplification model for a self-sustaining plasma discharges can be found in Equation 1.5:

$$i = \frac{i_o \exp(\alpha d)}{1 - \gamma\left[\exp(\alpha d) - 1\right]} \tag{2.5}$$

From Equation 2.5, the discharge is in a non-self sustained mode when the denominator is positive. Once the electric field becomes significantly high, which in turn amplifies the ionization coefficient α, the denominator of electric field goes to zero and the transition to self-sustained current results in gas breakdown. Equation 2.6 controls the condition for ignition of a self-sustained current in the gas gap. The current is self-sustained by secondary electron emission from the cathode and describes the Townsend breakdown mechanism:

$$\gamma\left[\exp(\alpha d) - 1\right] = 1,\ \alpha d = \left(\frac{1}{\gamma} + 1\right) \tag{2.6}$$

The critical electric field for breakdown of gases in the Townsend discharge can be derived by relating Townsend coefficient to the electric field with the following relation:

$$\frac{\alpha}{p} = A \exp\left(-\frac{B}{E/p}\right) \tag{2.7}$$

where A and B are constants which characterize the gas environment. By combining Equations 2.6 and 2.7, the experimental conditions leading to the easiest breakdown can be found by Equation 1.8:

$$V_{br} = \frac{B * pd}{\ln(A * pd) - \ln \ln\left[\left(1+\gamma\right)\gamma\right]},\ (pd)_{\min} = \frac{2.72}{A} \ln\left(1 + \frac{1}{\gamma}\right) \tag{2.8}$$

Numerical constants for A and B to calculate the first Townsend coefficient α can be found in Table 2.2 [2].

Table 2.2: Numerical constants for parameters A and B for calculation of Townsend coefficient α.

Gas	A, cm^{-1}-Torr	B, V/cm Torr
Air	15	365
Carbon Dioxide	20	466
Hydrogen	5	130
Neon	4	100
Nitrogen	10	310
Water	13	290
Helium	3	34
Argon	12	180

2.5.2 Streamer Breakdown

The Townsend discharge is generally found at low *pd* values. At higher pressures (*pd* < 4000, Torr cm), and at large discharge gaps (d>5 cm) a second type of breakdown occurs, spark or streamer breakdown. Streamer breakdown occurs when an over-voltage is applied to the planar gas gap. Streamers provide breakdown in thin local channels and breakdown does not have a direct relationship to electrode material or other phenomena such as secondary electron emission as in Townsend breakdown. In contrast to Townsend breakdown, streamer breakdown cannot be described by the multiplication of electron avalanches, where the fundamental property of a Townsend breakdown is for a single electron avalanche does not disturb the applied electric field. This property requires the number of electrons in the avalanche head to stay below a critical value N_{cr} of about 10^8:

$$\exp(\alpha d) \leq N_{cr} \tag{2.9}$$

If the electron amplification reaches or exceeds this critical value before arriving at the anode, a local space charge accumulates and a completely different discharge results, streamer breakdown. The concept of streamer breakdown is based on a thin conductive

plasma channel propagating through the gas gap. The thin channel ionizes the gas in front of the charged head as a result of the strong electric field induced by the charge head itself.

A streamer forms when a high amplification ($\exp(\alpha d)$) is present. As shown in Figure 2.9, the space charge distribution within the avalanche has the shape of an elliptic paraboloid due to electrostatic repulsion of electrons.

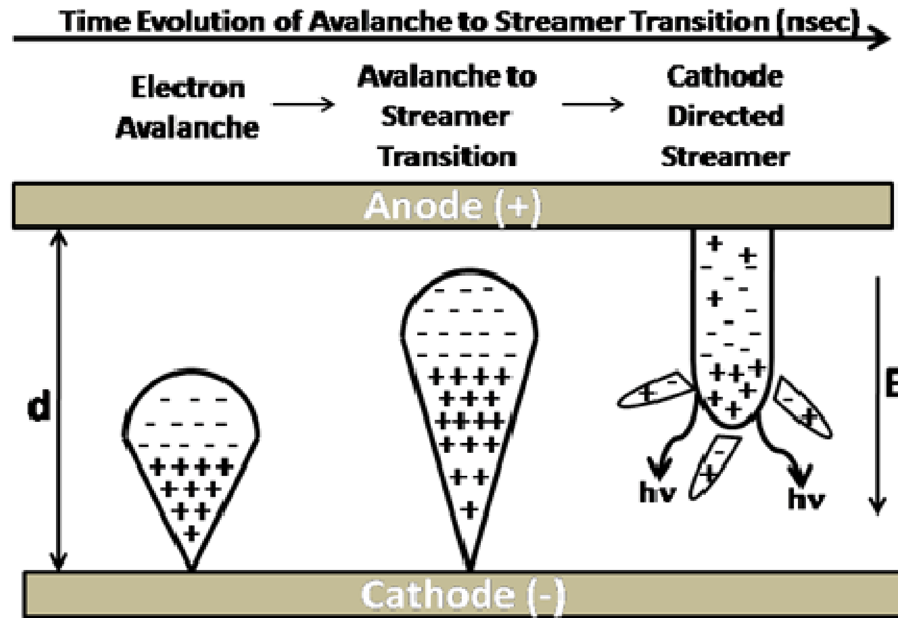

Figure 2.9: Streamer propagation head, time evolution of electron avalanche to streamer transition in nanoseconds (based on [2]).

The smaller electrons are concentrated at the head of the avalanche while the less mobile ions are distributed within the rest of the avalanche. The distribution of electrical charges produces a second electric field E'. The combination of the external field E with E' distorts the location of the avalanche and the net effect influences the process of ionization. The combined fields in front of the avalanche head adds up to a stronger field than E. Consequently, ionization is greatly enhanced at the streamer location. For an electron avalanche to transform to a streamer, a high amplification ($\exp(\alpha d)$) must be reached, or in

other words the space charge induced electric field E' must be comparable to the applied field E. The space charge electric field can be written as $E^{'} = e\frac{N_e}{R^2}$, if we assume the space charges in the avalanche are confined within a radius R where n_e is the total number of electrons in the avalanche, then the amplification can be expressed as the total number of electrons, $n_e * \exp(\alpha d)$. If E' equals E, streamer breakdown occurs where the fundamental criterion for streamer breakdown is found in Equation 2.10.

$$E^{'} = e\frac{N_e}{R^2} = \frac{\left(e \times \exp(\alpha d)\right)}{R^2} = E \tag{2.10}$$

This fundamental criterion for streamer breakdown is referred to as the Meek condition for streamer formation where the amplification factor $\exp(\alpha d)$ is approximately18-20 [3].

2.6 Low-Pressure (Vacuum) versus Atmospheric Plasmas

As the previous sections have described, operating considerations surrounding *pd* values can greatly change how a plasma behaves. This behavior greatly influences how plasmas are used in industrial manufacturing techniques. Low pressure plasmas serve many purposes for materials processing. Since the plasma environment is contained within a closed vessel, the plasma can be controlled very easily. In addition, the plasma is generally cold and applications such as deposition, etching, and surface modification are easily replicated in a low pressure environment. The limitations of low pressure plasmas are the capability to manufacture in a continuous manner. By the nature of operating in a vacuum (10 mTorr to 10 Torr), costs associated with capital equipment are higher. The large infrastructure associated with producing a low pressure plasma includes: closed vessels, large pumping systems, other controls for operation, and a larger footprint on the manufacturing floor adds complexity and cost to the process. Alternatively, atmospheric plasmas offer both economic and technical justification for use over low pressure plasmas. Since an atmospheric plasma is operated at ambient conditions, potential cost savings associated with higher throughput and faster production rates validate atmospheric plasma processing as a next generation

plasma-aided manufacturing processes. Additionally, lower capital costs associated with equipment and line space on the manufacturing floor provides further benefits to develop atmospheric pressure plasmas for plasma-aided manufacturing techniques.

One challenge that still holds for atmospheric plasmas in the manufacturing environment is the ability to produce a homogeneous and non-thermal plasma. Recent research has resulted in the development of many sources and configurations that can produce a homogeneous and non-thermal environment. Configurations such as the atmospheric pressure glow discharge (APGD), dielectric barrier discharge (DBD) and atmospheric pressure plasma jet (APPJ) have been demonstrated to operate in this manner and as such atmospheric plasmas are gradually gaining acceptance into plasma-aided manufacturing techniques [32, 41, 44, 51]. One limiting factor preventing full integration of atmospheric plasma processing is a complete understanding of the physics and mechanisms involved with producing a plasma at ambient conditions. The next sections of this dissertation, a discussion into the physics and mechanisms associated with producing a non-equilibrium discharges at atmospheric pressure will be reviewed. In these sections, the dielectric barrier discharge will be highlighted and key challenges for implementation into manufacturing will be investigated.

2.7 Non-Equilibrium Atmospheric Plasma Discharges

Non-equilibrium discharges at atmospheric pressure can be generated in many configurations. The configurations are generally specific to industrial application so the different techniques for producing the discharges are very broad [20, 37, 52-55]. The unique features and benefits of non-equilibrium plasma processing at atmospheric pressure present many solutions for industry. Non-equilibrium plasmas exhibit electron energies that are much higher than the ions and background neutral species. The reaction environment in non-thermal atmospheric plasma exhibits a higher level of ionization, dissociation, and excitation. With the relatively low energy associated with the ions and neutrals, the reaction environment tends not to increase the gas enthalpy so that materials in contact with the plasma have no thermal damage. With a low gas temperature, new applications for surface treating thermally sensitive substrates such as biological cells and polymer substrates are possible [56-68]. Additionally, collisions at atmospheric pressure lead to the utilization of useful third body reactions for the production of highly oxidizing species such as ozone and excimers (excited dimmers and trimmers) for illumination applications in VUV sources [20, 33, 42, 69-73]. In the past few decades, atmospheric discharges have been developed for applications related to the surface treatment of materials. These applications are mainly focused towards modifying the surface chemistry via deposition, etching or functionalization of the surface bonds [8-12].

Historically, the most common configurations have been operated in a jet or parallel plate [13]. Due to the difficulty in sustaining a discharge at atmospheric pressure, new challenges are presented for stable operation of the plasma. At atmospheric pressure, higher voltages are required for gas breakdown. The higher voltages often lead to arcing between the electrodes and a tendency for streamer like breakdown. To prevent arcing, pointed electrodes or insulating barriers have proven feasible in producing a stable discharge [14-18].

2.8 Barrier Discharge

Barrier discharges are a simple way to generate a stable and in some conditions, a uniform discharge. Starting with research by Siemens in 1857, a barrier discharge was found

to generate ozone for water purification applications [19]. The barrier discharge is often referred to as the dielectric barrier discharge (DBD) or silent discharge. The silent discharge was used as a description for the low amount of sound emanating from the discharge source. The characteristic feature of the DBD is insulating barriers are placed in contact with one or both electrodes. Due to the characteristic dielectric barrier, DC operation is not possible so a power source with pulsed DC or alternating current (AC) is used to generate the discharge. The applied frequencies vary from line frequency to MHz frequencies. The barrier discharge has found a number of industrial applications including VUV excimer radiation, polymer surface treatment, and more recent advancements in deposition of materials. Typical configurations are found in either a planar or cylindrical geometry as shown in Figure 2.10.

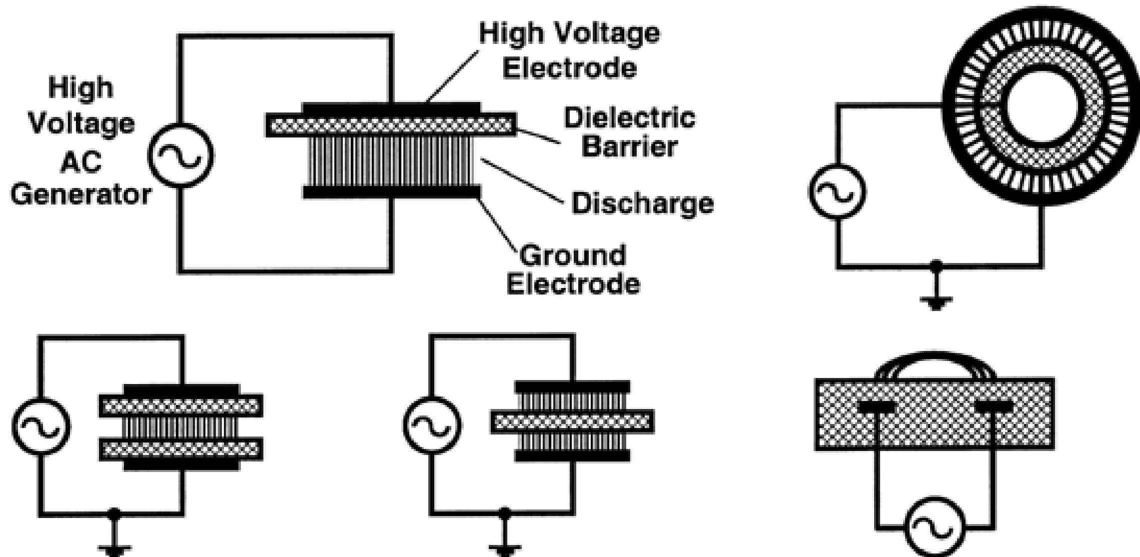

Figure 2.10: Common Dielectric Barrier Discharge configurations in the planar and cylindrical configurations [33].

In both geometries, a dielectric element is present in the current path between the electrodes. Although the dielectric element is present, the discharge still behaves as if the discharge was operated between two metal electrodes. The gas gap in a DBD is typically less than 1mm but discharges in gas gaps as large as several centimeters have been

demonstrated [20]. The placement of the dielectric element between the metal electrodes is for good reason. Due to the high collision frequency at atmospheric pressure the electron avalanche develops much faster. The fast ionization generates a number of highly conductive channels that are referred to as microdischarges or streamers. The mutual relationship between the highly conductive channel and resulting microdischarge results in a discharge that is filamentary and appears random. Physically speaking, under an applied electric field, charge carries move rapidly in the gas gap and charges begin to accumulate on the dielectric surface. The accumulated charges generate an induced electric field opposite to the external field and therefore limit the flow of current and transition to an arc. As a result, the external field is reduced and the electron avalanche decreases. When the applied voltage is reduced to a value below the self-sustaining criterion, the conductive channels are extinguished. During the next half AC cycle, the voltage polarity is reversed and the deposited negative charge accumulates on the opposite dielectric. As a result of the changing polarity and presence of a dielectric element, gas breakdown is easily achieved in a DBD configuration.

In most applications, DBD's are not uniform and the gas gap is filled with numerous microdischarges. Understanding of microdischarges can be drawn from the physics of the formation of streamers and how the conductive channel propagates and degrades [2]. Electrons in the gas gap form streamers. The streamers are formed through the half cycle. The electrons are dissipated in less than 100 ns but the heavier ions can last in the gas gap for several microseconds. In the half cycle, the conducting channel deposits electrons onto the dielectric barrier covering the anode. The charge accumulation prevents new streamers from forming until the next half cycle where the cathode and anode are reversed. These conditions prevail as long as the voltage applied to the gas gap is not much higher than the breakdown voltage necessary for gas breakdown. The polarity of the external field is reversed every 25 ms (applied frequency=20 kHz). After the polarity is reversed, the deposited electrons on the anode result in the formation of new streamers in the exact location of the previous streamer. The observed effect is a bright filament that appears to local and stationary in a permanent

location. The electron avalanche head distinguishes a streamer and microdischarge. The electron avalanche head develops by direct ionization from secondary electrons. If the avalanche head is large enough, $\exp(\alpha d) >$ 18-20, than a cathode directed streamer is formed towards the anode. The streamer bridges between the anode and cathode and forms a conducting channel. The conducting channel allows for a large electron current to flow until the local electric field is collapsed by charges deposited on the dielectric and ions left in the gas gap. The groups of local processes (ionization, dissociation, etc.) generated in the gas gap by the local deposition of charges on the dielectric are defined as the microdischarge. Once the electron current is terminated, electron-ion collisions cease, but the remaining high level of electronic and vibrational excitation left in the conducting channel is termed the microdischarge remnant [3].

The microdischarge remnant has been observed as the remaining area where positive ions left in the gas gap slowly move to the cathode, which results in a very low falling ion current. As a result, new microdischarges form in same exact spot. Evidence of this has been observed by Massines et al. through modeling of the DBD where very large ion densities where observed at the anode as compared to the cathode [74]. The decrease in ion current allows the observer of the plasma to see single filaments. Otherwise, if the microdischarge formed at a new location after every half cycle, the discharge would appear uniform. In a DBD, a family of streamers forms a single bright filament or large streamer. The filament is a group of microdischarges that form at the same spot during each half cycle. Since the microdischarge remnant is not fully dissipated each half cycle and a new microdischarge forms in place, generation of microdischarges in a DBD is defined in the literature as forming through a “memory effect” [74, 75].

The current-voltage characteristics of the DBD depend on the operating conditions (frequency, gas type, gap distance, and applied voltage). Depending on these conditions, the current waveform can exhibit either a single pulse per power half cycle or multiple pulses per half cycle. The single pulse per half cycle represents a homogenous discharge where as multiple pulses per half cycle represent a discharge with filamentary character.

Dielectric barrier discharges can exhibit two modes of operation: filamentary mode and glow or homogeneous mode. Although most DBD's are operated in a filamentary mode, a more recent advancement in producing a glow mode discharge has received considerable interest for potential uniform materials processing [54, 58, 76-79]. A brief description of both a filamentary and glow discharge is provided in the next two sections.

2.8.1 Filamentary Mode

In filamentary mode, gas breakdown occurs in a large number of tiny breakdown centers. The breakdown centers are referred to as microdischarges and are generated when an overvoltage is applied to the electron avalanches found in the gas gap. When the space charge in the avalanche head accumulates, extremely fast streamers are formed within the discharge region. The behavior and properties of the microdischarges have been extensively studied both experimentally and theoretically [14-16, 51, 80-90]. Summarized in Table 2.3 are the characteristic properties of an atmospheric pressure microdischarge in air at a 1mm gap distance.

Table 2.3: Properties of microdischarges in a DBD.

Duration	1-10 nsec
Peak Current	0.1 A
Current Density	100-1000 A cm^{-2}
Total Charge	0.1-1 nC
Filament Radius	~0.1 mm
Electron Energy	1-10 eV
Electron Density	10^{14}-10^{15} cm^{-3}
Gas Temperature	Room Temperature
Degree of Ionization	10^{-4}

Microdischarges start when the local electric field necessary for breakdown is reached and extinguish when the field is reduced such that electron attachment and recombination dominate over ionization. The microdischarges spread over the entire dielectric surface and the discharge region can be observed full of streamers. Due to the charge buildup on the dielectric surface, the local field collapses and the microdischarges extinguish within tens of nanoseconds [3]. Recent research has suggested the possibility that the filamentary mode of operation could be completely avoided if the power supply used for the discharge was a pulsed nanosecond source [91, 92]. If a pulsed nanosecond source was used in operation to produce a atmospheric pressure plasma, it has been suggested that streamers would be unable to form since the plasma would be operating at times shorter than the time required for streamer formation [3].

When observing streamers in a plasma they appear chaotic and random. Streamers actually behave in a predictable manner with a memory effect established in both theoretical and experimental work [27, 41]. It is believed as the voltage rises in the gas gap, microdischarges are formed and distributed evenly over the dielectric surface due to the presence of local fields from other microdischarges that have previously formed and as the half cycle progresses, the microdischarges extinguish. When the electrode polarity is reversed, the next microdischarges form at old microdischarge locations due to a "memory effect" from charge accumulation on the dielectrics. As a result, high voltage, low frequency operation tends to spread the location of microdischarges while operation at lower voltages and higher frequencies, tend to reignite old microdischarges in the same location [41]. A more detailed explanation of this effect will be provided in Chapter 4, where the electrical and optical properties of a DBD was studied in the kHz frequency range of operation.

2.8.2 Glow Mode

Operation in a glow mode is essential to uniform and homogeneous treatment of surfaces. Due to interest in obtaining a reliable discharge for industrial applications, recent work in DBD operation has been centered in understanding the exact operation of the mode. A detailed explanation of operation in the glow mode is still not fully understood. However, if

the electric field in the plasma discharge is less than the Meeks criterion for streamer formation, the discharge should operate in avalanche mode (Townsend mode), which is referred to as a dark discharge. In a dark discharge the current limits the rate of formation of primary electrons. Being that the dark discharge is not self-sustaining, the discharge is weak and not useful for practical applications. To transition from a non self-sustaining discharge to a self-sustaining discharge, one electron avalanche must produce $N_p = \exp(\alpha d - 1)$ positive ions. If the production of ions produces one electron from the dielectric surface, a new avalanche will be formed. Once new electron avalanches are formed, the discharge will transition to a self-sustained Townsend discharge where the criterion for dark to Townsend is $\gamma\left[\exp(\alpha d - 1)\right] > 1$, where γ is the coefficient of secondary electron emission. Once in Townsend mode, the current in the discharge is only limited by the dielectric surface. The limitation is overcome when the discharge current reaches a critical threshold value (space charge in avalanche becomes high enough) to cause perturbation in the applied field, which results in a transitions to glow mode.

Critical to the formation of an atmospheric plasma glow discharge is the survival time or "memory effect" of electrons on the dielectric surface. Since secondary electron emission from a dielectric surface depends on absorbed electrons with energies of approximately 1eV deposited between AC cycles, the electrons must survive switching cycles without recombining with positive ions or attachment with negative ions in an electronegative gas. This effect is weaker in electronegative gases due to loss of electrons from attachment.

In this thesis, the DBD configuration was used to outline experiments for investigations of the interaction of plasmas at atmospheric pressure and the decontamination of *Salmonella* spp. and *Listeria innocua*, plasma generation by a new low-frequency power source, development of a new pulsed PE-CVD deposition process at atmospheric pressure, synthesis of amorphous silicon carbon thin films produced by the pulsed PECVD process, and modification of lignocellulosic biomass for improved bioethanol production. Within these

experiments the area of interest was the role of the plasma and resulting chemistry on a particular application.

2.9 References

The references for this chapter can be found in Chapter 10. The references were gathered in one large chapter in order to eliminate duplication and overlap between chapters throughout the dissertation.

3. Equipment and Procedures

3.1 Introduction

The work described in the following chapters was performed in a dielectric barrier discharge (DBD) atmospheric plasma system specifically designed for conducting experiments related to testing the viability of using a DBD in various applications. The experimental results presented in the subsequent chapters were obtained using the equipment and experimental procedures described in the following subsections. A detailed description of each system and the equipment employed is presented below.

3.2 Dielectric Barrier Discharge (DBD) Reactor

The DBD reactor is shown in photographs in Figure 3.1 and Figure 3.2 respectively. The complete system consists of a two aluminum electrodes separated by a variable gap distance. In the experiments described in this dissertation, each electrode was covered with Pyrex dielectrics. To provide a base level of experimental purity and reproducibility, the active plasma environment was enclosed in a quartz chamber. Located on either side of the chamber are stainless steel flanges, which connect to the gas delivery system, rough pumping line, high voltage output of transformer, and grounding system. Other elements such as pressure gauges, thermocouple feed through, and feed through for the substrate heater was also located within these flanges. A dual stage mechanical pump is connected to the bottom flange of the chamber. The pump provides a base pressure of approximately 90 mTorr. Three 500 watt cartridge heaters installed on the bottom electrode allow for the bottom electrode to be heated to 500 C with a type k thermocouple placed on the opposite end of the electrode arrangement to measure temperature of electrode. A Watlow series SD PID controller specially designed with features such as ramping and automatic PID control controls the cartridge heaters.

Figure 3.1: DBD reactor shown in Riddick Hall just after completing the enclosure to house the reactor, pump, and high voltage transformers. To the left is the control rack with the MOD I power supply, function generator, oscilloscopes for monitoring power, and gas monitoring and control system.

Figure 3.2: Updated photograph of the DBD reactor, enclosure, power supply, and other process monitoring controls that were added to the control rack. Additions included a digital oscilloscope, computer to collect data and run the controllers, spectrometers, and substrate heater. Also, new MFC displays in order to accommodate the needs of the different projects in the atmospheric plasma area. Photograph captured in the new Engineering Building 1.

In Figure 3.2, a cylindrical DBD reactor sits next to the original parallel plate reactor. From time to time the enclosure that the original DBD reactor has served the need to try new experimental configurations for different project needs in order to share the power supply, high voltage transformer, and gas controls. Large heatsinks were attached to the outside of the cylindrical DBD reactor in order to control temperature in the reactor environment. A collection of photographs of the original six chamber cylindrical DBD reactor are shown in

Figure 3.3. The reactor was used to process waste biogas such as carbon dioxide and methane produced by hog lagoons into renewable fuels such as methanol.

Figure 3.3: Original cylindrical DBD reactor used to process gases into renewable fuels. The reactor consisted of six independent chambers where the dielectrics in the reactor were syringes used by the medical industry.

3.3 Enclosure

To protect the operator and other personal in the lab from the high voltage and hazardous gas products produced by the reactor, the overall DBD reactor was enclosed in a 36’x72’x34’ enclosure. The enclosure was constructed with the initial thought of separating the active experimental environment from the working components such as pump, mass flow controllers, and high voltage transformer of the DBD reactor. Located in the upper half of

the system is the DBD reactor with vacuum lines running to the bottom of the enclosure to the mechanical pump and out the top of the enclosure to the gas delivery system which is attached on the back of the enclosure. In the lower part of the enclosure, a small storage area and space for the high voltage transformer and optical emission spectrometer can be found.

After initially placing the mechanical pump into the designed area inside the enclosure, vibration issues to the system required moving the pump outside of the enclosure. Four switches were installed to the enclosure to protect the operator from the high voltage. A switch was installed at each access door, one to the main experimental area, one to the bay below the enclosure, and a switch to the door connected to the transformer bay. An additional switch was later installed to the large polycarbonate window to protect the operator from accidentally turning on the high voltage while performing maintenance on the reactor. The four interlocks are connected in series so each switch must be closed in order for the high voltage to be delivered from the transformer to the reactor. A later design built into the new power supply for powering the reactor added an extra step for the operator to turn on the high voltage after an interlocked switch was opened. The design requires the operator to manually push the power button back on to the power supply after the interlock circuit is opened. An exhausted duct was installed on top of the enclosure to protect the laboratory from the toxic gas byproducts produced by the DBD reactor. To protect the system from overpressure, a pressure relief valve was installed to blow at an overpressure of 900 Torr.

One of the features of the system was the vast gas supply for performing a variety of experiments. The initial gas supply consisted of three mass flow controllers hooked up to helium, nitrogen, and oxygen. Over the course of this project, the gas supply was expanded to over ten gases to include such gases as carbon tetrafluoride, ethylene, hydrogen, silane, and CVD capabilities to deposit with such monomers as tetramethylsilane (TMS) and zirconium tert-butoxide (ZTB). Inert gases such as helium, argon, and nitrogen were kept in cylinders next to the system and connected to the system through welded stainless steel lines. Other active but inert gases such as carbon tetrafluoride, carbon dioxide, and 5% hydrogen in

helium were also kept next the system and connected in most cases through welded gas lines. In some cases these gases were connected through either Teflon or polyethylene ¼" tubes to allow for quick interchange between experiments. Connecting through plastic tubing allowed for maximum flexibility and lowered costs in performing various types of experiments. The use of stainless steel tubing with VCR connections was not always feasible within the project scope of this work. In order to adjust to changing demands associated with the project work, we compromised and implemented plastic tubing with Swagelok connections, which are more likely to fail than the more commonly used VCR connections. Flammable and pyrophoric gases such as 2% silane in an inert gas, 100% hydrogen, methane and ethylene were placed in exhausted gas cabinets. The gas cabinets were connected to the building exhaust and sprinkler system. Gas sensors placed inside and outside the gas cabinets were connected to a control system located inside the laboratory to shut down gas flow to cabinets if one of these gases was detected at the sensors. The operational characteristics are as follows; if the one of the gases is detected inside the cabinet the laboratory alarms are set off and all personnel must exit, but if the gas sensors outside the gas cabinet the entire building alarm system are sounded and the building must be evacuated.

3.4 Operation of DBD Reactor

The design of the DBD reactor and associated components took many variations over the course of this project. Additionally the procedures for operating the reactor changed as we learned more about the chemistry in the DBD reactor. Initially, the DBD reactor was left at atmosphere every night after experimentation was completed. This left the system with a considerable amount of water vapor in the chamber and on the walls, as the first phase of this project was not in the new EB1 building but rather the almost 100 year old Riddick Hall. To improve the reproducibility and overall control in the reaction environment, a Granville-Phillips (GP) valve was installed on the system. The GP valve operates similarly to a needle plugging a hole. As the needle is opened a small amount of gas can be dialed into the system. When the DBD reactor is not operating the GP valve is opened to atmosphere to allow for air to be pumped into the chamber by the mechanical pump. The system was

pumped every night above 150 mTorr (above molecular flow) using the dial on the GP valve to regulate air flow. This pumping threshold is critical as below 150 mTorr backstreaming of oil from the mechanical pump can become a problem and hydrocarbons from the pump oil can redeposit on the chamber walls and affect the control of the processing environment.

3.5 Dielectric Selection

Experimental work with the dielectrics used as the barriers in the reactor also took on evolutionary steps of development. Initial work with the barriers used plain float glass that the group had leftover from low pressure chambers in the laboratory. As the work progressed, it was found when sudden increases in were heat applied to the float glass or arcing around the dielectrics from overvoltage from the power supply, the float glass would shatter very quickly. This was not so much a concern until we found working within these processing constraints limited experimental work. These motivations lead to finding a suitable replacement for the float glass. Aluminum oxide or alumina, Al_2O_3, was selected to be tested as a suitable dielectric replacement. Alumina is known to be able to withstand high temperatures, which was one of the main criterions for the selection, but the downside to alumina is the low thermal shock the material can withstand. As experiments with depositing materials at elevated substrate temperatures increased, this work found ramping the substrate heater even at rates as low as 50 ^{o}C/hr would result in a violent shattering of the dielectric plate. As a result of the internal stress built into the alumina dielectrics, the plates would shatter outward and break the walls of the quartz chamber. After many experiments to understand the exact cause of the shattering and three repairs to the chamber, alumina was removed for use as a dielectric material.

Research into selection of a replacement dielectric turned attention to finding a material with good thermal conductivity properties as well as good thermal shock properties. A few materials reviewed in this process were aluminum nitride and silicon carbide, but realistic engineering and economic considerations immediately excluded these materials as a replacement. Attention returned to using float glass as a dielectric since a chamber wall was never shattered during dielectric failure. After many calls to Coors Tek, the large ceramics

manufacturer in Golden, Colorado, quartz was recommended as suitable replacement. Quartz has superior thermal conductivity properties and excellent thermal shock properties, as quartz can be taken right from room temperature and be put into an oven at 1500 C and immediately be placed into an ice bath without fracture. After research into the cost of producing quartz into shape of the dielectrics used in the DBD reactor, a cost of anywhere form $250-400 was quoted as compared to about $12-20 per plate for the alumina dielectrics. After much deliberation, two quartz plates were purchased. Additionally, many plates from a similar material to quartz, pyrex, was also purchased for experimentation. Pyrex was selected due to its good thermal conductivity properties and better thermal shock properties than float glass. Additionally, the use of pyrex in almost every kitchen made the selection seem correct as the material can withstand going from room temp to 250 C in matter of minutes without trouble in any kitchen. The costs of purchasing pyrex varied between suppliers and markets conditions, but the approximate range was anywhere from $30-37 per plate. Quickly after receiving the quartz dielectrics, it was found the superior thermal properties of the plates were still no match for a large arc produced from overvoltage between the electrodes. After this effort and many experimental failures, pyrex was selected as the dielectric material and for the better part of the this work was the only dielectric used in the experiments presented in the following chapters. Although using pyrex has allowed for a more reliable experimental environment, the dielectrics, when heated always result in some level of concern. As recommended by the manufacturer of the pyrex, a ramp rate of 100 ^{o}C/hr was used to ensure the quartz chamber from possible fracture and to keep as many dielectrics in operation as possible.

One dielectric combination never fully researched but tested in a smaller DBD reactor was the idea of anodizing aluminum and using the thick oxide layer produced by the anodization process as the dielectric material. This idea is very cleaver as one problem associated with using a separate dielectric such as pyrex and electrode material as aluminum is the interface between these two materials where a large power drop is found at this interface. Although bonding and other ideas were tested, the most viable solution was

anodizing aluminum. Naturally aluminum has a passivated oxide layer which inhibits corrosion. Aluminum can be made stronger by increasing the oxide layer thickness. The process is simple, by sticking a piece of aluminum in a chemical bath of acetone, the aluminum can be hooked up to the positive cathode of a battery and with the bath as the negative anode, an electrical current passed through the bath results in the production of a very hard, non-conductive surface on the aluminum. With this process, an oxide layer of about 25 mils (~630 microns) can be produced on an aluminum plate. The limitation our group found when working with an anodized aluminum as a dielectric was from filaments formed in the plasma environment slowly braking down the thin coating which ultimately led to dielectric breakdown. Overall, the use of using anodized aluminum as a potential dielectric material was very promising and still needs further evaluation to overcome breakdown issues.

3.6 Power Source

3.6.1 Power Source MOD I

The initial power source and design was based on work by researchers from J. Reece Roth's group at the University of Tennessee, the design was constructed by fellow graduate student Peter J. Yancey to power the initial incarnation of the DBD reactor. The design consisted of high power car ignition coils powered by a QSC-2000 audio frequency power supply. The design was necessary for generating the high voltage for plasma generation at atmospheric pressure. The power supply was capable of delivering 2.5 kW of peak power. The power supply worked for early experimental work but was found to be insufficient for more advanced processing. A more detailed description of the workings of this power source and shortcomings can be found in Chapter 4.

3.6.2 Power Source MOD II: The AP Solutions AIR-DBD-5000 Supply

During the second phase of this project a more advanced, commercially available power supply was purchased to power the DBD reactor. The DBD-5000 power supply came with a high voltage transformer capable of operating at up to 5000 watts in air at atmospheric pressure. The power supply can treat a 1290 cm^2 surface area with a gas gap distance of

almost 10 mm. The output frequency of the power supply is from 30-160 kHz. The plasma can be operated manually, or can be automated in a pulsed mode with an OMRON multifunction digital timer circuit. Minimum plasma pulse times with the timer can be programmed down to 1 msec intervals. On the front of the power supply is a light to warn operators when the high voltage is active. The power supply also provides the ability to install a remote interlock system. For added safety a 12V signal from the back of the power supply is provided to the user to install a strobe light to warn users when the high voltage is active. A photograph of the front of the AIR-DBD-5000 power supply is provided below in Figure 3.4.

Figure 3.4: Shown in the photograph is the AP Solutions AIR-DBD-5000 power module used during the second phase of this research. Module has capability to generate up to 5000W of power.

3.7 Electrical Diagnostics

During processing, electrical measurements of the reactor were measured through placement of a high voltage probe on the cathode and current probe placed between the anode and ground. The high voltage probe used in the measurements was a Tektronix P6015A 100 MHz capacitively coupled probe. The current was measured by a Person Electronics model 4100 probe. A Tektronix 4-channel TDS-5034 350MHz model oscilloscope was used to monitor current and voltage during processing.

3.8 Optical Diagnostics

Chemical species generated by the plasma were identified with an Ocean Optics (Dunedin, FL) S-2000 spectrometer. The spectrometer has a 0.5 nm resolution and is capable of measuring wavelengths from 200-1150 nm. Light from the plasma source was collected by a 4-channel monochromator equipped with a four USB-2000 monochromators. The spectrometer setup starts with an Ocean Optics 74-UV lens to limit the volume of light collection to a 5 mm cylinder. The lens is connected to a 2m long quadfurcated fiber optic cable bundle. Each fiber transmits light to one of the four spectrometers built into the larger unit. The first fiber transmits UV-VIS light (200-420 nm), the second transmits VIS light (400-725 nm), the third transmits VIS-NIR light (600-900 nm), and the fourth fiber transmits NIR light (800-1050nm). Over the course of this project one the fibers in the bundle was damaged and as a consequence one channel was not used for optical detection in the plasma source. Since emission from the DBD plasma is mostly contained between the 200-800 nm wavelength range, the NIR (900-1150 nm) spectrometer was not used to collect experimental data from this work. The UV-VIS spectrometer has a 1200 grove/mm holographic UV grating, the VIS spectrometer has a 1200 groove/mm holographic VIS grating, the VIS-NIR spectrometer has a 1200 groove/mm NIR grating blazed at 750 nm, and the NIR spectrometer has a 1200 groove/mm NIR grating. To ensure the spectrometers was calibrated for wavelength, a mercury-argon light source from Ocean Optics was used. The mercury-argon light source is used for both the UV and UV-VIS spectrometers while only the argon source is used for the VIS-NIR and NIR spectrometers. The calibration was only

completed on the UV, UV-VIS, and VIS-NIR spectrometers. The measurement was performed by taking the experimentally measured calibration lines and compared to the actual lines provided by Ocean Optics. The experimental data taken from the three spectrometers can be found in Figure 3.5, Figure 3.6, and Figure 3.7.

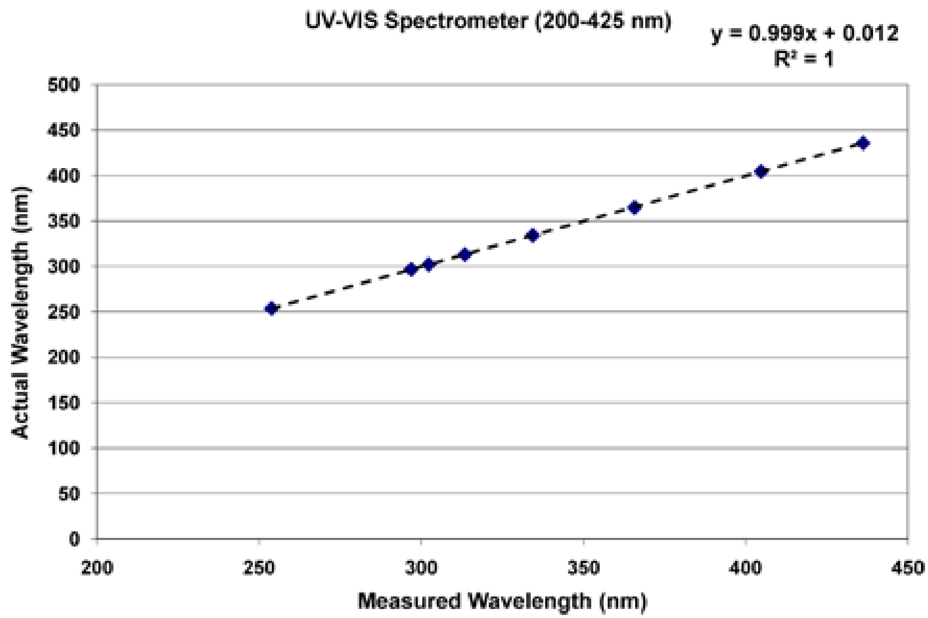

Figure 3.5: Wavelength calibration for UV-VIS spectrometer (200-425 nm).

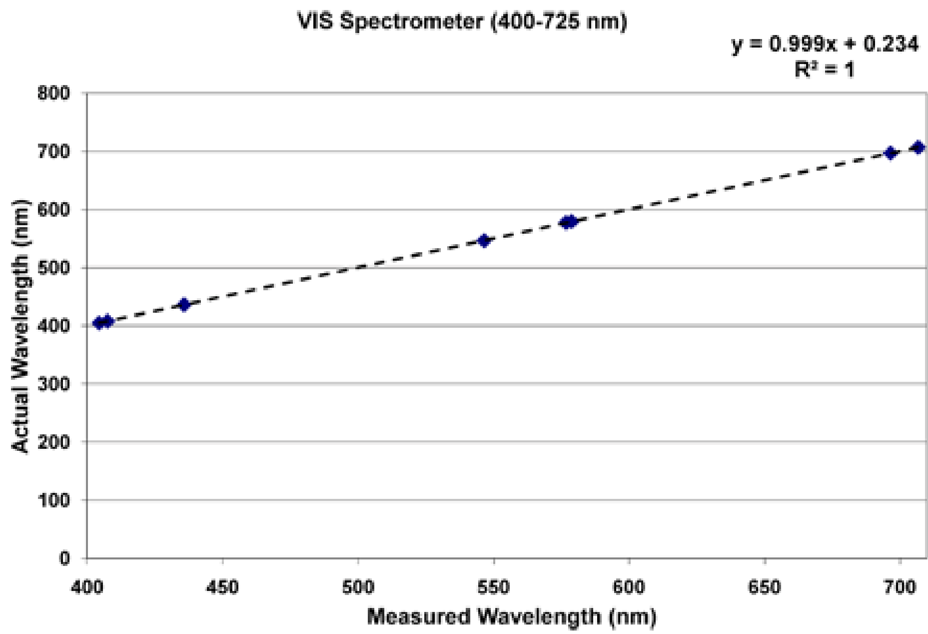

Figure 3.6: Wavelength calibration for VIS spectrometer (400-725 nm).

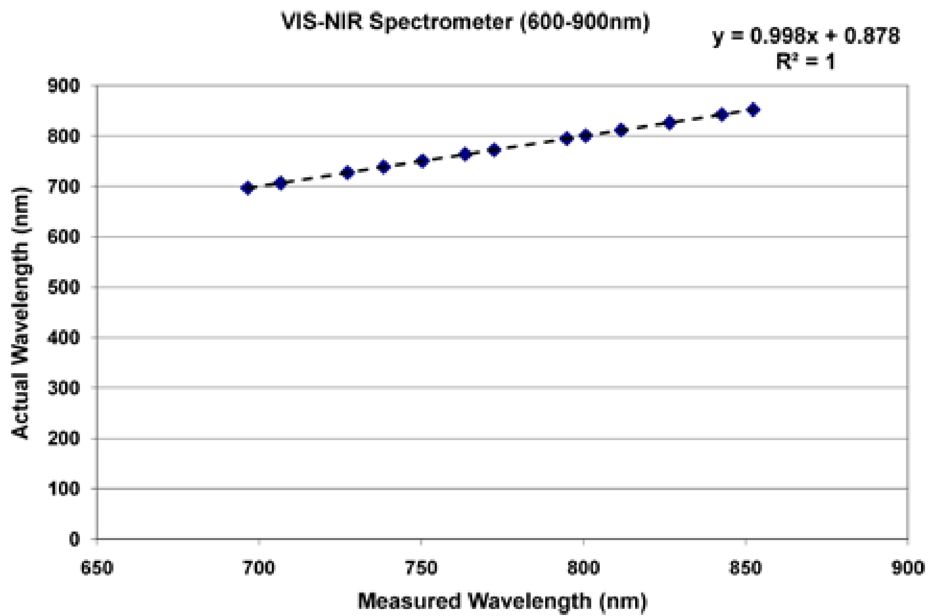

Figure 3.7: Wavelength calibration for VIS-NIR spectrometer (600-900 nm).

3.9 Gas Phase Diagnostics

Gas phase analysis was performed with a MKS Instruments residual gas analyzer (RGA), model Vac-Check. The RGA was used to analyze the process gas for contamination and to look at other gas phase analysis during processing. Located inside the RGA is a quadrupole mass analyzer, the mass analyzer has four metal rods that are hooked up to radio-frequency voltage. The four rods are set parallel to each other in the shape like a square. The rods act to filter ions in the analyzer based on the mass to charge ratio (m/z). The filter works by varying the electric field across the rods to separate ions based the stability of their trajectory path between the rods. Ions that travel all the way down the rods without touching the rods reach the detector, which analyzes the ions based on m/z ratio. This process selects ions of a particular m/z ratio or scanning a range of m/z ratios by varying the voltage across the metal rods. The mass range for the RGA used in the experiments is from 1-200, although typically, a mass range of only 1-50 was used. A photograph of the RGA used in these experiments is found in Figure 3.8.

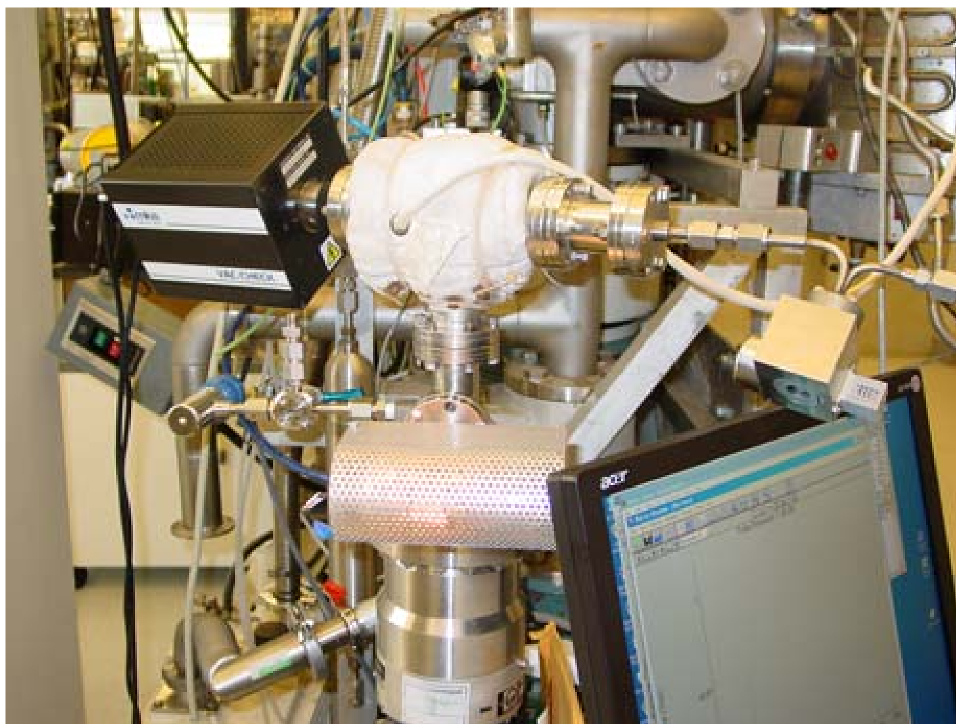

Figure 3.8: The MKS Instruments residual gas analyzer (RGA), mass range from 1-200.

4. Reduction of *Listeria innocua* and *Salmonella* spp. using Atmospheric Plasma Processing and Role of Reduction Mechanisms on Pathogen Growth after Plasma Exposure

Christopher J. Oldham [1], Scott A. Shore [2], Xin Li [3], Matthew R. King [1],
Brad A. Hartman [1], Peter J. Yancey [1], Brian W. Sheldon [4], Kevin M. Keener [2], and
Jerome J. Cuomo [1]

[1] *Department of Materials Science and Engineering,*
[2] *Department of Food Science*
[3] *College of Veterinary Medicine*
[4] *Department of Poultry Science*
North Carolina State University, Raleigh, NC 27695

Manuscript to be submitted to Trends in Food Science and Technology

4.1 Abstract

Recent consumer concern over food related recalls and possible threat to the nation's food supply from terrorist attack has increased pressure on private and public sectors for new technologies to ensure food safety. This work investigated the use of two atmospheric plasma sources for reduction of *Listeria innocua* and *Salmonella* spp., known food borne pathogens. The two plasma configurations, a dielectric barrier discharge and a portable atmospheric plasma torch, were used to investigate the role of equilibrium and non-equilibrium conditions in a plasma and how these conditions effect reduction mechanisms. The main reduction pathway from the DBD was determined be from oxidation from chemical species produced in the plasma and germicidal UV (220-280nm) exposure produced in the nitrogen and oxygen gas mixtures. The temperature of the N_2 rotational band (λ=391.4 nm) revealed the background gas temperature to be ~320K $\pm$ 80K and is believed to be a secondary reduction mechanism. Heat measured from the portable plasma pen is believed to be the only mechanism available in the reduction process since chemical species such as ozone and nitrogen oxides are known to not form at the extreme temperatures produced by this torch. Nevertheless, reductions were achieved in rapid time, a 3-log reduction of *Salmonella* spp. was completed in 0.41 seconds and a 4- and 6-log reduction of *Listeria innocua* was completed in just over one second.

4.2 Introduction

From the farm to the fork, foods are processed in many environments. There are many ways in which a food substance can be exposed to bacteria such as improper cleaning of equipment, unsanitary processing environments, and improper handling in the preparation stage. Development of new alternative technologies for food safety in the processing environment is critical not only to the food industry but also to the Department of Homeland Security due to concerns over possible tampering with the national food supply [93-95]. Additional threats posed by potential virus outbreaks of the avian influenza (bird flu) and Severe Acute Respiratory Syndrome (SARS) emphasize a greater need for an efficient, and rapid decontamination source. Presently, dry heat, steam, chemical disinfectants, ultraviolet light, ozone, and gamma irradiation are used for inactivation of food borne pathogens present in foods [96]. Although these sources are very effective for bacterial decontamination, significant disadvantages are posed by each technique. Dry heat, steam, and chemical disinfectants can change the appearance or structure of the final product and also damage the packaging material; ultraviolet light is a line of sight process; and safety considerations associated with ozone generation and gamma irradiation render these processes infeasible for a manufacturing environment [96].

Recent research in the field of non-equilibrium atmospheric plasmas has shown the technology as a possible candidate for applications involving food safety and homeland security [94, 97, 98]. Initially, sterilization mechanisms related to the plasma were poorly understood. Researchers would generate a helium plasma with a small admixture of oxygen [34, 35, 98, 99]. The samples would be treated for some time and a reduction in bacteria was observed. The group at the University of Tennessee [34] demonstrated a greater than 6-log reduction of *E. coli*, *S. aureus*, and *P. Aeruginosa* in less than 30 seconds using the One Atmosphere Uniform Glow Discharge Plasma (OAUGDP). The work first suggested chemical species such as ozone (O_3), the hydroxyl radical (OH), and nitrogen oxides (NO_x) were the primary sterilization mechanisms in the plasma. Kelly-Wintenberg *et al.* also demonstrated the kill efficiency did not change when the samples were treated in air or in

sealed opaque bags, suggesting ultraviolet (UV) exposure provides a reduction mechanism. In other experiments at Old Dominion University by Laroussi and Leipold [100], the roles of heat, chemically reactive species and UV radiation were investigated. Laroussi and Leipold concluded that chemical species played the most important role in the destruction of biological contaminants. They also concluded that heat and UV light are secondary processes for bacterial reduction. A reduction mechanism generated by the plasma, but not fully understood, is how the charged particles in the plasma (electrons and ions) interact with bacteria. Mendis *et al.* suggested a model for electrostatic disruption based on a physical process, namely, accumulated electric charge resulting in significant electrostatic stress placed on the outer cell membrane [101].

This paper studies the proposed mechanisms and presents a new approach for improving sterilization in food processing environments through a non-equilibrium plasma discharge and equilibrium plasma torch. The goal of this work is to provide a potential alternative to current approaches for rectifying food safety problems for on the farm production, in the post harvesting environment, and by retail vendors.

4.3 Experimental Methods

Plasma treatment of the food pathogens was completed at the North Carolina State University (NCSU) in the Department of Materials Science and Engineering. Bacterial culturing and analysis were performed at the Microbiology Laboratory located in the Department of Poultry Science. The following section includes a summary of the atmospheric plasma sources, microbiological preparation, and analytical methods used in these experiments.

4.3.1 Dielectric Barrier Discharge and Reactor Characteristics

Two parallel aluminum electrodes, each with a diameter of 11.5 cm, characterize the barrier discharge found in Figure 4.1. Pyrex plates with a diameter of 19 cm and thickness of 3 mm cover both electrodes. The barrier arrangement is enclosed in a quartz chamber to allow for transmission of light in the ultraviolet range. A Balzer’s mechanical pump and calibrated MKS mass flow controllers provide a controllable and reproducible environment

through pumping and subsequent purging of the system. High power car ignition coils, powered by a QSC-2000 (Costa Mesa, CA) audio frequency power supply, provide the necessary voltage for plasma generation. The power supply is capable of delivering 2.5 kW of peak power.

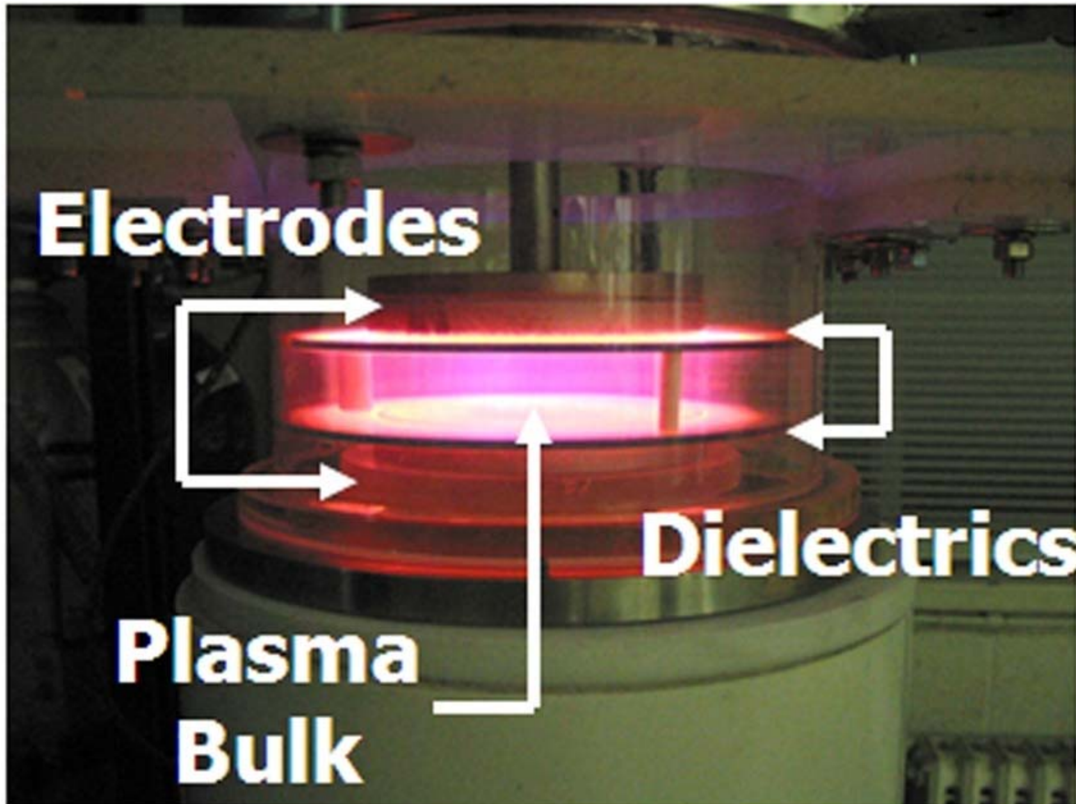

Figure 4.1: Schematic representation of dielectric barrier discharge (DBD) system used in Listeria innocua experiments.

A Tektronix (Beaverton, OR) TDS-5000 series 350 Mhz 4-channel digital oscilloscope monitors the power delivered to the reactor. A Tektronix 6015A high voltage probe and Person Electronics model 4100 high current probe monitor the power input to the discharge. Chemical species generated by the plasma are identified with an Ocean Optics (Dunedin, FL) S-2000 spectrometer. The spectrometer has a 0.5 nm resolution and is capable of measuring wavelengths from 200-900 nm. Light from the plasma source is collected by a 3-channel

monochromator equipped with a 1200 grove mm^{-1} holographic UV grating, 1200 groove mm^{-1} holographic VIS grating, and a 1200 groove mm^{-1} NIR grating blazed at 750 nm.

Throughout the study RF power levels were maintained at frequencies from 5-15 kHz but nominally at 10.75 kHz. RMS voltages were varied from 5-10.5 kV depending on the gas composition inside the reactor. Depending on gas composition, gas flow rates varied from 5-15 L/min. A gap distance of 15 mm was held constant for all experiments.

4.3.2 Handheld Plasma Source

The portable plasma pen found in Figure 4.2 is commercially available and was developed by PVA Tepla (Corona, CA). The system is referred to as the Tepla plasma pen and it consists of a driven center electrode and a surrounding grounded electrode. The power source for the handheld plasma pen is a pulsed DC power supply. This device is portable and operates from a standard 110 V outlet. The system is currently in use by the automobile industry to increase adhesion between two dislike materials (metal and rubber). The plasma produced by the pen is generated by flowing compressed air at 90 PSI between the electrodes.

Figure 4.2: Picture of Tepla plasma pen in an experiment to measure temperature of plasma. Tank of dry air hooked up as gas source with Tepla unit plugged directly into 110V outlet.

As shown in Figure 4.3, when a high voltage is placed across the electrodes, breakdown of the high flow of compressed air through the pen causes the plasma to eject from the end. The plasma pen operates at a frequency of 60 Hz and in ambient air. The plasma pen produces a treatment width of about 5-12 mm depending on distance to the treated substrate. The length of the plasma from the tip of the pen enclosure is approximately 25.4 mm and the diameter is about 3 mm.

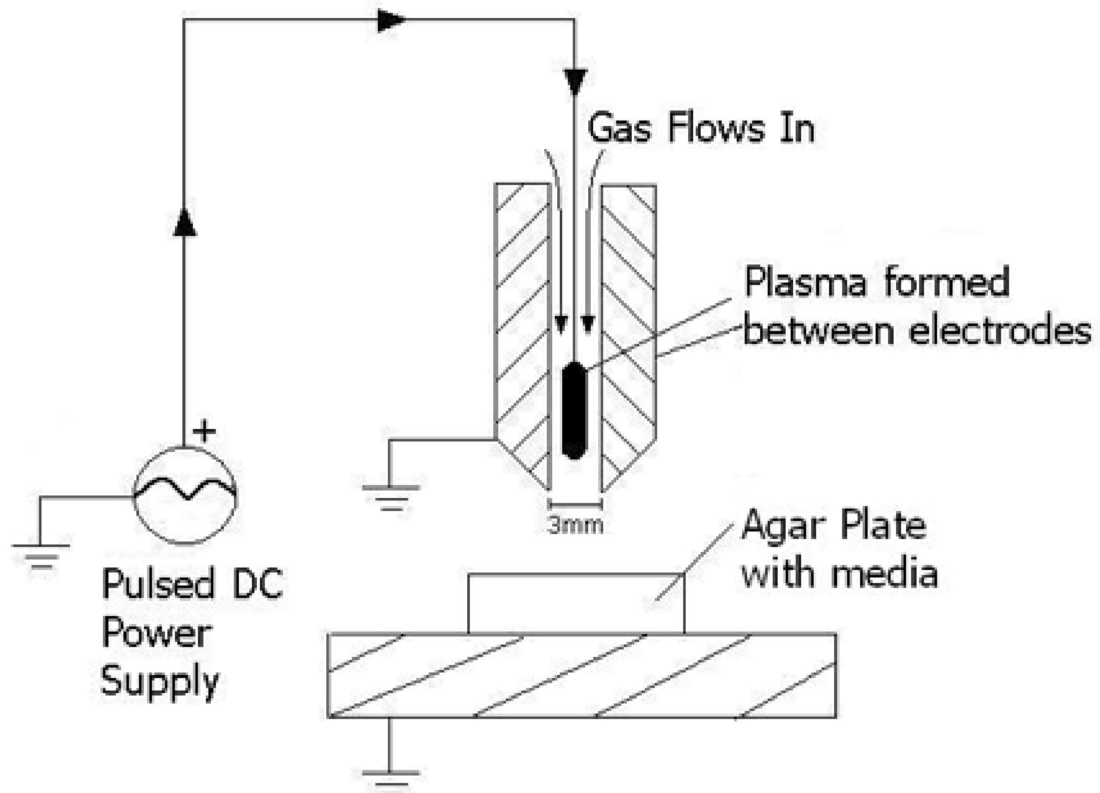

Figure 4.3: Schematic representation of Tepla plasma pen.

4.3.3 Pathogen Preparation

Listeria innocua was provided courtesy of the USDA to the Department of Poultry Science at NCSU. The culture of *Listeria innocua* was prepared and maintained as follows. The stock culture was maintained in a double strength of brain heart infusion (BHI, Becton Dickinson, Sparks, MD) broth plus 40% (vol/vol) glycerol and stored at -20ºC. For the experiments in this paper, each strain was subcultured on BHI agar plates for 24 hrs at 37 C, and an isolated colony was propagated twice in BHI broth for 22 to 24 hrs at 37 C. Following serial dilution in sterile peptone water, the strain was plated in duplicate onto BHI agar plates. The plates were incubated at 37 C for approximately 24 hrs. The initial colony count was determined to be 10^9 colony forming units per ml (CFU/ml). Plates with bacterial

population 10^4 (CFU/ml) and 10^6 (CFU/ml) were treated by the dielectric barrier discharge system in triplicate.

A five-strain cocktail of *Salmonella* spp., identified as the most common human enteric pathogens by the CDC (Center for Disease Control and Prevention), was prepared in the same manner as *Listeria innocua*. The five strains included in the cocktail were: *S. Enteritidis* ATCC 4931, *S. Typhimurium* ATCC 2564, *S. Typhimurium* ATCC 14028, *S. Heidelberg* ATCC 8326, and *S. Newport* ATCC 6962. Five colonies of each *Salmonella* spp. strain were combined into a common test tube containing 10 ml BHI broth. The BHI broth was incubated at 37 C in a shaker water bath for 18 hrs following serial dilution.

4.3.4 Experimental Design

The interaction of the DBD treatment of with *Listeria innocua* was investigated through the following set of experiments. A controlled set of gas mixtures was designed to investigate the role chemical species generated in the plasma and the role of these species in killing the cultured bacteria. Three plasma chemistries were investigated, the first involving a 100% helium mixture, the second involving a 1.5% nitrogen in helium mixture and the third composed of 1% oxygen and 4% nitrogen in helium.

The interaction of the handheld plasma source was tested in combination with a rotational track to hold the bacteria. The bacteria was rastered in the same spot at approximately 3-4 mm above the sample surface. A schematic of the rotational track is illustrated Figure 4.4.

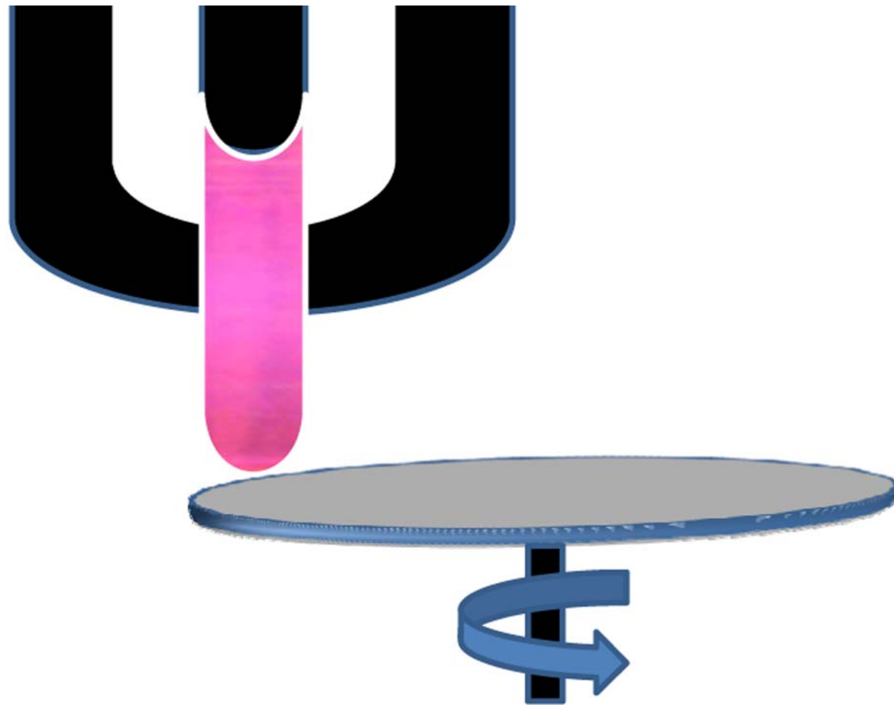

Figure 4.4: Experimental setup for Tepla plasma pen.

Listeria innocua samples were exposed under the plasma for one to six passes using an air based plasma. Additionally, a separate group of samples containing the *Salmonella* spp. culture was treated with a gas composition of 5, 20, and 30% oxygen (remaining percentage nitrogen) for 3, 6, and 9 passes at 40, 60, and 80 rotations per minute (RPM's). A summary of these runs can be found in Table 4.1.

Table 4.1: Exposure time for treating Listeria innocua Salmonella spp. with rotating substrate with the Tepla plasma pen.

RPM	Passes	RPS	Total Time (s)	Treatment Time (s)
80	3	1.33	2.25	0.41
	6	1.33	4.5	0.82
	9	1.33	6.75	1.23
60	3	1	3	0.54
	6	1	6	1.09
	9	1	9	1.63
40	3	0.67	4.5	0.82
	6	0.67	9	1.63
	9	0.67	13.5	2.45
Arc length	3.421	inches		
Circumuference	18.85	inches		

4.4 Results and Discussion

4.4.1 Results from the Dielectric Barrier Discharge (DBD) Plasma Treatments

Initial treatments demonstrated several orders of reduction after plasma exposure using the DBD configuration. Reductions varied by exposure time to the plasma and type of gas used to form the plasma background. To assess the general effectiveness of the DBD treatment, many control tests were completed to ensure the reductions resulted from the active plasma environment. To ensure the microorganisms did not blow off the agar plates from gas flow in the chamber, a set of gas only treatments without the plasma but with the gas flowing were included in the design of experiments. The gas only test was performed at a condition with no plasma exposure and only process gas flowing over the sample surface. Using a helium flow rate of 17 standard liters per minute (slm) for 15 minutes, three samples with a colony count of 10^4 CFU/ml and three samples with a 10^6 CFU/ml were tested. Two additional control plates from each bacterial population were plated with no exposure to gas or plasma. The control plates from both test tubes produced growth over the entire agar plate. A picture showing the growth on a control plate can be found in Figure 4.5.

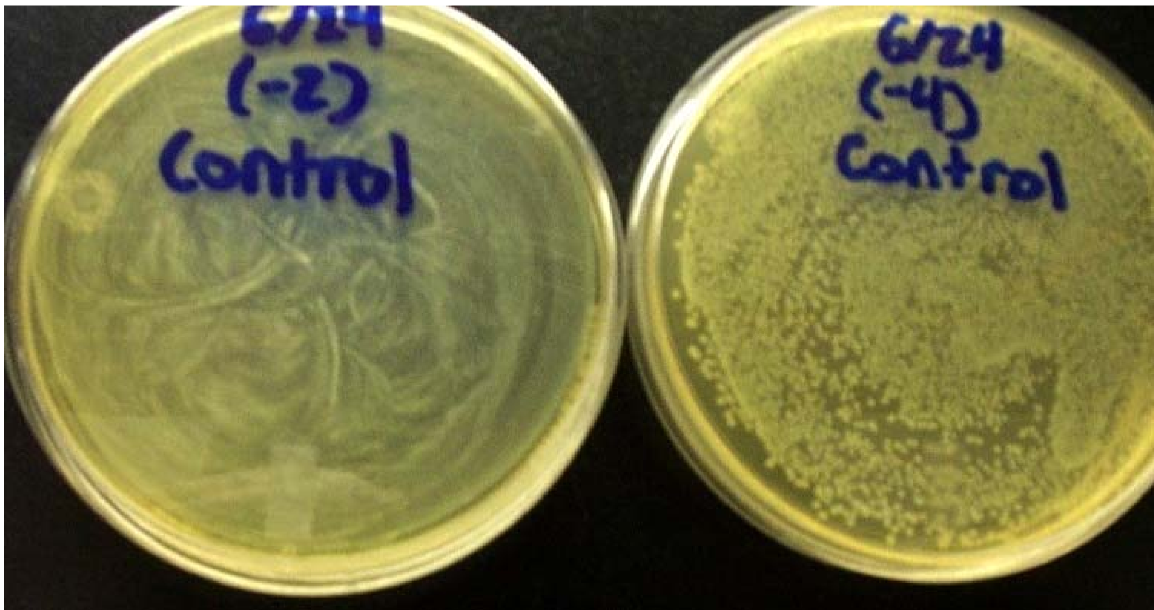

Figure 4.5: Growth of Listeria innocua on control plates of 10^4 and 10^6 CFU/ml.

For the 100% helium exposure runs, the voltage applied to the plasma was 5500V and the current input to the plasma was 0.04A. The *Listeria innocua* was exposed to the plasma for 1.25 and 2.5 minutes. For the 10^6 CFU/ml plate exposed for 1.25 minutes, the plasma did not reduce growth. For the 10^6 CFU/ml plate exposed for 2.5 minutes, a small reduction in growth was found in the outer edges of the agar plates. The plasma reduced growth for the 10^4 CFU/ml plate exposed for 1.25 minutes while the 2.5 minute plasma treatment completely reduced two of the three samples (4-log reduction) and the third had a small reduction in growth.

The 1.5% nitrogen (250 sccm) in helium (17 slm) exposure was also tested on samples from the 10^4 and 10^6 CFU/ml test tubes. Samples from each test tube were plated and tested three times at 1.25 and 2.5 minutes. In addition, one sample from each test tube was exposed to gas only, and one control plate with no exposure to plasma or gas was plated. All operating conditions remained constant (purge cycle, gap distance, etc.). The voltage applied to the plasma was approximately 5800V, and the current was about 0.04A. For the agar plates from the 10^4 CFU/ml test tube exposed for 1.25 minutes, one plate had no growth

while the other two had a large reduction in growth. For the 2.5 minute plasma exposure, two plates had no growth and the other one was greatly reduced. For the plates from the 10^6 CFU/ml test tube, the 1.25 minute exposure produced two plates with growth reduction while the third looked similar to the control growth. For the 2.5 minute exposure, all three plates had reduced growth, but it was again centralized in the agar plate. Found in Figure 4.6 is a picture of the centralized growth on the 1.25 and 2.5 minute nitrogen in helium plasma exposures.

Figure 4.6: Centralized growth pattern found after 1.25 and 2.5 minute plasma exposures of 1.5% nitrogen in helium.

Treatments of 1.25 and 2.5 minutes with a gas mixture of 4% nitrogen (750 sccm) and 1% oxygen (200 sccm) in helium was tested form three plates each from the 10^4 and 10^6 CFU/ml test tubes. One gas only sample and one control sample were also plated for comparison. For plasma exposure runs there was no growth on the agar plates (4-log and 6-log reductions). The gas only samples produced no change in growth pattern as compared to the control samples.

Comparing the three data points of helium, helium and nitrogen, and the mixture of helium, nitrogen, and oxygen at treatment times of 1.25 and 2.5 minutes, there is a trend in growth reduction. It appears using only helium as a reducing agent is not as effective for reducing the bacteria. The inactivation efficiency was improved with the addition of nitrogen, and when oxygen was added to the gas mixture, no growth was found on any of the plasma exposure samples. A summary of these results can be found in Table 4.2. The table describes the number of plates with complete inactivation at the different experimental conditions using the DBD configuration.

Table 4.2: Observed number of plates with complete inactivation of the Listeria innocua bacteria at the various gas mixing and treatment configurations from the DBD plasma.

Gas Mixture	Treatment Time (min)	10^4 CFU/ml	10^6 CFU/ml
He	1.25	0	0
	2.5	2	0
He/N_2	1.25	1	0
	2.5	2	0
$He/N_2/O_2$	1.25	3	3
	2.5	3	3

4.4.2 Results from PVA Tepla Plasma Pen

Reduction of *Listeria innocua* bacteria on an agar gel was performed by keeping the rotational speed of the track at 60 rotations per minute. A reduction in growth was found beginning around three passes for the plates from the 10^4 CFU/ml test tube. Complete kills were observed for four, five, and six passes on the plates from the 10^4 CFU/ml test tube. For the plates from the 10^6 CFU/ml test tube, full kills were observed at 5 passes.

Investigation of the treatment time and role of chemical species in the plasma to reduce the growth of *Salmonella* spp. was carried out at various rotation speeds and passes with varying levels of oxygen in the gas mixture. A cocktail of *Salmonella* spp. with 10^3 CFU/ml was exposed to the plasma pen. Each plate contained approximately 150,000 colonies of

Salmonella spp. Placing the plasma pen at a distance of 3-4mm from the plate, a group of samples was treated with a gas composition of 5, 20, and 30% oxygen (remaining percentage nitrogen) for 3, 6, and 9 passes at 40, 60, and 80 rotations per minute (RPM's). A general trend was observed whereby increasing the number of passes and reducing the RPM's increased the kill rate. A maximum amount of kills occurred between 20-30% oxygen. The small change in growth reductions observed between the 20% to 30% oxygen, leads to the conclusion that a saturation point in kill efficiency is established at or around the mixture of ambient air (20% oxygen in nitrogen). A summary of the results from kills found be treating the Salmonella spp. with the plasma pen can be found in Table 4.3.

Table 4.3: Results from Tepla plasma pen on Salmonella Spp.

% Oxygen	Number of Passes	RPM's	Kill Width on Pass 1	Kill Width on Pass 2
5	3	40	No Kill	No Kill
5	3	60	2 mm	3 mm
5	3	80	No Kill	No Kill
5	6	40	No Kill	No Kill
5	6	60	No Kill	No Kill
5	6	80	4mm	No Kill
5	9	40	1mm	1mm
5	9	60	No Kill	No Kill
5	9	80	No Kill	2mm
20	3	40	5mm	5mm
20	3	60	No Kill	No Kill
20	3	80	No Kill	No Kill
20	6	40	3 mm	4 mm
20	6	60	2mm	2 mm
20	6	80	2mm	2mm
20	9	40	4 mm	4mm
20	9	60	3 mm	3 mm
20	9	80	3mm	3mm
30	3	40	2 mm	2 mm
30	3	60	No Kill	No Kill
30	3	80	No Kill	No Kill
30	6	40	3mm	3 mm
30	6	60	1mm	No Kill
30	6	80	No Kill	No Kill
30	9	40	4 mm	4 mm
30	9	60	2mm	1mm
30	9	80	1mm	1mm

4.4.3 Role of Chemical Species, Temperature, UV Exposure, and Charged Particles in a Plasma Environment on Bacteria Growth

Many groups have researched reduction mechanisms of bacteria after plasma exposure. The four recognized mechanisms are oxidation from reactive species, electrostatic disruption from charged particles in the plasma, heat, and germicidal UV exposure (λ=220-280 nm) [25, 95, 100, 102]. The mechanism can vary and depend greatly on the equilibrium conditions of the plasma. Plasmas close to equilibrium (thermal plasmas) are similar to DC discharges and are associated with very high gas temperatures (>2000K). Plasmas far away from equilibrium (non-thermal) are associated with gas temperatures at or near room temperature and have highly active chemical environments. In the following sub section, a

review of the four mechanisms and role of equilibrium conditions of the plasma will be discussed.

4.4.3.1 Chemical species and role in food pathogen reduction

Reactive species in plasmas play a very important role in the reduction of food borne pathogens. In nitrogen and oxygen containing plasmas, reactive species such as atomic oxygen, ozone (O_3), nitrogen dioxide compounds (NO_x), and the hydroxyl radical (OH) are generated through electron impact excitation and dissociation reactions [103-105]. These species have a direct impact on the membranes which makeup the cells of the bacteria. Critical to the survival of the bacteria is the health of the lipid bilayers that are made up of unsaturated fatty acids [106]. The fatty acids act as the highway to transport ions and polar compounds in and out of the cell membrane walls. Also imbedded in the lipid bilayers are proteins made up of linear chains of amino acids, which control the overall passage of compounds in and out of the bacteria membrane. The amino acids are highly susceptible to oxidation and it is believed in rich chemical environments, nitrogen and oxygen containing species play a critical role in the reduction of food pathogens through oxidation mechanisms [34, 107]. For plasmas to produce a rich chemical environment, understanding the equilibrium conditions of the plasma is very important. Generally, thermal plasmas have a chemical reaction pathway that is accelerated very quickly by thermal dissociation [4]. Excited species produced by the plasma quickly transform chemical energy into thermal energy. As a result, the radical lifetime is very short and the amount of electrical energy dumped into resistive heating of the background gas results in a very poor active chemical environment. Non-equilibrium plasmas like the dielectric barrier discharge are considered cold plasmas because thermal dissociation does not take place and the background gas temperature is close to or near room temperature. The low gas temperature allows for long initiation and propagation of long chain chemical reactions that result in the production of highly active species.

4.4.3.2 Role of heat as an inactivation method

Heat as an inhibitor to bacteria growth can vary between equilibrium conditions. In thermal discharges, heat is recognized as the main inhibitor to bacteria growth since temperatures in a thermal plasma can easily exceed 2000K. Comparing the temperatures in plasmas to an acceptable food decontamination processes such as pasteurization, the process which retards bacteria growth in foods, shows the equilibrium conditions are very important for determining the role of heat on bacteria growth. For example, in the pasteurization of milk, a treatment process called high temperature/short time (HTST) is completed on milk. In the HTST process, milk flows between either parallel plates or through pipes that are heated to approximately 350K. After about 15-20 seconds of treatment time, 5-log (99.999%) reductions in bacteria growth are achieved [108]. Similarly, dry heat sterilization, a harsher form of pasteurization, is the process which uses temperatures of about 450K to sterilize bacteria [109]. The process requires about one hour of treatment time. In non-equilibrium discharges such as the DBD, heat is a secondary mechanism to other primary mechanisms since the temperatures are at or near room temperature. Still unclear is the role of treatment time in a heated plasma environment. Currently, it is thought if the temperature in a plasma meets or exceeds temperatures found in pasteurization processes, than the main reduction pathway is by heat [110].

4.4.3.3 Ultraviolet light and potential effects

Germicidal UV light (220-280 nm) produced by emission from certain plasma species can be a potentially lethal to bacteria. One of the effects of ultraviolet exposure is modification of nitrogen containing DNA base, thymine [111]. Typically a few doses of 220-280 nm UV light at several mW s/cm^2 are known to cause dimerization of the thymine bases in the DNA [112]. Many groups have reported on the lack of germicidal UV production in a DBD [97, 100, 112]. These groups report on the dominance of other bands in the emission spectra such as the N_2 rotational band 0-0 transition at 337nm and the rotational band of the OH A-X (0-0) transition at 306.6 nm (R branch) and 309.2 nm (P

branch) [44, 113-118]. Since the flux of emission was less than 1 mW s/cm^2 as measured by a calibrated spectrometer in Laroussi and Leipold's [31, 119] work, they concluded UV radiation does not have a direct impact on the decontamination process.

The role of equilibrium conditions on the generation of the NO_x band of germicidal UV commonly found varies by the plasma temperature [55]. The production of NO_x is highly dependent low gas temperatures, as the gas temperature increases, NO_x production decreases exponentially. Similarly, ozone production follows a similar trend and it is also found to not form in large amounts at higher temperatures[55]. As a result, germicidal UV in an air plasma would be highly likely from a plasma at low gas temperatures (non-thermal) than a plasma at higher temperatures (equilibrium) [55].

4.4.3.4 Electrostatic disruption and role in rupturing of cell membrane wall

It has been proposed by Mendis *et al.*, the reduction of food pathogens with plasmas can occur through a fourth pathway, by electrostatic disruption of the cell membrane from charged species in plasmas [101]. Charged particles in a plasma include the electrons and ions produced during plasma generation. Mendis *et al.* proposed when the accumulated charge on the surface of a cell membrane becomes significant enough, the resulting outward electrostatic stress is large enough to overcome the tensile strength of the cell membrane. Mendis *et al.* generated a simplified model showing the electrostatic forces on the outer surface of a cell membrane could overcome the tensile strength of the membrane and result by rupturing the outer cell wall. Using *E. coli* as the model bacteria, where *E. coli* is a gram-negative and roughly spherical bacteria with a few small surface defects. The model assumed that *E. coli.* was of an idealized radius R with a small irregularity (a "pimple") on the surface of radius r (where $r \ll R$). It was also assumed the outer membrane to have a thickness Δ (with $\ll$r, R) with a uniform surface potential Δ (in volts) [111]. The model states the cell disruption would occur by breaking off the pimple due to electrostatic disruption taking place over the surface with smallest radius due to higher electric field conditions at the smaller radius [120]. Equation 4.1 states the condition for electrostatic

disruption to rupture the cell wall is where the total electric force along the center axis of the larger cell membrane and smaller pimple exceeds the tensile force on the membrane along the same axis:

$$\int_0^r \left(\frac{E^2}{8\pi}\right) 2\pi \cdot \rho \cdot d\rho > F_t \cdot 2\pi \cdot r \cdot V \qquad (4.1)$$

where:

ρ=cylindrical coordinate normal to axis;

F_t=membrane tensile strength;

$\frac{E^2}{8\pi}$=electrostatic tension normal to the surface,

and the electric field on the surface of the cell equals $E = \phi / r$, which leads to the condition:

$$|\phi(V)| \geq 0.2\sqrt{r(\mu m) \cdot R(\mu m)} \sqrt{\frac{\Delta}{R}} F_t^{0.5} \qquad (4.2)$$

Assuming R=1 micron, r=0.02 micron, and Δ=0.008 micron, and with the knowledge that gram negative bacteria such as *E. coli* can withstand pressures of up to 5 ATM [111], the tensile strength of F_t was found to be ~$5x10^6$ dynes/cm^2. At this tensile strength, a surface potential of Ø=6 V was calculated to disrupt the surface of the cell membrane. It was also found to break the membrane in half, a potential ofØ=40 V was needed on the surface of the cell.

To help Mendis with his model, Laroussi *et al.* provided experimental data with the interaction of the outer cell membrane in food pathogens. In the work, a DBD similar to the work in this paper was used to experimentally verify the model [121]. An electron temperature between 1-5 eV was measured where the ions in the work were made up of largely He^+. It was found a surface potential of 15 V would be obtained at an electron temperature of 5 eV [122]. Mendis concluded the surface potential produced by a DBD was insufficient to break a gram-negative *E. coli* bacteria in half but that the tensile strength was large enough to tear the cell membrane if the surface had a few percent surface roughness.

Equilibrium considerations of a plasma can greatly effect the surface potential and tensile strength of the electrostatic charge produced by the plasma. Although calculations of the surface potential from equilibrium thermal plasmas has not been completed, it can be assumed the extreme temperatures that can reach over 10,000 K would generate energetic electrons and ions to exceed the 40 V surface potential predicted by Mendis *et al.* electrostatic model [101]. In Laroussi's work, a non-equilibrium based DBD discharge demonstrated the charged particles have sufficient energy to tear or rupture the surface of gram-negative bacteria of *E. coli* [121].

Before concluding the role of electrostatic disruption, it must be stated the difference between a gram-positive bacteria like *Listeria innocua* and gram-negative bacteria like *Salmonella* spp. is the thickness of the outer cell membrane and how the two classes of bacteria react to stains. If during staining the stain takes to the bacteria, it will turn purple and be considered gram-negative. If the stain does not take, the bacteria will stain pink and be considered gram-positive. Shown in Figure 4.7 is an example of the gram staining process where the gram-negative bacteria *E. coli.* is stained purple and the gram-positive bacteria *Staphylococcus aureus* is stained pink [111].

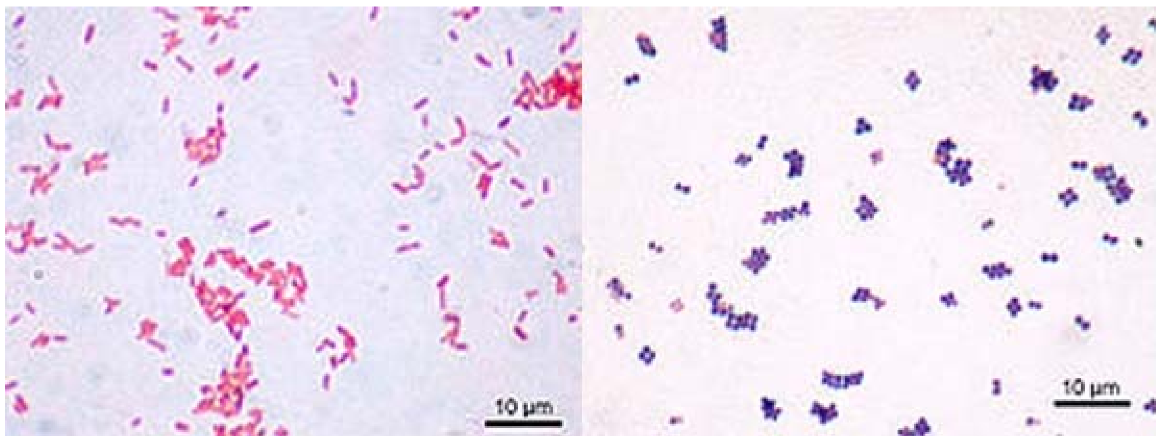

Figure 4.7: The gram staining process where the gram-negative bacteria E. coli. is stained purple (on the right) and the gram-positive bacteria Staphylococcus aureus is stained pink (on the left) [111].

The staining process is used to stereotype bacteria but it also provides a clue for understanding how electrostatic charge on the surface will effect either a gram positive or gram negative bacteria. For example, in gram-negative bacteria the reason the cell stains purple is a thinner cell wall made up a polymer known as peptidoglycan. Peptidoglycan consists of sugars and amino acids which form into a mesh structure outside of the membrane of the cell wall [111]. The peptidoglycan layer varies between 2-8 nm in gram-negative bacteria and can be as much as 80 nm in gram-positive bacteria [111, 123]. It is believed this difference provides the structural strength and resistance to electrostatic disruption from the charged species in the plasma. Consistent with this thought, Laroussi published research related to treatment of the gram-positive bacteria *Bacillus subtilis*. While Laroussi *et al.* was able to stop growth of the bacteria, further SEM micrographs revealed the cell wall remained intact, which confirmed early work the structural disruption by electrostatic stress is ineffective against gram positive bacteria [124]. The probable reduction was from another mechanism in the plasma such as the chemical species.

4.5 Proposed Reduction Mechanisms in the DBD and Plasma Pen Sources

Results after plasma exposure varied between plasma sources. From the previous discussion, the properties of the two plasma sources used in this work vary both in terms of equilibrium conditions but also in potential surface area treated by the plasma source. For example, the DBD is very efficient in producing chemical species needed for oxidization of DNA but it has been suggested germicidal UV light is not readily produced in a DBD based plasma source [124]. The work of Laroussi and Mendis suggests the electron and ion energies in a DBD are capable of disrupting the cell wall of gram-negative bacteria [101, 124]. And, the role of heat as a reduction pathway can vary greatly between plasma sources.

4.5.1 Reduction Mechanisms in DBD

In the DBD, chemical species such as the hydroxyl radical, atomic oxygen, and various nitrogen oxide compounds were formed and identified in the emission spectra. Figure 4.8, Figure 4.9, and Figure 4.10 are representative spectra taken from the 100% helium, 1.5% nitrogen in helium, and 4% oxygen with 1% nitrogen in helium mixtures respectively.

Identified emission lines in the 100% helium spectra found in Figure 4.8 are the 501.5 nm, 587.5 nm, 667.8 nm, 706.5 nm, and 728.1 nm from atomic helium peaks [125]. Additionally, the presence of a large amount of nitrogen and oxygen contamination showed emission from the (0-0) band of second positive N_2 system at 337.1 nm along with the OH rotational band at 306.6 nm (R branch) and the 309.2 nm (P branch) [85, 114, 126].

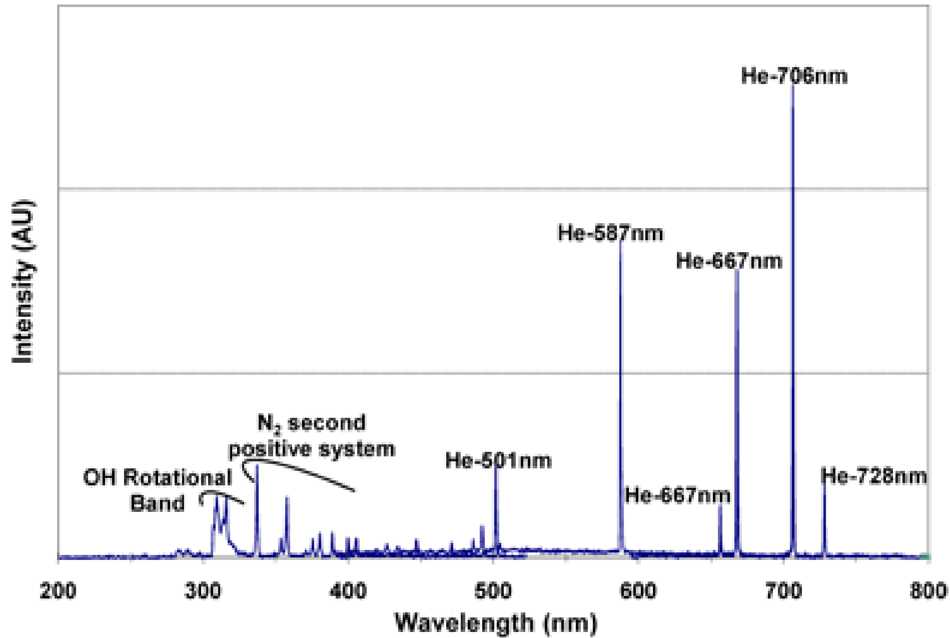

Figure 4.8: Representative spectra from DBD treatment of Listeria innocua in the 100% helium gas mixture. Emission lines at 501.5 nm, 587.5 nm, 667.8 nm, 706.5 nm, and 728.1 nm from atomic helium peaks [125], emission from the (0-0) band of second positive N_2 system at 337.1 nm along with the OH rotational band at 306.6 nm (R branch) and the 309.2 nm (P branch) [85, 114, 126].

Found in the 1.5% nitrogen in helium gas mixture, see Figure 4.9, is the detection of a large amount of germicidal UV, which contradicts data provided by Laroussi and Leipold [124]. Spectral lines indentified in this spectra include the nitrogen second positive (337.1 nm), the nitrogen first positive system (550-900nm), and the γ-band of NO radiation (213 nm, 224 nm, 234 nm, 245 nm, 257nm, 270 nm, 284 nm) [127, 128].

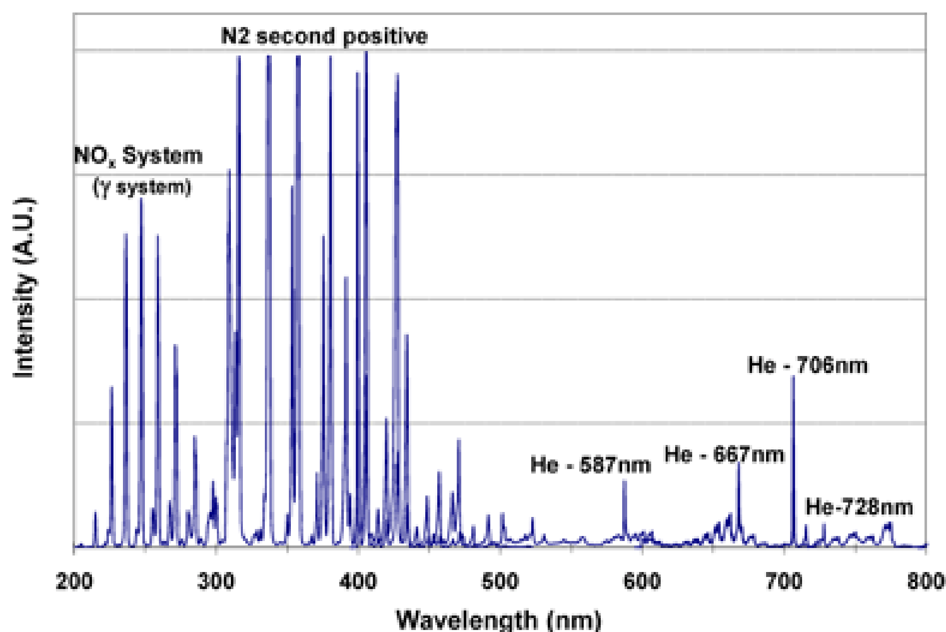

Figure 4.9: Representative spectra from DBD treatment of Listeria innocua in the 1.5% nitrogen in helium gas mixture. Spectral lines indentified in as the nitrogen second positive (337.1 nm), the nitrogen first positive system (550-900nm) along γ-band of NO radiation (213 nm, 224 nm, 234 nm, 245 nm, 257nm, 270 nm, 284 nm) [127, 128].

In the 1% oxygen and 4% nitrogen in helium gas mixtures, an emission line of atomic oxygen at 777.2 was identified along with the nitrogen second positive system, see Figure 4.10 [125]. Clearly, these figures represent that the DBD is efficient in producing the reactive species for the reduction process.

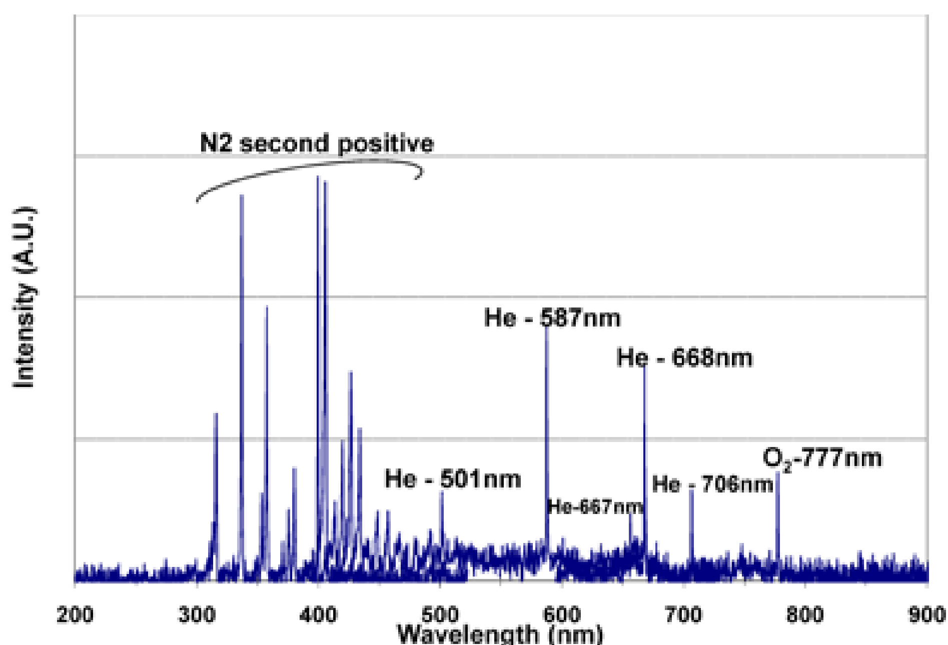

Figure 4.10: Representative spectra from DBD treatment of Listeria innocua in the 1% oxygen, 4% nitrogen in helium gas mixture. The nitrogen second positive system and an emission line of atomic oxygen at 777.2 was identified [125].

Temperature in the DBD environment was measured by two techniques. The first used a type K thermocouple to measurement the dielectric plate and electrodes directly after plasma exposure. The results after a 5 minute treatment in a helium/nitrogen gas mixture found the driven electrode temperature increased from room temperature to 53 C. For the grounded electrode, a temperature of 37 C was measured. Temperature of the top and bottom dielectrics increased to 41 C and 34 C respectively. The temperature of the agar gel directly after exposure was 40 C. Additionally, using the experimentally generated spectra, the N_2 rotational band (λ=391.4 nm) was fitted to provide a second temperature measurement. Fitting a profile to the N_2 rotational band gives a good indication of the plasma gas temperature and is very useful because the measurement does not perturb the plasma environment during treatment. The rotational band is measured from the intensity distributions in the emission spectra of the second positive system of the nitrogen ($C^3\pi_u$ (υ'=0)$\rightarrow B^3\pi_g$ (υ'''=2)) transition at the band head of 391.4 nm. A temperature of 320K ±

3.2K was measured by modeling the intensity distribution and fitting a temperature profile with LIFBASE 2.0 software. Since the temperature measurements are within or below the temperature for pasteurization (350K), it is believed pasteurization or a similar food sterilization process is not the mechanism for complete kills [106]. The fit of the N_2 rotational band can be found in Figure 4.11.

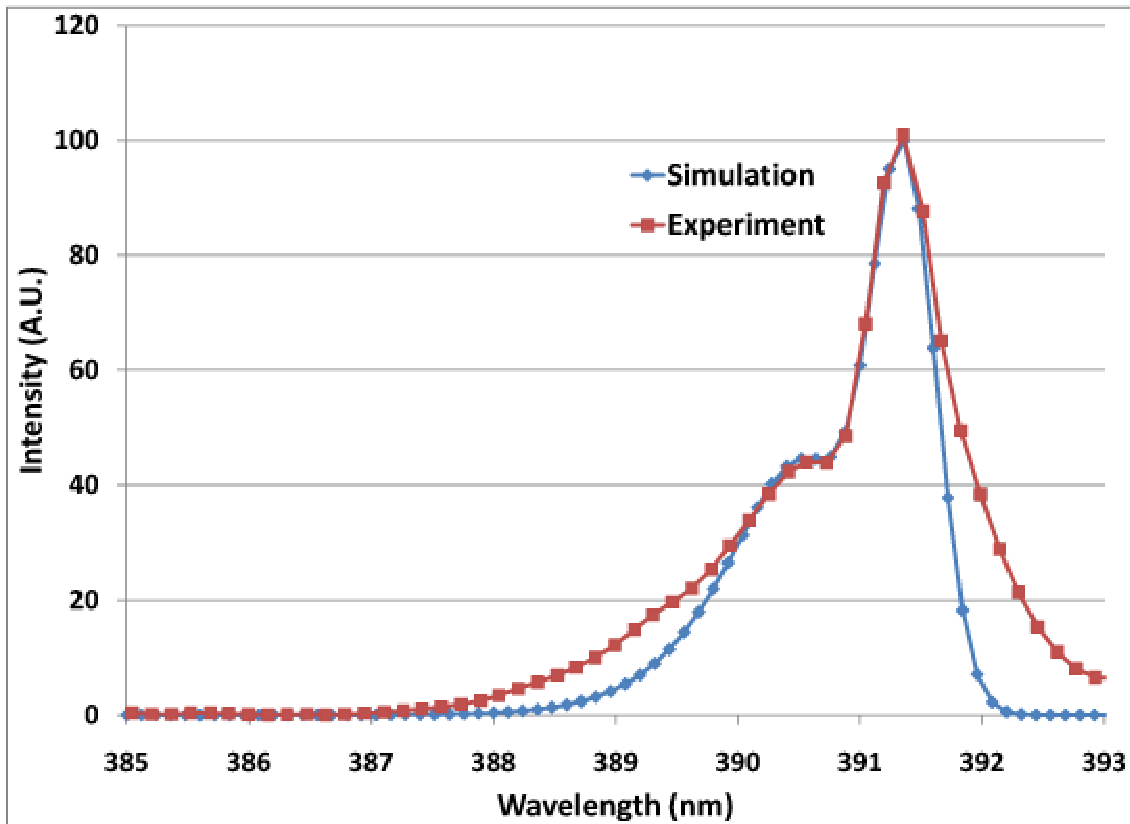

Figure 4.11: Fit profile of the second positive system of the nitrogen ($C^3\pi_u$ (υ'=0)→$B^3\pi_g$ (υ'"=2)) rotational band transition at 391.4 nm. A temperature of ~320K ± 3.2K was measured by modeling the intensity distribution and fitting a temperature profile with LIFBASE 2.0 software.

In the model, the residual difference between the experimental and fitted data was found to be less than 2%. The accuracy of the model is further confirmed by the fit of the shoulder to the left of the band head at about 390.4 nm, which was also found with residuals less than

2% to the model. Fitting the shoulder to the left of the band head at lower temperatures demonstrates the accuracy of the model since both the band head and higher order rotational states in the vibrational band fit well at lower temperatures and poorly at higher temperatures.

Additionally, it was observed that a large tail to the right of the band head was detected in the emission profile. The tail is artificial and cannot be modeled. The tail is a function of instrumental error from what is believed to be from a comatic aberration in the detector, which is affecting the optical path for detection of emission from the plasma source. This aberration is possibly an effect of one or all of the mirrors and or gratings in the spectrometer setup suffering from misalignment. This is obviously a limitation to the emission profile detection but it did not compromise the calculation to generate the model for the temperature profile.

The role of electrostatic disruption is not believed to be a mechanism in this work. In this work, the gram-positive bacteria *Listeria innocua* was investigated for reduction by plasma exposure. From the work of Laroussi and Mendis, the role of charged species in a DBD as a reduction pathway is well supported for gram-negative bacteria like *Salmonella* spp. and *Bacillus subtilus* [101, 124]. Laroussi's work supported Mendis's model that electrons within this energy range had sufficient enough energy to tear the surface of a gram negative bacteria but later found gram-positive bacteria such as *Listeria innocua* were not disrupted by the charged particles [121].

Because of these measurements and observations of DBD plasma treatments of *Listeria innocua*, it is likely the primary reduction pathway is not a single mechanism but a combination of radical species and germicidal UV light exposure. Evidence from an increase in radical generation and the production of a NO_x germicidal band in the nitrogen and oxygen gas mixtures supports the idea of a dual mechanism pathway to reduce the bacteria growth in the DBD. It is interesting to note Laroussi *et al.* used a similar setup to the one used in this work, but the germicidal UV band was not found [119]. It is unclear at this time why this additional mechanism appeared with this work. It is possible Laroussi mistakenly

measured plasma emission through some UV absorbing medium, which would not allow for UV transmission to the spectrometer. Although the temperature measured by the N_2 rotational band was close to the temperature for pasteurization, it is believed the treatment times in the plasma were too small and any effect from heat would act more as a secondary mechanism than primary mechanism. *Listeria innocua* is a gram-positive bacteria, the current results do not support charged particles as a reduction pathway due to the thick cell wall membrane inherent to gram-positive bacteria. The thick cell wall provides structural integrity to increase the tensile strength of the membrane against electrostatic disruption.

4.5.2 Reduction Mechanisms in Tepla Plasma Pen

More difficult to analyze is the reduction pathway in the Tepla plasma pen. Due to equilibrium or near equilibrium conditions in this plasma source, heat produced by resistive heating of the background gas during plasma operation is the primary mechanism. As an example, the amount of heat generated by the plasma pen was enough to melt two plastic substrates in just a few seconds, polycarbonate and polyethylene terephthalate (PET), with melting temperatures of 267C and 260C respectively. Additional, temperature measurements of the Tepla plasma pen were completed by PVA Tepla. By using a type K thermocouple, a temperature of 630 C (~900 K) was measured after just 20 seconds in the plasma [129]. Keeping in mind that other the process of pasteurization of fruit juices is currently recommended to operate at 72 C (345 K) for 15 seconds [15], demonstrates the extreme temperatures found in this plasma source. Additionally, the temperature of the plasma pen greatly effects the production of some key chemical species and UV producing radicals.

Compounds such as nitrogen oxides and ozone are very sensitive to temperature [55]. Temperatures greater than 500K shift the kinetic reaction pathway and limit the production of these compounds for use as a reduction mechanism [21]. A closer look at the work of Lu and King *et al.* shows how sensitive the reaction pathway is for both NO_2 and ozone production. From the Arrhenius relationship found in equation 4.3,

$$k = AT^{B}\left[\frac{-E(k)}{RT}\right] \tag{4.3}$$

where coefficients A,B, and E(k) are found in [55], the temperature dependence on NO_2 and ozone production can be calculated. Found in Table 4.4 and Table 4.5 are the reaction pathways to form these compounds.

Table 4.4: Found in the following table is the reaction mechanism and reaction rates for NO_2 production where the reaction rates depend on the relative velocities of collision partners. NO_2 production is dependent on a third body, $M = O_2$, N_2, the wall, or other third body to form NO_2.

NO_2 Related Reactions	A	B	E (K)
NO+O+M⇒NO2+N2	4.70E+24	-2.87E+00	7.80E+02
NO2+N2⇒NO+O+M	2.50E+28	-3.37E+00	3.76E+04
NO+O+M⇒NO2+O2	4.70E+24	-2.87E+00	7.80E+02
NO2+O2⇒NO+O+M	2.50E+28	-3.37E+00	3.76E+04
NO+O+M⇒NO2+NO	4.70E+24	-2.87E+00	7.80E+02
NO2+NO⇒NO+O+M	2.50E+28	-3.37E+00	3.76E+04
NO+O+M⇒NO2+O	4.70E+24	-2.87E+00	7.80E+02
NO2+O⇒NO+O+M	2.50E+28	-3.37E+00	3.76E+04
NO+NO⇒NO2+NO2	6.60E+00	2.70E+00	-1.60E+03
NO2+NO2⇒ NO+NO	1.60E+12	0.00E+00	1.31E+04
O+NO2⇒NO+O2	3.90E+12	0.00E+00	1.20E+02
NO+O3⇒NO2+O2	2.60E+12	0.00E+00	1.60E+03

Table 4.5: Found in the following table is the reaction mechanism and reaction rates for ozone production where the reaction rates depend on the relative velocities of collision partners. Ozone production is dependent on a third body, $M = O_2$, N_2, the wall, or other third body to form ozone.

Ozone Related Reactions	A	B	E (K)
O2+O+M⇒O3+O2	3.10E+17	-1.25E+00	0.00E+00
O3+O2⇒O2+O+M	4.40E+14	0.00E+00	1.14E+04
O2+O+M⇒O3+NO	3.10E+17	-1.25E+00	0.00E+00
O3+NO⇒O2+O+M	4.40E+14	0.00E+00	1.14E+04
O2+O+M⇒O3+N2	2.00E+19	-2.00E+00	0.00E+00
O3+N2⇒O2+O+M	4.40E+14	0.00E+00	1.14E+04
O2+O+M⇒O3+O	7.80E+13	0.00E+00	-3.45E+02
O3+O⇒O2+O2	1.10E+13	0.00E+00	2.30E+03

What can be observed from the kinetic data provided in these tables is the reaction pathways for NO_2 and ozone are competing due to both needing atomic oxygen for formation. Additionally, the rate coefficients are orders of magnitude lower for the ozone pathways which means the formation of ozone will be much slower than formation of NO_2. The reaction rates of the primary ozone formation are a few orders of magnitude smaller than competing reactions of NO_2, as a result the equilibrium between the forward and reverse reactions is less driven in the forward direction. The resulting dependence of gas temperature on the formation of NO_2 and ozone through the reactions pathways found in Table 4.4 and Table 4.5 can be represented in the graphs found in Figure 4.12 and Figure 4.13.

In Figure 4.12, the reaction pathway at higher temperatures (greater than ~750 K) is dependent on Reaction (1) where NO_2 is consumed at these temperatures. At lower temperatures (less than ~750 K), Reaction (2) dominates the reaction pathway and large amounts of NO_2 can be produced.

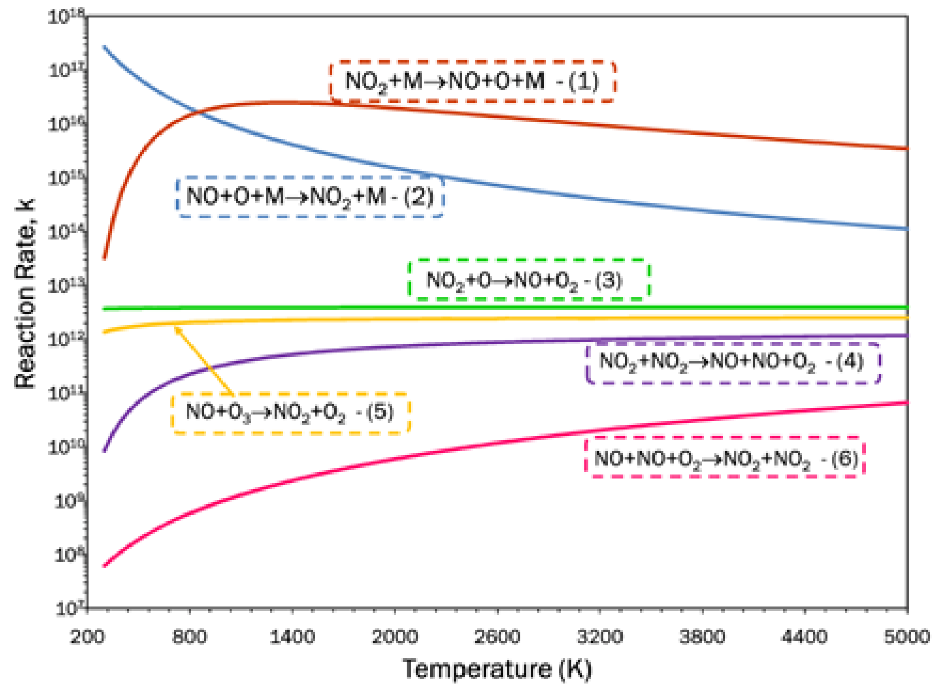

Figure 4.12: Shown in the figure is a graph describing the dependence of gas temperature on the production of NO_2. At higher temperatures, Reaction (1) consumes NO_2 and is the dominate reaction pathway. At lower temperatures and in the presence of an atomic oxygen source, Reaction (2) produces NO_2.

In Figure 4.13, the reaction pathway for ozone production is more subtle, but the gas temperature and presence of atomic oxygen still control ozone formation. At higher temperatures, Reaction (7) consumes all NO_2 in the reaction area. At lower gas temperatures, less than about 650 K and 750 K, Reactions (9) and (11) produce ozone in relatively large amounts although it is clear the difference in rate coefficients effects the speed of ozone production.

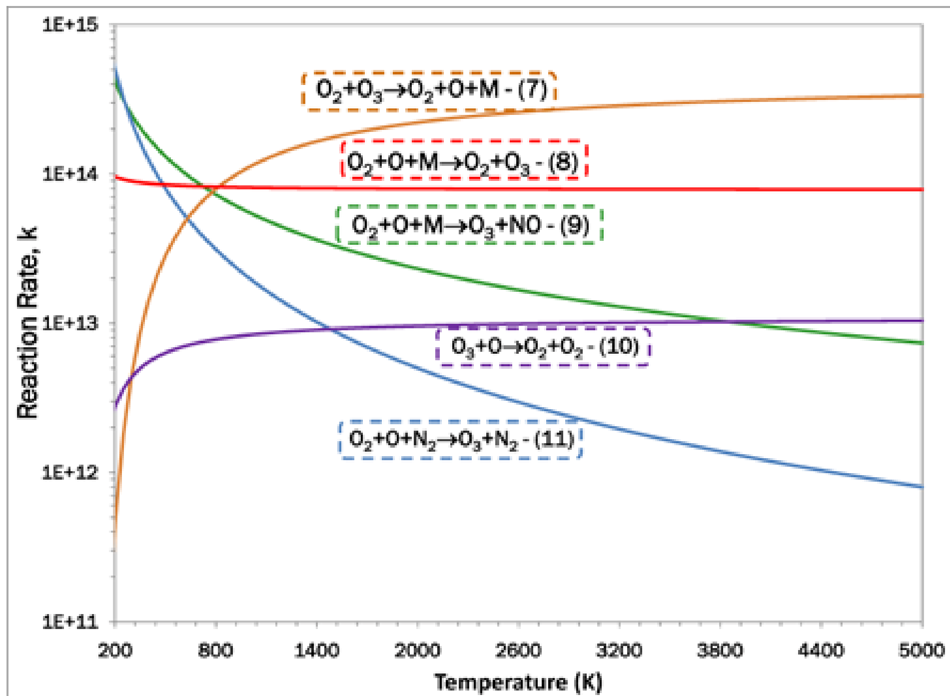

Figure 4.13: Shown in the figure is a graph describing the dependence of gas temperature on the production of ozone. In Reactions (7), the dependence of ozone production on temperature is shown, at higher temperatures more ozone is consumed. At lower gas temperatures, reactions (9) and (11) dominate the reaction pathway. If a source of atomic oxygen is present, ozone formation is favored at the lower temperatures.

Using the kinetic information found in these tables and plots it can be concluded the temperature of the plasma as measured by PVA Tepla (~900 K) greatly effects the production of ozone and NO_2 and from this it is not believed the chemical species in the

plasma are a primary reduction pathway in treatments with the plasma pen. Spectra taken from the plasma pen detected the presence of atomic oxygen. Found in Figure 3.14 is strong emission of the 777.2 nm and 844.6 nm lines associated with atomic oxygen [125]. Also found was emission from the nitrogen second positive system [128].

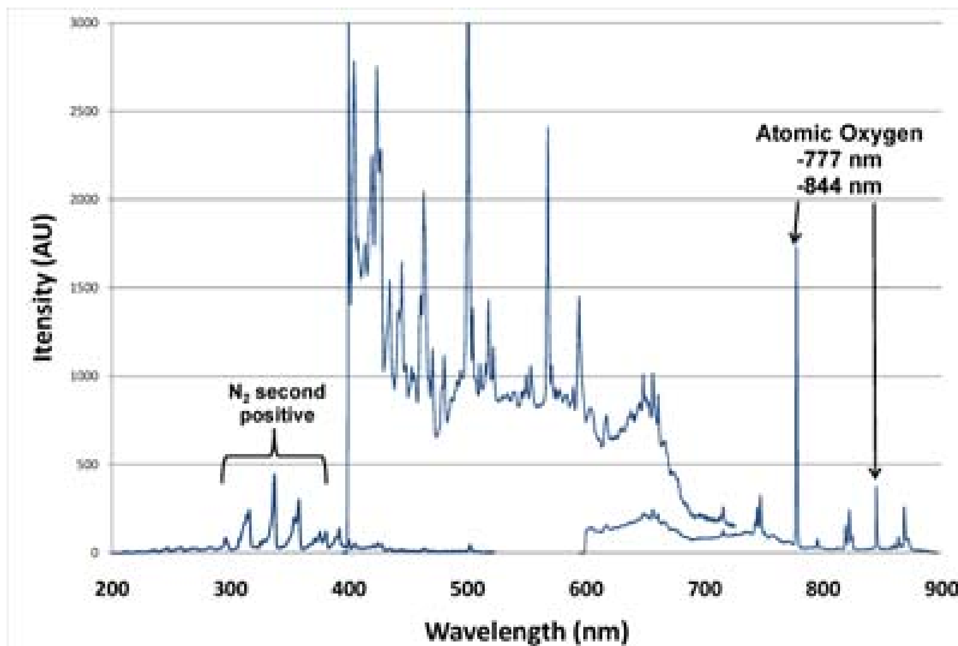

Figure 4.14: Representative spectra of a 100% air discharge from Tepla plasma pen. Strong emission of the 777.2 nm and 844.6 nm lines associated with atomic oxygen identified [125]. Also found was emission from the nitrogen second positive system [128]. Cutoff of the signal at ~400 nm is from channel cutoff between monochromators in the Ocean Optics S-2000 spectrometer setup.

Although there appears to be a good source of atomic oxygen for NO_2 and ozone production, the gas temperature in the plasma pen is too high for the reaction to take place. Overall, the kinetic data produced in Figure 4.12 and Figure 4.13 supports a reduction pathway by chemical species in low temperature plasma sources such as the DBD where gas temperatures are routinely measured to be less than 400K.

At this time it is unclear the role of charged particles from the plasma pen or other similar thermal plasma source on reducing bacteria. The critical energy needed for electrons in a plasma torch to rupture or tear the cell wall membrane is not known at this time. Additionally, it unclear how the two competing reduction processes, heat and charged particles, work together in the reduction process and if one of the two processes is the dominate mechanism. What is clear is how quickly the reduction process occurs. Treatments with the plasma pen proved to be very quick. A 3-log reduction of the gram-negative *Salmonella* spp. could be achieved and in as little as 0.41 seconds and in just over 1 second of treatment time, a 4-log and 6-log reduction of *Listeria innocua* was achieved.

The outlook for future research requires more work invested in understanding how each mechanism individually contributes to the reduction process. In addition to this, the equilibrium conditions from the many plasma configurations that can be used to reduce germs and bacteria and how the reduction mechanisms from these processes is currently poorly understood at this time. The knowledge developed from these two research areas would greatly increase the level of understanding for not only the food industry but also the medical and healthcare industries, government agencies, and other commercial groups interested in designing decontamination sources for protection against various biological hazards. Ultimately designing a decontamination source that easily kills both gram-negative and gram-positive bacteria along with more resistant germs such as *Aspergillus niger* and *Bacillius subtilis* is needed so that the many industries in need of a quick and portable decontamination source can be served.

4.6 Conclusions

The primary finding from these experiments is a DBD based and plasma torch based atmospheric plasma is capable of reducing both *Listeria innocua* and *Salmonella* spp. Both *Listeria innocua* and *Salmonella* spp. are problem organisms for the food industry. Due to the successful inactivation of *Listeria innocua*, it is believed atmospheric plasma treatments can also be successful against the pathogenic *Listeria monocytogenes*, a gram-positive bacteria found in milk, cheese, and vegetables. In evaluating the effectiveness of a portable

plasma pen, the atmospheric plasma quickly reduced the *Listeria innocua* and *Salmonella* spp. bacteria levels in less than 1 second and produces average kill widths as high as 5.3 mm. By setting up a number of these systems side by side, a large area treatment system can be created for possible application in the food industry. The portable plasma pen offers advantages in that the pen operates in ambient air, is portable, and is robust enough to be operated by robotic arms for more advanced treatment systems. The plasma pen can easily be installed in current processing environments and offers a promising alternative for an efficient, low cost solution to current issues presented on food safety. Additionally, other plasma sources with similar advantages of portability like the gliding arc discharge and atmospheric pressure plasma jet (APPJ) offer new ways for increasing the treated surface area.

This study has shown the gas composition to be an important factor in bacterial reductions using the DBD configuration. The addition of oxygen to the DBD based atmospheric system greatly reduced the necessary time to achieve a 6-log reduction of *Listeria innocua*. In addition, a large band of germicidal UV was detected in the emission spectra, leading to the conclusion that the primary reduction pathway is from not only from oxidation of the lipid bilayers but also from UV doses inducing dimerization of thymine bases in the *Listeria innocua* DNA. Heat was determined to be a secondary mechanism and the role charged particles is known not to effect gram-positive bacteria like *Listeria innocua*. The reduction pathway from the Tepla plasma pen is from heat. A temperature of ~630 C or ~900 K was measured from the active plasma environment. The extreme heat produced by the plasma pen also effects other reductions pathways such as chemical oxidation and UV generation. Although heat was found to be the main reduction pathway, 6-log reductions of *Listeria innocua* were achieved in about one second and 3-log reductions of *Salmonella spp.* were found in 0.41 seconds.

4.7 Acknowledgements

The authors of this work would like to thank Bernie Rapp at PVA Tepla for loaning the portable plasma pen used in the experiments described in this work.

4.8 References

The references for this chapter can be found in Chapter 10. The references were gathered in one large chapter in order to eliminate duplication and overlap between chapters throughout the dissertation.

5. Electrical and Optical Characteristics of a Low-Frequency Atmospheric Plasma Source for Powering a Dielectric Barrier Discharge at Atmospheric Pressure

Christopher J. Oldham, Matthew R. King, C. Richard Guarnieri, and Jerome J. Cuomo

Department of Materials Science and Engineering,
North Carolina State University, Raleigh, NC 27695

Manuscript to be submitted to the journal of IEEE Transactions on Plasma Science

5.1 Abstract

The electrical and optical properties of an atmospheric plasma discharge in a dielectric barrier discharge (DBD) arrangement were investigated using a new power supply design. It was found the power supply had three characteristic resonant modes of operation at 28 kHz, 81 kHz, and 160 kHz. Results from the electrical waveforms show the lower resonant mode at 28 kHz contained some non-linear characteristics. The non-linear characteristics are attributed to contributions from higher resonant modes operating at this resonant point. The higher resonant modes at 81 and 160 kHz operated without influence from higher resonant modes and the signal output of both modes was sinusoidal. The 100% helium discharge operated similarly to other atmospheric glow discharge plasmas in the field of DBD's. Operation with dielectrics in the gas gap resulted in a α-mode of operation, similar to the abnormal glow regime found in low pressure plasma discharges. Plasmas generated in the 0.5% nitrogen and 0.5% oxygen in helium gas mixtures resulted in a filamentary discharge. An α-γ mode transition was observed as power was increased with dielectrics in the gas gap. Without dielectric plates, only a γ-mode of operation could be produced. Large area plasma generation in the γ-mode was not shown with this power source.

5.2 Introduction

Atmospheric pressure glow discharges (APGD) are increasingly being investigated as a potential replacement for the widely used low pressure glow discharges for industrial needs in materials processing applications [8-10, 12, 32, 52, 54, 55, 58, 64, 84, 130-133]. Atmospheric pressure plasmas offer several advantages over the low pressure counterpart common to plasma processing applications. The advantages include the removal of complicated high vacuum equipment, ease of operation, lower capital equipment costs, and potential to operate continuously at ambient conditions [4, 6, 13, 36, 37, 53, 134]. Different types of atmospheric discharges have been developed for use in industrial applications; the dielectric barrier discharge (DBD) [11, 27, 41, 91, 135-137], the surface wave discharge [113, 138-145], atmospheric pressure plasma jet (APPJ) [24, 26, 34], the one atmosphere uniform glow discharge plasmas (OAUGDP), the resistive barrier discharge (RBD) [31], and most recently microplasmas [3, 41, 53, 133, 146].

Research into generation of an APGD has resulted in some difficulty in reproducing the same homogenous characteristics of a low pressure glow discharge. Although the two discharges operate in completely different collisional regimes, the physics associated with the two discharges are very similar [27]. One of the challenges with operating plasmas at atmospheric pressure is controlling the glow to arc transition. Controlling this transition is not a trivial task, although it has been achieved in a working gas of helium [20, 44, 51, 74, 75, 147, 148]. For the APGD to be realized as an industrially ready process, demonstration in less expensive gases such as nitrogen and argon is still needed. Unconventional electrode arrangements such as slotted electrodes, multiple electrodes and lithographic fabricated electrodes have shown an APGD can be produced in various gas mixtures [3, 4, 52].

Among the different types of plasma sources developed in the last number of years, the DBD configuration has attracted a great deal of attention as a configuration to produce an APGD for large area plasma treatment systems [20, 51, 54, 149, 150]. The DBD is a non-thermal, capacitive discharge generated between two parallel metallic electrodes, where either one or both electrodes are covered or coated with a dielectric material. Plasma

generation has been achieved over a wide spectrum of operating frequencies from pulsed DC through the kilohertz and megahertz regimes [1, 51, 151, 152].

5.2.1 Challenges for Operating a DBD as an Industrial Plasma Source

One of the challenges presented to integrate the DBD as a large area treatment source is finding a power supply capable of exciting a discharge over a large area while also providing a maintaining homogeneous glow throughout the treatment area. Generation of a homogeneous plasma environment has been difficult due to the current-voltage characteristics of the discharge. The discharge properties depend on the operating conditions (gas mixture, gap distance, and applied frequency,) used in plasma environment. The DBD is widely recognized as discharge with a filamentary nature [3, 37, 41, 74]. The filamentary nature is exhibited in the current waveform where multiple pulses per half cycle are commonly found [153]. A visible observation of the filamentary nature shows localized regions where intense streamers (or microdischarges) are present throughout the active plasma region. Of importance to use in industrial applications, the electron temperature, T_e, and densities, n_e, can range in these localized regions from 1-10 eV and 10^{14}-10^{15} cm^{-3} respectively. In contrast, the electron properties in a homogeneous DBD discharge can range from a T_e~0.2-0.5 eV and n_e~10^9-$10^{11}$$cm^{-3}$ [3]. This contrast shows the importance for producing a uniform plasma discharge for industrial applications since the change in electron properties greatly effects the treatment results. When the filamentary nature of the discharge is not controlled, areas of non-uniformity are commonly found after treating with a DBD based configuration.

Research into producing a stable discharge at atmospheric pressure is not a new idea. Siemens first achieved a stable discharge for the production of ozone in water purification applications in the year 1857 [19]. Siemens was the first to recognize that the insertion of a dielectric material in the active plasma environment resulted in a relatively stable discharge. Although Siemens was able to demonstrate a relatively stable discharge, the discharge was still filamentary in nature, with a large number of streamers about 100 μm in size across the dielectric surface [41]. Mechanisms for explaining the physics associated with producing a

APGD were completed by Kanzawa [44]. Kanzawa, showed under a few conditions, namely, working in a dilution gas of helium, frequency range of operation in the kHz range, and insertion of a dielectric material in the active plasma environment, a stable APGD could be produced. In other work by Roth et al., the group developed a DBD based reactor which they renamed the one atmosphere uniform glow discharge plasma (OUAGDP), and found similar results to the work of Kanzawa in producing a APGD [1]. However, Roth tried to explain the mechanism for the homogeneous glow was not based on operating conditions but rather a physical mechanism of "ion trapping" based on the frequency range of operation. The idea rests on Roth's theory that when the electrode are driven at high RF voltages and driven in the kilohertz range, the induced electrical field oscillates at a frequency high enough to trap the ions but not electrons in the gas gap. Further, Roth's theory explains the trapped ions go on to facilitate ionization events while the electrons recombine at the electrode surfaces. Roth concludes that it is this process of "ion trapping" that leads to a homogenous discharge at atmospheric pressure [1]. Although Roth makes many supporting points to his theory, the "ion trapping" mechanism has been disqualified by many groups working on theoretical and experimental reasoning to the homogenous mechanism.

A model by Kogelschatz, points to problems with the theory on the basis of the highly collisional regime of ambient conditions [41]. Kogelschatz explains the high collisional rate would not allow for trapping of charged particles in a single electric field. The model goes on to point out that if ions were trapped and electrodes recombined at the electrodes, an ambipolar electric field would be established to repel electrons away and bring the ions towards the electrodes. Further theoretical and experimental work by Massines et al. cleared up the mechanism behind forming a homogeneous discharge at atmospheric pressure. Massines et al. concluded, since the discharge is separated by dielectrics, the dielectrics act like a capacitor in series where the gas gap and as a result the dielectrics act to self-pulse the plasma by trapping electrons and metastable atoms between cycles [74]. The trapped particles act as seed particles to allow for a Townsend type discharge instead of a filamentary type discharge. In helium, the threshold for this transition is controlled through direct

mechanisms such as ionization (electron atom collisions) and indirect mechanisms such as collisions between metastable helium states with impurity atoms such as nitrogen and oxygen [153]. The numerical model described the small amounts of impurities in a discharge were responsible for controlling the glow to arc transition. Since the lowest energy level of metastable state of helium has a threshold of 19.8 eV, most impurities have a lower ionization potential than the threshold for the helium metastables, so impurities are easily ionized through Penning ionization events. It was also shown there are lower and upper limits to the percentage of impurities for inducing a homogenous glow discharge. If the percentage of impurities are too low there will not enough Penning ionization events to control the electron avalanche and filaments will form. If the impurities are too high (>0.05%), destruction of metastable species will occur and the discharge will transition to filamentary regime before the next half cycle pulse due to the lack of metastable Penning ionization events.

Of interest to this work was the investigation of a new power source and role of producing a stable glow discharge. Up until the time of this research, other atmospheric plasma DBD research groups along with our group had long used a power source that operated in the 1-20 kHz regime [1]. The power source is a simple design based on high power automotive ignition coils, an audio amplifier, and function generator. The design of the power source was economical, on the order of $1000, but experimental work with this source revealed serious limitations for powering a DBD configuration. First, the high power ignition coils are very capable of powering a helium gas gap but the addition of reactive gases such as oxygen, nitrogen, or carbon tetrafluoride put severe strains on the power supply components. For example, when an admixture of about 5% oxygen in helium was used, impedance mismatching between the power source, transformer, and gas gap (capacitor) would cutoff the power source in approximately 5-10 minutes from overheating of the internal solid state components. Secondly, if too much stress was applied to the components from impedance mismatching between the source and load, the automotive ignition coils would short between the primary and secondary. These results lead to the motivation of

finding a new source for powering the DBD discharge. Developmental work by Yancey and Lowery in the field of solid state power electronics lead to the idea of developing a new solid state power source as a power source for the DBD configuration [154]. It was believed at the time the only constraint limiting use of the DBD as a large area plasma treatment source was designing a power source that was capable of producing voltages of 10,000 V and also maintained the working integrity of the internal circuitry of the power module. In this work, a brief description of the results from implementation of a power source is presented. Of importance is checking the discharge for homogeneity while investigating the electrical and optical characteristics of the discharge.

5.3 Experimental

The barrier discharge used in this work is characterized by two parallel aluminum electrodes, each with a diameter of 11.5 cm. Pyrex plates with a diameter of 19 cm and thickness of 3mm cover both electrodes. The barrier arrangement is enclosed in a quartz chamber to allow for transmission of light in the ultraviolet range. A Balzer's mechanical pump and calibrated MKS mass flow controllers provide a controllable and reproducible environment through pumping and subsequent purging of the system.

The prototype power source used in these experiments was designed by AP Solutions Inc. (Cary, NC). The model is referred to as the AIR-DBD-5000 power module. The power supply is capable of delivering 5000 watts of peak power. The internal circuitry is based on a proprietary design and the specifics of the design were not disclosed for discussion in this work.

A Tektronix (Beaverton, OR) TDS-5000 series 350 Mhz 4-channel digital oscilloscope monitors the power delivered to the reactor. A Tektronix 6015A high voltage probe (1:1000) and Person Electronics model 4100 high current probe (1:1) monitor the power input to the discharge. Chemical species generated by the plasma are identified with an Ocean Optics (Dunedin, FL) S-2000 spectrometer. The spectrometer has a 0.5 nm resolution and is capable of measuring wavelengths from 200-900 nm. Light from the plasma source is collected by a 3-channel monochromator equipped with a 1200 grove/mm^{-1} holographic UV

grating, 1200 groove/mm^{-1} holographic VIS grating, and a 1200 groove/mm^{-1} NIR grating blazed at 750 nm. Optical pictures of the discharge were taken on a Nikon D60 digital camera.

Three resonance frequencies at approximately 28, 81, and 160 kHz were studied in this work. For all experiments, a RMS voltage of 1.9 kV and RMS current of 100 mA was applied to the plasma discharge although these power levels fluctuated slightly during the different frequency and gas mixtures. Gas flow rates ranged from 2.5-3 L/min, and the gap distance was held constant at 10 mm for all experiments. Three plasma chemistries were investigated for this work; 100% helium, 0.5% nitrogen in helium, and 0.5% oxygen in helium. To determine a spatial profile of the discharge, light emission was collected through a 200 micron pin hole aperture that was cut into a 4 inch aluminum tube. The aperture was placed between the source and detector. A spatial profile of about 1.6 mm was determined by drawing a sketch of the setup in Autocad.

5.4 Results and Discussion

5.4.1 Pre and Post Characteristics of the Discharge

Experimental data from fast Fourier transforms (FFT's) and current-voltage (I-V) results show distinctively different operational regimes of the power source. Tuning of the power source found three resonant points at 28, 81, and 160 kHz. Additionally, the pre (before ignition) and post (after ignition) characteristics of the discharge show the design of the driver circuit of load in this power source. In the design, when the 60 Hz AC line source is feed into the power supply, the line frequency is rectified to convert the AC signal to DC. Once the signal is rectified, the signal is then inverted to a high frequency continuous wave AC signal. In traditional designs, inverters normally power loads that are some combination of inductive and resistive components for use in household transformers and motors. The combination of these components gives rise to the wave shape of the output signal. In more advanced power supply designs, the primary of the transformer is driven with solid state power oscillators such as FET's, BJT's, and IGBT's. Driving the primary with these oscillators results in an output on the secondary that looks like a continuous wave. This is

favored result since in previous power supply designs to generate high voltage, where pulsing of the primary was achieved through methods such as a spark gap and large capacitor bank. The result of the pulsing through a spark gap signal produces oscillations on the primary side of the transformer that are discontinuous and pulsed. This is not an ideal situation for powering applications such as plasmas where a homogenous output of the power module is critical to many treatment applications.

Once the signal is rectified to obtain a stable DC voltage, the signal is applied to the high voltage transformer through a bridge of solid state switches. Pulses from this bridge are fed to two large capacitors that pulse the primary through a charge cycle that is monitored with an internal power supply controller. In the power supply controller, the charge cycle monitors the charge cycle in order to turn on and off the two capacitors pulsing the primary side of the transformer. The timing cycle to correctly pulse the primary is critical in the design of the converter in order to maintain and almost stable voltage from the output of the secondary. Pulses from 250 Hz and up can be used in the high frequency circuit topology.

Additionally, in the driver circuit to pulse the primary, design of the inverter in the high frequency circuit is very important to the overall power delivery and stability of the power source. The inverter in the circuit normally power loads that have some combination of resistance and inductance, like a motor. Since most inverters are some form of a square wave output the result of the inductance in load translates the output signal that is triangular or sawtooth in shape. This results in a circuit that when the load current is at a maximum, the voltage has to change polarity and the electronics components in the circuit have to switch a large amount of current. In contrast, when powering a plasma discharge, a capacitive component is added to the load, which forms a harmonic oscillator (RLC circuit), and as a result this combination works most favorably in resonant mode at particular frequencies (its naturals resonant frequency) [155].

In the resonant condition, if the load is driven with a square wave voltage waveform, the current flow in the output will be sinusoidal. The mechanics of the sinusoidal output comes from operation at the resonant frequency. At this frequency, the square voltage waveform

contains frequencies from the fundamental and all odd harmonics of the frequency. The load or output of the current only sees the fundamental frequency so as a result the output current contains only the fundamental frequency, which is sinusoidal in shape. This results in a circuit topology that allows for the load current to pass through zero at the same time as the voltage changes polarity. As a result, the limited current required to be switched by the inverter reduces stress on the inverter and provides for a longer lifetime of the power supply components. From Figure 5.1, a sine wave with non-linear characteristics was found before plasma ignition. The non-linear characteristics are most likely from the odd harmonics detected in the square wave voltage waveform.

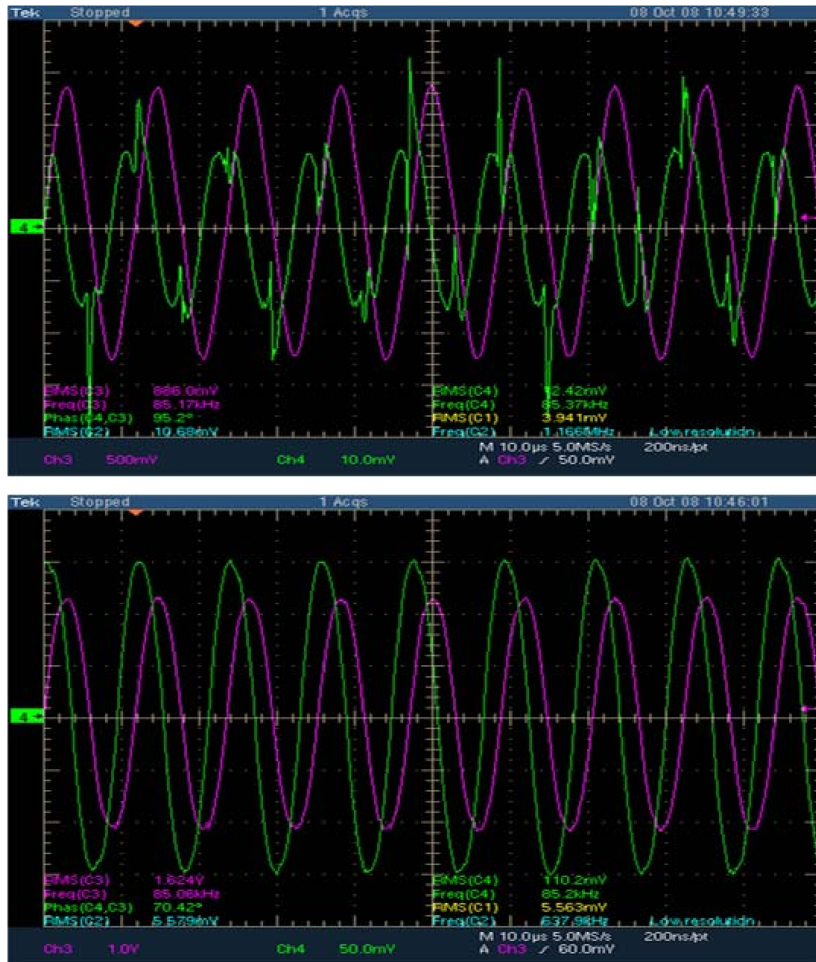

Figure 5.1: Inverter signal of APS AIR-DBD-5000 power source indicating the type of inverter used to power the load is from a true sine wave signal. Top waveform is before plasma ignition and bottom waveform is after plasma ignition. In the figure, the voltage is shown in pink and the current is shown in green.

The output after plasma ignition was also a sine wave which indicates the inverter used to power the load was of a square wave since the output signal is sinusoidal and appears to be free of any other odd harmonics.

From the FFT in Figure 5.2, a fundamental frequency referred to as the lower resonant mode was found at 28 kHz. Higher resonant frequency modes at the 87, 158, 203, and 263 kHz were also found.

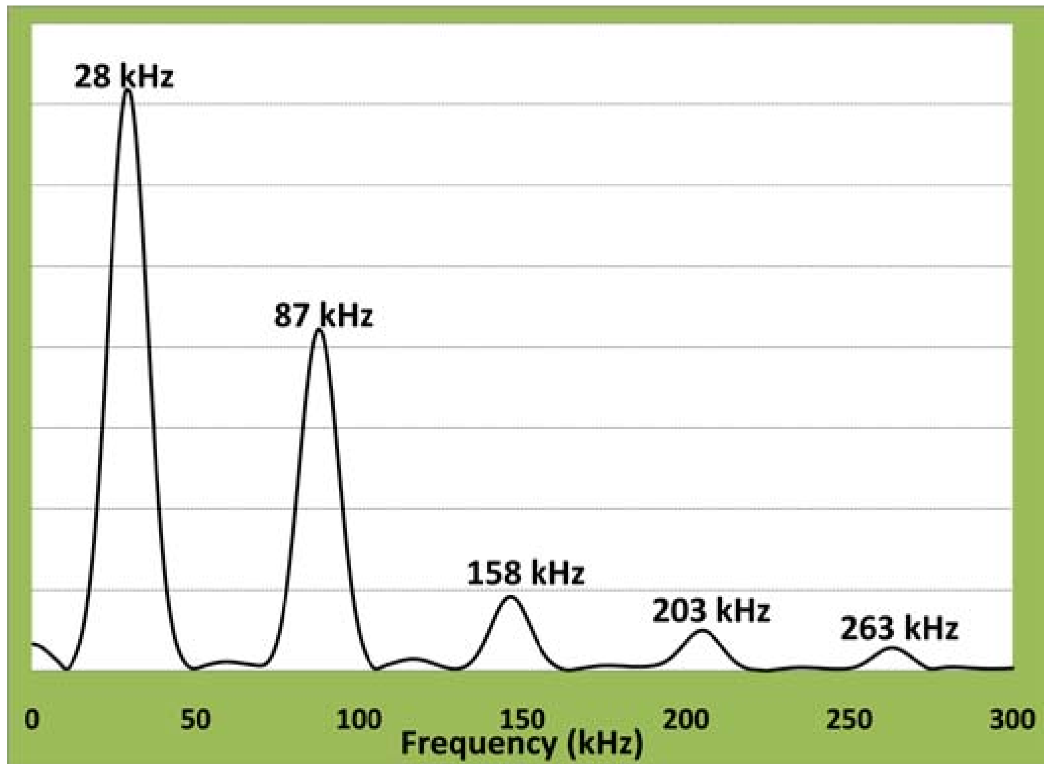

Figure 5.2: A fast Fourier transform of the APS AIR-DBD-5000 power source, taken at the lower resonant mode of operation, 28 kHz.

The electrical waveforms found in Figure 5.3 show the non-linear characteristics of the lower resonant mode of operation. The multiple pulses along the output cycle appear to be a result of the higher resonant modes found in this mode of operation. In contrast, the FFT and waveform results of the main resonant mode at 81 kHz and higher resonant mode at 160 kHz was found to behave differently than the lower resonant mode.

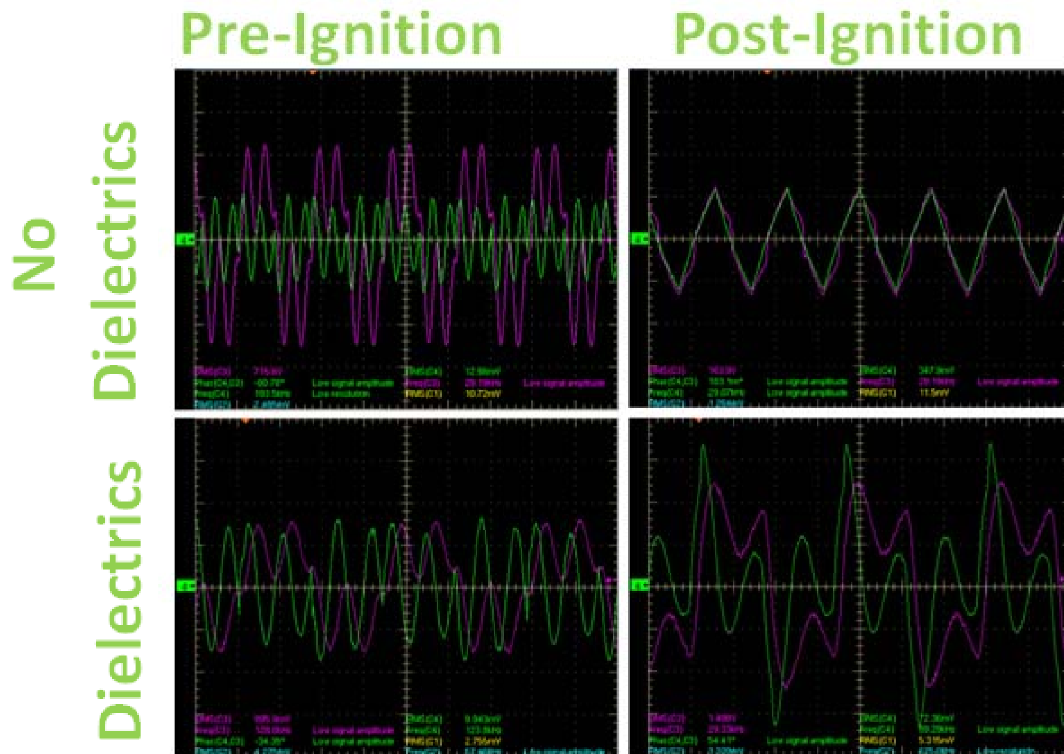

Figure 5.3: Shown in the Figure are the output I-V waveforms before and after ignition at the lower resonant mode of 29 kHz. In the figure, the voltage is shown in pink and the current is shown in green. Also shown in the figure are the I-V characteristics with and without dielectrics in the gas gap.

As shown in Figure 5.4, the FFT of the main resonant mode at 81 kHz showed little contribution from higher resonant modes.

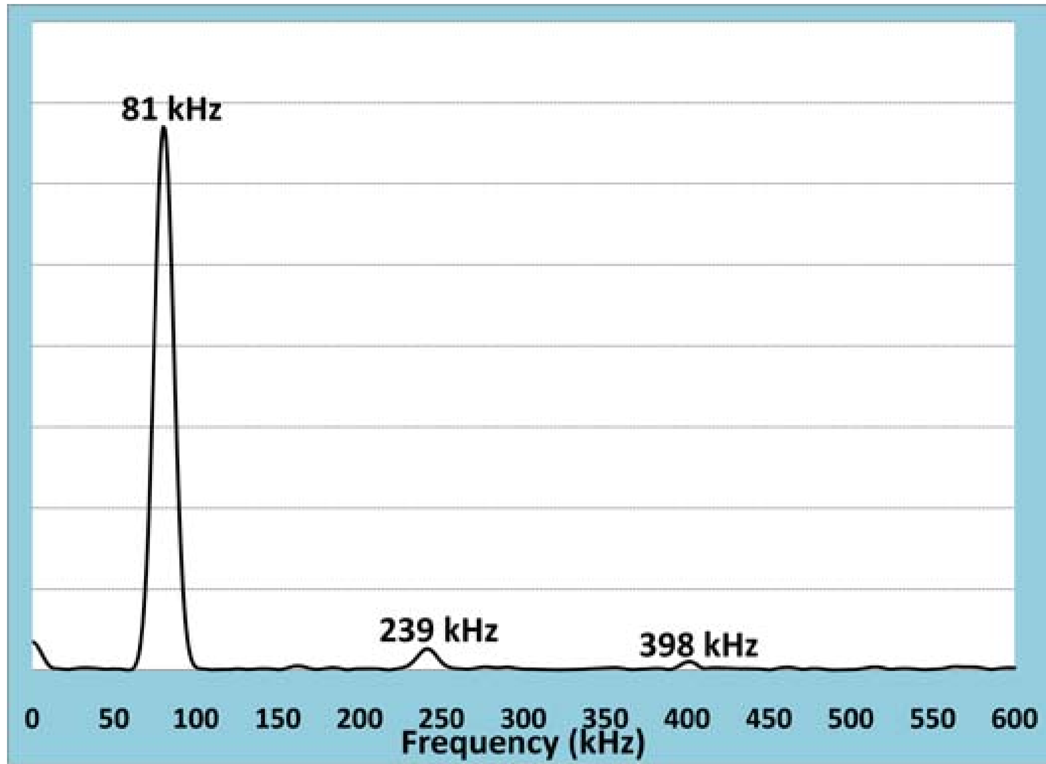

Figure 5.4: A fast Fourier transform of the APS AIR-DBD-5000 power source, taken at the main resonant mode of operation, 81 kHz.

Additionally, the electrical waveforms from this mode showed little to no contribution and were very smooth and sinusoidal in shape, the waveforms can be found in Figure 5.5.

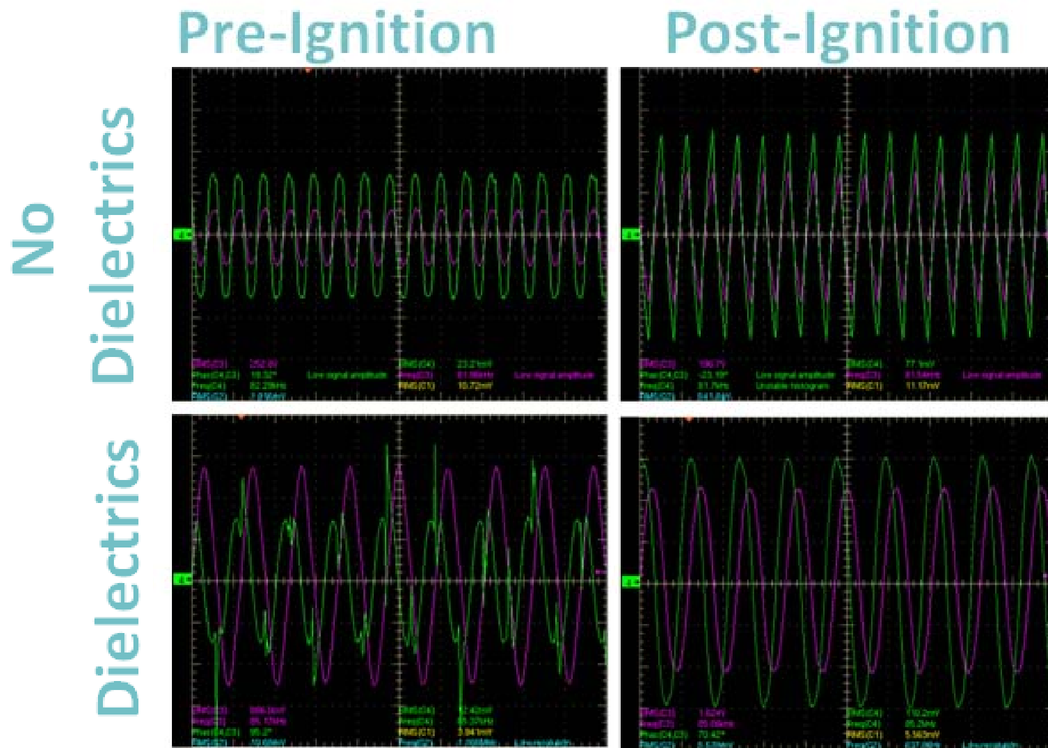

Figure 5.5: Shown in the Figure are the output I-V waveforms before and after ignition at the main resonant mode of 81 kHz. In the figure, the voltage is shown in pink and the current is shown in green. Also shown in the figure are the I-V characteristics with and without dielectrics in the gas gap.

From Figure 5.6, the FFT of the higher resonant mode at 160 kHz behaved very similar to the main resonant mode with little contribution to any other harmonic effects.

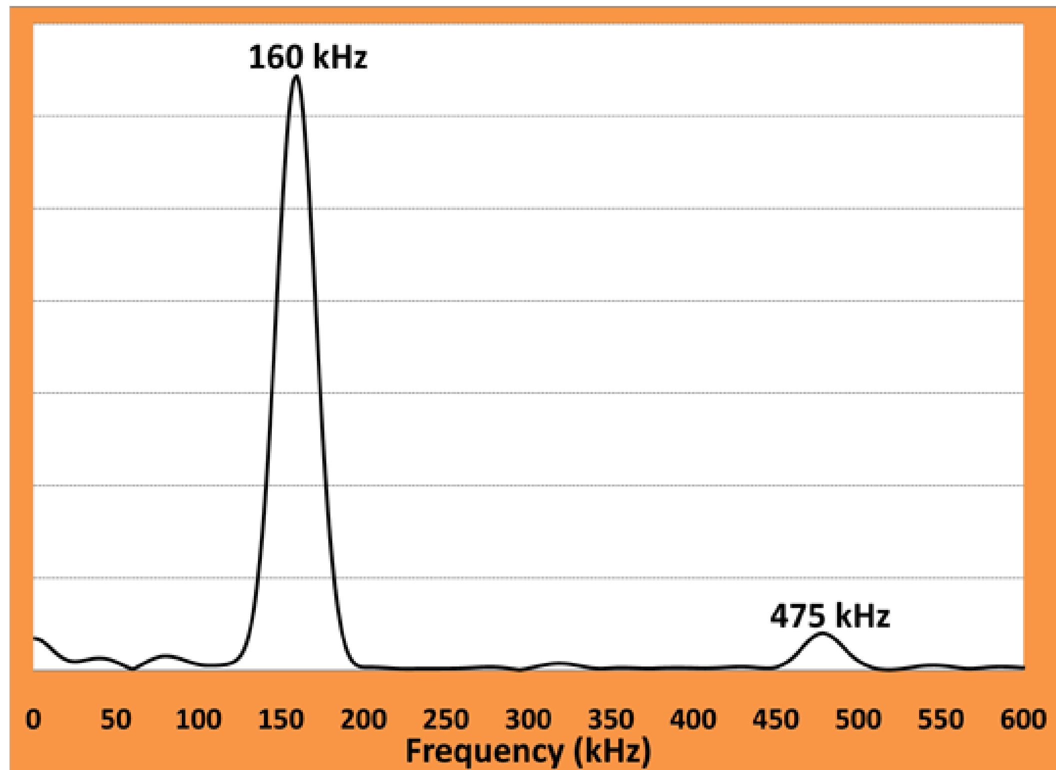

Figure 5.6: A fast Fourier transform of the APS AIR-DBD-5000 power source, taken at the higher resonant mode of operation, 160 kHz.

The electrical waveforms from the higher resonant mode are found in Figure 5.7. The waveforms were sinusoidal both before and after plasma ignition.

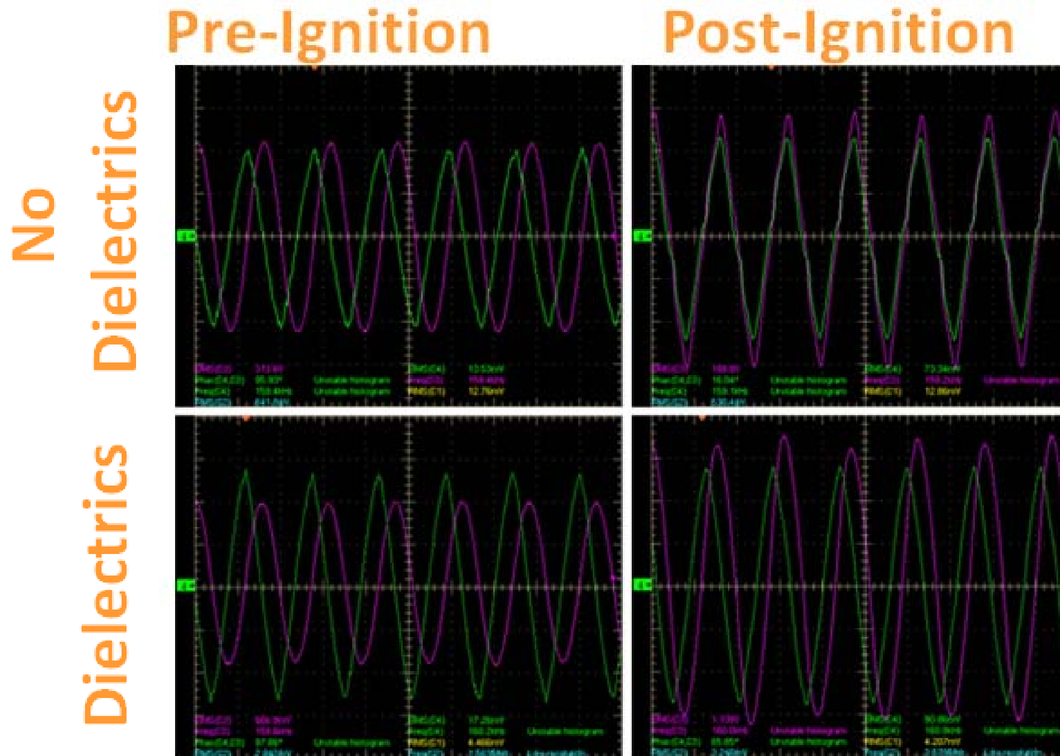

Figure 5.7: Shown in the Figure are the output I-V waveforms before and after ignition at the higher resonant mode of 160 kHz. In the figure, the voltage is shown in pink and the current is shown in green. Also shown in the figure are the I-V characteristics with and without dielectrics in the gas gap.

The APS AIR-DBD-5000 power module provides the flexibility to drive the transformer at three resonant modes. It has been shown the higher resonant mode acts very similar to other power supply designs where at the 160 kHz point of operation, little voltage or current is produced. It is believed this resonant mode is the "half wave" mode design. In traditional designs, the fundamental frequency is referred to as the "quarter wave" of the circuit design. The quarter wave refers to other harmonic systems such as a guitar string. The quarter wave in these systems represents the lowest frequency peak in response to the resonator and as a

result provides the maximum output rise from the resonator. Traditionally, the point of the quarter wave is the point where power supply designers want to drive the secondary in the transformer since it is the point where a maximum rise in voltage can be found. Similarly, when the transformer is driven at about twice the frequency, the voltage maximum rises at the center of the length of the wave and a minimum at the end of the wave. This is referred to as the half wave and only about half of the voltage is produced at this point compared to the quarter wave mode. In these results, a peak in voltage produced was found at the main resonant point of 81 kHz, while only about half of voltage could be produced at the higher resonant point of 160 kHz.

At the lower resonant mode (28 kHz), a large contribution from higher order resonant points in the power supply design was found. These contributions lead to a non-linear electrical waveform and demonstrate a leakage of the higher resonant modes. Current research with this module does not support a theory for the leakage of these modes, but it is thought switching of the MOSFET's or IGBT's in the solid state bridge design may not be well controlled at this mode of operation. The leakage may also be due to a large non-linear voltage rise along the coil length of the secondary transformer. Additionally, the non-linear behavior could be associated with a self-capacitance along the coil length. This effect is magnified at lower frequencies due to large contributions from the capacitive reactance in the design. At higher frequencies this effect is not as prevalent where the capacitive reactance, Cp, is $Cp = \frac{1}{2\pi(Freq)(C)}$. This conclusion is supported by the trend of sinusoidal responses found at the main resonant and higher resonant modes of operation. Removal of the higher resonant modes can be removed in future designs of this module by incorporating a capacitor and inductor design referred to as a low pass filter or resonant filter.

5.4.2 Electrical, Optical and Visual Characteristics of the Discharge

In Figure 5.8, Figure 5.9, and Figure 5.10 are the I-V curves for the lower, main, and higher resonant modes of operation are shown in 100% helium, 0.5% nitrogen in helium, and 0.5% oxygen in helium discharges with dielectrics in the gas gap. As a comparison, I-V

curves without dielectrics were also found. For the I-V curve for the 100% helium discharge found in Figure 5.8, a pink-purple discharge was struck at a voltage of 848 V and current of 32 mA for the lower resonant mode, a voltage of 832 V and current 20 mA for the higher resonant mode, and 851 V and 36 mA for the higher resonant mode.

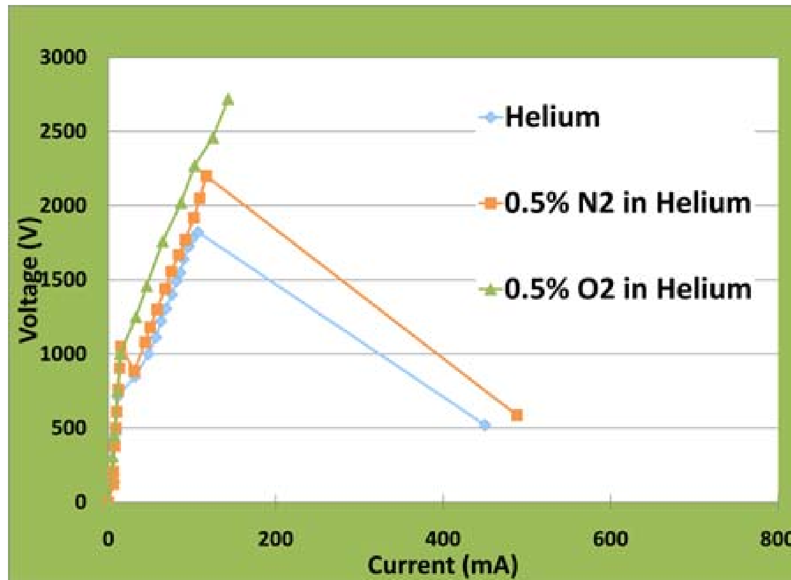

Figure 5.8: Current-voltage characteristics of the lower resonant mode of operation in 100% helium, 0.5% nitrogen in helium, and 0.5% oxygen in helium. Dielectrics inserted in the gas gap during plasma ignition.

For the 0.5% nitrogen in helium mixture in Figure 5.9, a filamentary pink discharge was struck at a voltage of 885 V and current of 32 mA for the lower resonant mode, a voltage of 1120 V and current 80 mA for the higher resonant mode, and 794 V and 44 mA for the higher resonant mode.

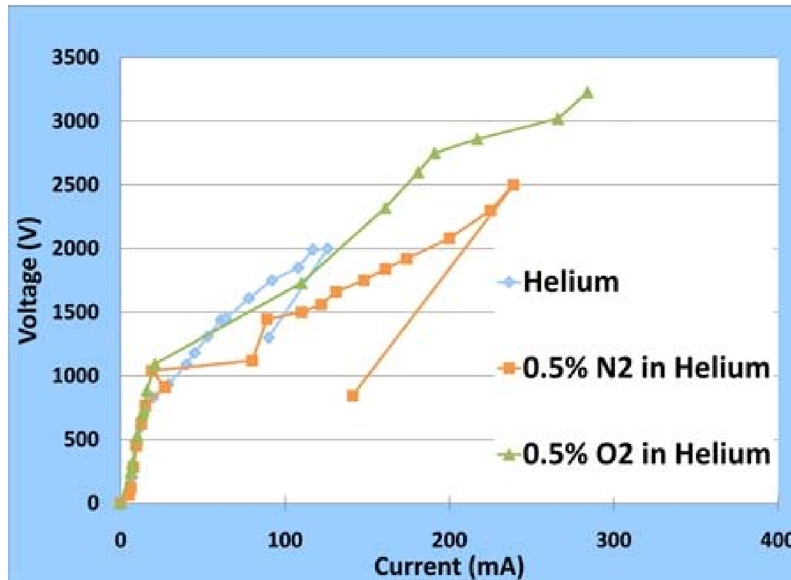

Figure 5.9: Current-voltage characteristics of the main resonant mode of operation in 100% helium, 0.5% nitrogen in helium, and 0.5% oxygen in helium. Dielectrics inserted in the gas gap during plasma ignition.

For the 0.5% oxygen in helium mixture in Figure 5.10, a filamentary white discharge was struck at a voltage of 1460 V and current of 46 mA for the lower resonant mode, a voltage of 1730 V and current 110 mA for the higher resonant mode, and 818 V and 28 mA for the higher resonant mode.

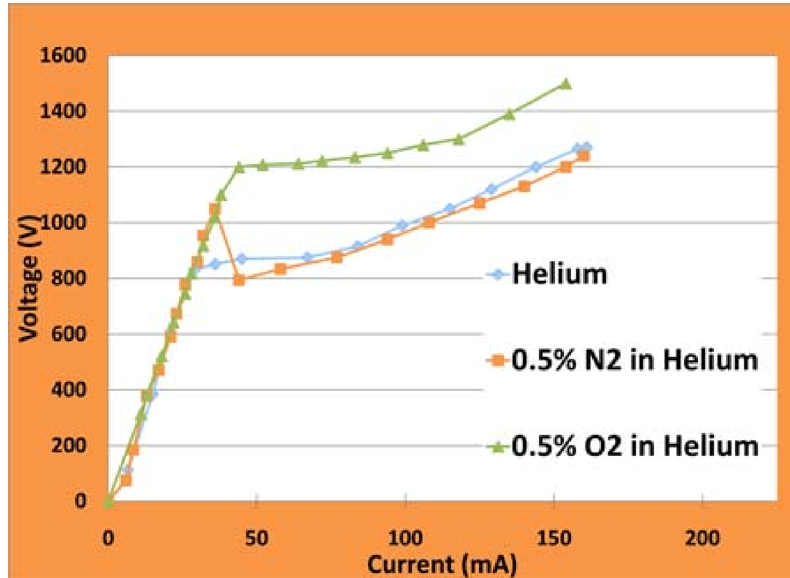

Figure 5.10: Current-voltage characteristics of the higher resonant mode of operation in 100% helium, 0.5% nitrogen in helium, and 0.5% oxygen in helium. Dielectrics inserted in the gas gap during plasma ignition.

The I-V characteristics of all three resonant modes increased linearly with increasing power from the source. This characteristic is similar to the abnormal glow operating regime of the α-mode shown by other researchers [32, 79, 156] and will be supported in the following paragraphs with spatial profile measurements of the discharge path. Upon increasing the power past breakdown, the glow discharge grew in intensity until at a critical point of increasing the power, an abrupt transition from α-mode to γ-mode occurred. This transition was accompanied by an expansion of the plasma at the lower resonance along with a sharp increase in current. At the main resonant mode this transition was followed by a sharp constriction of the plasma column and a large decrease in current in the plasma discharge. For the higher resonant mode, this transition could not be induced because the

power supply would not support such a power increase at this resonant mode. The α -γ transition observed at the lower and main resonant points has been observed in other studies of atmospheric plasma discharges [82, 147].

The I-V characteristics without dielectrics in the gas gap behaved very differently than when dielectrics are inserted in the gas gap. As shown in Figure 5.11, Figure 5.12, and Figure 5.13, the voltage rose linearly until breakdown, where at breakdown the current increase was sharp and the voltage dropped considerably. These characteristics are comparable to the same discharge characteristics found in a DC discharge [1].

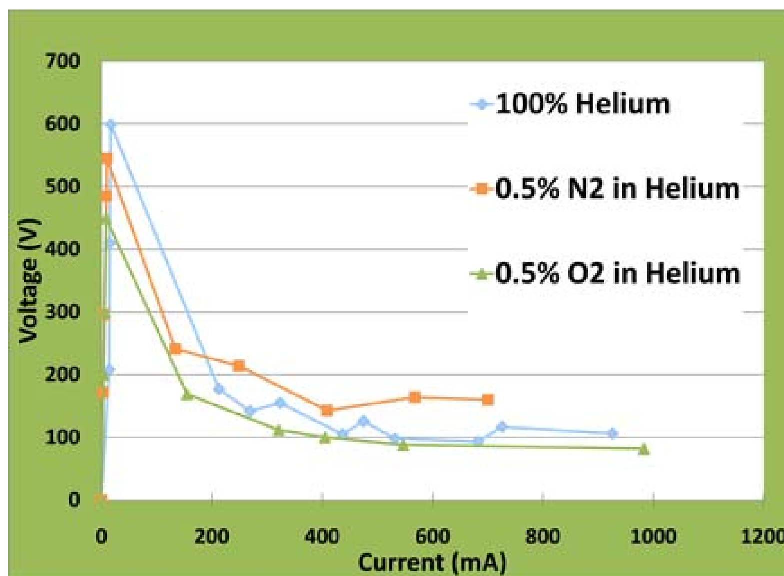

Figure 5.11: Current-voltage characteristics of the lower resonant mode of operation in 100% helium, 0.5% nitrogen in helium, and 0.5% oxygen in helium. No dielectrics inserted in the gas gap during plasma ignition.

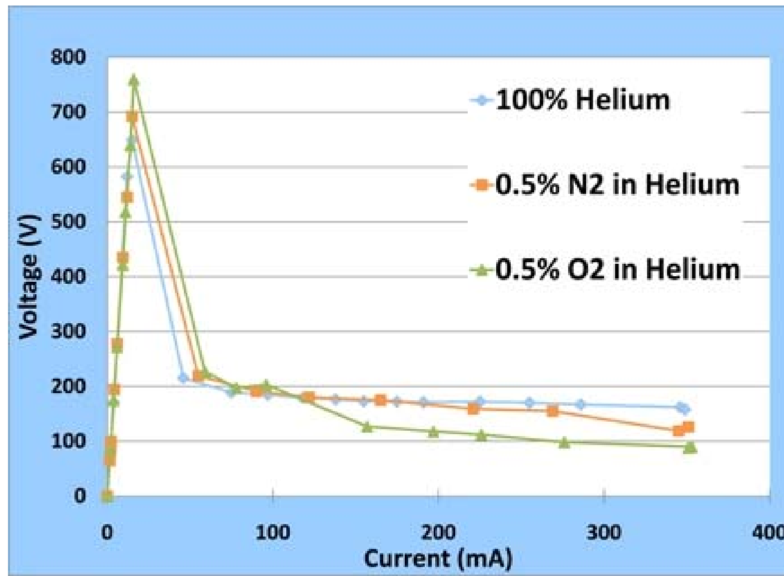

Figure 5.12: Current-voltage characteristics of the main resonant mode of operation in 100% helium, 0.5% nitrogen in helium, and 0.5% oxygen in helium. No dielectrics inserted in the gas gap during plasma ignition.

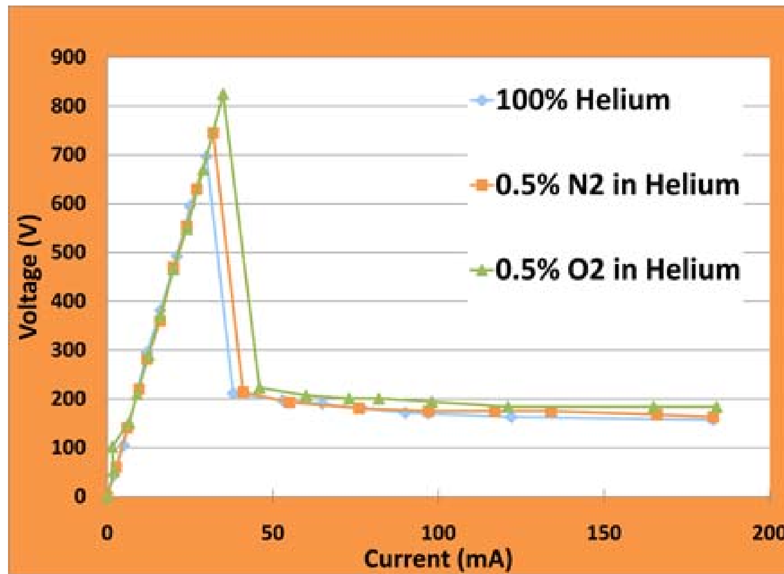

Figure 5.13: Current-voltage characteristics of the higher resonant mode of operation in 100% helium, 0.5% nitrogen in helium, and 0.5% oxygen in helium. No dielectrics inserted in the gas gap during plasma ignition.

In the composite images found in Figure 5.14, Figure 5.15, and Figure 5.16, are photographs of the gas gap with and without dielectrics. For the 100% helium discharge found in Figure 5.14 (a) with dielectrics at the lower resonant mode, the discharge gap was free of filaments and had the characteristics of an APGD. For the 0.5% nitrogen and 0.5% oxygen in helium gas discharges with dielectrics found in Figure 5.14 (a) and Figure 5.16 (a) respectively, the gas gap was more filamentary. The oxygen gas mixture contained a significant number more filaments from visual observation in the gas gap. These characteristics were the same for all three resonant modes of operation.

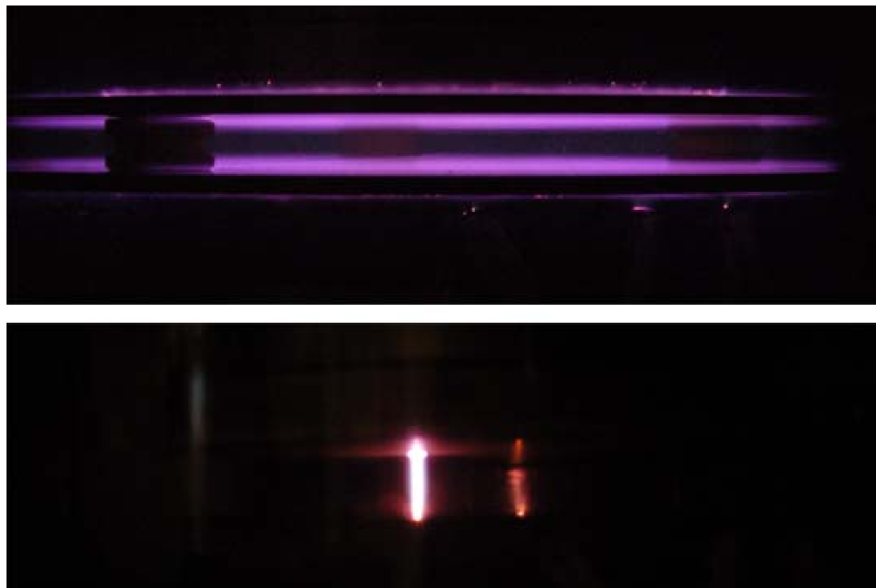

Figure 5.14: Photograph of the 100% helium discharge; (a) top photo with dielectrics and (b) bottom photo without dielectrics.

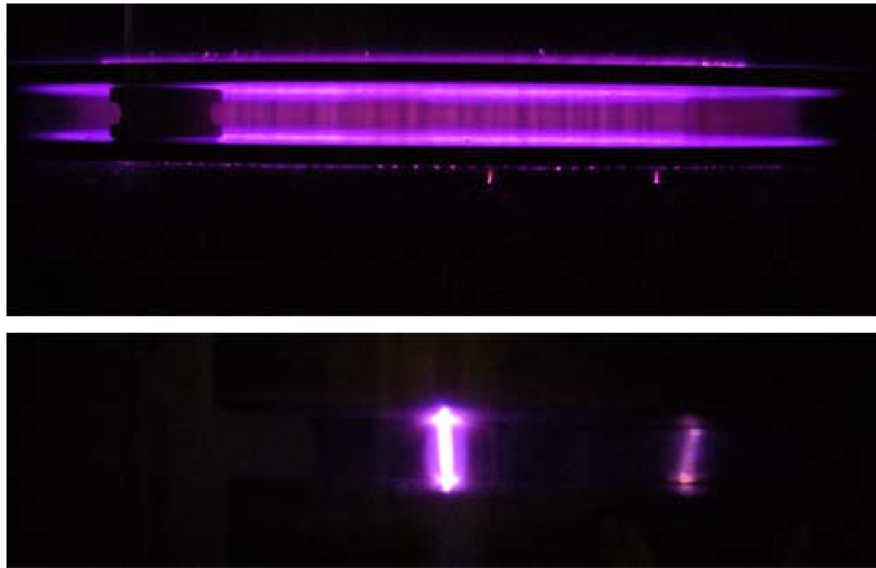

Figure 5.15: Photograph of the 0.5% nitrogen in helium discharge; (a) top photo with dielectrics and (b) bottom photo without dielectrics.

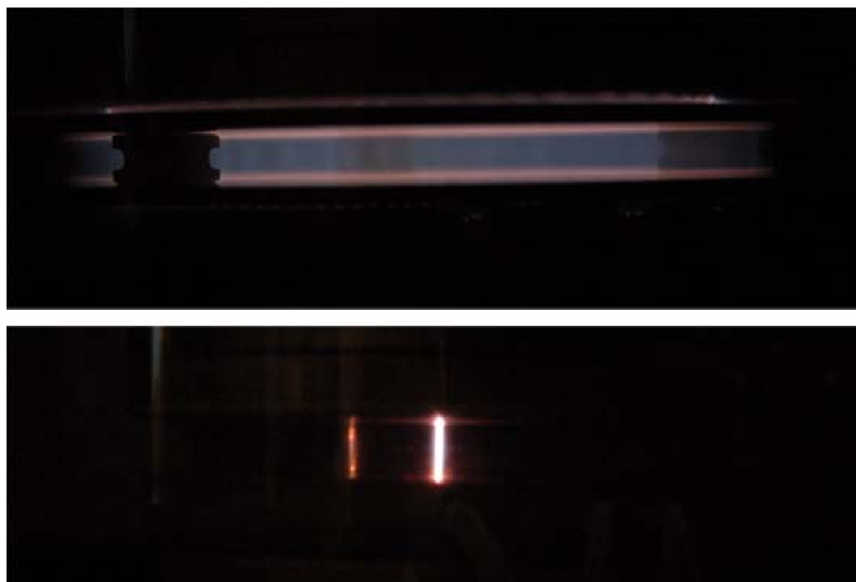

Figure 5.16: Photograph of the 0.5% oxygen in helium discharge; (a) top photo with dielectrics and (b) bottom photo without dielectrics.

For all three gas mixtures, when the dielectrics were removed from the gas gap, a single γ-mode plasma discharge was observed [51, 147]. The γ-mode of operation is shown in the

bottom images from Figure 5.14 (b), Figure 5.15 (b), and Figure 5.16 (b) for the 100% helium, 0.5% nitrogen in helium, and 0.5% oxygen in helium discharges respectively. The discharge for all three gas mixtures had the shape of a small dumbbell. The motion of the γ-mode discharge was not stationary and moved randomly throughout the gas gap. Increasing power to the discharge changed only the intensity of the discharge and expansion of the discharge in this mode to fill the gas gap were unsuccessful. A similar γ-mode discharge was replicated at the main and higher resonant modes of operation for the power module.

A spatial profile of the helium I emission at 706.5 nm showed for the 100% helium discharge in helium with dielectrics showed the emission intensity was symmetric across the gas gap. The spatial profile can be found in Figure 5.17.

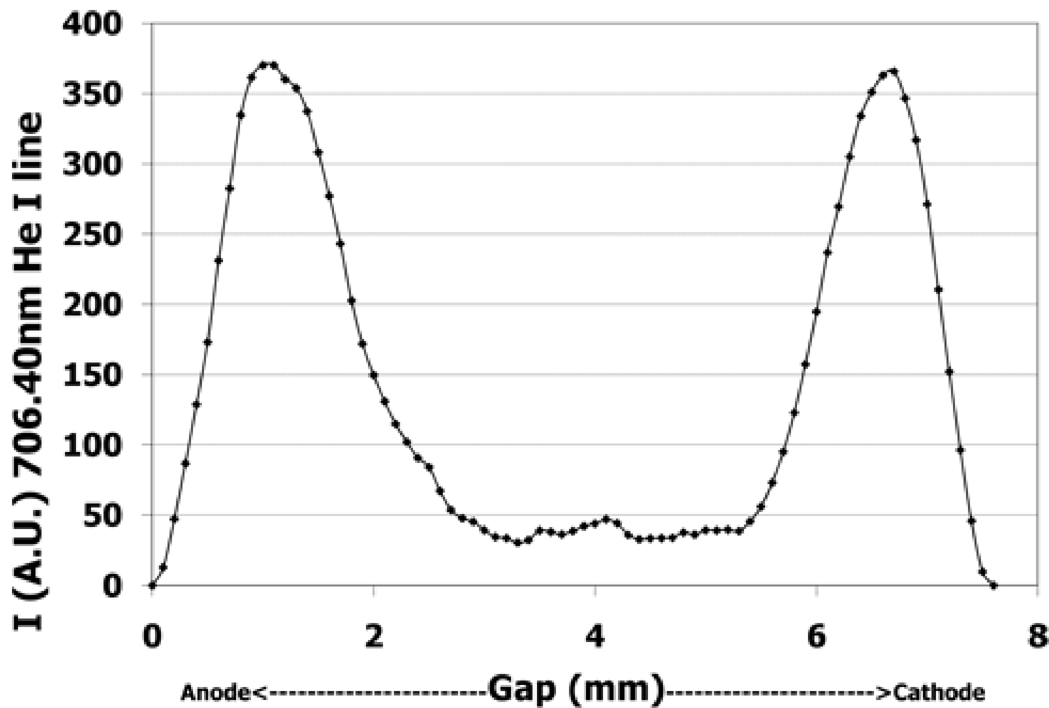

Figure 5.17: Spatial profile of the emission intensity between the electrodes for the α-mode of operation from the 100% helium discharge at 28 kHz.

The emission reached a maximum intensity about 1 mm away from the electrodes. The center darker emission region spanned about 3.5 mm. The decrease in intensity from the

maximum to the dark region was about one third. The layered structure produced by this discharge is characteristic of an α-mode discharge in which the discharge is sustained by bulk ionization of the gas [157]. Spatial profiles of the discharges produced without dielectrics were not completed. The discharge was not stationary and the measurement could not be completed due to the randomness of the discharge path along the gas gap. From other work with atmospheric plasmas, the discharge found without dielectrics is consistent with a γ-mode of operation where the discharge is sustained by secondary electron emission from the electrode surfaces [157].

Optical spectra collected from both discharges at the lower resonant modes of operation showed emission from the helium I atomic lines at 501.5 nm, 587.5 nm, 667.8 nm, 706.5 nm, and 728.1 nm [125] along with emission from the nitrogen second positive system (337.1 nm) [128].

Emission from atomic oxygen was detected at 777 and 844 nm in the oxygen containing mixtures [125]. The intensity of the emission was increased during operation without dielectrics in the γ-mode of operation although this increase could be an artifact of the measurement since it was very difficult to obtain spectra from the random discharge. Found in Figure 5.18 and Figure 5.19 are representative spectra produced by the power source with and without dielectrics respectively.

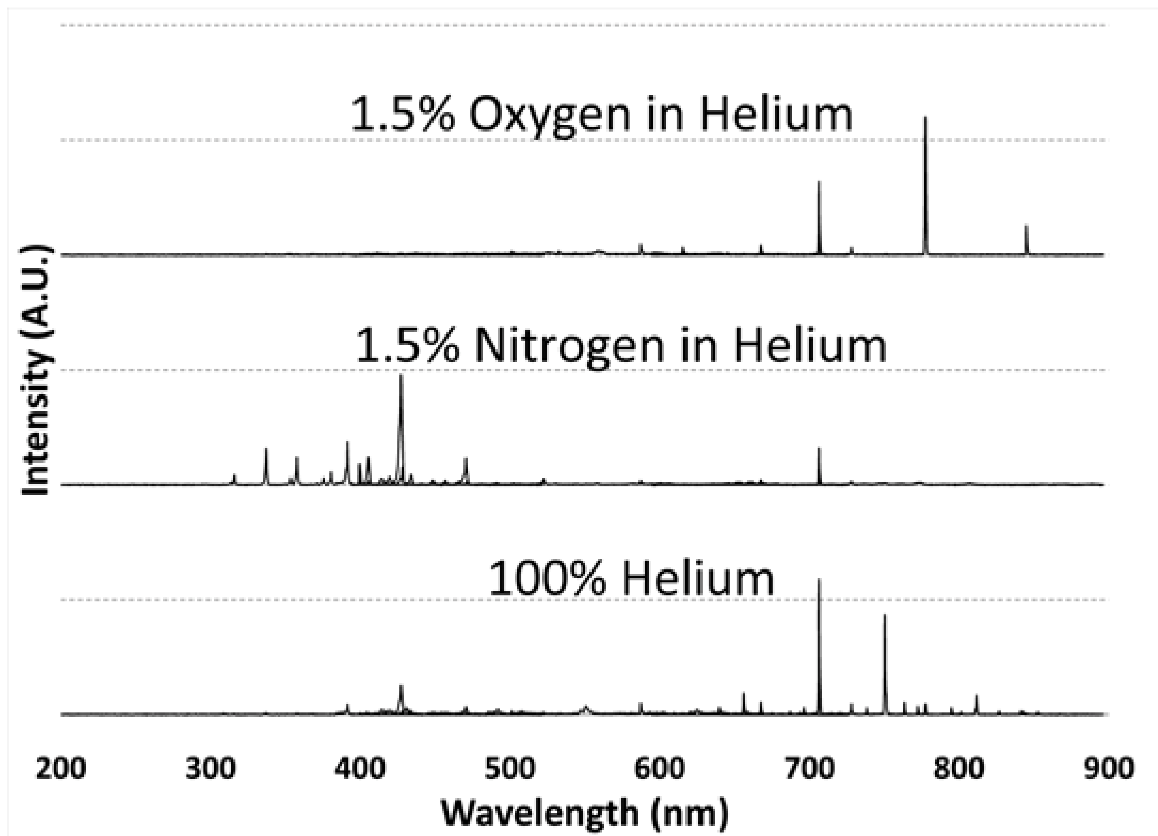

Figure 5.18: Optical emission spectra from the three gas mixture with dielectrics inserted in the gas gap.

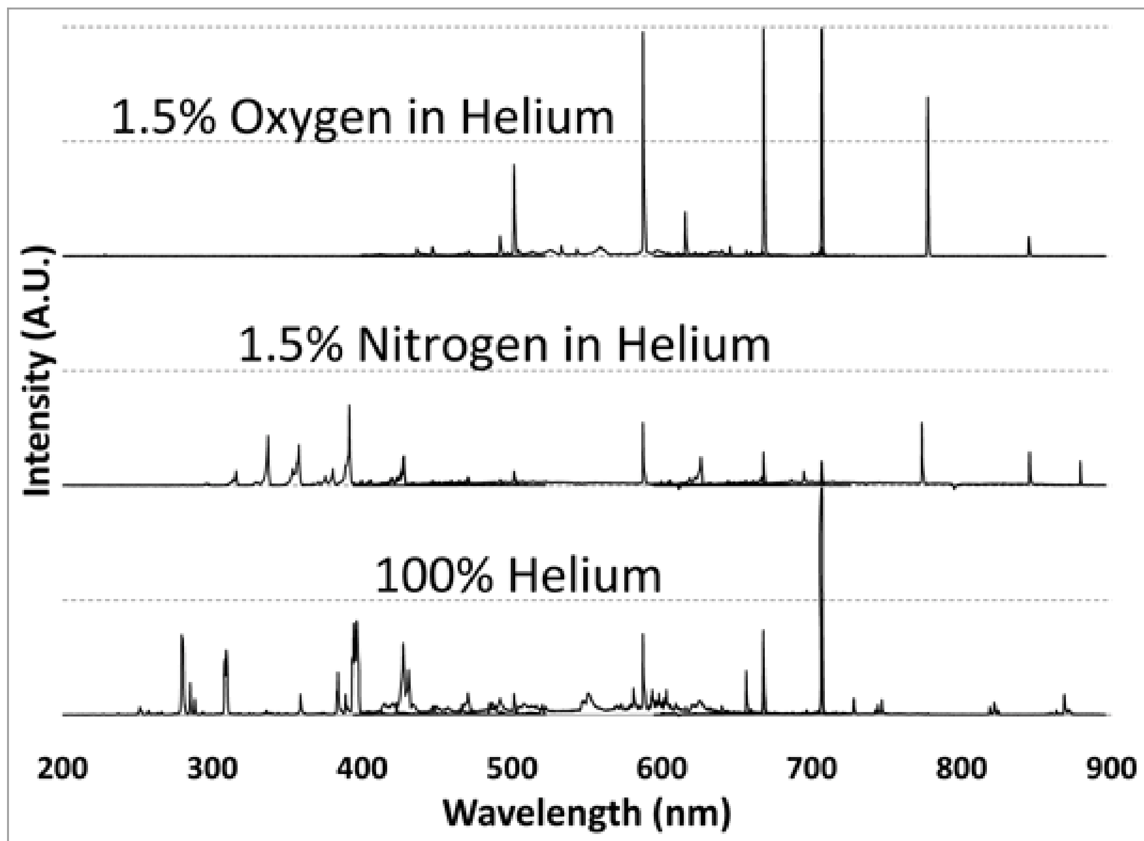

Figure 5.19: Optical emission spectra from the three gas mixture without dielectrics inserted in the gas gap.

5.5 Conclusions

This work investigated the properties of power supply design based on solid state components for powering a dielectric barrier discharge (DBD) configuration. It was shown the power supply has three characteristic resonant modes of operation at 28 kHz, 81 kHz, and 160 kHz. The lower resonant mode at 28 kHz operated with non-linear characteristics from contributions related to higher resonant modes. The main and higher resonant modes at 81 and 160 kHz respectively operated without the influence of higher resonant modes and the signal output of both modes was sinusoidal. The 100% helium discharge operated similarly to other atmospheric glow discharge plasmas in the field of DBD's. Operation with dielectrics in the gas gap resulted in a α-mode of operation, similar to the abnormal glow

regime found in low pressure plasma discharges. Plasmas generated in the 0.5% nitrogen and 0.5% oxygen in helium gas mixtures resulted in a filamentary discharge. A α-γ mode transition was observed as power was increased a with dielectrics in the gas gap. Without dielectric plates, only a γ-mode of operation could be generated. Large area plasma generation in the γ-mode was not shown with this power source.

From this work, the AP Solutions DBD-5000 power supply has been demonstrated to be a possible solution for industrial applications in need of generating large area homogenous plasmas at atmospheric pressures. The power source provides a commercially available solution to current laboratory based power supply designs and potential applications for deposition, etching, and surface modification with plasma processing at ambient conditions can now be realized for industrial application.

5.6 References

The references for this chapter can be found in Chapter 10. The references were gathered in one large chapter in order to eliminate duplication and overlap between chapters throughout the dissertation.

6. Development of a Pulsed DBD Assisted PE-CVD Process at Atmospheric Pressure for the Deposition of Hybrid Coatings

Christopher J. Oldham, C. Richard Guarnieri, and Jerome J. Cuomo

Department of Materials Science and Engineering,
North Carolina State University, Raleigh, NC 27695

Manuscript to be submitted to the Journal of Chemical Vapor Deposition

6.1 Abstract

The aim of this work was to develop a process for depositing hybrid inorganic/organic coating systems. Deposition of amorphous silicon carbide was attempted, with the end goal to utilize the coating systems in applications such as environmental barrier coatings, adhesion promotion layers, and corrosion protection layers. Coatings were prepared using a dielectric barrier discharge (DBD) assisted plasma enhanced chemical vapor deposition (PECVD) system. The system was operated at atmospheric pressure and at a frequency of 30 kHz. Coatings were deposited from silane (SiH_4) and methane (CH_4) in a carrier gas of helium. In continuous wave (CW) mode operation of the plasma source, homogenous gas phase nucleation was found at lower substrate temperatures (<225 C) and gas phase depletion was found at higher temperatures (>225 C).

It was found by introducing a pulsed plasma discharge during the deposition process, both gas phase nucleation and gas phase depletion effects were reduced. Pulse lengths from 0.5-10 sec with varying duty cycles from 10-90% were studied. Conformal thin film growth was found at pulse lenths of 1 sec with plasma on periods of 0.25-0.5 sec (25-50% duty cycle). Deposition rates from 100-250 angtroms/min were recorded. Pulse lengths greater than 2.5 sec and 50% duty cycle, resulted in a deposition process that resembled CW mode. Supported by analysis with a one-dimensional plug fow reactor, large concentration gradients were observed during deposition. Despite these gradients, XPS analysis showed the coatings contained good Si-C bonding. In the C 1s peak, Si-C bonding was on the order of 60% and in the Si 2P peak, Si-C bonding was found to be about 62%.

6.2 Introduction

Deposition methods for thin film growth are classified into two categories, physical or chemical [158]. In a physical process, deposition occurs through evaporation, sputtering, or sublimation and is referred to as physical vapor deposition (PVD) [158]. In a chemical process, deposition occurs through chemical reaction from a vapor source. The chemical process is referred to as chemical vapor deposition (CVD) and over the years has spawned many variants such as metal-organic CVD (MOCVD), atomic layer deposition (ALD), and molecular beam epitaxy (MBE) [159].

Both techniques have unique advantages and disadvantages for preparing thin films. Predominately the driving force behind the selection of the process is the ability to produce highly complex circuits for the electronics industry. As the circuitry for electronic devices has continued to evolve and devices have become more complex, selection of one film deposition method as a standard has changed with application and desired outcome. CVD processes are often a superior process to PVD processes due to the conformal properties of the deposited materials onto the substrate. CVD processes offer a high level of throwing power, which is the ability to uniformly coat complex substrates that have difficult topographical structures [160]. Alternatively, material deposited by PVD approaches are highly directional, the deposition process covers horizontal surfaces but fails to deposit in deep holes or trenches, a requirement in the development of integrated circuits in the semiconductor industry [158]. Additionally, CVD processes often produce films with highly desirable properties by accident. For example, in flat panel displays, the display is divided into thousands and sometimes millions of pixels. Each pixel is turned on and off by individual transistors. The transistors are formed from semiconductors of a silicon matrix by doping the matrix with either phosphorus or boron. PVD deposition of silicon results in films that have a high number of defects with a large number of broken bonds. This results in flat panel displays with poor electrical properties. CVD deposition of silicon results in the incorporation of a large amount of hydrogen [159]. The hydrogen impurity actually is quite beneficial to the electronic properties of the display, as the hydrogen terminates the dangling

bonds of the silicon and improves the ability of the material to be doped, thus improving the semiconducting properties of the silicon and electrical performance of the display [159].

CVD methods are distinguished by the conditions used to carry out the process. CVD methods vary from ultrahigh vacuum (UHV-CVD), low pressure (LP-CVD), and atmospheric pressure (AP-CVD) [161]. In general, the deposition process and overall effect on deposition rate and film properties is controlled through the amount of energy supplied to the precursor, precursor properties and purity, substrate temperature, gas flow rates, ratio of reactants to background gas species, operating pressure, geometry of reaction chamber, and surface properties of the substrate [159]. Most reactions taking place in a CVD reactor are endothermic meaning the reaction has some activation energy in order to initiate the deposition process. Thin films produced by CVD processes are formed by the providing energy which is sufficient to promote precursor reactions in the gaseous state. The energy must overcome the activation barrier and can be supplied by a number of sources [162]. Generally, heat has been used to thermally dissociate the vapor source, which in turn controls the chemical reactions for thin film growth. Other methods have been developed to assist the chemical reaction pathway through the incorporation of plasma discharges, plasma enhanced (PE-CVD), and photo excitation (photo-CVD or laser-CVD). For example, in a LP-CVD process, the energy needed to deposit epitaxial silicon is 2.1 eV (>650 C), in a AP-CVD process, the energy needed to deposit the same system is on the order of 3.5 eV (>900 C) [162].

As deposition needs have changed to incorporate low melting point metals and soft materials with polymer or bio-material backbones, thermal based and some low pressure CVD processes are excluded for application in these processes [163]. Additionally, in thermal-CVD or LP-CVD processes, the deposition rate and film structure are tied directly to changes in operating conditions [159]. Changes in the process adjusts both parameters directly and independent control over phase structure and film properties can only be achieved if the energy necessary for bond cleavage is supplied by a secondary energy source. One source for promoting this bond cleavage is through introduction of energetic electrons

into the CVD reactor [162]. One such method for introducing high energy electrons is through plasma discharges (PE-CVD). In a plasma discharge, generally electrical energy is supplied to a neutral gas, such that free electrons in the gas gain kinetic energy from the electric field. Through electron impact collision events such as ionization, excitation, and dissociation, species such as positive ions, metastable species, photons and radicals are produced [160]. Production of these energetic species allows for second energy source to be integrated into the CVD process and thereby permits kinetic boundaries found in thermal and low-pressure CVD processes to be overcome.

6.2.1 Chemistry in a Plasma Enhanced Chemical Vapor Deposition

In a plasma enhanced CVD growth process, two basic functions are performed to enhance thin film growth during the deposition process. The first is production of chemical species through electron impact collisions with background gas species and precursors introduced into the chemical reactor. The second is production of energetic species such as ions, metastable species, and photons for modifying the growing thin film. These energetic species collide with all surfaces in the reaction zone and aid the deposition process by supplying energy to the growing film through inelastic collisions. The combination of the chemical and physical aspects of the PECVD process results in film properties that are achievable in few other processes.

With the wide range of chemical reactions occurring in a plasma discharge, reactions are generally divided into two groups; homogeneous gas phase collisions and heterogeneous surface interactions [164]. In a homogeneous gas phase reaction, the process represents the production of metastables, free radicals, and ions produced in the discharge by electron impact reactions [163]. The reactions events can take many kinetic pathways and are dependent on the electron energy distribution in the discharge. The second type of homogeneous reaction occurring in a CVD reactor is the interaction of the energetic species in the plasma discharge (Penning events) with unreacted precursor species. Penning events occur when long lifetime metastable species collide with neutral species. The transfer of excess energy initiates new dissociation and ionization events. In a deposition process

Penning events are very important in gases such as helium, nitrogen, and argon where these gases have many long lifetime metastable states. The metastable states aid the deposition process by lowering the activation energy needed to deposit materials. Vibrational excitation is also important, but concerns only polyatomic species. This is especially true for molecules with large bond energies. When vibrational excitation takes place, the electron energy required for dissociation is significantly reduced.

The second chemical process that occurs during PE-CVD processing is heterogeneous surface reactions through interaction of plasma species and solid surfaces [163]. As proposed by Winters, elementary surface processes for plasma deposition include ion-surface interactions resulting in processes such as sputtering, electron-surface interactions that produce secondary electron emission and electron-induced chemistry, and radical-surface interactions resulting in such processes as etching and deposition [165]. The surface events can result in positive changes to a growing film such as changes in film crystallinity and growth rate and negative effects such as defect generation and contamination

Although particle bombardment can alter the deposited film greatly, the complexity of the plasma environment and interplay between surface and gas-phase chemistry is difficult to separate [166]. Interaction between these reaction zones ultimately determines the film structure and properties of the thin film. At the core of this interaction is the fuel or energy required to initiate chain reactions, namely electron impact collisions. From these chain reactions, a chemical soup is produced that is full of electrons, ions, metastables, radicals, and photons. From this chemical soup, deposition in a CVD environment can be achieved at relatively low temperatures (~300 C). Insight into the power provided by PE-CVD processing is provided in Table 2.1, where a list of bond energies for various gas compositions used in CVD processing is provided. From the table, the energy needed to break a chemical bond can be from about 1-5 eV.

Table 6.1: Representative bond energies of hydrogen, silicon, carbon, nitrogen, oxygen, and fluorine with various species.

Bonds with Hydrogen	kJ/mole	eV/atom
H-H	435	4.51
H-C	414	4.29
H-N	389	4.03
H-O	464	4.81
H-Si	318	3.30
H-Cl	430	4.46

Bonds with Silicon	kJ/mole	eV/atom
Si-O	451	4.67
Si-F	564	5.85
Si-Si	221	2.29
Si-Cl	380	3.94

Bonds with Carbon	kJ/mole	eV/atom
C-C	347	3.60
C=C	610	6.32
C-N	305	3.16
C=N	614	6.36
C-F	484	5.02
C-O	359	3.72
C=O	735	7.62
C-Si	301	3.12
C-Cl	339	3.51

Other Bonding Types	kJ/mole	eV/atom
N-O	221	2.29
N-F	272	2.82
O-O	195	2.02
O=O	250	2.59
O-F	188	1.95

To understand how a plasma can be so efficient at breaking chemical bonds, one must look to the two variations that a plasma can be used during processing, either hot (thermal) or cold (non-thermal). In a thermal plasma, the average energy of all particles in the plasma is so high that atoms are easily separated from electrons on a regular basis, typically temperatures larger than 5000 K are routinely found in thermal plasmas. In a non-thermal plasma, only the electrons sustain a high energy (>10,000K or about 1-10 eV) while the background neutrals and ions are left at or near room temperature, about 300-1000 K. The large temperature difference results in an interesting environment for plasma chemistry to take place. The hot electrons are used to ionize, dissociate, and excite the vapor source while the cool ions impinge the growing film.

PE-CVD reactors have historically been operated under low pressure [166]. Fundamentally, low pressure operation has been the dominate pressure regime since it limits background gas heating and keeps the plasma discharge in a non-thermal mode of operation. Low pressure CVD reactors are designed to so that the size of the system is much smaller than the mean free path (distance between collisions, with either a wall or other gas species). Using this environment helps minimize energy transfer between electrons and heavy species, and allows electrons to sustain a much higher average energy. In a low pressure process, the

electron temperature is much higher than the gas temperature and electron collisions with precursor and neutral species results in the formation of chemically active species. Low pressure CVD processes have been implemented in a wide range of applications where organic and inorganic products are desired. However, the low pressure CVD process is not without limitations. Since a low pressure CVD process requires the use of vacuum chambers, load locks, and pumping stations, many industrial deposition applications are not practical. The high cost needed to invest in capital infrastructure and ongoing operating costs have pushed CVD techniques to atmospheric pressure [54, 167].

6.2.2 Deposition at Atmospheric Pressure

Historically, deposition at atmospheric pressure has been found with a process of spraying a powder through a hot plasma torch [168-171]. In the plasma spray process, powder is injecting into a hot plasma environment at temperatures above 10,000K. The powder is heated to a molten state where it is ejected from the plasma jet for deposition onto a desired substrate. The process is capable of very fast deposition rates and can deposit a range of materials that include metals, ceramics, and composites. The thermal spray process is a line of sight deposition technique and cannot adequately coat large area substrates. As a result, limitations with the thermal plasma spray process have been overcome by development of atmospheric plasmas that operate in a non-thermal mode of operation [4]. The discharges are typically of low frequency such as the dielectric barrier discharge but also radio frequency discharges in small gaps and microwave discharges have been demonstrated [3]. The main characteristic of these discharges is the background gas temperature remains relatively cold. That is, the electron temperature for these non-equilibrium discharges lies in a very narrow range from 1-10 eV, while the temperature of the background and precursor species does not usually exceed 1000K. These characteristics are very similar to low pressure CVD processes where the average electron temperature is also between 1-10 eV and the background gas temperature is also very low.

From this information the characteristics of PE-CVD at atmospheric pressure should be very similar low pressure PE-CVD, but there are some distinct differences with operating at

high pressure that can greatly influence transport and kinetic pathways to deposition. The differences include:

- At atmospheric pressure, the partial pressures of the precursors are about three orders of magnitude higher than low pressure CVD systems. This results in an increase in homogeneous reactions and the formation of powders in the gas phase and powder incorporation into the films grown heterogeneously.
- The increase in partial pressures also can lead to higher growth rates than found with low pressure systems. This in turn can lead to a depletion of the precursor or active species in the desired deposition zone and poor uniformity.
- Mass transport limitations are much more significant at higher pressures and can lead to poor thickness uniformity.

These considerations have not limited interest into the development of PE-CVD processes at atmospheric pressure. Potential problems have to be taken into account when developing equipment and choosing precursors for deposition. The absence of vacuum equipment means the potential upside for reduced operating costs and simplifying the deposition equipment is considerable. One promising technique for PE-CVD processing at atmospheric pressure is through a dielectric barrier discharge (DBD) [163].

6.2.3 Dielectric Barrier Discharge and Application to PECVD Processing

The DBD is generally arranged in a planar, capacitive driven arrangement. One either one or both electrodes, an insulating material is inserted to prevent overcharging of the discharge gap. The DBD is usually operated in a frequency range from 50-500 kHz with gap distances from just a few millimeters to over a centimeter. Breakdown is initiated at around 5-15 kV and in most gases small microdischarges on the order of 0.1 mm in diameter are found to present in the gas gap [41]. Research on coating application using a DBD at atmospheric pressure has been performed on wide variety of substrates over the last number of years. The gamut of attempted coating systems varies from organic coatings on plastic substrates and other thermally sensitive materials, to protective coatings on metal substrates,

to inorganic material deposition for electronic and photovoltaic applications [20, 64, 172-178].

Increasing performance demands for coatings have precipitated the development of hybrid materials or multi-component systems, where a hybrid coating system contains both an organic and inorganic structure [177, 179, 180]. The demand for these materials comes from the potential of combining the inherent properties found in organic polymers with those of inorganic materials. The classical hybrid material system is defined as a composite, where complementary properties are found when two or more materials were mixed. Often the synergistic effects are not always achieved in these systems due to incompatibility. A more powerful method for producing these hybrid structures can be achieved by combining the precursors in a plasma for deposition. The hybrid coating systems offer a wide range of applicability where the structural elements and tailoring of coating properties can be achieved in a PE-CVD approach. The desired properties of these coatings are often focused at improving the resistance to chemicals and abrasion, antireflection, barrier coatings, and corrosion protection.

This chapter is devoted to the development of one such hybrid coating system, silicon carbide, deposited at atmospheric pressure from silane and methane using a dielectric barrier discharge plasma source. Up to this point, the effect of adding two precursors into an atmospheric plasma discharge has been rarely studied. Most DBD assisted PECVD studies have been focused at developing a single material system where the material properties are focused at a single application [20, 167, 179, 181, 182]. The outcome of this work is largely unknown and additional processing challenges for achieving thin film growth at atmospheric pressure with two precursors in the active plasma environment cannot be predicted. The results of this work discuss the development and mechanisms leading to conformal thin film growth from a two precursor system in a DBD assisted PECVD reactor.

The DBD process was analyzed in the context of a 1D plug flow model. Process parameters related to substrate temperature, gas gap distance, and flow rates of the precursor gases were varied in order to compare experimental conditions to the results in the plug flow

model. Additionally, power applied to the plasma discharge was varied from a continuous wave mode to a pulsed wave mode in order to study gas phase nucleation and gas phase depletion effects in the reactor. Ultimately, a process was developed where operation in a pulsed mode resulted in conformal film growth of amorphous silicon carbide at deposition rates from 100-250 Angstroms/min. The details surrounding the development of the process are given in the sections below.

6.3 Experimental

6.3.1 DBD Assisted PE-CVD Reactor

The DBD discharge used in this work was produced between two parallel aluminum electrodes, each with a diameter of 11.5 cm. Pyrex plates with a diameter of 19 cm and thickness of 3mm cover both electrodes. The barrier arrangement is enclosed in a quartz chamber to allow for transmission of light in the ultraviolet range. The gap between the electrodes can be varied from 3 mm to 25 mm. In this work, variable gap distances at 7 and 20 mm were investigated during the deposition process. A prototype power source used in these experiments was designed by AP Solutions Inc. (Cary, NC). The model is referred to as the AIR-DBD-5000 power module. The power supply is capable of delivering 5000 watts of peak power. The internal circuitry is based on a proprietary design and the specifics of the design were not disclosed for discussion in this work. The frequency during operation was fixed at 28 kHz while the output power was held constant at about 250 W although power fluctuations during depositions were about ± 20%.

In the present setup the top electrode is connected to the high voltage power source while the bottom electrode was grounded. Substrates used during deposition included glass, p-type (100) silicon, nickel foil and aluminum foil. Substrates were cleaned in an acetone and ethyl alcohol rinse, which was followed by drying the samples with a nitrogen gun. The carrier gas and precursor molecules were mixed in the gas delivery line where, once mixed, the gases were injected at the top of the chamber. A Balzer's mechanical pump was connected to the bottom of the chamber enclosure, which is where the gas was also removed during processing. The DBD enhanced CVD reactor is shown in Figure 6.1. The reactor is

mounted in a closed chamber to improve continuity between runs and to avoid contamination from the outside atmosphere. The deposition process is started by pumping the chamber down to a base pressure of about 100 mTorr where upon reaching this pressure, the MFC's to the carrier gas and precursors would be turned on. Upon reaching atmospheric pressure, over pressurizing the chamber was avoided by opening up the exhaust valve.

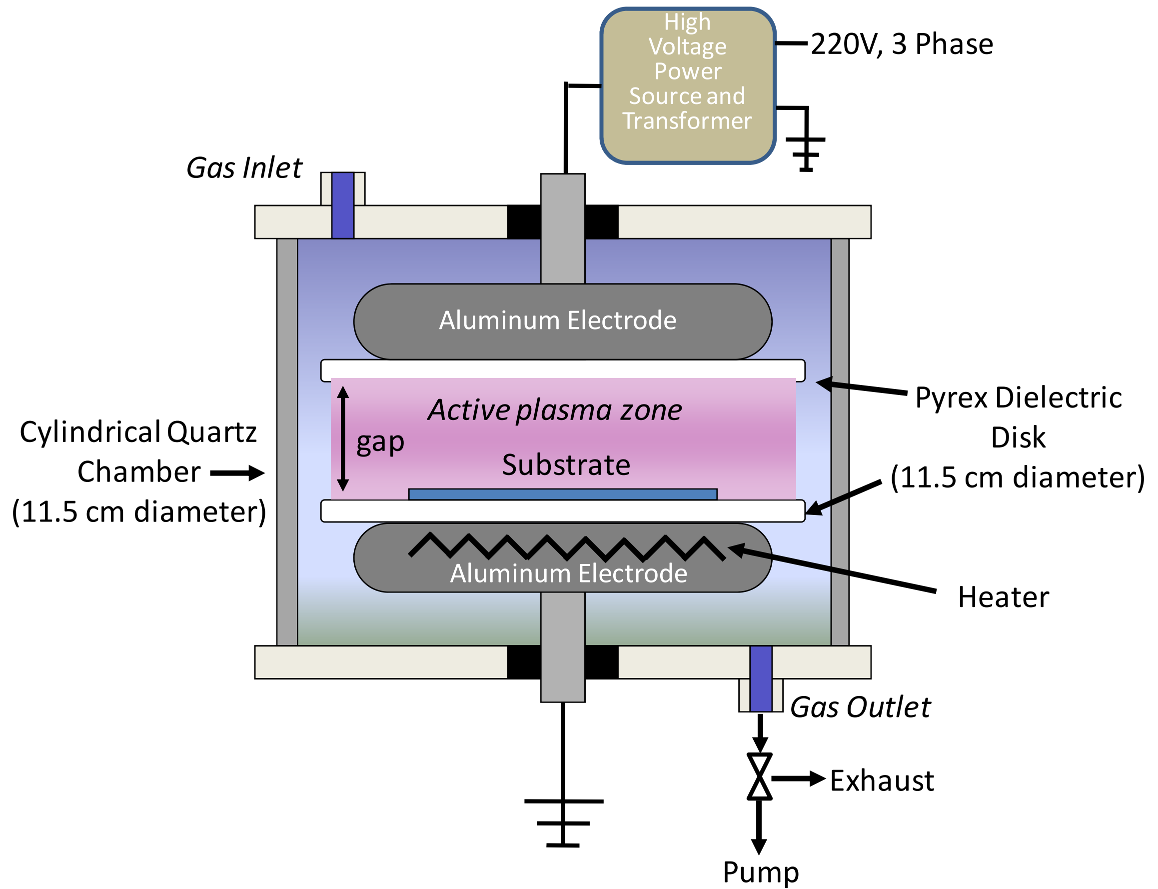

Figure 6.1: Schematic representation of the DBD used in experiments for this work.

6.3.2 Materials and Methods

A Tektronix (Beaverton, OR) TDS-5000 series 350 Mhz 4-channel digital oscilloscope monitors the power delivered to the reactor. A Tektronix 6015A high voltage probe (1:1000) and Person Electronics model 4100 high current probe (1:1) monitor the power input to the discharge. Chemical species generated by the plasma are identified with an Ocean Optics (Dunedin, FL) S-2000 spectrometer. The spectrometer has a 0.5 nm resolution and is capable of measuring wavelengths from 200-900 nm. Light from the plasma source is collected by a 3-channel monochromator equipped with a 1200 grove/mm^{-1} holographic UV grating, 1200 groove/mm^{-1} holographic VIS grating, and a 1200 groove/mm^{-1} NIR grating blazed at 750 nm.

Research grade (99.9999%) helium (Machine & Welding Supply Company) was used as the carrier gas during deposition. The total flow rate of helium was varied between about 1-5 L min^{-1}. A 2% silane in argon mixture was used as the silicon source while methane was used for the carbon source.

The power source was operated in a continuous wave mode and pulsed wave mode in order to test the viability of producing conformal coatings. In general the total deposition time was limited to around 15 min while the processing time was varied up to 2 hrs. In pulsed mode the duty cycle was varied between 10%-90%. The pulse cycle was varied from 0.5-10 sec intervals.

Initial depositions were completed at room temperature. During the course of the experiments, a 1500 W substrate heater was installed on the grounded electrode. The heater consisted of three 500 W cartridge heaters that were placed inside an aluminum disc. The top of disc was in direct contact as the bottom dielectric to heat the substrates. Substrate temperatures from room temperature to 400 C were used during experimentation. The walls of the reactor were left cold, although at higher substrate temperatures, radiant heat warmed all surfaces in the reactor to above 150 C.

6.4 Results and Discussion

6.4.1 One-Dimensional Plug Flow Analysis of CVD at Atmospheric Pressure

CVD processing is at atmospheric pressure is a difficult task. Part of the complexity arises from mass transport issues since by definition, a CVD process transports precursors from a supply point to a surface for deposition. In a CVD reactor, the rate of deposition is controlled by either the surface reaction rate (surface limited) or mass transport rate (mass transport limited). The simplest analysis of a CVD reactor can be completed by setting up a plug flow reactor. A plug flow reactor is used to predict chemical reactions and approximate how fluid flow in a reactor may behave. In a plug flow reactor, the main assumption is the fluid is perfectly mixed in the radial direction but not in the axial direction (forward or backward) [162]. To setup the plug flow reactor, the boundary conditions need to be defined. For the calculations, it is assumed the deposition chamber is a rectangular box of dimensions 12.7 cm by 12.7 cm with a height of 2 cm operating at 760 Torr and 300 C. A gas flow rate of 2500 sccm of helium was used for all calculation, to simulate conditions in the DBD reactor used in this work. A schematic of the plug flow reactor can be found in Figure 6.2.

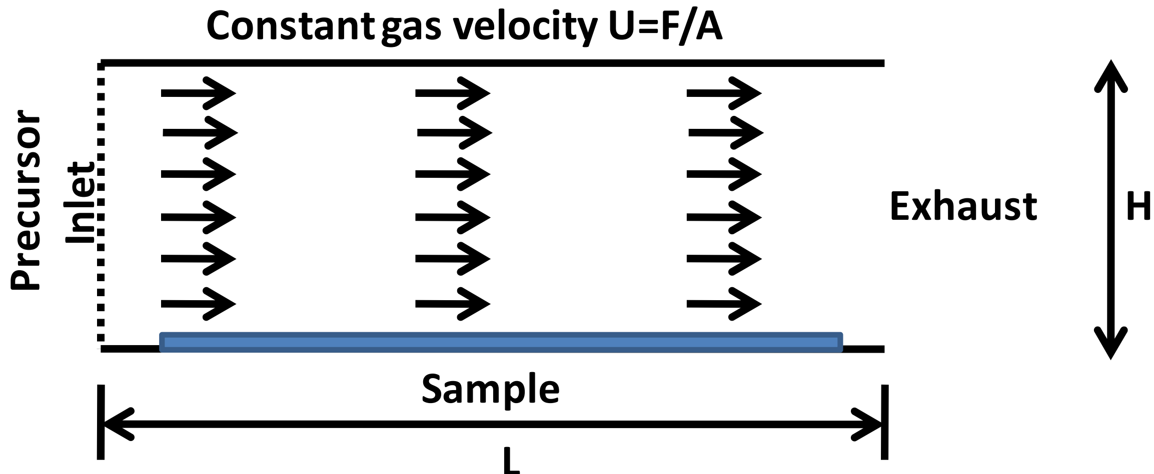

Figure 6.2: Schematic representation of plug flow reactor.

The starting point for transport considerations is to look at the convection (motion of the gas) in the CVD reactor. The convective flux describes the amount of material carried past a plane with an area that is perpendicular to the velocity. The flux is the product of the velocity and concentration of the gas, where the flux can be expressed in any form such as molecular (units: molecules m^{-2} sec^{-1}) and can be found in equation 6.1.

$$J = U * n_{molecular} \tag{6.1}$$

By itself, convective flux cannot lead to deposition on a substrate. A transport mechanism is needed to carry material across the reactor. The mechanism is through diffusion, which is the process that describes macroscopic result of random motion on a microscopic scale. Diffusion is written as Fick's first law and can be found in equation 6.1, where the flux in the gas stream is proportional to the gradient in concentration:

$$J = -D\frac{dn}{dx} \tag{6.2}$$

A rough estimate of the diffusion constant can be calculated by the simple hard sphere estimate and is found equation 6.3 [162]:

$$D = \sqrt{\frac{k^3}{\pi m}}\frac{T^{3/2}}{Pa^2} \tag{6.3}$$

where k is the Boltzmann constant, T is temperature, P is pressure, and m is mass of atom or molecule, and a is the radius of the atom or molecule. A typical value of 0.1-1 cm^2/sec can be found for light gases such as helium at atmospheric pressure [162]. These equations are helpful in starting the analysis, but a better examination of the parameters that effect CVD growth will help determine how the process operates at atmospheric pressure. One such parameter is the diffusion length, where the diffusion length is the characteristics length for the diffusion equation to follow. The diffusion length is a factor expressed as $L_d = \sqrt{4D(L/U)}$, where L is diffusion distance and U is the gas velocity. In this plug flow reactor, the diffusion length is about 4 cm, but compared to our reactor chamber (12.5 cm), it is much smaller. In this case the deposition chamber is quite large in comparison to the

diffusing species and as a result we would expect huge differences in the concentrations in the deposition zone [162]. A schematic representation of the concentration gradients can be found in Figure 6.3.

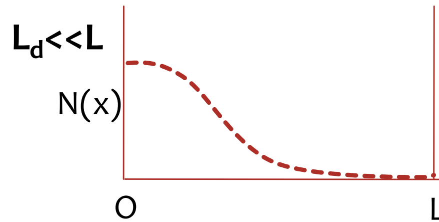

Figure 6.3: A schematic representation of the concentration gradients expected in the DBD assisted PE-CVD reactor.

From Figure 6.3, concentrations can differ drastically from one part of the reactor to another. Gradients are expected to be very large, and the concentrations will be highly time dependent. Alternatively, if the diffusion length is much longer than the system size, the profiles of concentration will be essentially linear, and independent of time. A schematic representation of the concentration gradients is found in Figure 6.4. A process with this characteristic is dominated by diffusion forces and is commonly found in low pressure CVD [162].

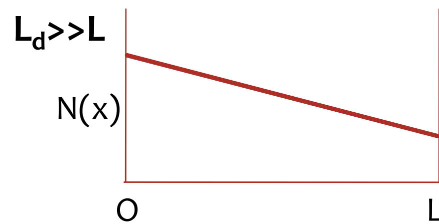

Figure 6.4: A schematic representation of linear change in concentration, a process that is essentially linear and independent of time.

To further examine the concentration gradients in the reactor the diffusion time can be found. The diffusion time for a given system, L, is found as $t_{diff} = L^2 / 4D$. A diffusion time of about 400 sec was calculated based on the plug flow analysis. This diffusion time is large

compared to the gas residence time in the reactor (~50 sec). As a result of the difference in gas flow, large concentration gradients in different parts would be expected when depositing at atmospheric pressure [162]. If on the other hand the residence time in the reactor was much larger than the diffusion time, the reactor would reach a sort of equilibrium and the gases would be in a steady state [162]. The concentrations would follow some linear function determined by the boundary conditions in the chamber and deposition would be dominated by diffusion to the surface of the substrate.

Additionally, mass transport in the reactor can be characterized by a few dimensionless parameters that arise from scaling of the governing transport equation [183]. The dimensionless parameters allow insight to the basic fluid mechanics of a CVD system. To start, an understanding of the gas phase collisions is needed to calculate the first dimensionless parameter. Collision frequency in the gas phase is determined by the mean free path, where the mean free path defines the distance a gas molecule travels before colliding with another molecule or third body. The mean free path in a system is proportional to the number density (n) of gas molecules in a system and the collision cross sectional area (πr^2), which is determined by the diameter of the molecule (2r). The formula for calculating the mean free path is found in equation 6.4.

$$\lambda = \frac{1}{\sqrt{2}\pi a^2 n} \tag{6.4}$$

In this plug flow analysis, the number density of gas molecules is found from the ideal gas law and is about 2.5E19 molecules/cm^3. Helium's atomic diameter is about 6.2 pm which results in a mean free path in the model of about 2.4 μm. Comparatively, if nitrogen was used in the model, the mean free path would be approximately 7 nm. This reduction is due to the increase in the molecular diameter (a_{N2}=370 pm) of nitrogen. From the mean free path, the Knudsen number can be found and is shown in equation 6.5. The Knudsen number is used to determine the flow regime of a fluid.

$$Kn = \frac{\lambda_{MFP}}{L} \tag{6.5}$$

In equation 6.5, L is the characteristic length of the deposition chamber. In the plug flow reactor, a Kn<<1 was found and the deposition chamber operates well outside of molecular flow and into a viscous flow regime. To further examine fluid flow in this one dimensional reactor, the Reynolds number can be calculated. The Reynolds number measures the relative importance of inertia forces (resistance of an object to change trajectory) and viscous forces (resistance to shear stress), and how these forces impact flow trajectories in a CVD reactor. The Reynolds number can be found in equation 6.6:

$$\mathrm{Re} = \frac{\rho U L}{\mu} \tag{6.6}$$

where μ is the viscosity, U is the velocity, ρ is the density, and L is the characteristic length of a reactor. Laminar flow occurs at low Reynolds numbers (Re<2100), transient flow (2100<Re<4000), while turbulent flow occurs at Re>4000. In this analysis, a Re of 497 was calculated, indicating flow in the chamber operates in a laminar flow regime where inertial forces dominate and the flow inside the reactor is dominated by viscous forces, and is characterized by smooth, constant fluid motion. From this finding, an understanding of the boundary layer can found where the boundary layer is defined as the region in which the flow velocity changes from zero at the wall to the velocity of the gas away from the wall [162]. A schematic representation of boundary layer formation in a laminar flow regime is found in Figure 6.5. Inside the boundary layer there is no gas flow but outside the boundary layer gas flow is free and in a smooth and constant motion.

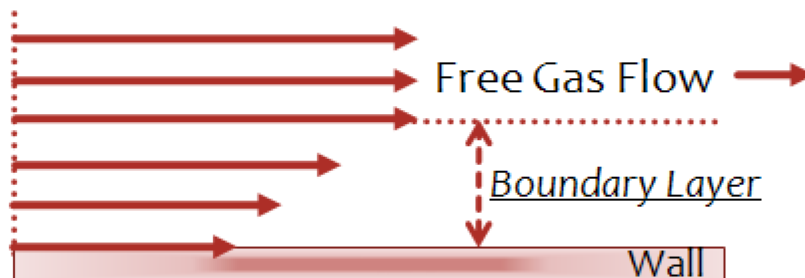

Figure 6.5: Schematic representation showing the formation of a boundary layer in a laminar flow regime.

The thickness of the boundary layer can be found from equation 6.7:

$$\Delta = \sqrt{\frac{L}{Re}} \tag{6.7}$$

where L is the characteristic length of the reactor and Re is the Reynolds number. A boundary layer of 0.15 cm (1.5 mm) was found from the analysis. A schematic representation of the boundary layer in the DBD assisted PE-CVD reactor can be found in Figure 6.6, where a boundary is shown to form on either dielectric plate in the PE-CVD reactor. Reactant gases flowing above the lower boundary layer have to diffuse through this layer to reach the deposition surface. In this case the boundary layer is not large, but operation at atmospheric pressure results in a very low diffusion coefficient and as a result the boundary layer thickness could prevent material deposition to the desired substrates [162].

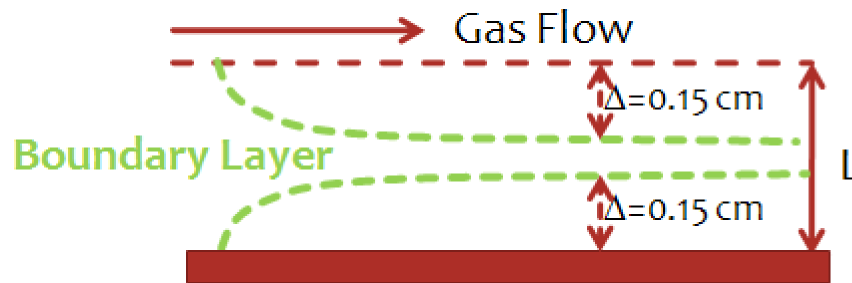

Figure 6.6: Representation of the boundary layer formed in the DBD assisted PE-CVD reactor. Boundary layer calculated to be 0.15 cm.

Additionally, from the calculation of the Reynolds number, a similar dimensionless number, the Peclet number, can be calculated to give an indication to whether diffusion or transport dominates the deposition process. The calculation for Peclet number can be found in equation 6.8:

$$Pe = \frac{LU}{D} \tag{6.8}$$

where the same characteristic parameters are used for the calculation. If Pe<<1, diffusion dominates transport and deposition is linear whereas if Pe>>1, mass transport dominates and large gradients in concentration would be expected [162]. In this model, a Peclet number of 32 was calculated and is consistent with the other analysis completed thus far. That is, the reactor should operate in a manner that produces large concentration gradients and poor deposition uniformity. The last dimensionless parameter, the Damkohler number, describes chemical reaction rates in the gas among species either at the surface or in the gas phase. The Damkohler number can be expressed as the ratio of consumption at the surface to diffusion at the surface, this relation is found in equation 6.9:

$$\frac{\text{Consumption at surface}}{\text{Diffusion at surface}} = \frac{K_s n}{Dn / H} = \frac{K_s H}{D} \tag{6.9}$$

where Ks is the consumption of material at the surface and can be found from equation 6.10, and H is the gap distance of CVD reactor in equation 6.9 and 6.10.

$$K_s = \frac{HD}{L^2} \tag{6.10}$$

For the case where KsH/D >> 1, consumption at the surface is so rapid that basically the concentration at the surface is zero. Deposition in this mode is controlled by the gradient at the surface or the flux to the surface [162]. A reactor operating in this regime is in a transport limited and slow gas transport through the boundary layer limits any rapid surface reaction. Conversely, when KsH/D << 1, diffusion is much more rapid than consumption at the surface, which results in a uniform concentration in the y-direction of the reactor and a concentration gradient in the x-direction [162]. Specifically, concentration is reduced in the positive x-direction. In this case deposition is surface limited and film uniformity is independent of fluid dynamics of the gas. It depends instead on the substrate temperature. In this analysis, a gap distance (H) of 2 cm was used. The resulting Damkohler number was about .02, which results in a prediction that the process will operate in a transport limited regime [162]. Additionally, if a gap distance (H) of .7 cm (7 mm) was used in the analysis, a

Damkohler number of 18 was found. In these conditions the process is predicted to operate in a surface limited regime [162].

In summary, CVD processes are generally operated at low pressures. This is for good reason since parameters such as diffusivity and velocity scale with pressure and temperature [164]. As a result of fluid dynamic considerations, operation of a low pressure CVD is performed in the surface limited regime. Operation in this regime encourages deposition uniformity by slowing depletion of species in the deposition zone, but results in slower deposition rates [159]. This tradeoff is often avoided and deposition rates are increased by increasing the deposition temperature. On the other hand, high pressure CVD processes like the one found in this work are operated in a regime where mass transport across the boundary layer limits deposition. Additionally, further problems from concentration gradients result in more complications with operation of an atmospheric pressure CVD reactor. The analysis of this plug flow reactor provides a useful description of expectations for the deposition process used in this work. The analysis shows pressure has a limited effect on flow and the balance between diffusion and convective forces. Where pressure does have a large effect is on the overall transport and deposition properties in a CVD chamber. One such example is the transition from a transport limited regime of operation to a surface reaction rate limited regime by simply changing the gap distance in the reactor. The change between these two regimes would push the deposition rate from being low in a mass transport regime to high in a surface limited regime.

Some expectations from this analysis and effect on depositing thin films in a DBD assisted PECVD process at atmospheric pressure includes:

- This deposition process should have large concentration gradients within the reactor from mass transfer issues. The mass transfer issues are a manifestation of the gas gap, diffusion length, velocity of gas, consumption of reactants at the surface, and pressure regime of operation.
- The process can be operated either in a surface limited or transfer limited regime by simply changing the gas gap distance.

- Homogenous gas reactions may be a problem during deposition due to operation outside a laminar flow regime.
- Depletion effects of precursor species in the deposition zone may be substantial from the large boundary layer to the substrate.
- Diffusion of precursor species to the desired substrate may be prevented as the flux of species to the substrate is decreased. Since the flux is inversely proportional to the thickness of the boundary layer, operation at atmospheric pressure results in a large boundary layer and small diffusion coefficient and as a result lower flux of species to the substrate.

6.4.2 Development of the Pulsed DBD Assisted PE-CVD Process

Initial depositions were completed with a gap distance of 7 mm and no heat applied to the substrate. The flow rates used during deposition were helium 2500 sccm, silane 6 sccm, and methane 60 sccm. Results of these runs produced gas phase nucleation and powdery substances around the chamber. Next, depositions were attempted at substrate temperatures of 300 C with lower precursor flow rates of 2 sccm of silane and 2 sccm of methane. Depositions were much improved with conformal film growth being observed in a portion of the deposition chamber. Additionally, a new process issue in the deposition zone was observed. The new problem was from gas phase depletion of reactants in the deposition zone. Deposited material was quite substantial at the outer edges of the deposition zone while almost zero material was accumulated inside the middle zone of the reactor. A schematic of this depletion effect is represented in Figure 6.7 and Figure 6.8.

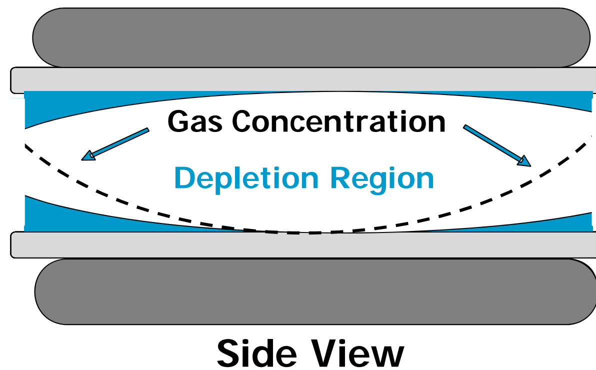

Figure 6.7: Side view of depletion during deposition in the DBD reactor.

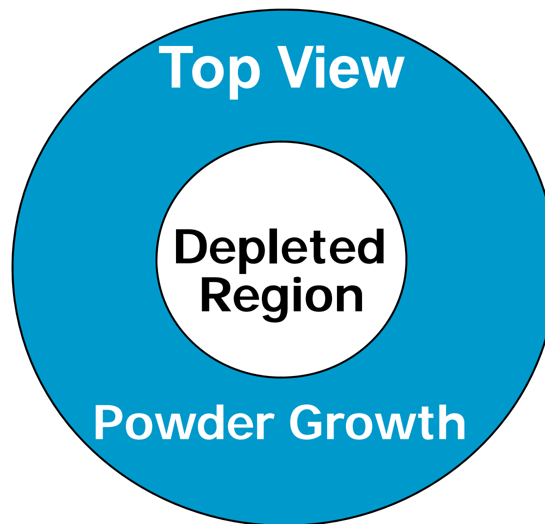

Figure 6.8: Top view of depletion over dielectric plate during deposition process.

To allievate the depletion zone, the deposition process was transferred from a surface limited reaction regime to a transport reaction regime by increasing the gas gap distance in the plasma dishcarge. This resulted in an increase in reactant concentration to the desired region of the deposition zone; however, the middle zone of the deposition area was still starved for reactants. This result demonstrates the deposition process still contained many mass transport problems where simple process design changes would not allow for conformal film growth within the depostion region. From these results, it assumed the plug

flow model that predicted film growth in a transport dominated regime did not accurately take in to consideration the role that the plasma would play in starving the deposition zone of reactants. In the plasma, efficient generation of species such as SiH_n and CH_n can be found, but before the reactans can go through nucleation and growth steps on the desired substrates, the species are pumped away. Additionally, in the transport limited case, the concentration is nearly zero at the surface of deposition while the characteristic diffusion length is controlled by the diffusion time in the chamber. This is a result of the short residence time (50 sec) as compared to the diffusion time (400 sec) in the reactor. As a result of the short residence time in the reactor, diffusion of the reactants through the boundary layer is limited and deposition in this region is almost zero.

To balance this relationship and reduce the effects of gas phase depletion, the residence time in the reactor can be increased. One must be careful, however, because this can push the deposition process into a regime of powder formation. To increase the residence time in the reactor, either the voume of the chamber must be increased or the flow rate of the gases inside the chamber must decrease. In our DBD reactor the volume is fixed, so the flow rate was decreased to check for depletion effects. By decreasing the total flow rate from 2500 sccm to about 750 sccm, the residence time in the reactor is roughly equal to the diffusion time. Deposition with this flow rate produced homogenoueous nucleation in the gas phase and conformal film growth was not found. Further attempts to improve film conformity failed and as result a new process was developed for depositing thin films without a depletion effect.

In order to reduce the depletion effect, the consumption of depositing species in the deposition zone had to be reduced. It was found by varying the duty cycle of the on/off times of the plasma discharge, the depletion effect was eliminated. Additionally, homogeneous gas phase nucleation was limited. The pulsing method used in this work experiemented with various pulse lenghts from 0.5-10 sec. The duty cycle during these pulse lengths was varied from 10-90%. An example of the pulse deposition process can be found in Figure 6.9:

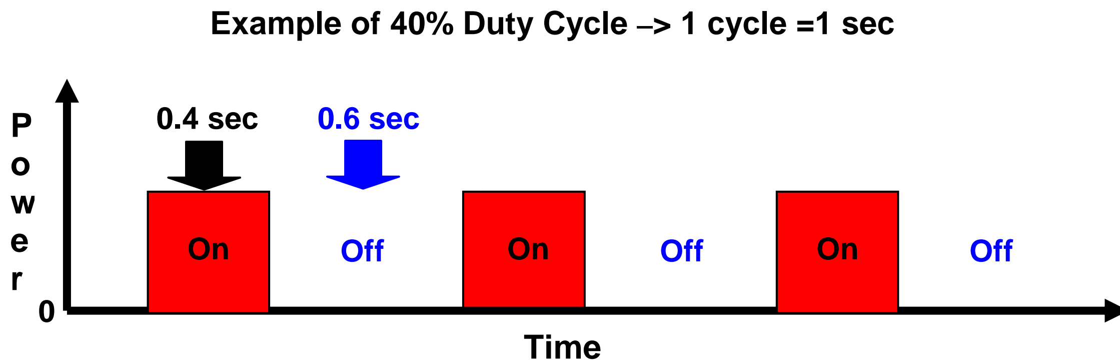

Figure 6.9: Example of pulsed plasma process used during depositions.

where the pulse period is 1 sec and the plasma on period is 0.4 sec and the plasma off period is 0.6 sec (40% duty cycle). Features of the pulse plasma CVD process include:

- Reduction in gas phase depletion to the desired deposition zone.
- Reduction in homogeneous gas phase nucleation.
- Improvement in conformal thin film growth at atmospheric pressure.
- Wider processing range for PECVD operation at atmospheric pressure.

At a substrate temperature of 300 C, it was found for pulse times at 0.1, 0.5, and 2.5 seconds under a 50% duty cycle, material deposition increased to the center region, but at the 2.5 second mark gas phase growth increased. At a pulse frequency of 10 seconds, the substrates appeared similar to a continuous discharge due to the long pulse cycling times and gas phase nucleation was very prevalent throughout the deposition zone. Overall it was found the optimum condition for depositing material was found with 1 second pulse lengths with a duty cycle of 20-40%. The fastest deposition rate found using a 20% duty cycle under 4 second pulses. The resulting deposition rates of about 100-250 angstroms/minute were found under these conditions. A picture showing the effect of pulsing frequency can be found in Figure 6.10.

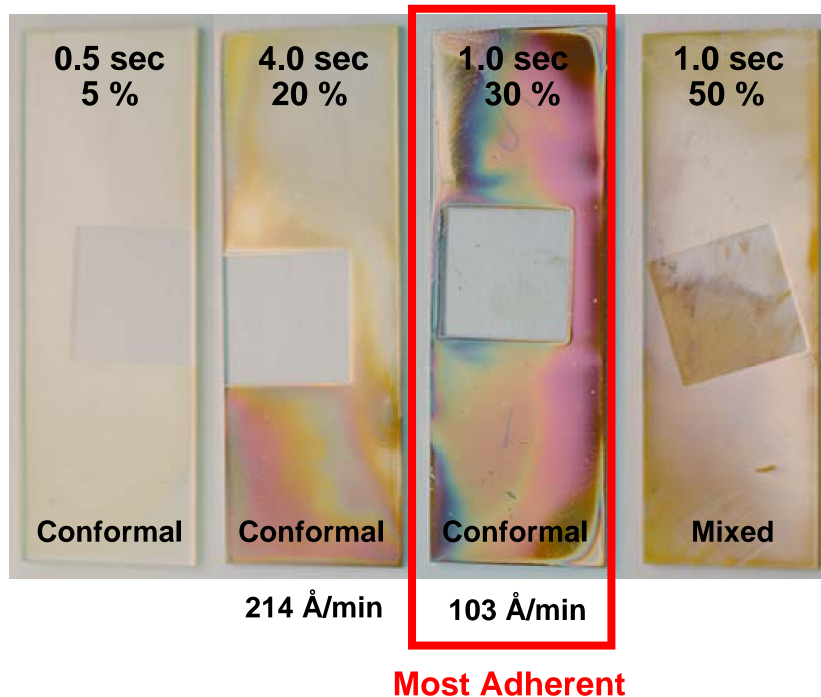

Figure 6.10: Deposition results at varying duty cycles and pulse lengths.

With conformal thin film growth achieved, further process refinement and understanding was completed to understand the role of substrate temperature and film growth. Using a flow rate of 1.25 sccm of silane and methane in 5000 sccm of helium, growth was attempted at 100, 200, 300, 350, and 400 C. Conformal films were found at 225 C and higher using a 30% duty cycle with 1 sec pulse lengths. Homogeneous gas phase nucleation was observed at temperatures below about 225 C. A picture showing the film growth at varying substrate temperatures is found in Figure 6.11. Film rates varied from approximately 100-200 angstroms/min.

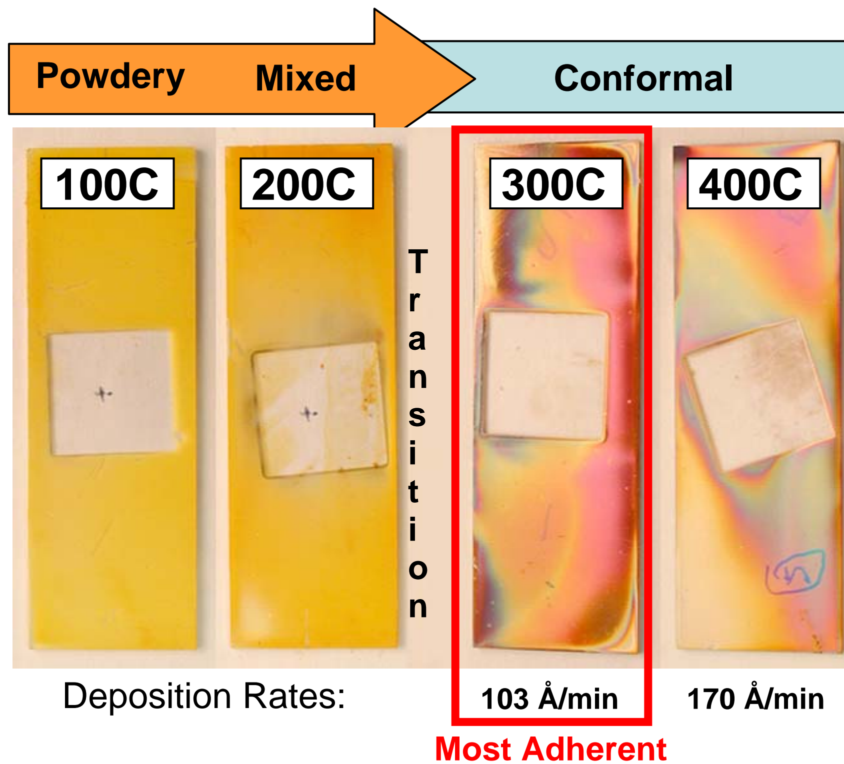

Figure 6.11: Deposition results of SiC at varying substrate temperatures while depositing during a 1 sec pulse lengths with a 30% duty cycle.

It is shown when film conformal thin film growth was achieved, the resulting films have problems with uniformity. Film uniformity was not improved under any of the processing conditions. This result is expected, as the plug flow analysis predicted large concentration gradients in the deposition zone. From a visual analysis of the thin films, it appears large eddies or vortices are present in the gas flow during deposition. This effect is further evident in attempting to deposit a hybrid coating system such as silicon carbide where two precursors are introduced into the reaction environment. In the gas flow, it is expected the concentration of both the methane and silane can vary greatly and as a result the thin films appear to be different material systems with varying amounts of silicon and carbon contained in the matrix. Through XPS analysis of one of the thin films produced by the pulsed process, good silicon to carbon bonding was achieved despite these gradients. XPS analysis of the

thin film showed silicon-carbon bonding in the matrix was about 60% in the carbon 1s peak and about 62% in the silicon 2p peak. The spectra of from this analysis can be found in Figure 6.12.

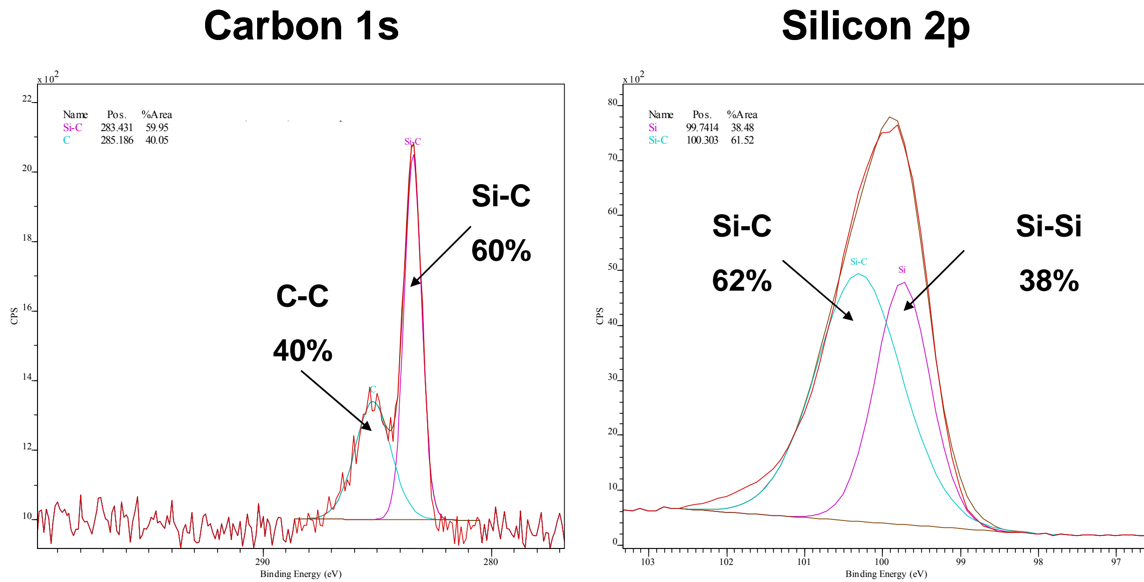

Figure 6.12: XPS spectra of bonding in an as deposited amorphous silicon carbide thin film.

6.4.3 Pulsed Plasma Deposition Mechanism

The pulsed deposition process used in this work can best be described as a variant of plasma enhanced atomic layer deposition (PEALD) and pulsed plasma polymerization. In ALD processing, the reaction is operated in a surface limited regime. Deposition proceeds through alternating, self limiting surface reactions. In ALD processing, a two precursor system of AB and CD is cycled into the reactor for a defined pulse length (0.1-1 sec). Precursor AB reacts with the surface and is chemisorbed (covalent bonding) with bond energies on the order of 1.0 eV. Additional layers deposited during the pulse period react further with the surface and are physisorbed (van der Waals bonding) with bond energies on the order 0.4 eV. Through subsequent pumping and cycling, the desorption time of the chemisorbed species (seconds) and residence time of the physisorbed species (fractions of a

second) leaves only the chemisorbed species on the substrate. By pulsing with the second precursor CD, subsequent pumping and cycling of precursors AB and CD form a solid film of AD. The process described in this work is not an exact replicate of an ALD process, but the nature by which deposition proceeds is believed to be through this step of precursor chemisorption between the plasma on and plasma off pulse periods.

Additionally, it is believed the deposition process proceeds through a plasma polymerization process. That is, during pulsed conditions reactive species are created in the brief plasma on periods and consumed during plasma off periods. In particular, the species are consumed during the plasma off periods by adsorption onto the desired substrate or from removal through pumping. Plasma polymerization is believed to be the deposition mechanism because of the many reactive species produced (ions, neutral radical, metastables, etc.) in the plasma. The chemical reactions that occur in the gas phase are initiated by ionization of the organic methane molecule. In the gas phase, the methane radicals (CH_n) begin to go though secondary chain reactions where the methyl radicals begin to combine and recombine with other CH_n radicals and SiH_n radicals. During this process, new chain molecules absorb, condense, and reform where a polymerization process starts the growth on the substrate. In the polymerization process, the more reactive species produced by the plasma on periods are believed to be consumed more rapidly during the plasma off periods. This analysis is consistent with the results found in this work where when the pulse lengths of the plasma on periods were too long (similar to CW mode). That is, the generation of reactive species would be so large, that gas phase nucleation and depletion would dominate the process. When the pulse lengths are too short, inefficient production of reactive species is believed to occur and little to no deposition is found in the desired zone of deposition.

Drawing from both the ALD and plasma polymerization processes, a process window has been generated to portray how deposition of thin films using the pulsed DBD assisted PECVD process at atmospheric pressure operates. The depiction can be found in Figure 6.13.

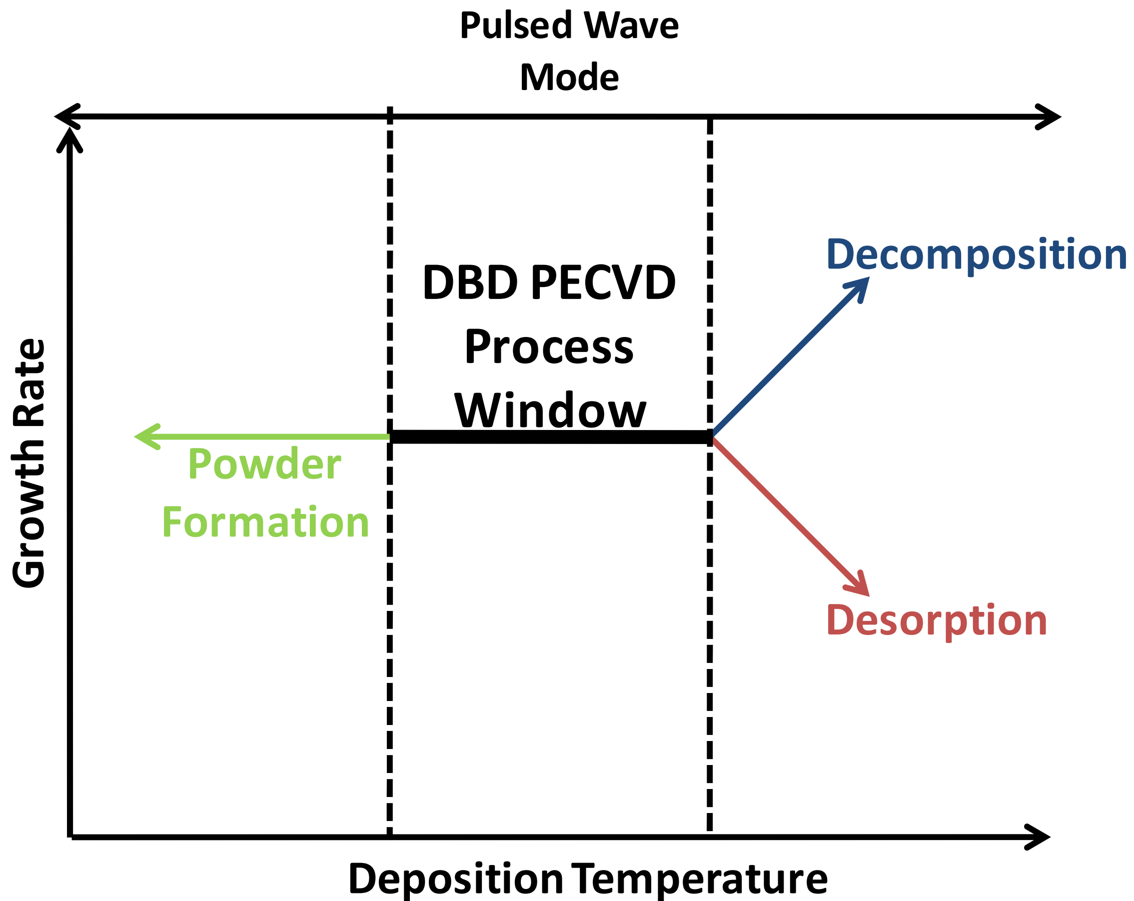

Figure 6.13: The pulsed DBD assisted PE-CVD processing window, depicting the dependency of conformal film growth and deposition rate. The process window is depicted with the bolded line where changes in process conditions (substrate temperature) shifts the reaction outside of the window and into a powder growth, desorption, and decomposition mode.

Additionally, it is noted the plasma on periods are much longer than previous reports of pulsed PE-CVD. More work is needed to fully understand why longer plasma on periods (seconds) are required in order to achieve thin film growth, previous published results used pulse lengths on the order of 0.1 sec [184]. A possible mechanism behind the need for longer pulse steps is related to transport issues at atmospheric pressure, where longer plasma on periods are required in order to generate enough species for diffusion through the

boundary layer. Through further modeling and design changes to the reactor, the pulse length period may be significantly reduced.

6.5 Conclusions

In this work, a plug flow analysis was completed to simulate the fluid flow conditions at atmospheric pressure. The results of this analysis predicted the process could be operated in either a surface limited or mass transport limited regime. From this analysis, deposition of amorphous silicon carbide was attempted in a continuous wave (CW) mode of the plasma discharge. Homogenous gas phase nucleation and gas phase depletion dominated the reactions mechanism in CW mode. The process was limited in range and deposition was not successful. By implementing a pulsed plasma mode into the deposition process, it was shown for first time that deposition of a hybrid coating system at atmospheric pressure using a DBD process could be achieved. Operation of the PECVD reactor in a pulsed wave mode as opposed to a CW mode decreased homogeneous gas phase nucleation and gas phase depletion. It is proposed the deposition process proceeds through generation of reactive species during plasma on periods and consumption of these species during plasma off periods through chemisorption and subsequent polymerization in the gas phase and on the substrate to produce solid films.

Further optimization is required in order to understand the direct mechanisms of the pulsed PE-CVD process. Optimization may include attempts to deposit under an ALD like condition where both the organic and inorganic material are pulsed in the plasma discharge at separate times, gas pulses would coincide with plasma on periods. Further process refinement would be needed in order to attempt a modified ALD process and the process would have to be modified in order to accommodate subsequent purging of the precursor species in between pulse steps. It is also desired that the deposition rate be increased in order to accommodate high throughput, continuous processing applications. In order to achieve this further modeling and subsequent changes to the process reactor will need to be completed. It is believed in order for the DBD assisted pulsed PE-CVD process to be commercially viable, a high mass flow rate of activated species to the substrate would be

required in order to transport through the large boundary layer found in the process. Current results support further development and process refinement in order to meet the needs of a robust, scalable PE-CVD reactor at atmospheric pressure for deposition and coating applications.

6.6 Acknowledgments

This work was funded in part by the AFOSR on contract number FA9550-05-C-0063. The authors of this work would like to gratefully acknowledge the donation of the DBD-5000 power supply by AP Solutions, Inc. during the time of this grant. The authors of this work would also like to acknowledge the staff at AP Solutions, Inc. for assisting with preparation of Figures 6.1 and 6.7-6.12 during the time of this grant.

6.7 References

The references for this chapter can be found in Chapter 10. The references were gathered in one large chapter in order to eliminate duplication and overlap between chapters throughout the dissertation.

7. Pulsed Plasma-Enhanced Chemical Vapor Deposition (P-PECVD) of Amorphous Silicon Carbon with a Low-Frequency Dielectric Barrier Discharge (DBD) using a Factorial Design of Experiments

Christopher J. Oldham, Matthew R. King, C. Richard Guarnieri, and
Jerome J. Cuomo

Department of Materials Science and Engineering,
North Carolina State University, Raleigh, NC 27695

Manuscript to be submitted to the Journal of Thin Solid Films

7.1 Abstract

Amorphous silicon carbide films were deposited using a newly-developed process which operates at atmospheric pressure. It is called Pulsed Plasma-Enhanced Chemical Vapor Deposition and utilizes a dielectric barrier discharge configuration. The films were prepared on glass and quartz substrates at atmospheric pressure using a low-frequency (30 kHz) source from gas mixtures containing He, SiH_4, CH_4, and H_2. Films were prepared according to an experimental design methodology to investigate the influence of process parameters on film characteristics. The experimental design used was a 2^4 factorial design of experiment. The factors of interest were the substrate temperature and the silane, methane, and hydrogen flow rates. The response variables studied were the growth rate, optical gap energy, and bonding in the Si2p peak from XPS. Powder growth was found on two of the sixteen runs; these samples were excluded from the statistical analysis.

It was found the hydrogen flow rate was the main factor influencing the growth rate. Five interactions between parameters included the three other response variables also showed statistically significance influence on the growth rate. The hydrogen flow rate also showed a statistically significant influence on the optical gap energy. Optical band gaps between 1.7-3.2 eV were found. XPS compositional analysis revealed Si-C bond formation in the deposited films. The analysis also detected the presence of oxygen in the film matrix. The source of the oxygen was studied through a depth profile study. The study revealed about 10% oxygen was present throughout the film matrix. The source of this oxygen is attributed to desorption or etching of oxygen or water species off the chamber walls.

7.2 Introduction

In recent years, deposition of amorphous silicon carbide (a-SiC) and hydrogenated amorphous silicon carbide (a-SiC:H) thin films has been investigated due to interest in a wide range of potential applications. These applications are mainly focused at developing next generation optoelectronic devices for use in light emitting diodes, LCD displays, solar cells, and sensors [137, 185-189]. Many techniques have been used to deposit a-SiC, including metal organic chemical vapor deposition (MOCVD) [113], pulsed laser deposition (PLD) [190, 191], sputtering [192, 193], and plasma PE-CVD [104]. PE-CVD methods have been the most widely studied in order to reduce deposition costs for large area applications. The most widely studied gases for depositing a-SiC are from mixtures of silane (SiH_4) or disilane (Si_2H_6) with a hydrocarbon in the form of C_xH_y (CH_4, C_2H_4, and C_3H_8). The properties of the as deposited a-SiC depend greatly on process parameters used during deposition conditions. For example, in applications such as solar cells, the optical band gap can be varied by changing the amount of carbon content in the film matrix [194]. Optical gaps from a-Si (~1.75 eV) to a-C (4.0 eV) have been reported [195, 196].

Generally, reports of PE-CVD deposition of a-SiC have been at low pressure [152]. The only know reports of depositing a-SiC at atmospheric pressure in a PE-CVD reactor is by the Ohmi group at Osaka University in Japan [197]. The group reported deposition of a-SiC at very high rates, about 50 nm/sec, through implementation of a rotary electrode with a very high frequency (VHF) power source [198]. The Ohmi group has continued work in the area and has demonstrated the ability to deposit small crystallites of a 3C-SiC orientation in a high power density orientation [199]. Additionally, it is noted there are no other published reports of depositing a-SiC with other types of reactors in a PE-CVD configuration at atmospheric pressure.

This work focuses on deposition of a-SiC and a-SiC:H in a dielectric barrier discharge (DBD) arrangement at atmospheric pressure. The precursors used in this study were silane and methane. Through a systematic design of experiments, the relationship between the four parameters was compared to the output of three variables, deposition rate, optical gap, and

bonding ratio found in the Si2p peak from XPS analysis. The four parameters studied were the silane flow rate, methane flow rate, substrate temperature, and effect of the hydrogen in the plasma discharge.

7.2.1 Background to Statistical Analysis

Statistics is a mathematical science that can be used as a tool to provide insight and information to a particular process or product. The basis for gathering information through statistical techniques is to model patterns in a way that takes into consideration the randomness and uncertainty in the responses. Traditional statistics models patterns in data by drawing inferences about the responses in the form of answers to yes/no questions (hypothesis testing) [200]. Hypothesis testing is performed when the number of degrees of freedom (samples) is quite large. A large number of samples are required in order to account for random error and to allow for comparison to a larger population. It is assumed the sample data follows a normal Gaussian distribution.

Through hypothesis testing, the results of the model can be compared to examine if the responses are statistically significant. The most frequently used method to determine significance is through a *t-test*. In a *t-test*, the means of two normally distributed populations are compared in order to determine if they are equal within a range of statistical significance. This is referred to as the null hypothesis. Once a *t value* is determined, the level of significance can be determined by looking up a *p-value* in a Student *t's* distribution table. If the calculated *p-value* is below the threshold chosen for significance (1%, 5%, or 10%), the null hypothesis is rejected. The null hypothesis is rejected because in most cases the hypothesis states the two groups are not different. If the null hypothesis is rejected, an alternative hypothesis is selected, which usually states that the two groups are in fact different and this difference is due to some statistical significance.

More recent statistical modeling techniques such as screening, factorial design, or response surface methods attempt to provide insight into a process when the degrees of freedom (number of samples) are small. While traditional statistical techniques focus on the residuals (deviations of a sample from the mean), surface response techniques are not very

good at estimating variations of samples from the mean due to the lower amount samples replications [201]. Such techniques are referred to as near-saturated or saturated designs and focus on predicting an equation to model the process or the effect of the interactions between factors [202]. In a saturated design, the number of test runs required is one less than the number of factors tested. In most cases, a near saturated design is used where the goal of the experiment is to optimize settings rather than show statistical significance compared to a normal distribution. Interactions between parameters are of overriding interest in order to determine the predicted response of the system. No estimate of experimental error (residuals) can be determined in a saturated or near-saturated design [203].

Although a saturated design contains a small number of experiments, it is possible to estimate the average level of response of main effects, interactions, and higher-order interactions from such a design. This method is extremely powerful because it maximizes the amount of information that can be obtained from experimentation while minimizing cost [204]. As such, the methodology used in these experiments was a near-saturated full factorial design where the main parameters, interactions, and higher order interactions were investigated in order to test the significance of factors involved in the deposition of amorphous silicon carbide.

A model was developed by fitting the data using the bootstrap method. The bootstrap method is used in near saturated or saturated DOE's in order to gather statistical data on small sample sets. The bootstrap method uses data produced in the sample population and approximates the distribution by creating a pseudo data set. The pseudo data set is created by sampling the data set many times and replacing each sample within the subpopulation of the data set. This process creates a large number of phantom samples known as bootstrap samples in order to test the data set for statistical significance. Statistical significance is determined by computing the *p-values* from the pseudo data set. *Pseudo p-values* are calculated from the *t-value* on the pseudo data-set.

7.2.2 Design of Experiment (DOE) Approach

Many parameters are involved in a deposition process and complex interactions between parameters can often confound interpretation of output variables. In general, most experimental design work is completed by changing one variable at a time. The one factor at a time approach is not a preferred approach for several reasons. These include:

- Requires more experiments to find a desired response than implementing a design of experiments (DOE) approach,
- Cannot predict interactions between parameters,
- Misses optimization of parameters used in the process.

In contrast, by designing a systematic set of experiments, a wider range of process conditions and interactions between parameters can be determined. Generally most DOE's are designed based on a response surface. The results of the DOE are analyzed and a predictive model of a process can be generated. The model predicts how the output of a process responds to changes in the inputs of a process. It should be noted here that the model is purely empirical, that is, based on non-linear fitting of predicted and experimental data, but has significant advantages when describing parameter interactions. The advantages to using a response surface model include:

- A quantitative understanding of the system behavior can be determined,
- Optimum conditions for a process or product performance can be calculated,
- Conditions for process stability or product uniformity can be found from the model results.

The surface response model is most often determined through a Box-Behnken experimental design [205]. In the Box-Behnken model, a second-order polynomial function (quadratic model) is fit to determine the response of the process parameters. To fit a quadratic model, a parameter has to be tested at least three levels (low, mid, and high point) [206]. The model can be described as a 3^k design, where the number three is the number of levels tested and k indicates the number of screening parameters. In using the Box-Behnken design method, many experiments are needed in order to determine response parameters.

For example, if a set of experiments called for four factors to be tested, 81 experiments (3^4) would be required in order to determine the model output. The high level of experiments needed to evaluate a process can raise concerns when economic resources are limited to complete the study.

An alternative approach for designing a screening DOE is by using a two-level factorial design. Two-level factorial designs (2^k) are useful in a wide variety of problems. The advantages include:

- The design is easy to plan, implement, and analyze,
- Can be used to estimate factor effects on output process parameters,
- Can be used to investigate interaction effects (assuming linear response).

The two-level approach provides a user the same advantages of other surface response models with much less experimentation. For example, in a two-level design, two levels (low and high point) are tested. If four factors are needed for an experiment, only 16 (2^4) experiments are required to complete the model. For this reason, a 2^k (2-level) factorial DOE was designed and implemented in this work to investigate four parameters and ultimately the response of these parameters on the properties of the deposited films.

In the 2^4 factorial DOE used in this work, the parameters of interest were the substrate temperature and the silane, methane, and hydrogen flow rates. The response variables of interest were the deposition rate, optical band gap, and bonding ratio in the Si2p peak after XPS analysis. A schematic representation of the 2^4 DOE used can be found in Figure 7.1. The 16 experiments were completed in random order determined by the random number generator in the program SAS JMP 7.0. Each corner of the two boxes found in Figure 7.1 represents one experimental condition.

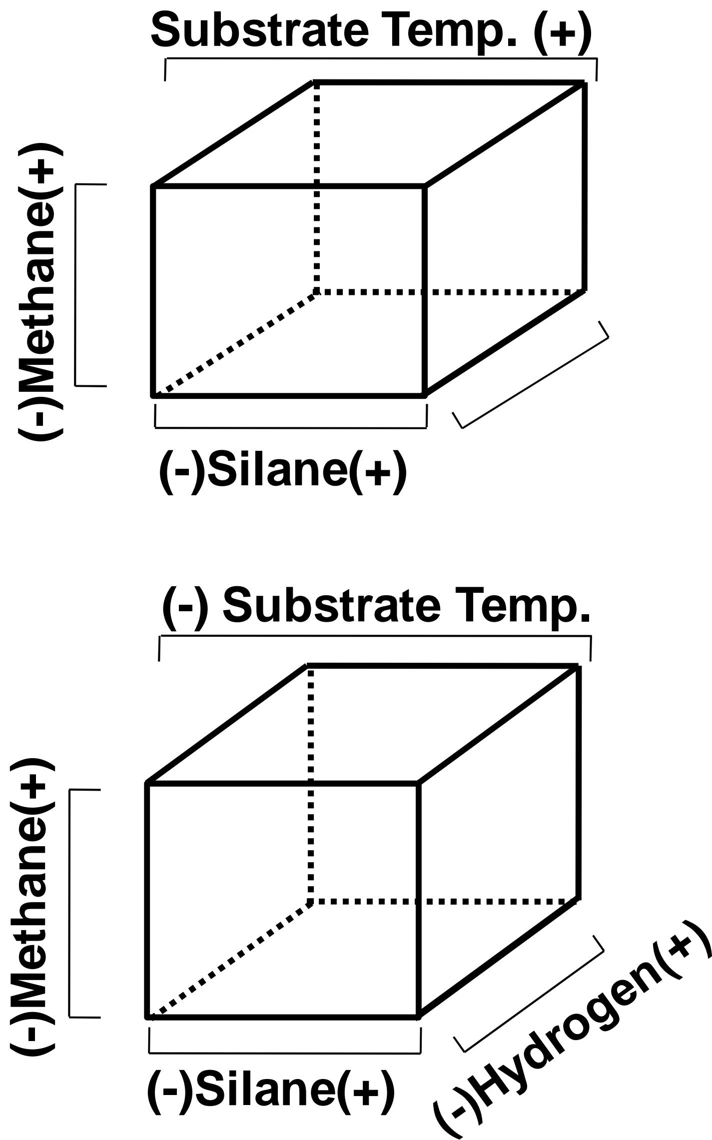

Figure 7.1: Geometric illustration of four factor, 2-level factorial DOE used in these experiments.

The different levels appointed to the study can be found in Table 7.1. The coded values (-/+) from Figure 7.1 are summarized in the table.

Table 7.1: Definitions and levels of factors used in DOE.

		Coded Values	
Factor	Symbol	-	+
Silane Flow Rate (sccm)	SF	0.25	0.5
Methane Flow Rate(sccm)	MF	2	10
Hydrogen Flow Rate (sccm)	HF	0	125
Substrate Temeprature	T	250	400

7.3 Experimental

7.3.1 DBD Assisted CVD Reactor

The DBD discharge used in this work was produced between two parallel aluminum electrodes, each with a diameter of 11.5 cm. Pyrex plates with a diameter of 19 cm and thickness of 3mm cover both electrodes. The barrier arrangement is enclosed in a quartz chamber to allow for transmission of light in the ultraviolet range. The gap between the electrodes can be varied from 3 mm to 25 mm. In this work, a gap distance of 20 mm was used during depositions. A prototype power source used in these experiments was designed by AP Solutions Inc. (Cary, NC). The model is referred to as the AIR-DBD-5000 power module. The power supply is capable of delivering 5000 watts of peak power. The internal circuitry is based on a proprietary design and the specifics of the design were not disclosed for discussion in this work. The frequency during operation was fixed at 28 kHz while the output power was held constant at about 250 W although power fluctuations during depositions were about ± 20%. The power source was operated in a pulsed wave mode where a pulse cycle of 1 sec was used at a 25% duty cycle. The deposition time for all runs was 40 min (10 minutes of plasma on time).

A Tektronix (Beaverton, OR) TDS-5000 series 350 Mhz 4-channel digital oscilloscope was used to monitor power delivered to the reactor. The power was monitored with a Tektronix 6015A high voltage probe (1:1000) and Person Electronics model 4100 high current probe (1:1). Chemical species generated by the plasma were identified with an Ocean Optics (Dunedin, FL) S-2000 spectrometer (0.5 nm resolution, 200-900 nm). The

spectrometer has a. Light from the plasma source was collected by a 3-channel spectrometer (three separate monochromators) equipped with a 1200 grove/mm^{-1} holographic UV grating, 1200 groove/mm^{-1} holographic VIS grating, and a 1200 groove/mm^{-1} NIR grating blazed at 750 nm.

In the present setup, the top electrode was connected to the high voltage power source while the bottom electrode was grounded. Substrates used during deposition included glass, quartz, and p-type (100) silicon. Substrates were cleaned in an acetone and methyl alcohol rinse, which was followed by blowing the samples with dry nitrogen to remove any unwanted particulates on the substrate surface. The carrier gas and precursor molecules were mixed in the gas delivery line where once mixed, the gases were injected at the top of the chamber. A Balzer's mechanical pump was connected to the bottom of the chamber enclosure, which is where the gas was also ejected during processing. The DBD enhanced CVD reactor is shown in Figure 7.2. The reactor was mounted in a closed chamber to improve continuity between runs and to avoid contamination from the outside atmosphere.

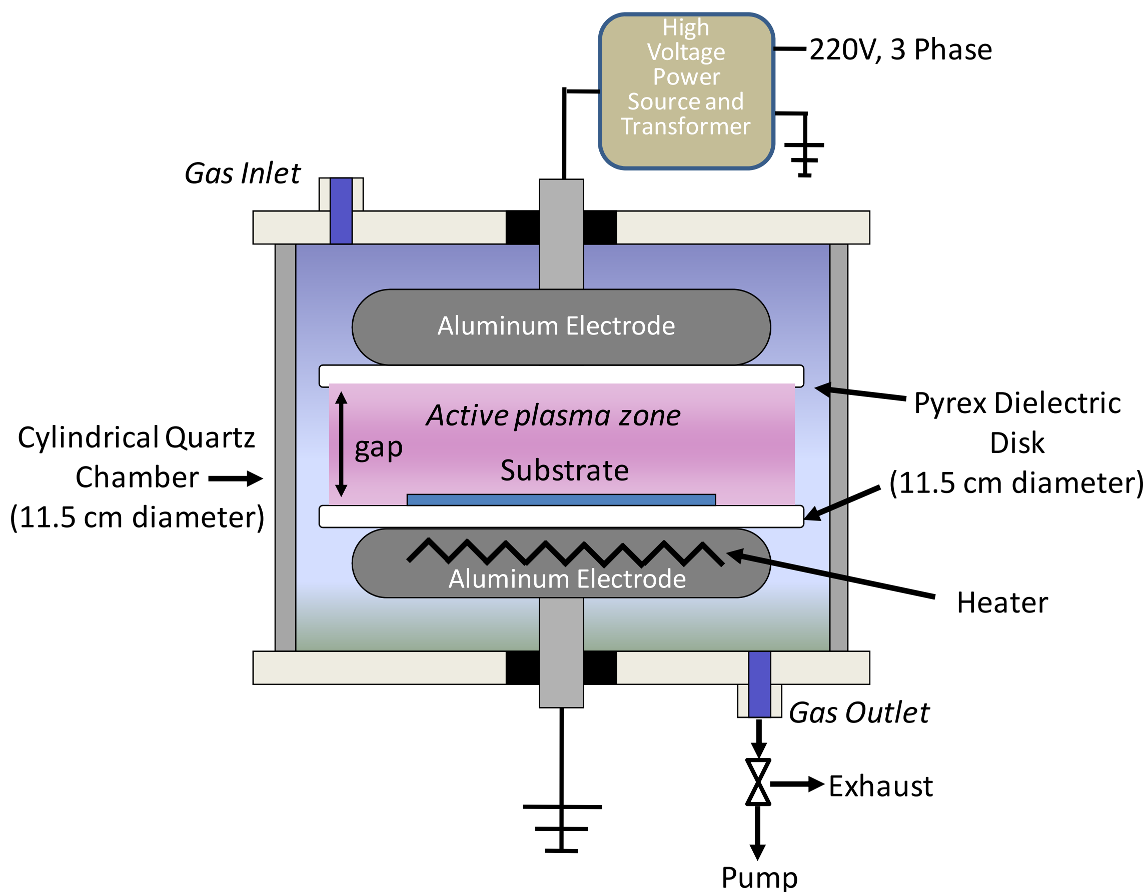

Figure 7.2: Schematic representation of the DBD used in experiments for this work.

A 1500 W substrate heater installed on the grounded electrode heated samples at 250 and 400 C. The heater consists of three 500 W cartridge heaters that were placed inside an aluminum disc. The top of disc was in direct contact with the bottom electrode, and therefore provided a constant temperature source. Substrate temperatures from room temperature to 400 C were used during experimentation. The walls of the reactor were left cold, although at higher substrate temperatures radiant heat from the heater warmed all surfaces in the reactor to above 150 C.

Helium (99.9999%, Machine & Welding Supply Company) was used as the carrier gas during deposition. The total flow rate of helium was 2500 sccm. A 2% silane in helium

mixture was used as the silicon source and methane was used for the carbon source. Flow rates of silane were 0.25 and 0.50 sccm and the flow rates of methane used was 2 and 10 sccm. For hydrogen, the two levels of the experimental design were 0 sccm (that is, no hydrogen) and 125 sccm. The low and high values for each gas flow rate were selected based on initial experiments, where outside the values either no film growth occurred or gas phase nucleation was the dominate mechanism for deposition. From these extremes, a better understanding of the process parameters which control deposition can be determined.

7.3.2 Film Characterization

The thickness of the deposited thin films was measured with a Veeco Dektak 150. Five measurements were taken on the step edge and the measurements were averaged in order to determine the thickness of the deposited thin film. A UV/VIS spectrometer (Varian Cary 5) was used for optical absorption measurements to calculate the optical gap in the deposited films. The optical gap was determined according to the Tauc formula, detail about this calculation can be found in section 7.4.3. The compositions of the thin films were determined by X-ray photoelectron spectroscopy (Kratos Axis Ultra DLD X-ray Photoelectron Spectrometer), using a monochromatized Al kα X-ray source (15 keV, 20 mA emission current). During analysis it was necessary to use the charge neutralizer (charge balance: 2V, filament current: 1.6 A, filament bias: 0.9V). Due to charging, the peak positions were shifted by about 2 eV. An analyzer pass energy of 100 eV with step widths of 1 eV were used in the survey scans. High resolution scans of the Si2p, C1s, O1s, and N1s peaks were performed with a pass energy of 20 eV with step widths of 0.1 eV. Curve fitting was completed with CASA XPS data fitting software.

7.4 Results and Discussion

7.4.1 Statistical Analysis

Using a model generated in the program SAS JMP 7.0, *pseudo t-values* and *p-values* were calculated for the three response variables studied in this experiment. Found in Table 7.2 and Table 7.4 are the statistical analysis of the process parameter effects on two of the response variables, deposition rate and optical band gap respectively. The tables can be

found in the following sub-sections of this chapter. The response variable of the Si2p bond formation was not found to contain any terms that were statistically significant. Two of the samples were excluded from the analysis due to powder observed on the substrate. Powder was observed at the following run conditions;

- (coded value:- - + -), 0.25 sccm SiH4, 2 sccm CH4, 125 sccm H2, and 250C,
- (coded value: + + + -), 0.50 sccm SiH4, 10 sccm CH4, 125 sccm H2, and 250C.

The tables found in the following sub sections show estimates of the linear terms, cross effect between factors, and higher order effects between factors with the model. The *pseudo p-values* of the process parameters shown in the table are determined significant when $p<0.05$ (95% confidence interval).

7.4.2 Deposition Rate

The thickness of the thin films, as measured by profilometry, ranged from 81-345 nm. The deposition rate varied from 1-6 Angstroms/sec. It was observed from the sample data that the deposition rates were about two times thicker when hydrogen was added to the deposition environment. It was also observed when operating at higher substrate temperatures, the deposition rate increased. To verify these observations, Table 7.2 was produced to show what factors and interactions between factors influenced the deposition rate. The only individual parameter that was found to be significant was the hydrogen flow rate (HF). To a lesser extent the silane flow rate (SF) was somewhat significant with a *pseudo p-value* of 0.11, while the methane flow rate (MF) and substrate temperature (T) alone had a trivial effect. However, interactions between parameters such as MF and T were determined statistically significant when combined with the hydrogen flow rate (HF) and silane flow rate (MF). The higher order parameters with significant influences were SF*HF*T, SF*MF*HF, MF*HF, HF*T, and SF*HF because their *pseudo p-values* were less than 0.05.

Table 7.2: The pseudo t-value and probability for the main factors and interaction effects in the deposition rate discussion.

Y	Term	Pseudo t-value	Pseudo p-value
DR	SF*HF*T	13.7165	3.70E-05
DR	SF*MF*HF	-12.4474	0.0001
DR	MF*HF	10.8053	0.0001
DR	HF*T	-10.6200	0.0001
DR	SF*HF	-7.9402	0.0005
DR	HF	5.9711	0.0019
DR	SF	-1.9077	0.1147
DR	SF*MF	1.1708	0.2944
DR	SF*T	0.8394	0.4395
DR	MF*T	-0.4940	0.6423
DR	T	-0.2740	0.7950
DR	MF	-0.1435	0.8915
DR	SF*MF*T	-0.0976	0.9260

From Table 7.2, it was found the common term between the factors and interactions parameters with statistical significance was from the flow rate of hydrogen. To better understand why the hydrogen flow rate influenced the deposition rate, response surface contours were generated. Shown in Figure 7.3 is a surface contour plot of the deposition rate as a function of interaction between the silane flow rate and hydrogen flow rate at the two substrate temperatures. It was found at T_{sub}=250C, the deposition rate decreased when the concentration of silane in the gas mixture was lower and hydrogen is added to the gas mixture. The opposite effect was found with operation at T_{sub}=400C, where higher deposition rates are found when hydrogen is added to the gas mixture and higher concentrations of silane are in the gas mixture.

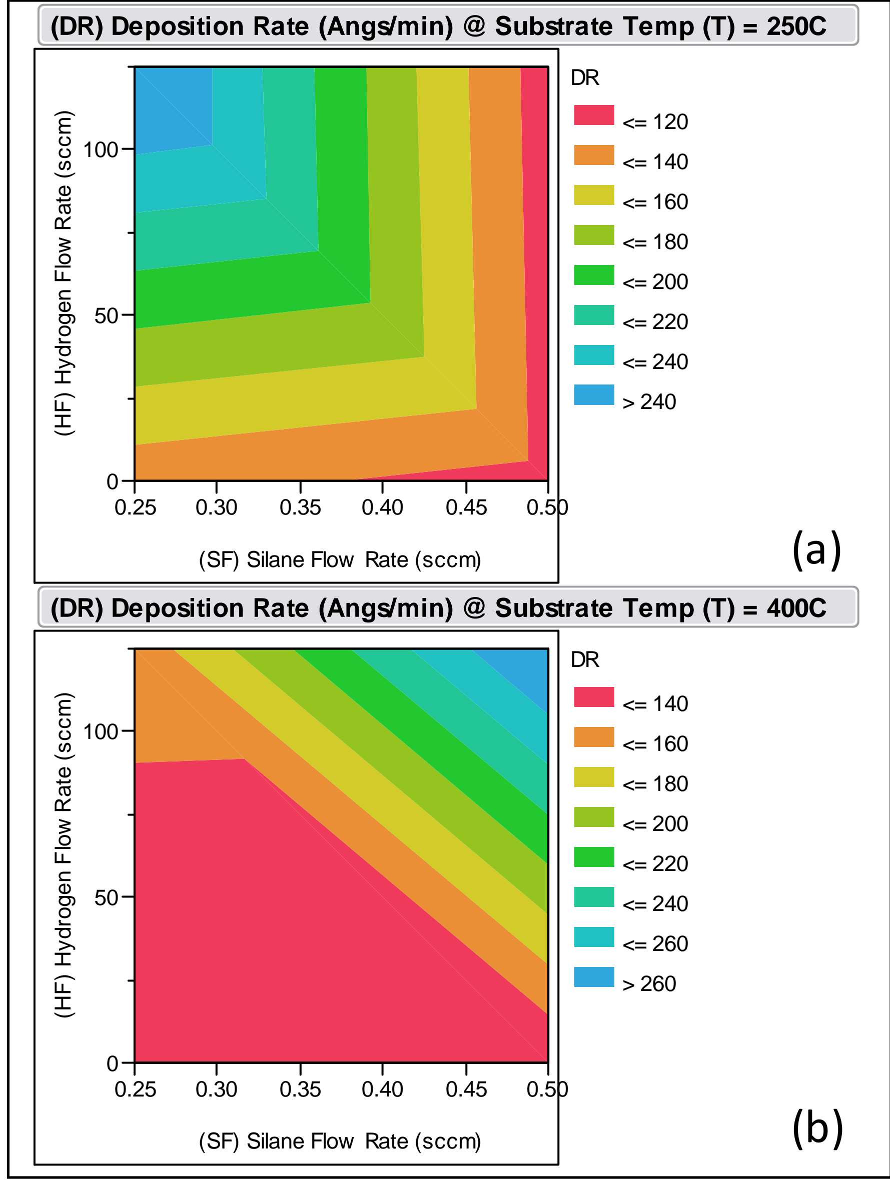

Figure 7.3: Response surface contours of the deposition rate as a function of silane and hydrogen flow rates at (a) Substrate temperature at 250 C and (b) Substrate temperature at 400 C.

Shown in Figure 7.4 is a surface contour plot of the deposition rate as a function of the interaction between the methane and hydrogen flow rate at the two silane flow rates. It is shown at the lower flow rate of methane, the deposition rate follows the same pattern as Figure 7.3a where the rate increases at the higher silane and hydrogen flow rates. At the higher flow rates of methane in the surface contour plot shown in Figure 7.4b, the deposition rate is greatly influenced by the flow of hydrogen. The contour bands are relatively flat and the deposition rate increases rapidly as the hydrogen flow is increased.

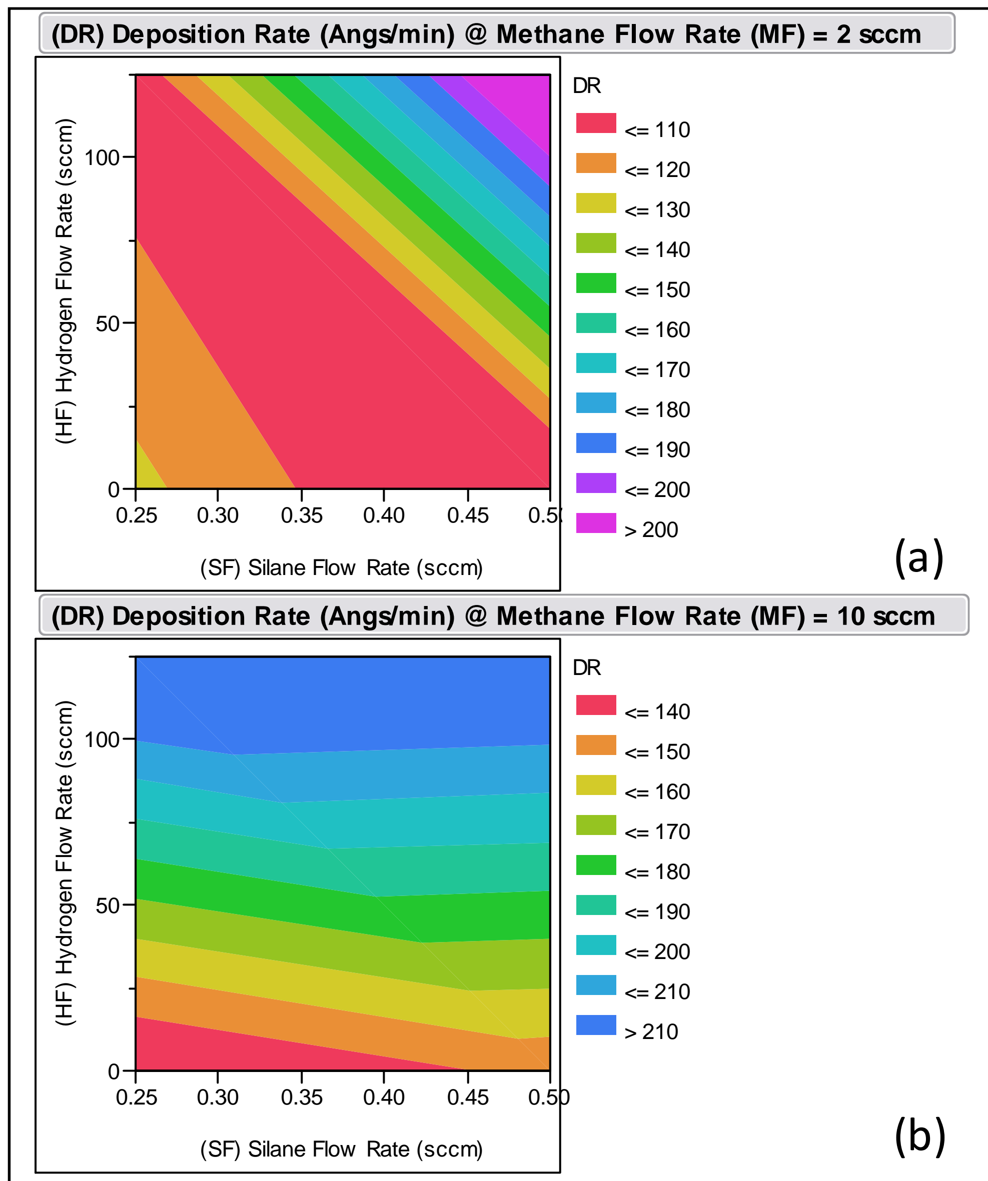

Figure 7.4: Response surface contours of the deposition rate (Angs/min) as a function of silane and hydrogen flow rates at (a) Methane flow rate of 2 sccm and (b) Methane flow rate of 10 sccm.

Combined interactions between SF*HF, MF*HF, and T*HF also show the deposition rate strongly depends on the hydrogen flow rate. Found in Figure 7.5, Figure 7.6, and Figure 7.7 are the three contour plots from these interaction parameters.

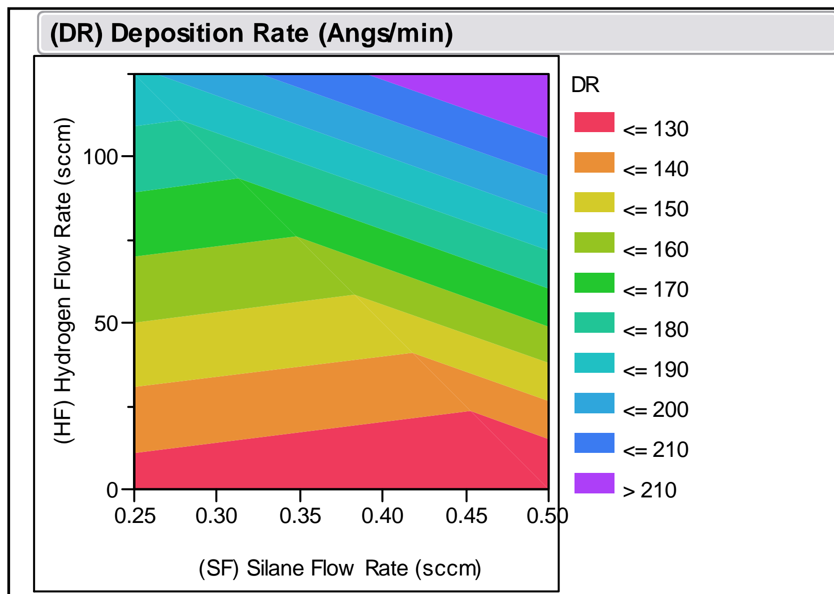

Figure 7.5: Response surface contours of the deposition rate (Angs/min) as a function of silane and hydrogen flow rates.

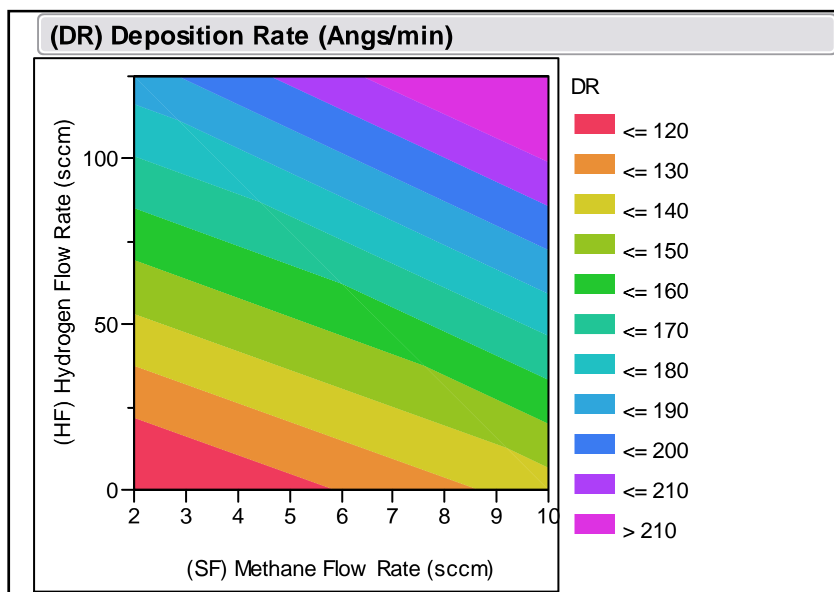

Figure 7.6: Response surface contours of the deposition rate (Angs/min) as a function of methane and hydrogen flow rates.

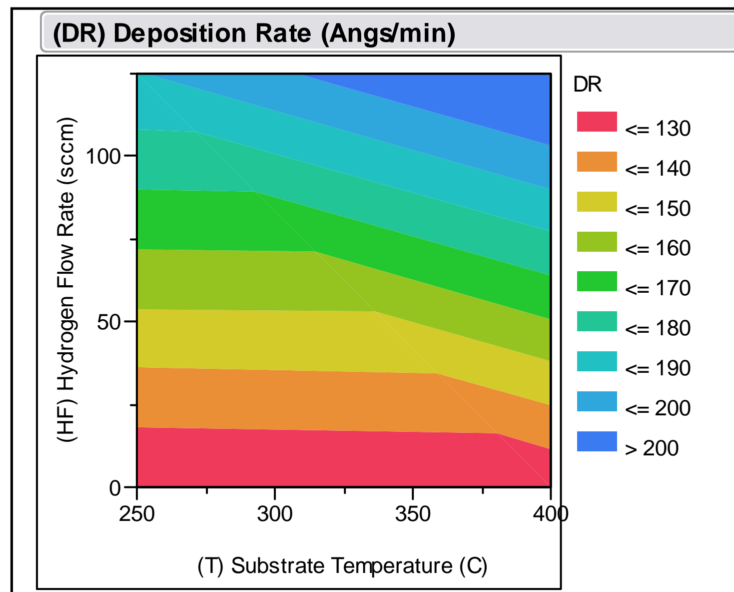

Figure 7.7: Response surface contours of the deposition rate (Angs/min) as a function of substrate temperature and hydrogen flow rate.

The results of this analysis can be interpreted by the looking at how the decomposition of SiH_4, CH_4, and H_2 proceeds in the plasma environment. Both precursors are decomposed in the gas phase through electron-molecule reactions while hydrogen is dissociated through two-electron impact events or through excitation with metastable species. During deposition SiH_4 and CH_4 are decomposed into SiH_{x-1} (x=2-4), Si, CH_{x-1} (x=2-4), C, and H within the discharge. High energy electrons within the plasma promote reactions which generate Si-C, $SiCH_n$, Si-Si, and $Si\text{-}H_n$ radicals. It is this group of molecules which actually facilitate film growth. Work by Kakiuchi *et al.* suggests the deposition of SiC is highly dependent on the dissociation of the SiH_4 molecule [199]. They proposed the concentration of highly dissociated silane radicals such as SiH_n is the dominant factor that influences the deposition rate. The report further suggests that by increasing the dissociation rate of silane, the production of Si-C bonds is increased, and thus the deposition rate is dependent on the dissociation of silane.

From Figure 7.3a, the deposition rate was found to increase at lower silane flows when the substrate temperature was at lower temperatures. This result is opposite to the

mechanism proposed in the previous paragraph and may arise from a number of factors. It may be a result of higher incorporation efficiency of Si in the films due to sticking considerations of the precursor species at lower temperatures. That is, at lower substrate temperatures, a higher coefficient of sticking is found for SiH_n radicals on the substrate [207]. The lower deposition rate could also be a function of hydrogen etching in the plasma environment at the high concentrations of hydrogen in the plasma. Alternatively, in Figure 7.3b, the deposition rate is increased as the silane and hydrogen flow rates were increased. This result follows very well with the results of Ohmi *et al.*, where by increasing the silane flow rates in a hydrogen environment results in faster deposition rates from an increase in Si-C bond formation [148].

To examine the dissociation rate of SIH_4, a deeper look into the plasma chemistry using optical emission spectroscopy (OES) was used to provide useful information to the dissociation process. The optical spectra collected from a few experimental conditions are summarized in Figure 7.8.

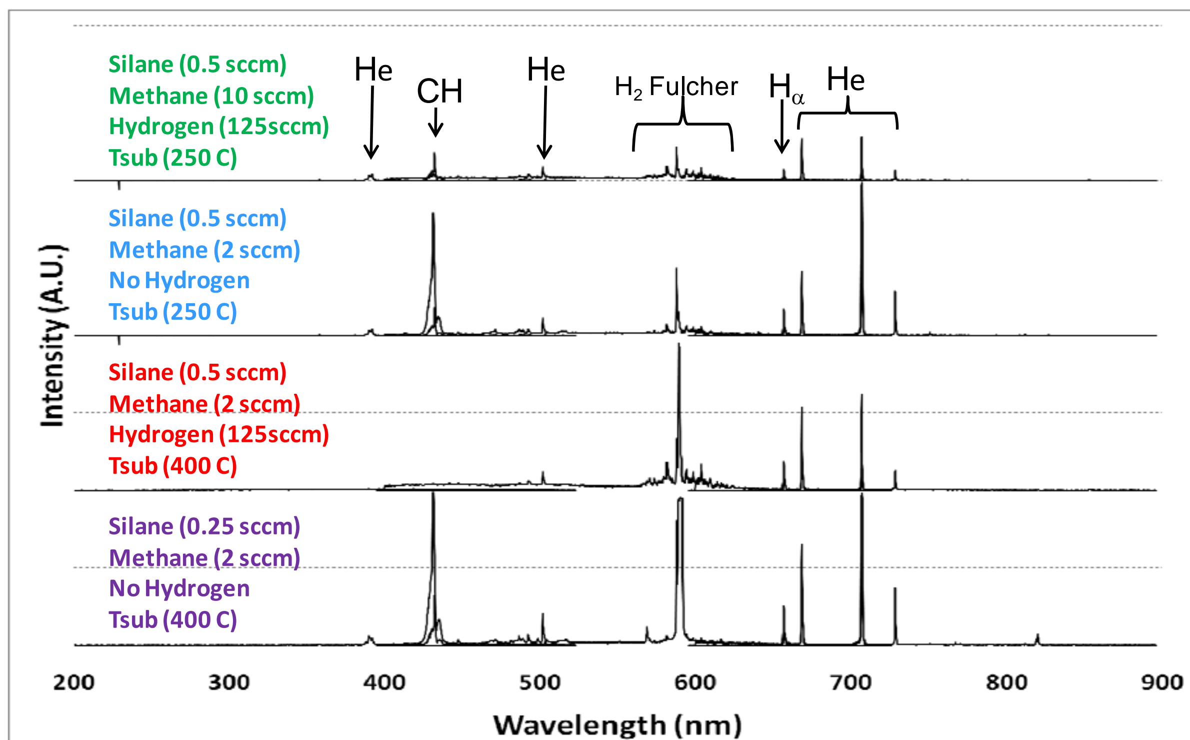

Figure 7.8: Optical emission spectra generated at various experimental conditions.

For each spectrum, emission lines from excited helium (728.1, 706.5, 667.8, 587.6, and 388.9 nm) are seen with those from atomic hydrogen (H_α, 656.3 nm) and the radical from CH_4 (CH, 431 nm) [125]. Emission lines from C_2 (517 nm), SiH (414 nm), and Si atoms (251 and 288 nm) were not observed in the spectra [125]. It is expected these lines would appear in the spectra but they are not distinguishable from the broad emission (200-500 nm) due to relaxation of the H_2 molecules [199]. Additionally, the existence of emission the Fulcher system of H_2 molecules is clearly seen in the 560-640 nm range [199].

From the spectral analysis, it can be argued the strong presence of atomic hydrogen lines and CH species suggests the CH_4 molecule is effectively decomposed through interaction with atomic hydrogen ($CH_m + H \rightarrow CH_{m+1}$), while the lack of intensity from the SiH radical and Si atoms implies the decomposition of SiH_n species may be preferentially suppressed ($SiH_n + H \rightarrow SiH_{n-1} + H_2$). Both SiH species and Si atoms are expected in the plasma chemistry, but the lack of intensity in emission lines suggests either a gas phase reaction or

reaction at the growing film surface is occurring between the deposition precursors and the SiH_n species and Si atoms. It is expected a small amount of these species are produced but it is reasonable to note the deposition rate in these results may be limited by lack a highly dissociated silane species. The growth rate, which is dependent on Si-C bond formation, relies on repeated interactions of SiH_n species with CH_4 molecules in the gas phase or at the film growing surface. It is speculated the lack of intensity from the SiH_n species and Si atoms is a result of the low concentration of silane in the original gas mixtures. As shown from Table 7.2, the hydrogen flow rate was determined to be the common significant factor effecting deposition rate, it is proposed that production of atomic hydrogen is the key factor in generating precursor species used during deposition [199].

Table 7.3: Bond strengths of H2, SiH4, and CH4 molecules.

Bond	Bonding Energy (eV)
H-H	4.53
H-CH	4.42
H-CH_2	4.81
H-CH_3	4.56
H-Si	3.12
H-SiH	3.66
H-SiH_2	2.79
H-SiH_3	3.99

Considering the bond strengths of H_2, CH_4, and SiH_4 molecules listed in Table 7.3, SiH_n species are found to decompose more easily the CH_m species. It is reasonable to expect when the concentration of hydrogen in the gas mixture increases, the concentration of atomic hydrogen will also be increased. The increase in atomic hydrogen may contribute to the increase in deposition rate through efficient production of CH_m radicals. The CH_m radicals can recombine with SiH_n radicals in the gas phase or at growth interface to form Si-C bonds for film formation. This is supported by the contour plot generated in Figure 7.4 where the fastest deposition rates are found at the highest flow rates of methane. It is speculated at the

higher flow rates of methane, more CH_m radicals are produced, and interaction with atomic hydrogen improves incorporation of C atoms into the film and as result the deposition rate increases.

In contrast to low pressure PE-CVD of a-SiC deposition where film formation occurs between active species at the surface, Kakiuchi et al. proposed deposition at atmospheric pressure results in the formation of Si-C bonds in the gas phase between CH_m radicals and dissociated silane species [199]. The work showed by working with other precursors such as monomethylsilane (MMS, CH_3SiH_3), where the MMS molecule contains a Si-C bonding structure in the backbone of molecule, the probability of preserving the Si-C structure in the gas phase was increased. As a result, growth rates were increased. From the results in this work, it is speculated the deposition process is controlled through reactions at the film growing surface. It is believed the optical spectra collected in Figure 7.8 supports this conclusion where species such as SiH, Si, and C_2 were not observed. It is believed these species are produced in the plasma environment, but rapid secondary reactions at the surface incorporate the species into the film matrix. Supporting this conclusion, activation energies of deposition process were found by the Arrhenius equation, shown in equation 7.1:

$$k = A\,e^{-\frac{E_A}{RT}} \tag{7.1}$$

where k is the number of collisions which result in a reaction per second, A is the total number of collisions that lead to a reaction per second, and $-E_A / RT$ is the probability that any given collision will result in a reaction. Equation 7.1 can be simplified to a usable form found in equation 7.2:

$$\ln(k) = \ln(A) - (\frac{E_A}{RT}) \tag{7.2}$$

When a reaction has a rate constant which obeys the Arrhenius equation, a plot of ln(*k*) versus T^{-1} gives a straight line, where the slope is used to determine the activation energy (E_A). In these results the a plot of ln(deposition rate) versus T^{-1} was used to determine E_A.

Using equation 7.2, activation energies from 0.02-0.18 eV were calculated from the deposition rates. A plot of the calculation can be found in Figure 7.9.

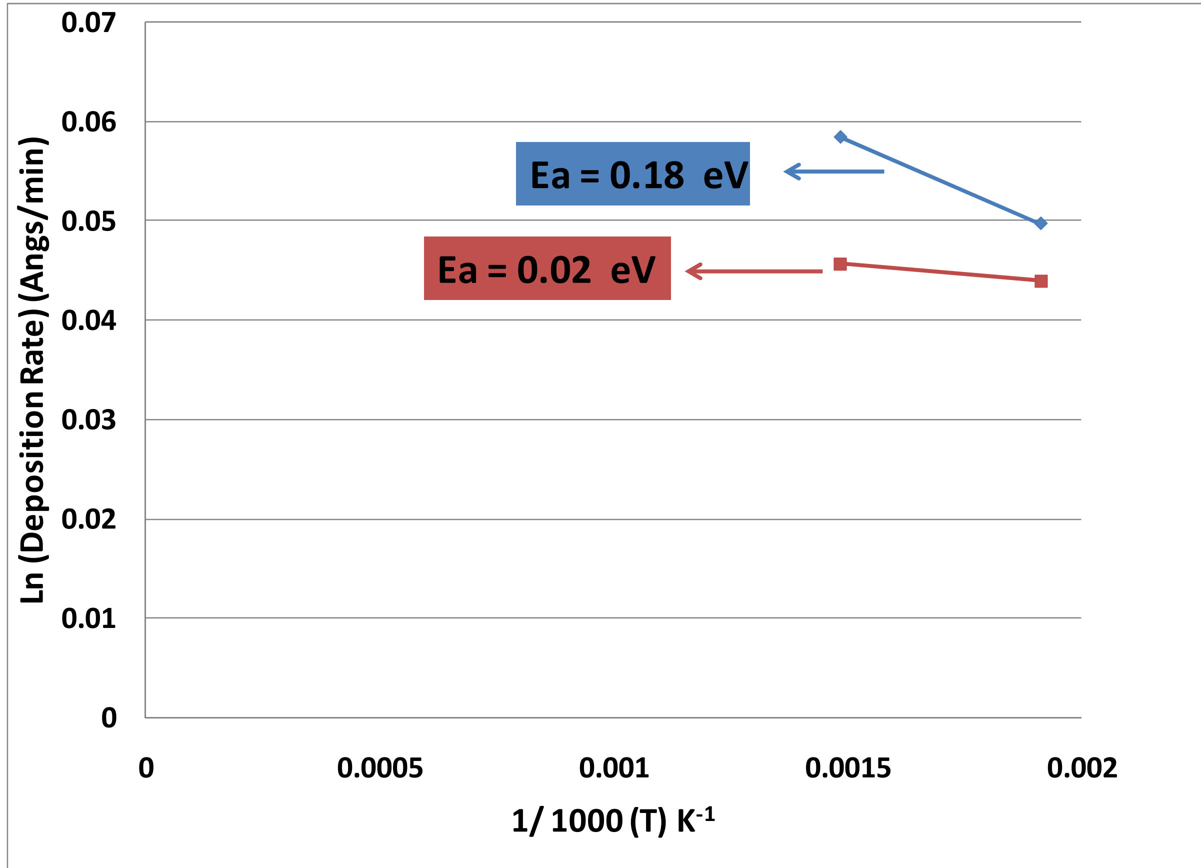

Figure 7.9: Calculation of the activation energies in the DBD assisted pulsed PE-CVD process. Activation energies from 0.02-0.18 were found from the process.

Similar work at atmospheric pressure from Kakiuchi *et al*. found activation energies using the same SiH_4 and CH_4 precursors was found to be 0.13 eV [197]. The low activation energies indicate the process is controlled through a T_{sub} independent process rather than decomposition of gas phase species at the substrate surface (low pressure PE-CVD), which is confirmed by the statistical analysis since the substrate temperature was not shown to have any significance over the growth rate. The low activation energy in hydrogen plasmas at atmospheric pressure is a result of generation of a high density of hydrogen atoms. The

production of the hydrogen atoms enhances Si-C bond reactions at the film growing surface and lowers the activation energy required for deposition. This effect has also been shown in other work in the growth of 3C-SiC at atmospheric pressure [199].

One open question that surrounds this work is how the deposition rate might be increased. Increasing the rate of deposition using SiH_4 and CH_4 precursors will require implementation of a number of process changes. First, the concentration of silane must be increased in order to promote SiH_n interactions with atomic hydrogen. This will require some operational design changes due to problems from gas phase nucleation in the growth chamber when flow rates higher than 0.5 sccm of silane are used. The concentration may be increased by increasing the gas circulation rate either through higher flow rates of dilution gases or by adding a gas circulation pump to the chamber. Additionally, increasing the hydrogen flow rate and as a result the concentration of atomic hydrogen may lead to more atomic hydrogen producing chain reactions. These interactions are important for promoting reactions that lead to Si-C bond formation. Further work investigating the absolute radical densities of SiH_n and atomic hydrogen may lead to better understanding of growth mechanisms involved in the deposition of a-SiC and a-SiC:H. These species may be measured through techniques such as optical absorption spectroscopy.

7.4.3 Optical Band Gap

The optical band gap, E_{opt}, was determined by measuring the ratio of transmitted light to the incident light (%T) with a UV-VIS spectrophotometer. The transmission (%T) can be used to calculate the optical density (OD) of the films and ultimately the absorption coefficient (α) as found in equation 7.3 [208].

$$\alpha = 2.303 \times OD = \frac{-2.303}{\text{film thickness}} \log_{10}(\%T) \tag{7.3}$$

The optical gap was determined from the Tauc formula. The Tauc formula can be found in equation 7.4 [208]:

$$(\alpha h\upsilon)^{1/2} = B(h\upsilon - E_{opt}) \tag{7.4}$$

where α is the absorption coefficient and $h\upsilon$ is the photon energy. The gap is obtained by plotting $(\alpha h\upsilon)^{1/2}$ versus $h\upsilon$. The optical gap (E_{opt}) is determined by extrapolating the linear region of the curve to the $h\upsilon$ axis. The slope of the line, B, is dependent on the product of the oscillator strength of the transition, the deformation potential, and the mean deviation of the atomic coordinates. The B value can be used as a measure of the structural disorder in thin films. Larger B value indicates a film has a lower degree of structural disorder. From Figure 7.10, the relationship between $(\alpha h\upsilon)^{1/2}$ and $h\upsilon$ was determined for the fourteen runs. As seen from Figure 7.10, the band gap varied between 1.3-3.2 eV. As a comparison, reported material band gaps for silicon, silicon carbide, and carbon thin film are 1.1, 2.9, and 4.0 eV respectively [209]. This data suggests the band gaps produced by this process can be varied from a silicon rich to a more carbon rich chemical structure where the majority of optical band gaps were found between 2.2-2.9 eV.

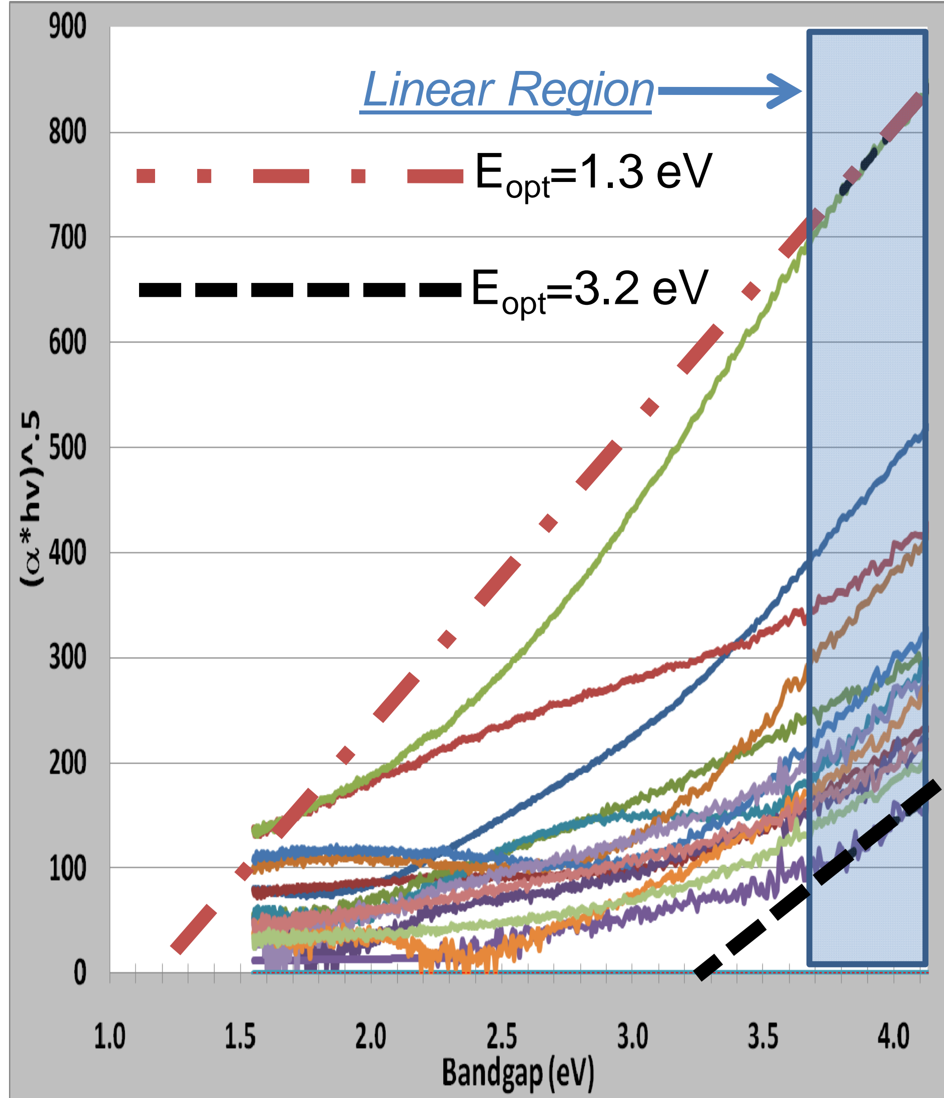

Figure 7.10: Relationship between $(\alpha h\upsilon)^{1/2}$ ***and*** $h\upsilon$ ***of the thin films deposited by the process. Each line represents a different sample. The optical band gap is determined by extrapolating the linear region to the x-axis. Optical band gaps between 1.3 and 3.2 eV were observed.***

As shown from Figure 7.10, the optical band gap can be changed over a wide range of values. To understand what parameters are most significant in the deposition process in controlling the optical gap, Table 7.4 was produced. Similar to the deposition rate analysis, the hydrogen flow rate had a statistical influence on the optical band gap energy. As seen

from Table 7.4, only two interactions were found to be statistically significant with *pseudo p-value* < 0.05. The two interaction parameters are the MF*HF and MF*HF*SF.

Table 7.4: The pseudo t-value and probability for the main factors and interaction effects in the optical band gap discussion.

Y	Term	Pseudo t-value	Pseudo p-value
OG	MF*HF	3.3587	0.0201
OG	SF*MF*HF	-2.6763	0.0440
OG	SF*MF*T	1.4853	0.1976
OG	MF*T	-1.2584	0.2638
OG	HF	-0.9083	0.4054
OG	SF*MF	-0.8927	0.4129
OG	SF*HF*T	0.7847	0.4682
OG	MF	0.5487	0.6068
OG	SF*HF	-0.2379	0.8214
OG	SF*T	-0.2099	0.8421
OG	T	-0.1917	0.8555
OG	HF*T	0.1507	0.8861
OG	SF	-0.1486	0.8877

Shown in Figure 7.11, is the response surface contour plot of the interaction between the methane and hydrogen flow rates. It was found at the both the lower and higher flow rates of both gases, the optical gap increases. This is similar to the statistical analysis completed on the deposition rate where both the methane and hydrogen flow rates increased the deposition rate.

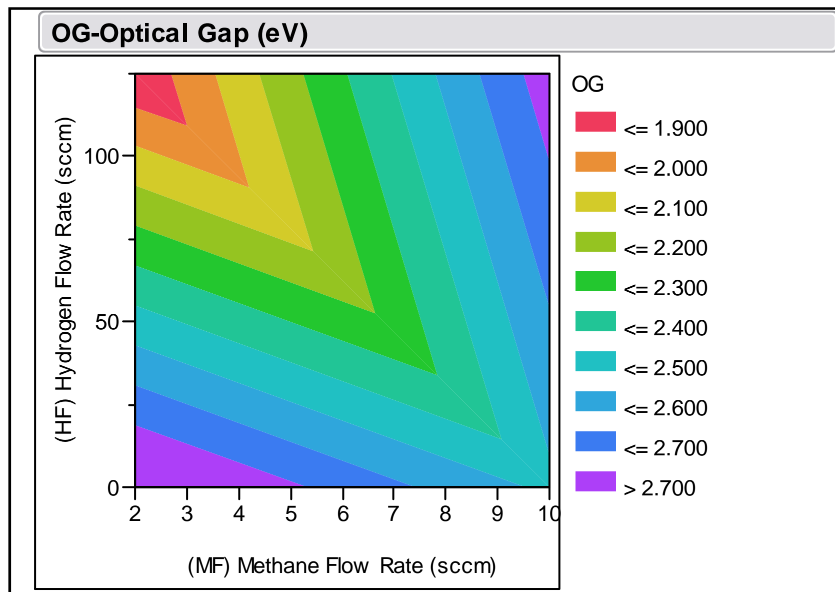

Figure 7.11: Response surface contours of the optical gap (eV) as a function of methane and hydrogen flow rates.

In Figure 7.11, the optical gap increases when both the methane and hydrogen flow rates are at very low and high values. From the literature, the optical gap increases when the Si-C bond fraction increases due to the incorporation of more carbon into the film matrix [199]. In the case of higher optical gaps predicted at the lower methane flow rates, the surface contour plot is opposite to known reactions where increases in carbon concentration result in C-C single bond formation. C-C bond formation results in a preference for sp^3 bonding and a narrowing of the optical gaps [199]. In SiH_4 and CH_4 plasma chemistries where SiH_4 and CH_4 are decomposed, the radicals and atoms produced are SiH_n, Si, CH_n, C, and H. From repeated interactions between SiH_n radicals and CH_4 molecules in the gas phase chemistry, Si-C bonds are formed. The more Si-C bond formed, the larger the optical gap should be, but from Figure 7.11 the optical gap is predicted to increase at lower flow rates. It is believed the predicted plot is not accurate at the lower flow rate of methane and hydrogen and the predicted higher optical gap is a function of the thinner films produced at these conditions. At these conditions it was observed the films were almost 100% transparent. This results in optical gaps that believed to be greatly influenced by the substrate (glass). At

the higher flow rates of methane, the contour plots do appear to follow normal trends and the optical gap increases. This trend follows very well with the proposed reaction chemistry where an increase in methane molecules and atomic hydrogen should increase the mechanism by which Si-C bonds form [197]. As a side note, in the area of the contour plot where low methane flow rates and high hydrogen flow rates are used, a lower optical gap $\leq$ 1.9 was predicted. This indicates in this regime, atomic hydrogen production is sufficient enough to decompose the silane molecules and as a result a silicon rich film should result using these conditions.

Additionally, a surface contour plot of the interaction between the methane, hydrogen, and silane flow rates was generated. The contour plot can be found in Figure 7.12.

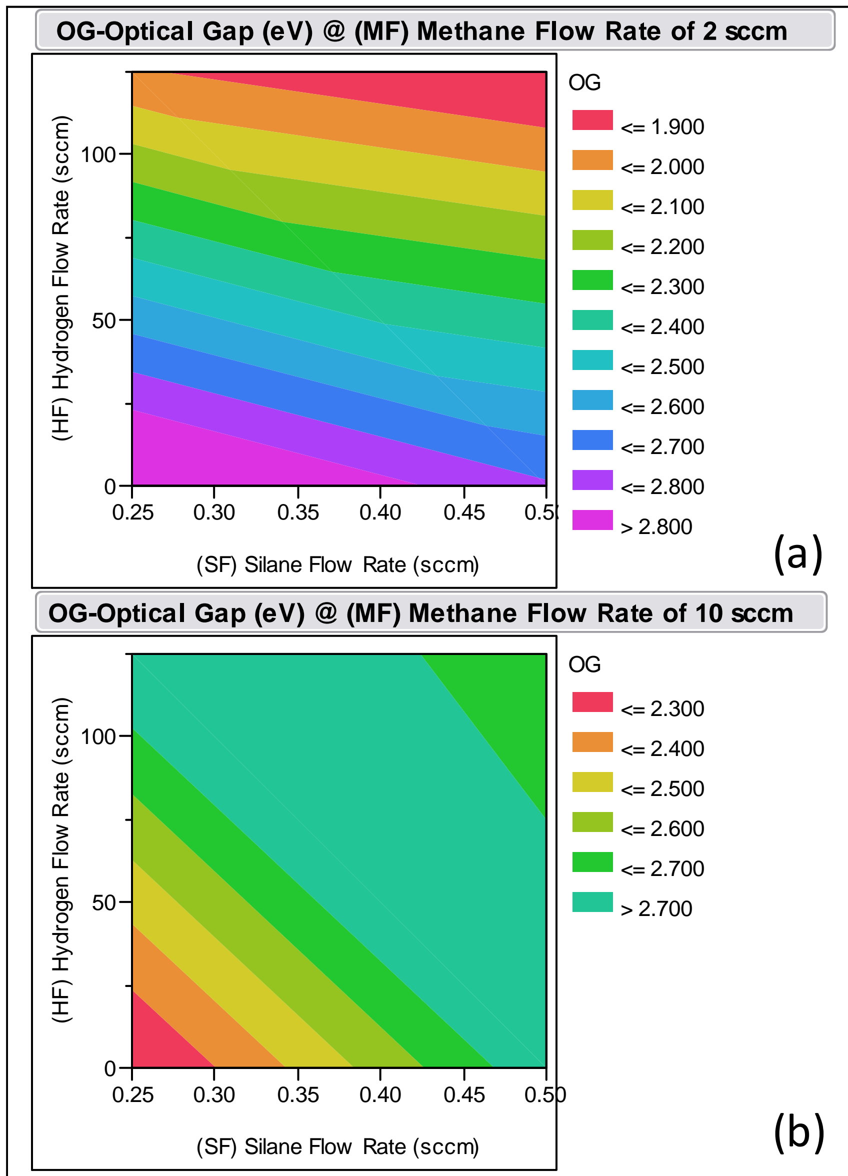

Figure 7.12: Response surface contours of the optical gap (eV) as a function of silane and hydrogen flow rates at (a) Methane flow rate of 2 sccm and (b) Methane flow rate of 10 sccm.

The contour plots generated in Figure 7.12 reveal some interesting characteristics about the deposition process and chemistry occurring during deposition. For example, In Figure 7.12a, the optical gap varies from carbon rich at lower hydrogen flow rates to silicon rich at

higher hydrogen flow rates. This supports the proposed mechanism that Si-C bond formation is greatly influenced by the amount of atomic hydrogen produced in the plasma, where more atomic hydrogen production induces dissociation events of silane. Any increase in the produce of silane radicals such as SiH_n will in turn promote Si-C bond formation with methane molecules. In Figure 7.12b, a much narrower range of optical gaps was predicted when a large methane flow rate was used. This indicates that dissociation of the methane molecule may be in a saturated regime where the number of methane radicals produced dominates bond formation to a Si-C structure or possibly C-C bonding formation. It is known, when the carbon ratio increases, the optical gap is greatly influenced by the sp^2 and sp^3 bonding in a C-C bond [194]. Additionally, hydrogen promotes C sp^3 over sp^2 bonding, the preferentially bonding results in large optical gaps, often greater than 3.5 eV, from a lowering of the valence band and leads to a sharper, more abrupt band edge. The sharper band edge is a product of an increase in the disorder of localized states at the band edge is has been attributed to the many bonding configurations that carbon can maintain, specifically sp^3, sp^2, and sp^1 hybridization [210]. Further evidence is needed in order to quantify whether C sp^3 over sp^2 is occurring. This analysis should be conducted in future studies with Raman spectroscopy.

An interesting observation can be made when Figure 7.11 and Figure 7.12 are recalled; specifically, the fact that the optical gap changed greatly depending on the carbon content in the plasma. By controlling the carbon content in the films, the optical properties can be controlled or tuned over a wide range of deposition conditions. In other words, control of the methane and hydrogen flow rates allows selection of desired band gap energies. This control shows promise for applications in optoelectronic devices. For example, in single junction solar cells, Si rich a-SiC:H have been used as transparent doped layers for the window material to increase conversion efficiency while C rich films have shown promise in large area displays due to room temperature photoluminescence (PL) [211]. The current results support further work to investigate how amorphous silicon carbide thin films produced by the DBD assisted PECVD process can be used in optoelectronic devices.

7.4.4 Chemical Structure of Deposited Films

The elemental and bonding configurations of the films have been investigated by X-ray photoelectron spectroscopy (XPS). XPS analysis provides direct information about the bonding and composition of the atoms in the solid phases by detecting chemical shifts in the bonding energy of the photoelectron peaks when there is a change in the valance state of the bonding atoms. The experimental configuration used to collect the survey scans was described in the experimental section. For each element detected, the relative atomic concentration of the species was estimated from the areas below the prominent spectral lines. Normalization to a calibrated standard was not completed due to issues with sample charging. Determination of the chemical shift is complicated and is commonly completed through correction with adventitious carbon (284.6 eV) on the surface or with a metal standard such as gold or silver. This correction was not completed and in its place, relative peak difference was calculated to understand relative trends and not absolute trends with the sample data. The core level fitting was performed through a Voigt profile which included a 20% Lorentzian function (accounting for lifetime broadening) and an 80% Gaussian function (accounting for instrumental broadening). The Voigt profile is used to account for the natural line shape of an atom which is Lorentzian but contributions from components such as the source and detector introduce Gaussian effects on the signal so both effects have to be accounted for in the analysis. The fitting routine also included a Shirley background to account for electron losses due to collisions with other species when ejected from the core. The background is corrected to account for shifts from secondary electron emission in the background of the sample data.

Broadband scan XPS spectra of the samples revealed the presence of distinct bands at binding energies which correspond to Si2p, C1s, O1s, N1s and Na1s core levels. From the DOE, detection of the Si2p and C1s core levels were expected but the presence of the O1s peak was not expected. The N1s peak was found in five of the fourteen samples, and the atomic concentration of nitrogen in these peaks was found to be less than 1%. The Na1s core level was detected in six of the eight samples deposited at 400 C and 2 of the eight samples

deposited at 250 C. The sodium percentage varied from about 0.9-7.7% in the eight samples. The detection of sodium is attributed to diffusion from the glass substrates. It is thought the at the higher substrates temperatures, the diffusion is faster and for this reason six of the eight samples showed sodium diffusion when depositing at the 400 C substrate temperature condition. For the samples for which XPS analysis did not reveal the presence of sodium, it is believed the chemistry in these films may be acting as a barrier to sodium diffusion. Further investigations on this effect are needed in order to confirm this assumption.

High resolution scans taken on the Si2p peak reveal variations in the bonding chemistry in the deposited thin films. From the scans, two distinct bonding configurations were found. In the first configuration found in Figure 7.13, the bonding orientation shown from the experimental conditions at coded value (+, -, +, +) revealed two component peaks from deconvolution and were assigned at 98.0 and 99.4 eV. The peak at 99.0 eV is attributed to Si-Si/Si-H bonds and the peak at 99.4 eV is attributed to Si-C bonds in the film matrix.

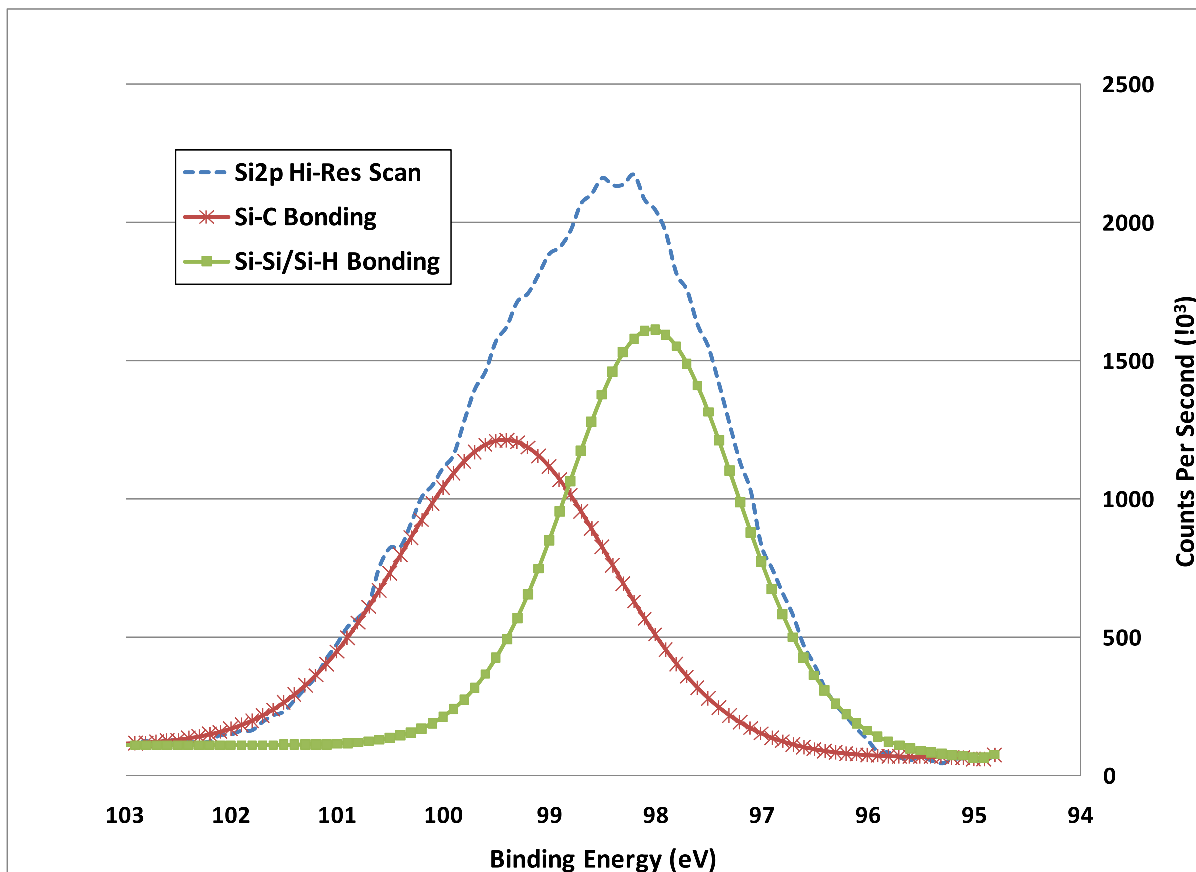

Figure 7.13: High Resolution XPS scan of Si2p peak at the experimental condition of (+, -, +, +); 0.50 sccm of silane, 2 sccm of methane, 125 sccm of hydrogen, and 400 C.

In the second bonding configuration, contributions from oxygen were found to modify the film matrix. As shown from Figure 7.14, three peaks were deconvoluted from the experimental condition found in coded value (-, +, -, +). In Figure 7.14, a clear shoulder was found, which indicates the formation of an oxide. The three peaks are assigned at binding energies of 97.7, 98.8, and 100.5 eV.

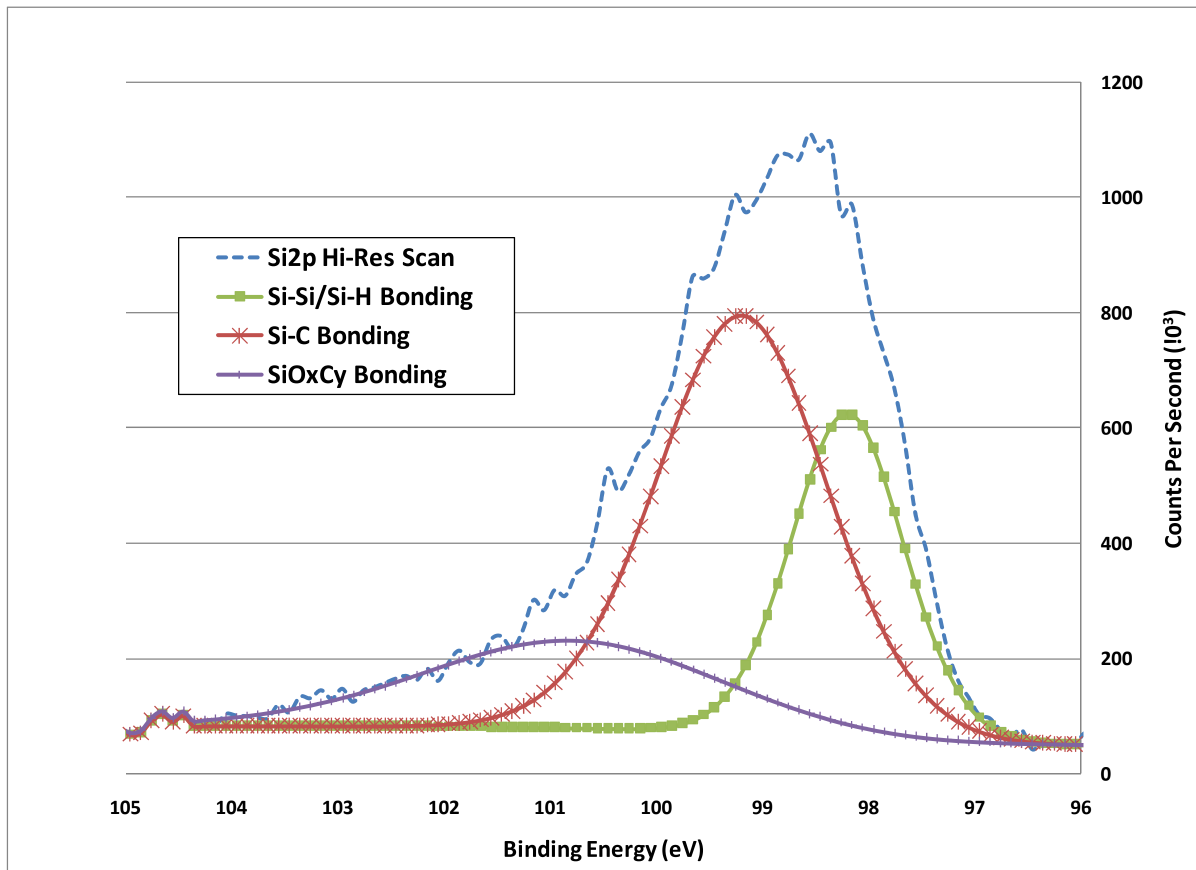

Figure 7.14: High Resolution XPS scan of Si2p peak at the experimental condition of (-, +, -, +); 0.25 sccm of silane, 10 sccm of methane, 0 sccm of hydrogen, and 400 C.

The peaks at 97.7 and 98.8 are assigned to Si-Si/Si-H bonds and Si-C bonds in the film matrix. The peak assigned to 100.5 eV is lower than a bonding peak attributed to SiO_2 (~102.6 eV) and it is likely this peak is from formation of a silicon oxycarbide, such as $SiOC_3$, SiO_2C, and SiO_3C [212]. The relative concentration of each silicon oxycarbide component was not determined. Hence, the peak identified as SiO_xC_y represents the unknown distribution of the three silicon oxycarbide species formed in the film matrix. The size and shape of this shoulder varied between experiments and its role is contributed to two potential contamination sources. The first may be from etching or desorption of residual water and oxygen species off the quartz chamber walls by atomic hydrogen or other plasma species. The second may arise from passivation of dangling bonds by species in the

atmosphere or moisture present in the chamber that may occur after the film is exposed to the ambient atmosphere [213].

As shown in Table 7.5, the bonding percentages between the three orientations varied significantly.

Table 7.5: Atomic concentrations from the Si2p deconvoluted peak. The atomic concentrations are from the experimental DOE with the coded values as shown described in Table 7.1. The peaks are Si-Si/Si-H, Si-C, and SiC_xO_y bonding configurations.

Coded Value	Si-Si %	Si-C %	SiO_xC_y %
(- - - -)	14.78	61.89	23.33
(- - - +)	40.79	59.21	0
(- - + -)	Powder	Powder	Powder
(- - + +)	32.56	35.38	32.06
(- + - -)	37.94	62.06	0
(- + - +)	27.54	53.12	19.34
(- + + -)	54.34	45.66	0
(- + + +)	39.31	60.69	0
(+ - - -)	46.46	53.54	0
(+ - -+)	16.2	40.29	43.51
(+ -+ -)	29.97	25.24	44.79
(+ - + +)	52.6	47.4	0
(+ + - -)	47.43	52.57	0
(+ + - +)	38.43	61.57	0
(+ + + -)	Powder	Powder	Powder
(+ + + +)	46.55	53.45	0

To investigate whether the four process parameters had any statistical influence on the bonding configuration, a statistical analysis was completed on Table 7.5. From the analysis, it was determined there were no significant factors or interactions that influenced the bonding configurations. The lowest *pseudo p-value* of 0.15 was found for the interaction between the methane and hydrogen flow rates and was related to the Si-C bonding orientation. All other *pseudo p-values* of the factors and interaction parameters were found to be greater than 0.40 for the three bonding orientations.

From Table 7.5, the bonding configurations between the Si-Si/Si-H and Si-C varied significantly. In general, the bonding could be varied from a Si rich to a Si-C rich bonding orientation, where under a few conditions the bonding between these orientations was almost equal. Unknown at this time is the effect and role of the oxygen contamination on the bonding or optical properties of the thin films. Considering the sample depth of the XPS analysis is only about 5 nm, it is possible to investigate whether the oxide structure is only found on the surface from exposure to the ambient atmosphere or whether a constant source of oxygen is responsible for the oxide formation in the deposition environment. To do this, two experimental conditions were repeated in order to get a baseline atomic percentage for silicon, carbon, and oxygen in the film matrix. The coded values of the experiment were (+, -, -, -) and (+, -, -, +) where the only difference between the experiments was the substrate temperature, 250 and 400 C. Additionally, the films were deposited on both glass and quartz substrates in order to check whether impurities in the glass substrates effected the overall atomic concentrations. Initial baseline atomic concentrations were collected on the four substrates. After the baseline was collected, the sample surface was sputtered with argon ions (primary beam energy 5 keV, emission current 10 mA) to depth of approximately 10 nm (sputter rate≈1 nm/min), the survey area was about 2x2 mm in size. At a depth of about 10 nm, a survey was collected in the exact location as the previous measurement on the Si2p, C1s, and O1s peaks. This process was repeated at a depth of ~30 nm and ~60 nm on each of the four substrates. Found in Figure 7.15 is a depth profile of the samples deposited at 250 C.

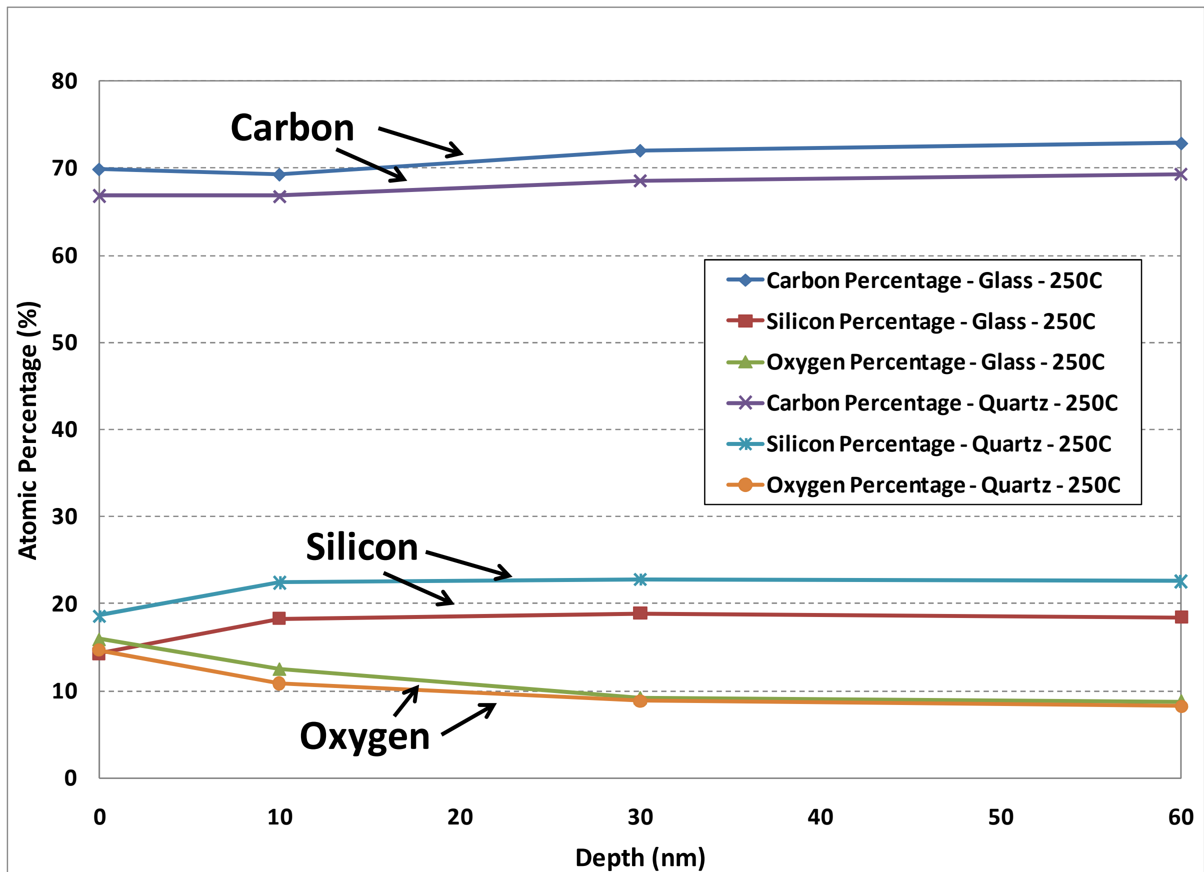

Figure 7.15: Depth profile of atomic concentrations of carbon, silicon, and oxygen at the (+, -, -, -) condition; 0.50 sccm of silane, 2 sccm of methane, 0 sccm of hydrogen, and 250 C.

It is shown the atomic oxygen concentration decreases with increasing depth into the sample surface, but even at ~60 nm about 8% oxygen was still found in the film matrix. Found in Figure 7.16 is the depth profile for the films deposited at 400 C. Again, an atomic percentage of about 10% was found in the film matrix.

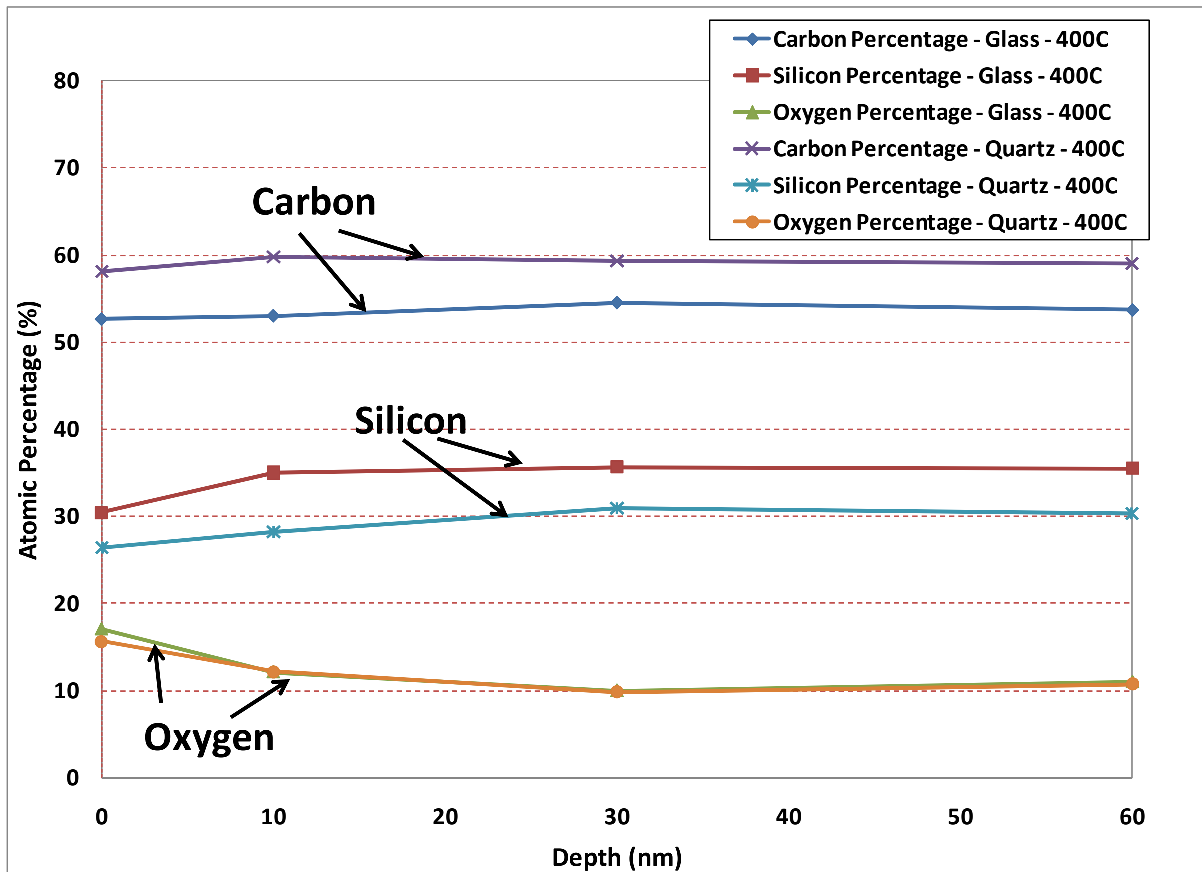

Figure 7.16: Depth profile of atomic concentrations of carbon, silicon, and oxygen at the (+, -, -, +) condition; 0.50 sccm of silane, 2 sccm of methane, 0 sccm of hydrogen, and 400 C.

From both figures it is found the oxide formation was greatest on the surface. This indicates the films undergo some reaction with the outside atmosphere after deposition. At deeper depths into the film matrix, Figure 7.15 and Figure 7.16 show the atomic oxygen concentration trace the same pattern on both the quartz and glass substrates. It is unknown at this time whether self diffusion of oxygen from the two substrates or the presence of some continuous oxygen source is contributing to the large oxygen presence in the film matrix. It should be noted , the atomic concentrations of both the silicon and carbon do not trace each other and the percentages of each element or greatly different depending on the substrate material. This indicates that the silane and methane have different growth and nucleation

mechanisms and possible the oxygen source is from self diffusion from the substrate material. It is proposed, if the source is from inside the deposition chamber, the source of this oxygen is from either desorption or etching of water or oxygen species on the chamber walls or from the feed gases used in the deposition process. Further work is needed in order to fully discover the source of oxygen. The source of oxygen may be separated by depositing on a clean surface of a metal foil and repeating the depth profile analysis.

7.5 Conclusions

In this work, deposition of amorphous silicon carbide thin films was studied through a factorial design of experiments. The DOE was used to investigate how four parameters affected the growth rate, optical properties, and film composition of the deposited thin films. It was found the growth rate was dependent on a number of interactions between the four factors. The common significant term between the interactions was found to be hydrogen. From the optical spectra, atomic hydrogen is believed to be the key factor for producing deposition species such as SiH_n and CH_m that ultimately lead to Si-C bond formation. Optical band gaps produced by the process varied between 1.3-3.2 eV, though most fell between 2.2-2.9 eV. The hydrogen flow rate was also found to greatly influence the optical gap, where it is believed the production of atomic hydrogen results in effective dissociation of the SiH_4 and CH_4 molecules. Compositional analysis revealed the presence of Si-C bonding in all deposited thin films. It was found in a number of samples that an oxide had formed in the film matrix. The oxide formation is believed to be from formation of a silicon oxycarbide, i.e. $SiOC_3$, SiO_2C, and SiO_3C due to either etching or desorption of residual water and oxygen species off the quartz chamber walls or reactions with dangling bonds after the film is exposed to the ambient atmosphere. From a depth profile analysis, the oxygen content was found to be about 10% at 60 nm below the sample surface. This indicated the oxygen formation was most likely due to incorporation of oxygen from moisture in the chamber.

7.6 References

The references for this chapter can be found in Chapter 10. The references were gathered in one large chapter in order to eliminate duplication and overlap between chapters throughout the dissertation.

8. Experimental Study of a Hybrid Biomass Treatment: Atmospheric Plasma Enhanced Two-Step Acid Hydrolysis Process

Christopher J. Oldham [1], Matthew R. King [1], Steven M. Disseler [1], Mary E. Rebovich [1], Lisa O. Dean [2], and Jerome J. Cuomo [1]

[1] Department of Materials Science and Engineering, Campus Box 7907
[2] Department of Food Science, USDA Laboratory, Campus Box 7624
North Carolina State University, Raleigh, NC 27695

Manuscript to be submitted to the Journal of Renewable Energy

8.1 Abstract

Our investigation found the addition of atmospheric plasma processing to a conventional 2-step acid hydrolysis process increased fermentable sugar production by 50%. Physical and chemical analysis indicates the biomass substrate was degraded and the lignin capability for protecting the underlying sugars was decreased. Chemical analysis from FT-IR spectroscopy and optical emission spectroscopy shows both the lignin and crystalline cellulose components were chemically modified after plasma treatment. These results indicate the chemical radicals produced in the plasma are a key mechanism for increasing sugar production. From the experimental design, the only process parameter which promoted a significant increase in sugar production was treatment time in the plasma environment and despite the two plasma chemistries producing vastly different chemical radicals, similar increases in sugar production were found in both chemistries.

8.2 Introduction

Due to price fluctuations and the unreliable and insufficient supply of petroleum based fuels, renewable sources of energy have gained favor again [214]. Current interest lies in utilizing untapped resources such as biomass to reduce our reliance on fossil fuels. Biomass is a lignocellulosic feedstock which includes herbaceous (e.g. switchgrass) and woody (e.g. poplar, pine, and oak trees) crops, forestry residues (e.g. sawdust), and agricultural waste (e.g. wheat straw, sugar cane residue and corn stover) [215]. The lignocellulosic feedstocks contain valuable sources of fermentable sugars for bioethanol (CH_3CH_2OH) production and offer a significant opportunity to reduce U.S. dependence on foreign energy sources. Today, the U.S. holds approximately 3% of known oil reserves but consumes about 25% of all oil produced [215]. As an added concern, about 60% of known oil fields are located within volatile regions of the world such as Iran and Venezuela [215].

The most widely accepted technology for producing bioethanol is from corn sacchrification. High production costs associated with this process hinder the implementation of bioethanol as a gasoline additive or alternative fuel source. Other problems associated with price spikes in the commodities markets have resulted in higher costs for farmers to produce food based products from corn sources. Consequently, conversion of biomass to bioethanol is now of great interest in many sectors of the U.S. government and economy [193, 216].

To explore alternative and complementary techniques to the 2-step acid hydrolysis process, our group investigated the role of a plasma, in particular how an atmospheric plasma could aid in improving the conversion of loblolly pine to fermentable sugars. From the understanding surrounding the many decades of research with etching photoresists in the semiconductor industry and the more recent developments surrounding biological decontamination of organic species in the food industry, we hypothesized atmospheric plasmas could disrupt the organic lignocellulosic structure.

Atmospheric plasmas are a relatively new media through which chemistry can be controlled by the process parameters. In recent years, atmospheric pressure plasmas have

garnered considerable interest for potential use in hydrocarbon processing, syngas formation, removal of organic coatings, and material synthesis [20, 37, 113, 177, 217]. Atmospheric plasma treatments are advantageous because the system does not require costly vacuum equipment, operates at low temperatures, and can be portable [10, 29, 67, 104, 143, 218-221].

In this work, a configuration called the dielectric barrier discharge (DBD) was employed. The DBD is characterized by two metal electrodes separated by some distance, generally less than 25mm. One of the electrodes is connected to a high voltage transformer while the other electrode serves as ground to the high voltage. The configuration is called a barrier discharge since one or both electrodes are covered by a dielectric material, generally Pyrex or quartz. A simple schematic of the barrier discharge reactor can be found in Figure 8.1.

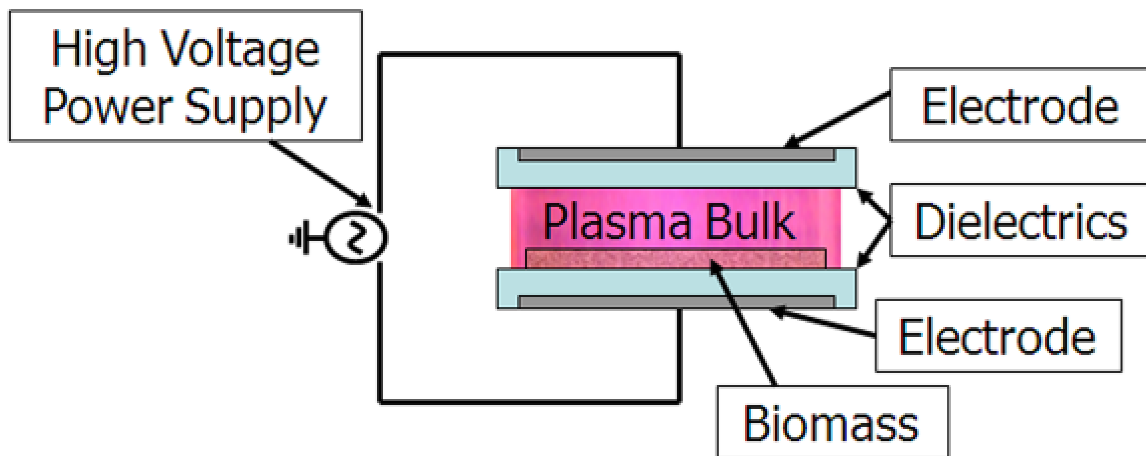

Figure 8.1: Schematic representation of dielectric barrier discharge (DBD) used to process biomass substrates.

8.3 Experimental

8.3.1 Dielectric Barrier Discharge and Reactor Characteristics

The barrier discharge used in this study is characterized by two parallel aluminum electrodes, each with a diameter of 11.5 cm. Pyrex plates with a diameter of 19 cm and

thickness of 3mm cover both electrodes. The barrier arrangement is enclosed in a quartz chamber to allow for transmission of light in the ultraviolet range. A Balzer's mechanical pump and calibrated MKS mass flow controllers provide a controllable and reproducible environment through pumping and subsequent purging of the system. An AP Solutions Inc. (Cary, NC) model AIR-DBD-5000 power module powers the barrier discharge. The power supply is capable of delivering 5000 watts of peak power.

A Tektronix (Beaverton, OR) TDS-5000 series 350 Mhz 4-channel digital oscilloscope monitors the power delivered to the reactor. A Tektronix 6015A high voltage probe and Person Electronics model 4100 high current probe monitor the power input to the discharge. Chemical species generated by the plasma are identified with an Ocean Optics (Dunedin, FL) S-2000 spectrometer. The spectrometer has a 0.5 nm resolution and is capable of measuring wavelengths from 200-900 nm. Light from the plasma source is collected by a 3-channel monochromator equipped with a 1200 grove/mm^{-1} holographic UV grating, 1200 groove/mm^{-1} holographic VIS grating, and a 1200 groove/mm^{-1} NIR grating blazed at 750 nm.

Throughout the study RF power levels were maintained at frequencies from 89-125 kHz. For all experiments, a RMS voltage of 1.9 kV and RMS current of 100 mA was applied to the plasma discharge. Gas flow rates ranged from 2.5-3 L/min, and the gap distance was held constant at 7 mm for all experiments. The DBD reactor provides the flexibility to apply power (cathode) to either the top or bottom electrode. Samples were treated in both the anode and cathode positions. Two plasma chemistries were investigated, the first involving a 5.6% oxygen in helium mixture and the second involving a 5.6% air in helium mixture.

8.3.2 Biomass Source: Loblolly Pine (e.g. Southern Pine)

The biomass source used in the experiments was Loblolly pine (southern pine). Loblolly pine contains approximately 29% lignin [222]. The large fraction of lignin adds difficulty in fully hydrolyzing the biomass structure. Loblolly pine chips were prepared by placing the chips into a Wiley mill. The milled southern pine was collected with a #20 sieve (particle size collected 0.85-2 mm).

8.3.3 Experimental Design

The interaction of atmospheric plasmas with biomass and in particular the lignin component was investigated through the following design of experiments. The 2-step acid hydrolysis process developed by Choi and Mathews [64] was modified with the insertion of an atmospheric plasma treatment between the two acid hydrolysis steps. A flow diagram of the design of experiments is provided in Figure 8.2.

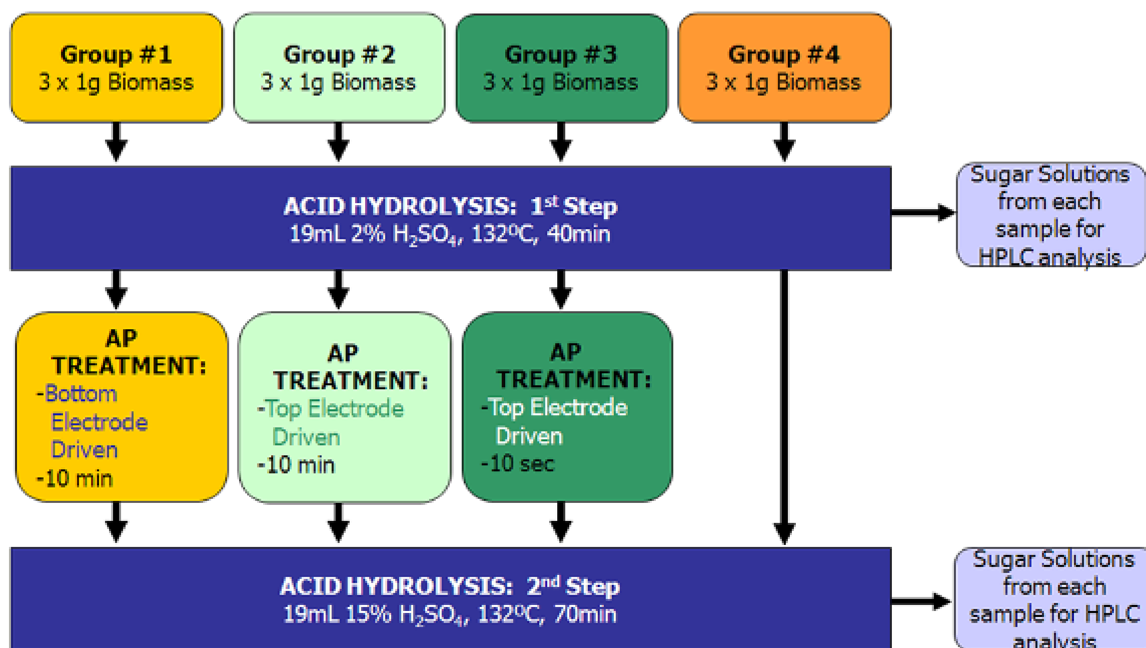

Figure 8.2: Design of experiments flow diagram. Four sample groups and the treatment conditions are described. Washed samples of the loblolly pine were collected after each hydrolysis step for relating sugar production to the experimental conditions found in the diagram.

The diagram depicts four sample groups. Within each sample group, one gram loblolly pine samples were processed in triplicate and in random order according to the experimental recipe. The random number was selected with the software found at reference [71]. In the first step, four sample groups were treated for 40 minutes at 132˚C in a dilute acid hydrolysis bath using a 2% (v/v) solution of H_2SO_4. All samples were cooled for 5 minutes in an ice

bath to reduce formation of degradation products and quench the reaction. After each sample was cooled, each was rinsed with deionized water and the sugar solutions were collected for HPLC analysis. The remaining solid biomass samples were then dried overnight at ambient temperature and pressure. Once dried, three of the four sample groups were plasma treated in a reactive gas mixture, either 5.6% oxygen or air in helium, according to the previously described experimental procedure. The samples were then immediately subjected to the second hydrolysis step. The second hydrolysis step was performed for 70 minutes with a 15% (v/v) H_2SO_4 solution. After hydrolysis, the samples were again placed in an ice bath for 5 minutes, washed, and the five and six carbon sugars were collected for further HPLC analysis. The plasma treatment conditions for groups 1, 2 and 3 are as follows. Sample groups 1 and 2 were both treated for 10 minutes in the plasma environment. The difference in treatment conditions between sample groups 1 and 2 is found in the driven electrode polarity. For sample group 1, the top electrode received the applied power while the bottom electrode (sample location) was grounded (anode). In sample group 2, the bottom electrode received the applied power while the top electrode was grounded. In the third sample group, the biomass was treated for 10 seconds with the top electrode powered. This experimental design allows for the evaluation of treatment time, electrode polarity, and plasma chemistry in terms of overall sugar production. Additional analysis was performed by characterizing the treated samples for physical degradation and chemical modification.

8.4 Results and Discussion

8.4.1 HPLC Results

High-performance liquid chromatography (HPLC) was used to measure the xylose and glucose content of the hydrolyzates. The apparatus was a Dionex BioLC AD 50 (Sunnyvale, CA) HPLC with a Dionex CarboPac column, model PA-10 (250mm x 4mm) with a sodium hydroxide mobile phase. Sugar yields from the first hydrolysis step were much lower than previously cited in the literature [64, 179]. In the results found with Choi and Mathews, the conversion yields of the first hydrolysis step of hemicelluose to xylose exceeded 80% [64]. Yields on the order of 8.5% were found for each of the three samples in the four sample

groups. Although the conversion yield was lower when compared to the prior work, the yields were consistent for all samples processed with the first hydrolysis step, indicating the first hydrolysis treatment was uniform for each sample. After the first hydrolysis step, each sample was immediately placed in an ice bath for 5 minutes to reduce the formation of degradation products and quench the reaction.

Sugar yields after plasma exposure indicate similar trends between both plasma chemistries. For the 5.6% oxygen in helium mixture, groups 1 and 2 produced the greatest amount of sugars. Both groups correspond to a 10-minute plasma exposure with the only experimental difference being the cathode and anode orientation. As shown in Figure 8.3, the HPLC analysis found both groups produced an almost equal amount of sugars from both plasma treatments.

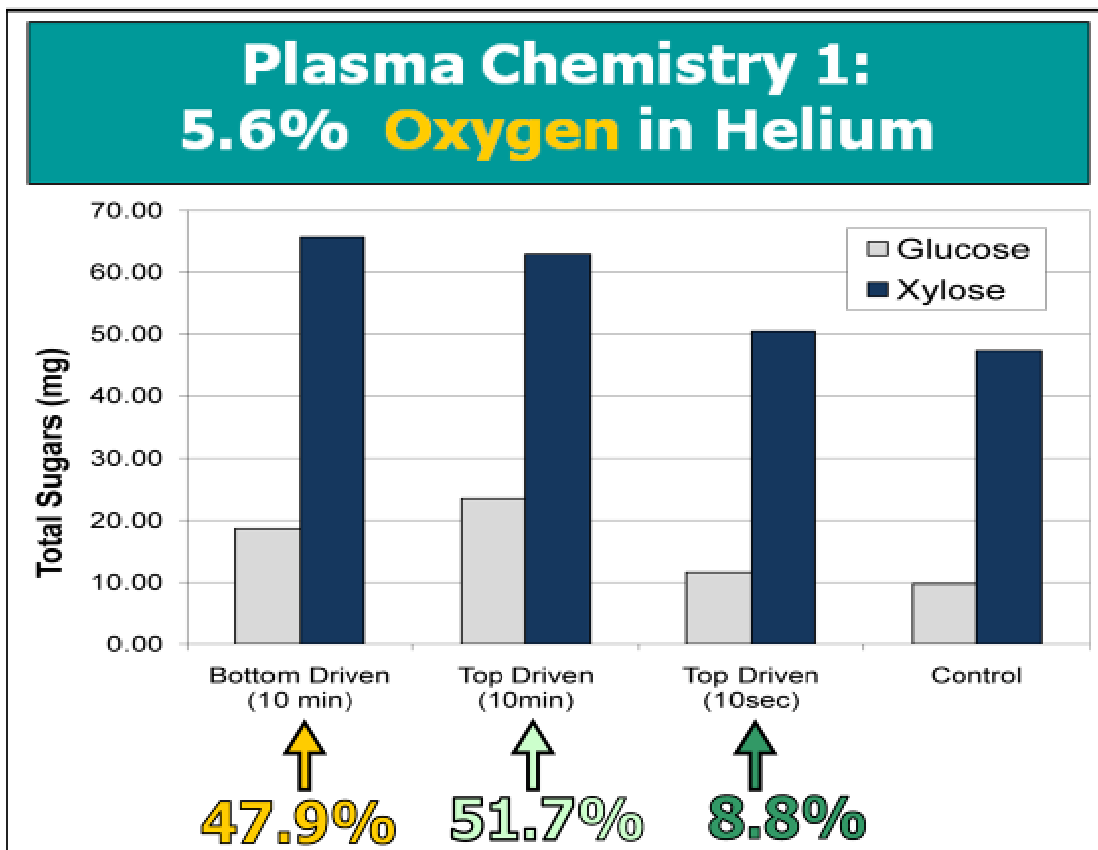

Figure 8.3: Percent improvement of sugar production over sample group 4 (control) for sample group 1-3 from the 5.6% oxygen in helium plasma exposure. Total sugars were collected and measured after all treatment steps were completed; first acid hydrolysis, plasma exposure, and second acid hydrolysis.

For group 1, with the bottom electrode as the cathode, an average of 84.4 mg of xylose and glucose sugars was produced. For group 2, with the top electrode as the cathode, an average of 86.5 mg of xylose and glucose sugars was produced. The control group, group 4, which received the first and second hydrolysis steps and no plasma treatment, an average of 57.0 mg of sugars was found. The resulting increase in total sugar production over the control group was 47.9% for group 1 and 51.7% for group 2. An increase of 62.0 mg in sugar production was found which corresponded to 8.8% increase of xylose and glucose sugars after plasma exposure.

As shown in Figure 8.4, a similar trend was found for the chemistry containing 5.6% air in helium.

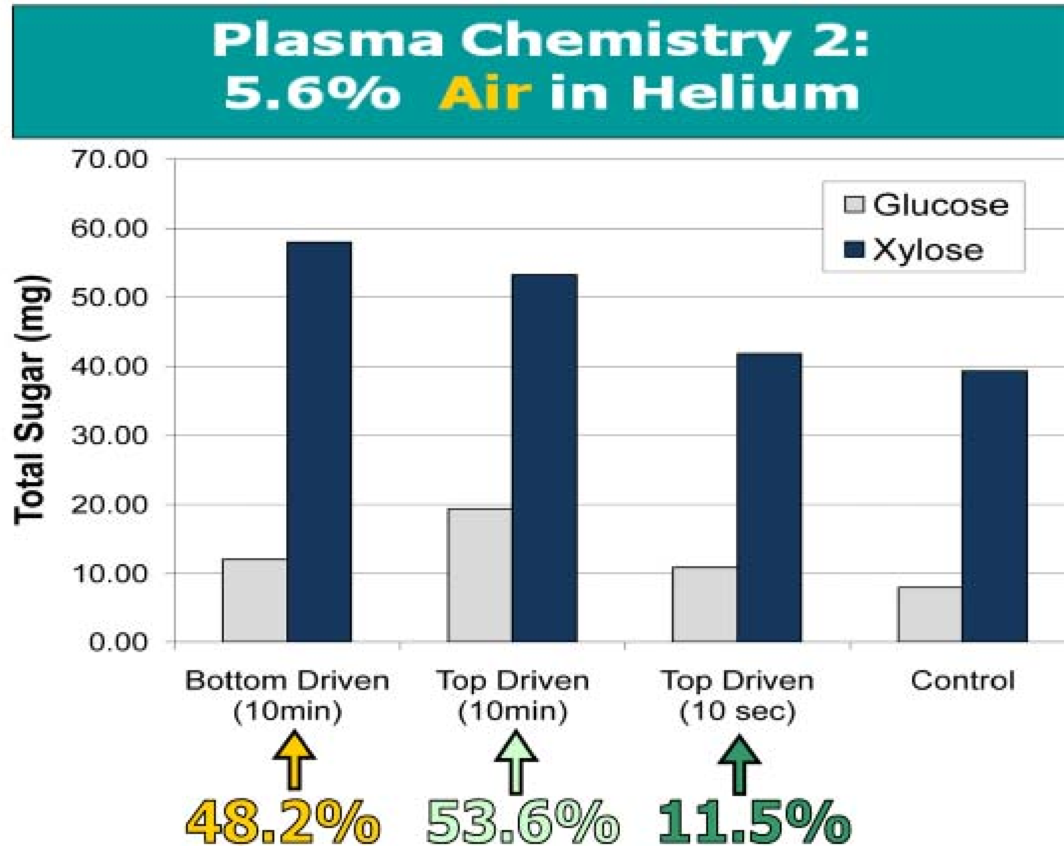

Figure 8.4: Percent improvement of sugar production over sample group 4 (control) for sample group 1-3 from the 5.6% air in helium plasma exposure. Total sugars were collected and measured after all treatment steps were completed, first acid hydrolysis, plasma exposure, and second acid hydrolysis.

Sample groups 1 and 2 were treated with a 10-minute plasma exposure. Group 1 produced an average of 70.0 mg of xylose and glucose sugars while group two produced an average of 72.6 mg of sugars compared to the control group (group 4), an increase of 48.2% and 53.6% respectively. The 10-second treatment, group 3, averaged 52.7 mg of xylose and glucose sugars. Similar trends were observed in sugar production when comparing the two plasma chemistries. Only a small difference was observed from altering the electrode

polarity, which indicates little or no contribution to a sheath effect in the plasma. This is contrary to the expectation that sugar production would be greater if the cathode was placed on the substrate which is analogous to a reactive ion etching process where high energy ions in the plasma attack and react with the substrate. In terms of electrode polarity no clear difference was observed in sugar production. Treatment time in the plasma greatly improved sugar production, but further work is needed to fully understand the exact mechanism and whether a maximum in sugar production may appear at a particular exposure time.

8.4.2 SEM Results

Investigation of the physical degradation of the loblolly pine was performed using a JEOL SEM, model JSM-6360SLV, at a beam voltage of 20kV. The SEM was operated at a pressure of 60 Pa in backscatter electron detection mode. The samples were prepared by cleaving a flat surface on a 6 mm^2 loblolly pine sample with a razor blade. The untreated sample was then placed in the SEM for analysis. Following analysis, the sample was treated with the first acid hydrolysis step and within two hours another micrograph was captured. Next, a plasma treatment was performed on the same sample and again within two hours another micrograph was captured.

The micrographs from the acid and plasma treatment steps indicate the biomass was degraded. Micrographs from the untreated biomass sample show the pores and trachea of the biomass sample undisturbed. Little or no evidence of cracking or physical degradation was observed in the micrographs of the untreated biomass samples. Micrographs after the first acid hydrolysis step indicate swollen pores after hydrolysis. The resulting micrographs from plasma treatments in both plasma chemistries indicate more severe swelling of the pores, cracking and bubbling of the trachea surface. Additional shredding and further deterioration of the trachea wall and lignin component after plasma treatment was evident. Found in Figure 8.5 is a composite of micrographs from before and after the first hydrolysis steps.

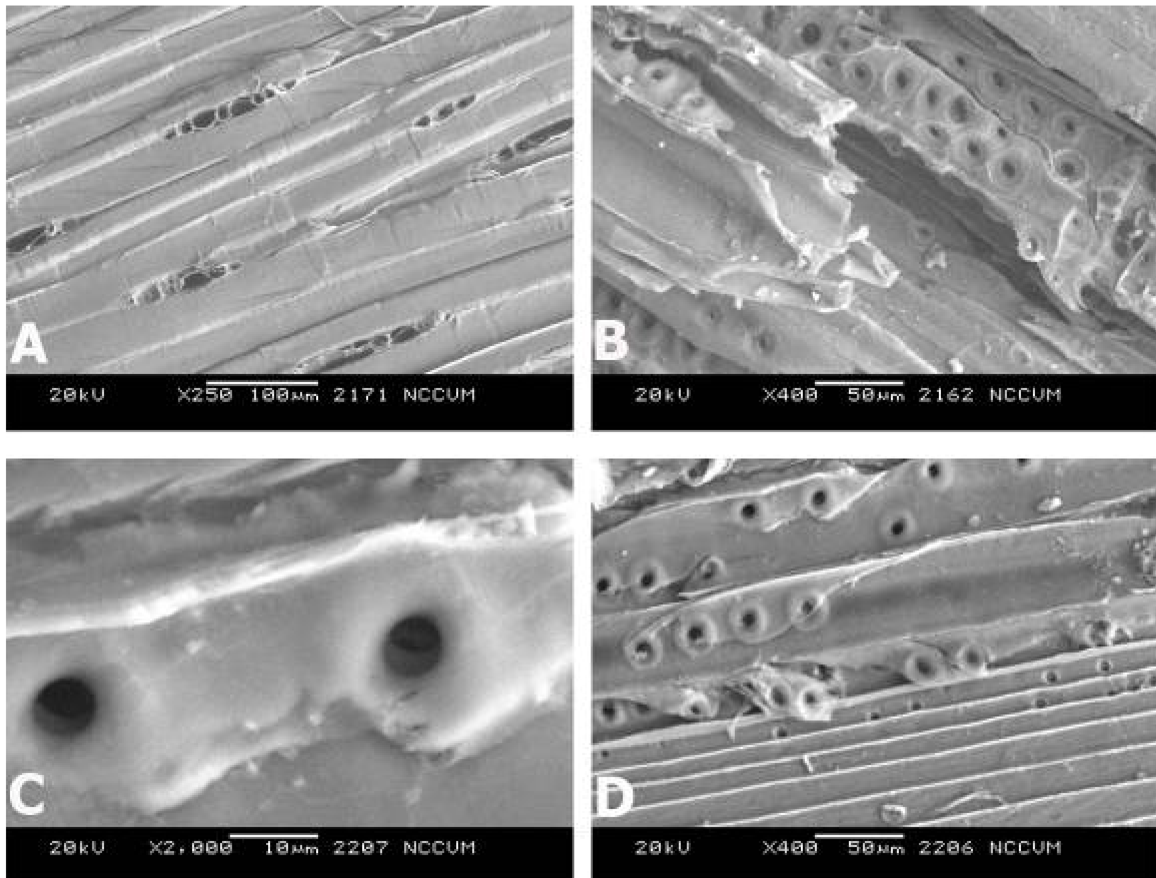

Figure 8.5: SEM micrographs: A) Untreated biomass B) Untreated biomass C) After first acid hydrolysis step D) After first acid hydrolysis step. A backscatter electron detector was used to collect the electron signal. The SEM was operated at a pressure of 60 Pa to prevent charging of the biomass substrate.

The micrographs found in Figure 8.6 were captured after the first acid hydrolysis step and after the 10 minute plasma treatment in 5.6% air in helium.

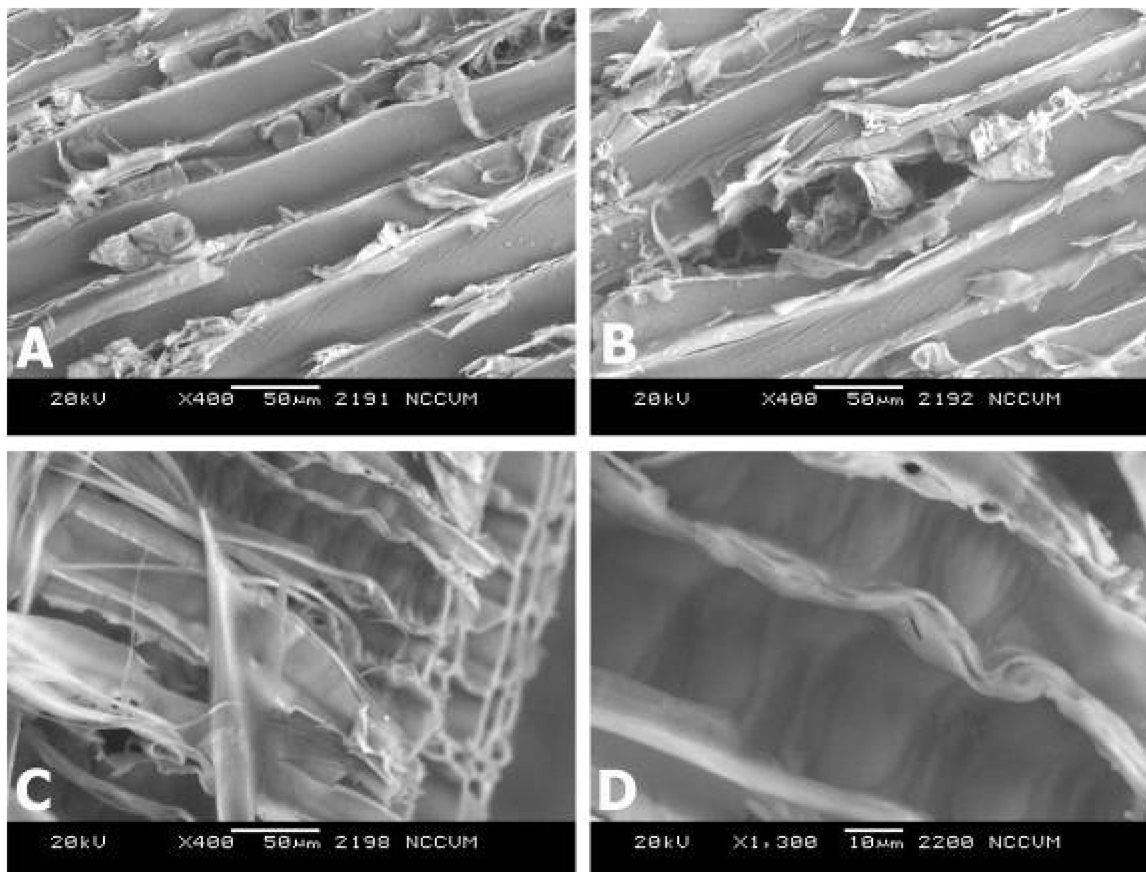

Figure 8.6: SEM micrographs A-D after first acid hydrolysis step and 10-minute plasma treatment in 5.6% air in helium gas mixture. The SEM was operated at 60 Pa with a backscatter electron detector.

8.4.3 FTIR Results

A Bio-Rad-Digilab FTS-6000 Fourier transform infrared (FT-IR) spectrometer with an attached infrared microscope (model #UMA-500) and mounted germanium crystal was used to collect chemical information about the biomass. The spectrometer was mounted with an attenuated total internal reflection (ATR) sampling attachment. The spectrometer collects a normal spectral response from 650 to 5500 cm^{-1}. FT-IR analysis was used to provide

specific peak contributions of the three main biomass constituents-cellulose, hemicellulose, and lignin in the so-called fingerprint region [223]. The analysis found, after treating the biomass with the first acid step and plasma treatment using either chemistry, the lignin and cellulose peak contributions were degraded. Found in Figure 8.7 is a representative spectrum where the peak contributions of the cellulose component found at 1375 and 1162 cm^{-1} were shifted [223].

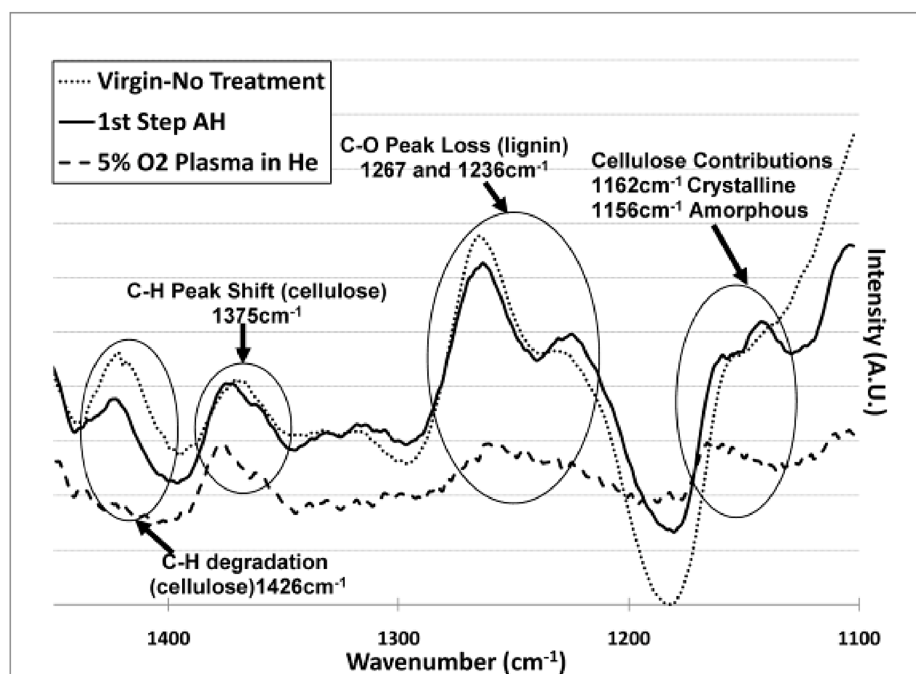

Figure 8.7: FTIR results from 1450-1100 cm^{-1}. Peak contributions related to cellulose and lignin peaks were collected from representative samples with no treatment, after the first acid hydrolysis step, and the 5% oxygen in helium plasma exposure for 10 minutes. Results from the 5% air spectrum also detected the same degradation of the cellulose peak structure.

Peak shifting of cellulose component indicates the underlying chemical makeup was modified after both treatments. A spectrum of the sample receiving only the first acid treatment is provided to confirm the peak shift was the result of the addition of the plasma treatment to the process step. The spectrum shows after the first acid treatment both peaks shifted, but analysis of a peak contribution at 1426 cm^{-1} [223] shows the peak was

completely lost only after the addition of the plasma treatment. Similarly, lignin peak contributions at 1595 and 1510 cm^{-1} [223] were not degraded after the first acid treatment. As shown in Figure 8.8, the addition of the atmospheric plasma treatment resulted in the characteristic lignin peaks to be shifted or completely removed from the chemical makeup.

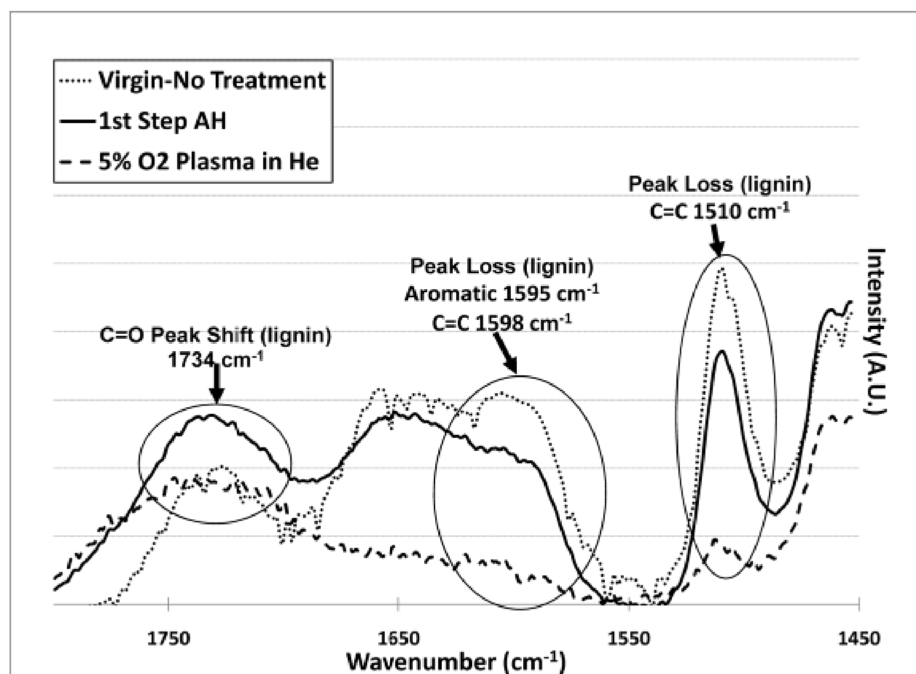

Figure 8.8: FTIR results from 1800-1450cm^{-1}. Peak contributions related to lignin peaks were collected from representative samples with no treatment, after the first acid hydrolysis step, and 5% oxygen in helium plasma exposure for 10 minutes. Results from the 5% air spectrum also detected the same degradation of the lignin peak structure.

8.4.4 Plasma Mechanism

The resulting increase in sugar production after plasma treatment and further analysis with SEM and FT-IR indicates four possible mechanisms for the degradation of the biomass substrate.

- Mechanism 1: Etching of the biomass; removal of the surface biomass components including protective inhibitors.
- Mechanism 2: Cross-linking or degradation of cellulose, hemicellulose, and lignin polymers.
- Mechanism 3: Functionalization of the biomass substrate.
- Mechanism 4: Degradation of lignin via oxidation in the plasma environment.

A key to fully understanding the mechanism may be found in the FT-IR analysis of the lignin contribution. The plasma appears to have easily degraded the lignin structure and thus may be the key contributor for the 50% increase in sugar production. As noted in the literature, lignin can be degraded via oxidative processes similar to that found in the plasma environment [223]. Plasmas containing both oxygen and nitrogen are known to produce highly oxidizing products such as ozone, hydroxyl radicals, nitrogen oxide compounds, and molecular oxygen [36, 117, 126, 224-227], lignin degradation via oxidation is the most likely mechanism. Investigation of atomic, ionic, and molecular species in the plasma chemistry was done via optical emission spectroscopy. Figure 8.9 and Figure 8.10 are representative spectrums of the two plasma chemistries.

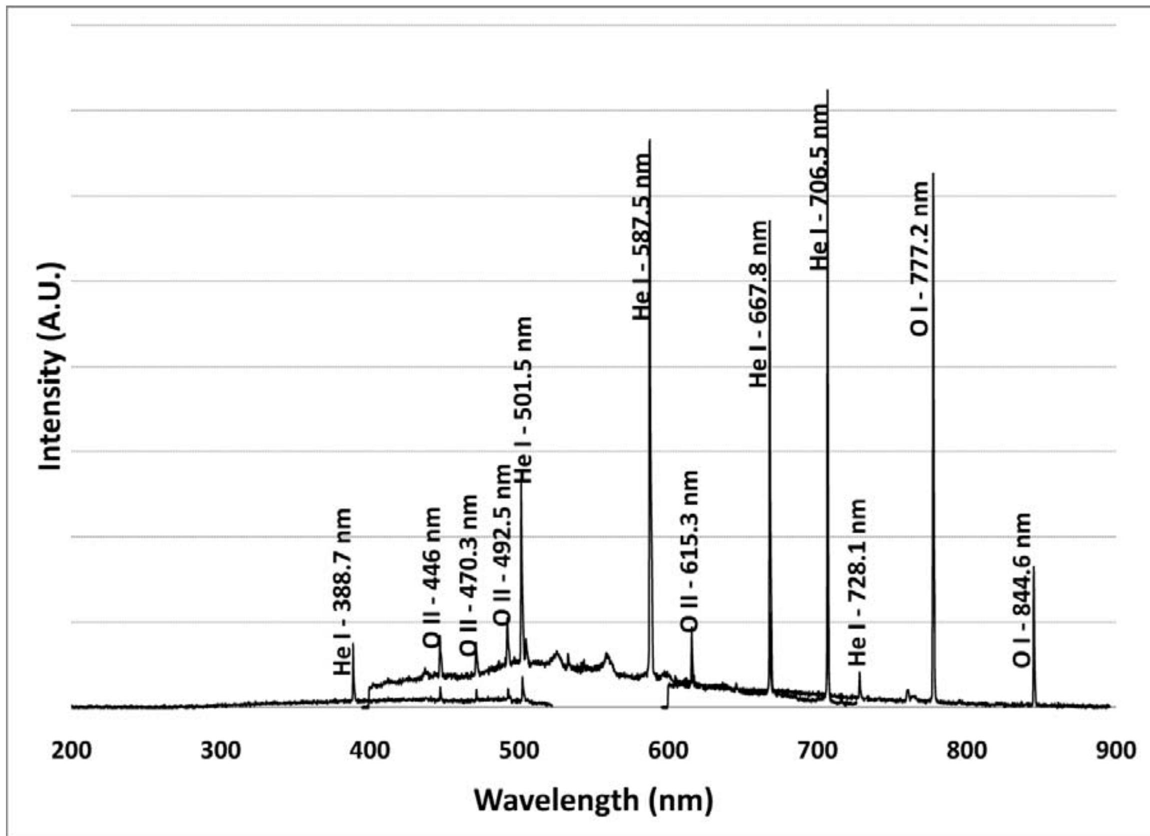

Figure 8.9: A representative emission spectrum recorded from a gas mixture of (5% oxygen in helium). Found in the emission profile were atomic helium, atomic oxygen, and singly ionized oxygen emission lines. The emission profile was collected at a pressure of 760 torr, plasma current of 100mA, driving frequency of 89-110 kHz, and gas flow rate of 3 L/min. Spectral resolution=0.5 nm.

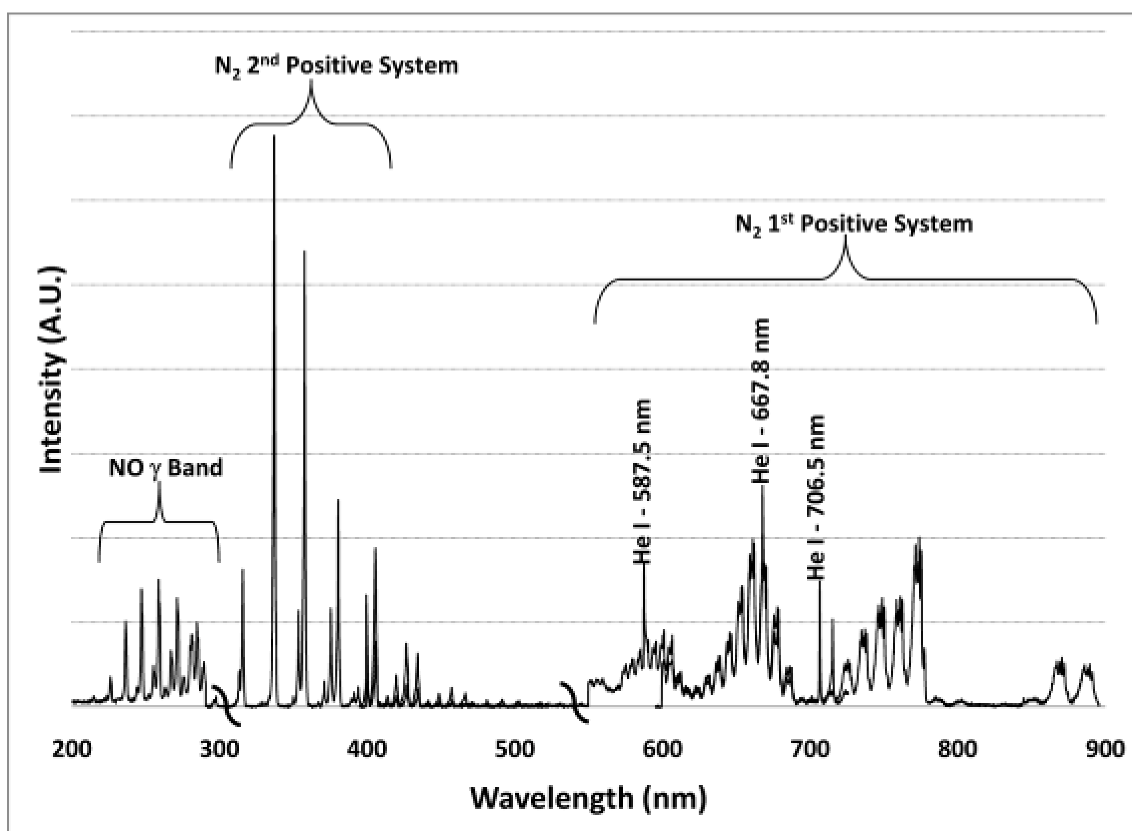

Figure 8.10: A representative emission spectrum recorded from a gas mixture of (5% air in helium). Found in the emission profile were band heads of the NO_γ, N_2 second positive, and N_2 first positive systems. Emission lines from atomic helium were also detected. Marks on the x-axis represent overlay of three spectra from the same experiment at different signal to noise times for presentation of separate bands in emission profile. The emission profile was collected at a pressure of 760 torr, plasma current of 100mA, driving frequency of 89-110 kHz and total gas flow rate of 3 L/min. Spectral resolution=0.5 nm.

Emission lines attributed to atomic helium peaks (388.7 nm, 501.5 nm, 587.5 nm, 667.8 nm, 706.5 nm, and 728.1 nm) were clearly identified in both spectrums [125]. In the 5% oxygen mixture, strong radiation from atomic oxygen lines (777.2 nm and 844.6 nm) and first ionization states of oxygen (446.6 nm, 470.3nm, 492.5nm, and 615.3 nm) were observed [125, 128]. In the 5% air mixture, radiation from the nitrogen second positive (337.1 nm) and the nitrogen first positive system (550-900nm) was found along with strong emission of

the γ-band of NO radiation (213 nm, 224 nm, 234 nm, 245 nm, 257nm, 270 nm, 284 nm) [127, 128].

This plasma configuration also produces a significant amount of ozone (O_3). Ozone (O_3) forms via a three body reaction in the plasma environment. The reaction starts with the dissociation of an O_2 molecule by electron interaction and the subsequent third body reaction occurs upon collision with a third partner. It is believed that in the 5% air mixture, ozone would form through the following reactions.

$$e^- + O_2 \rightarrow 2O + e^- \quad (7.1)$$

$$O + O_2 + M \rightarrow O_3 + M \quad (7.2)$$

where M = O, O_2, O_3, or N_2 [72]. Further optical absorption measurements are needed to identify the bands associated with UV absorption of ozone molecules, namely the Schumann–Runge band (240-270 nm).

8.5 Conclusions

The addition of atmospheric plasma processing to a conventional 2-step acid hydrolysis process increased fermentable sugar production by 50%. SEM and FTIR analysis indicates the loblolly pine was degraded only after plasma exposure. Highly oxidizing compounds and radicals present in the plasma are the most likely mechanism for the degradation of the biomass structure. The technique has been termed the atmospheric plasma enhanced (APE)-soft hydrolysis process and offers new possibilities for processing biomass sources for bioethanol production. The hybrid biomass treatment indicates lignin degradation can be efficiently degraded by the addition of atmospheric plasma processing. The process has the potential to yield greater amounts of sugars at lower costs.

Future work will explore the implementation of a plasma enhanced process such as a fluidized bed to address treating the biomass continuously. Additional experiments to measure the concentration of ozone, NO_x, and other oxidative species will be performed with optical absorption measurements. A final study investigating the role of sugar production related in relation to plasma exposure time will be conducted.

8.6 Acknowledgements

The authors of this work would like to thank Dr. Simon Lappi in the Laser Spectroscopy Laboratory for assistance in completing the FTIR analysis. The authors would also like to thank Dr. John Gilligan and the Office for Research and Graduate Studies and Dean Louis Martin-Vega of the College of Engineering at NCSU and Dr. Mike Rigsbee of the Department of Materials Science and Engineering for financial support of this work. The authors would like to acknowledge Dr. Hasan Jameel and his laboratory from the Department of Wood and Paper Science at NC State University for supplying the southern pine used in this manuscript. The authors are also very grateful for the detailed review of the manuscript by Robert C. Roth of the IMST at NC State University.

8.7 References

The references for this chapter can be found in Chapter 10. The references were gathered in one large chapter in order to eliminate duplication and overlap between chapters throughout the dissertation.

9. Concluding Remarks and Future Directions

9.1 Summary

This work sought to develop a non-thermal atmospheric plasma discharge, the dielectric barrier discharge (DBD), to reduce the growth of food borne pathogens, deposit hybrid coatings of an inorganic/organic matrix, and modify the surface chemistry of lignocellulosic biomass. The DBD used in this work was of a large area, homogeneous nature. Through the development of the underlying physical processes leading to successful integration of the DBD in each application, the role of the plasma components was determined.

In the results of bacterial reductions using the DBD configuration, the addition of oxygen to the DBD based atmospheric system greatly reduced the necessary time to achieve a 6-log reduction of *Listeria innocua*. In addition, a large band of germicidal UV was detected in the emission spectra, leading to the conclusion that the primary reduction pathway is from not only from oxidation of the lipid bilayers but also from UV doses inducing dimerization of thymine bases in the *Listeria innocua* DNA. Temperatures in the DBD discharge were measured to be about 320K indicating heat was not a factor in the bacterial growth reduction process. Results using the Tepla portable plasma pen produced a 6-log reduction of *Listeria innocua* in about one second and 3-log reduction of *Salmonella spp.* in about 0.41 seconds. A temperature of 900 K was measured from the active plasma environment in the plasma pen. The heat produced by the plasma pen was shown to affect reductions pathways such as chemical oxidation and UV generation, but it is unclear whether the primary reduction pathway is from heat, chemical species, or some combination of the two.

The outlook for future research using non-thermal and thermal plasma sources for decontamination will require more work invested in understanding how each mechanism individually contributes to the reduction process. The knowledge developed from investigating the reduction pathways in each plasma source will greatly increase the level of understanding for not only the food industry but also the medical and healthcare industries, government agencies, and other commercial groups interested in designing decontamination

sources for protection against various biological hazards. Ultimately, designing a decontamination source that easily kills both gram-negative and gram-positive bacteria along with more resistant germs such as *Aspergillus niger* and *Bacillius subtilis* is needed so that the many industries in need of a quick and portable decontamination source can be served. Both the DBD source and Tepla plasma pen offer advantages over current decontamination techniques. The plasma pen operates in ambient air, is portable, and is robust enough to be operated by robotic arms for more advanced treatment systems. The plasma pen can easily be installed in current processing environments and offers a promising alternative for an efficient, low cost solution to current issues presented on food safety. Additionally, other plasma sources with similar advantages of portability like the gliding arc discharge and atmospheric pressure plasma jet (APPJ) should be investigated to increase the surface treatment area. The DBD is an ideal candidate for manufacturing environments since scaling of the discharge can be easily completed and as a result large area decontamination can be realized.

In the results from the deposition of amorphous silicon carbide (a-SiC:H) using a pulsed DBD assisted PECVD process, a plug flow analysis was completed to simulate fluid flow conditions at atmospheric pressure. The results of this analysis predicted the process could be operated in either a surface limited or mass transport limited regime. From this analysis, deposition of amorphous silicon carbide was attempted in a continuous wave (CW) mode of the plasma discharge. Homogenous gas phase nucleation and gas phase depletion dominated the reactions mechanism in CW mode. The process was limited in range and deposition was not successful. By implementing a pulsed plasma mode into the deposition process, it was shown for first time that deposition of a hybrid coating system at atmospheric pressure using a DBD process could be achieved. Operation of the PECVD reactor in a pulsed wave mode as opposed to a CW mode decreased homogeneous gas phase nucleation and gas phase depletion. In other work using the pulsed DBD assisted PECVD process, a 2^4 factorial design of experiments (DOE) was used to investigate underlying mechanisms that control the deposition process. The DOE was used to investigate how four parameters (substrate

temperature and silane, methane, and hydrogen flow rates) affected the growth rate, optical properties, and film composition of the deposited thin films. The thickness of the thin films ranged from 81-345 nm while the deposition rate varied from 1-6 Angstroms/sec. It was found the growth rate was dependent on a number of interactions between the four factors. The common significant term between the interactions was found to be the hydrogen flow rate. Optical spectra produced by the process found a predominance of atomic hydrogen species. It was concluded atomic hydrogen is the key factor for producing depositing species such as SiH_n and CH_m that ultimately lead to Si-C bond formation. Optical band gaps produced by the process varied between 1.3-3.2 eV, though most fell between 2.2-2.9 eV. Once again, the hydrogen flow rate was also found to be a determining factor influencing the film properties. Also found to influence the optical gap was the methane flow rate. It is believed the production of atomic hydrogen ultimately leads to formation of CH_m species and incorporation of carbon species into the films. Compositional analysis revealed the presence of Si-C bonding in all deposited thin films. It was found in a number of samples an oxide had formed in the film matrix. The oxide formation is believed to be from formation of a silicon oxycarbide, i.e. $SiOC_3$, SiO_2C, and SiO_3C due to either etching or desorption of residual water and oxygen species off the quartz chamber walls or reactions with dangling bonds after the film is exposed to the ambient atmosphere. From a depth profile analysis, the oxygen content was found to be about 10% at 60 nm below the sample surface. The current results show great promise for use in optoelectronic devices where a process that can tune or control the optical properties over a wide range of values is highly desired. Such control would be very attractive for applications in optoelectronic devices where transparent doped layers of Si rich a-SiC:H have been used as the window material such in solar cells while C rich a-SiC:H films used in large area displays. The results shown in this work demonstrate great promise for the DBD assisted pulsed PE-CVD process to synthesize similar materials.

Future work using the pulsed DBD assisted PECVD process will require further optimization in order to understand the direct mechanisms of the DBD assisted pulsed PE-CVD process. Optimization may include attempts to deposit under an ALD like condition

where both the organic and inorganic material are pulsed in the plasma discharge at separate times, gas pulses would coincide with plasma on periods. Further process refinement would be needed in order to attempt a modified ALD process and the process would have to be modified in order to accommodate subsequent purging of the precursor species in between pulse steps. It is also desired that the deposition rate be increased in order to accommodate high throughput, continuous processing applications. In order to achieve this, further modeling and subsequent changes to the process reactor will need to be completed. It is believed in order for the DBD assisted pulsed PECVD process to be commercially viable, a high mass flow rate of activated species to the substrate would be required in order to transport through the large boundary layer found in the process. Current results support further development and process refinement in order to meet the needs of a robust, scalable PECVD reactor at atmospheric pressure for deposition and coating applications.

Finally, it was found by adding an oxygen based DBD plasma treatment to a conventional 2-step acid hydrolysis process increased fermentable sugar production by 50%. SEM and FTIR analysis indicated the loblolly pine was degraded only after plasma exposure. Highly oxidizing compounds and radicals present in the plasma are the most likely mechanism for the degradation of the biomass structure. The hybrid biomass treatment indicates lignin degradation occurs with the addition of the atmospheric plasma treatment. The process has the potential to yield greater amounts of sugars at lower costs.

Future work will explore the implementation of other atmospheric plasma configurations on the treatment of biomass. Maximizing sugar production with the addition of plasma treatments is not fully understood with the current results. Further work is required in order to test the viability of producing fermentable sugars from a single plasma treatment step or some combination of conventional pretreatments (biological, chemical, or mechanical).

9.2 Future Outlook

Other work not presented in this thesis but examined over the course of this project included the removal of paint on metal and composite surfaces, production of methanol from waste biogas (methane and carbon dioxide) found in hog lagoons and landfills, and production of syngas (hydrogen and carbon monoxide). The additional work in these other areas demonstrates atmospheric plasma as a technology can impact a wide range of industries.

From this work, three patent applications were successfully applied for in order to protect the intellectual property discovered during the research effort. With two of the patent applications showing little to no prior art in the literature, we have high expectations these patents will be awarded full patent protection.

To conclude, future work should focus further on applying new configurations to the applications presented in this work while also exploring new applications where plasma-aided manufacturing techniques at atmospheric pressure can impact existing and new industries. The focus of any such effort should be centered on developing a fundamental understanding surrounding the mechanisms and role the plasma plays in a particular application.

In summary, atmospheric plasmas can be a solution to many industrial problems, but specific questions need to be addressed in order to correctly apply the technology. The results found in this project should aid in the advancement of such efforts to develop atmospheric plasmas for new applications.

10. References

[1] J. R. Roth, *Industrial Plasma Engineering, Principles Vol.1*. Bristol: Institute of Physics, 1995.

[2] A. A. Fridman and L. A. Kennedy, *Plasma Physics and Engineering*. New York: Taylor and Francis, 2004.

[3] K. H. Becker, K. H. Schoenbach, and J. G. Eden, "Microplasmas and applications," *Journal of Physics D-Applied Physics*, vol. 39, pp. R55-R70, 2006.

[4] A. Fridman, A. Chirokov, and A. Gutsol, "Non-thermal atmospheric pressure discharges," *Journal of Physics D-Applied Physics*, vol. 38, pp. R1-R24, 2005.

[5] "Google Images."

[6] U. Kogelschatz, "Atmospheric-pressure plasma technology," *Plasma Physics and Controlled Fusion*, vol. 46, pp. B63-B75, 2004.

[7] E. Pfender, "Electric arcs and arc gas heaters," in *Gaseous Electronics: Elctrical Discharges*, vol. 1, M. H. a. H. Oskam, Ed. New York: Academic, 1978, pp. 291-398.

[8] J. Kedzierski, J. Engemann, M. Teschke, and D. Korzec, "Atmospheric pressure plasma jets for 2D and 3D materials processing," in *Particle Beams & Plasma Interaction on Materials and Ion & Plasma Surface Finishing 2004*, vol. 107, *Solid State Phenomena*, T. B. D. T. C. Vilaithong, Ed., 2005, pp. 119-123.

[9] T. Nakano, "Some recent topics of non-equilibrium discharge plasma technologies - Their widespread use from low pressure to atmospheric pressure," *Ieee Transactions on Dielectrics and Electrical Insulation*, vol. 14, pp. 1081-1087, 2007.

[10] K. Okazaki and T. Nozaki, "Ultrashort pulsed barrier discharges and applications," *Pure and Applied Chemistry*, vol. 74, pp. 447-452, 2002.

[11] C. Sarra-Bournet, S. Turgeon, D. Mantovani, and G. Laroche, "Comparison of atmospheric-pressure plasma versus low-pressure RF plasma for surface functionalization of PTFE for biomedical applications," *Plasma Processes and Polymers*, vol. 3, pp. 506-515, 2006.

[12] T. Wakida and S. Tokino, "Surface modification of fibre and polymeric materials by discharge treatment and its application to textile processing," *Indian Journal of Fibre & Textile Research*, vol. 21, pp. 69-78, 1996.

[13] C. Tendero, C. Tixier, P. Tristant, J. Desmaison, and P. Leprince, "Atmospheric pressure plasmas: A review," *Spectrochimica Acta Part B-Atomic Spectroscopy*, vol. 61, pp. 2-30, 2006.

[14] Y. Sakiyama, D. B. Graves, and E. Stoffels, "Influence of electrical properties of treated surface on RF-excited plasma needle at atmospheric pressure," *Journal of Physics D-Applied Physics*, vol. 41, 2008.

[15] Y. Sakiyama and D. B. Graves, "Corona-glow transition in the atmospheric pressure RF-excited plasma needle," *Journal of Physics D-Applied Physics*, vol. 39, pp. 3644-3652, 2006.

[16] C. S. Ren, T. C. Ma, D. Z. Wang, J. L. Zhang, and Y. N. Wang, "A study of cross-gas-flow to stabilize an atmospheric pressure glow plasma in a multi-pin-to-multi-cupped-plane negative corona discharge," *Journal of Electrostatics*, vol. 64, pp. 23-28, 2006.

[17] B. Qi, C. S. Ren, T. C. Ma, Y. N. Wang, and D. Z. Wang, "Stabilization of the multi-pin to multi-sphere plane negative corona discharge," *Acta Physica Sinica*, vol. 55, pp. 331-336, 2006.

[18] C. S. Ren, T. C. Ma, D. Z. Wang, W. C. Wang, J. L. Zhang, and Y. N. Wang, "Stable and diffuse atmospheric pressure glow plasma in a multipoint-to-plane configuration in air," *Ieee Transactions on Plasma Science*, vol. 33, pp. 210-211, 2005.

[19] W. Siemens, *Poggendorffs Ann. Phys. Chem.*, vol. 102, pp. 66-102, 1857.

[20] B. G. Guo, W. Wei, T. Shinoda, and C. L. Liu, "Influence of wall-charge accumulation on the gas dielectric barrier discharge in alternating current plasma display panel," *Applied Physics Letters*, vol. 90, 2007.

[21] M. R. King, C. J. Oldham, J. R. Puckett, C. G. Guarnieri, and J. J. Cuomo, "Production of atomic oxygen in an atmospheric pressure arc in air and its implications for NO2 generation," presented at Gaseous Electronics Conference, Dallas, Tx, 2008.

[22] P. Hudson, *The Industrial Revolution*: Oxford University Press, 1992.

[23] B. Ravi, "Metal Casting Overview." Bombay[24] J. R. Roth, S. Nourgostar, and T. A. Bonds, "The one atmosphere uniform glow discharge plasma (OAUGDP) - A platform technology for the 21st century," *Ieee Transactions on Plasma Science*, vol. 35, pp. 233-250, 2007.

[25] M. Laroussi, "Low temperature plasma-based sterilization: Overview and state-of-the-art," *Plasma Processes and Polymers*, vol. 2, pp. 391-400, 2005.

[26] J. R. Roth, "Potential industrial applications of the one atmosphere uniform glow discharge plasma operating in ambient air," *Physics of Plasmas*, vol. 12, 2005.

[27] U. Kogelschatz, "Dielectric-barrier discharges: Their history, discharge physics, and industrial applications," *Plasma Chemistry and Plasma Processing*, vol. 23, pp. 1-46, 2003.

[28] U. Kogelschatz, "Filamentary, patterned, and diffuse barrier discharges," *Ieee Transactions on Plasma Science*, vol. 30, pp. 1400-1408, 2002.

[29] M. Laroussi, "Nonthermal decontamination of biological media by atmospheric-pressure plasmas: Review, analysis, and prospects," *Ieee Transactions on Plasma Science*, vol. 30, pp. 1409-1415, 2002.

[30] U. Kogelschatz, "Industrial innovation based on fundamental physics," *Plasma Sources Science & Technology*, vol. 11, pp. A1-A6, 2002.

[31] M. Laroussi, I. Alexeff, J. P. Richardson, and F. F. Dyer, "The resistive barrier discharge," *Ieee Transactions on Plasma Science*, vol. 30, pp. 158-159, 2002.

[32] J. Park, I. Henins, H. W. Herrmann, G. S. Selwyn, and R. F. Hicks, "Discharge phenomena of an atmospheric pressure radio-frequency capacitive plasma source," *Journal of Applied Physics*, vol. 89, pp. 20-28, 2001.

[33] U. Kogelschatz, B. Eliasson, and W. Egli, "From ozone generators to flat television screens: history and future potential of dielectric-barrier discharges," *Pure and Applied Chemistry*, vol. 71, pp. 1819-1828, 1999.

[34] T. C. Montie, K. Kelly-Wintenberg, and J. R. Roth, "An overview of research using the one atmosphere uniform glow discharge plasma (OAUGDP) for sterilization of surfaces and materials," *Ieee Transactions on Plasma Science*, vol. 28, pp. 41-50, 2000.

[35] J. R. Roth, D. M. Sherman, R. Ben Gadri, F. Karakaya, Z. Y. Chen, T. C. Montie, K. Kelly-Wintenberg, and P. P. Y. Tsai, "A remote exposure reactor (RER) for plasma processing and sterilization by plasma active species at one atmosphere," *Ieee Transactions on Plasma Science*, vol. 28, pp. 56-63, 2000.

[36] J. Park, I. Henins, H. W. Herrmann, G. S. Selwyn, J. Y. Jeong, R. F. Hicks, D. Shim, and C. S. Chang, "An atmospheric pressure plasma source," *Applied Physics Letters*, vol. 76, pp. 288-290, 2000.

[37] A. Schutze, J. Y. Jeong, S. E. Babayan, J. Park, G. S. Selwyn, and R. F. Hicks, "The atmospheric-pressure plasma jet: A review and comparison to other plasma sources," *Ieee Transactions on Plasma Science*, vol. 26, pp. 1685-1694, 1998.

[38] L. M. Zhou, B. Xue, U. Kogelschatz, and B. Eliasson, "Nonequilibrium plasma reforming of greenhouse gases to synthesis gas," *Energy & Fuels*, vol. 12, pp. 1191-1199, 1998.

[39] J. Y. Jeong, S. E. Babayan, V. J. Tu, J. Park, I. Henins, R. F. Hicks, and G. S. Selwyn, "Etching materials with an atmospheric-pressure plasma jet," *Plasma Sources Science & Technology*, vol. 7, pp. 282-285, 1998.

[40] S. E. Babayan, J. Y. Jeong, V. J. Tu, J. Park, G. S. Selwyn, and R. F. Hicks, "Deposition of silicon dioxide films with an atmospheric-pressure plasma jet," *Plasma Sources Science & Technology*, vol. 7, pp. 286-288, 1998.

[41] U. Kogelschatz, B. Eliasson, and W. Egli, "Dielectric-barrier discharges. Principle and applications," *Journal De Physique Iv*, vol. 7, pp. 47-66, 1997.

[42] M. Kogoma and S. Okazaki, "Raising of Ozone Formation Efficiency in a Homogeneous Glow-Discharge Plasma at Atmospheric-Pressure," *Journal of Physics D-Applied Physics*, vol. 27, pp. 1985-1987, 1994.

[43] T. Yokoyama, M. Kogoma, T. Moriwaki, and S. Okazaki, "The Mechanism of the Stabilization of Glow Plasma at Atmospheric-Pressure," *Journal of Physics D-Applied Physics*, vol. 23, pp. 1125-1128, 1990.

[44] T. Yokoyama, M. Kogoma, S. Kanazawa, T. Moriwaki, and S. Okazaki, "The Improvement of the Atmospheric-Pressure Glow Plasma Method and the Deposition of Organic Films," *Journal of Physics D-Applied Physics*, vol. 23, pp. 374-377, 1990.

[45] J. L. Shohet, "Plasma-Aided Manufacturing," *IEEE Transactions on Plasma Science*, vol. 19, pp. 725-733, 1991.

[46] B. N. Chapman, *Glow discharge processes : sputtering and plasma etching*. New York: Wiley, 1980.

[47] U. Fantz, "Basics of plasma spectroscopy," *Plasma Sources Science & Technology*, vol. 15, pp. S137-S147, 2006.

[48] D. Knight, *Humphry Davy, Science and Power*. Cambridge, MA, UK: Cambridge Univ. Press 1992.

[49] M. Druyvesteyn and F. Penning, *Rev. Mod. Phys.*, vol. 12, pp. 87-174, 1940.

[50] K. Vollrath and G. Thomer, "Kurzzeitphysik," *(Wein: Springer)*, pp. 81, 1967.

[51] H. Akashi, A. Oda, and Y. Sakai, "Modeling of multifilaments formation in dielectric barrier discharge excimer lamp," *Ieee Transactions on Plasma Science*, vol. 33, pp. 308-309, 2005.

[52] H. Barankova and L. Bardos, "Hollow cathode plasma sources for large area surface treatment," *Surface & Coatings Technology*, vol. 146, pp. 486-490, 2001.

[53] R. Foest, M. Schmidt, and K. Becker, "Microplasmas, an emerging field of low-temperature plasma science and technology," *International Journal of Mass Spectrometry*, vol. 248, pp. 87-102, 2006.

[54] V. Hopfe and D. W. Sheel, "Atmospheric-pressure PECVD coating and plasma chemical etching for continuous processing," *Ieee Transactions on Plasma Science*, vol. 35, pp. 204-214, 2007.

[55] S. R. Wylie, A. I. Al-Shamma'a, and J. Lucas, "Microwave plasma system for material processing," *Ieee Transactions on Plasma Science*, vol. 33, pp. 340-341, 2005.

[56] A. N. Bhoj and M. J. Kushner, "Plasma-polymer interactions in a dielectric barrier discharge," *Ieee Transactions on Plasma Science*, vol. 33, pp. 250-251, 2005.

[57] A. Bismarck, W. Brostow, R. Chiu, H. E. H. Lobland, and K. K. C. Ho, "Effects of surface plasma treatment on tribology of thermoplastic polymers," *Polymer Engineering and Science*, vol. 48, pp. 1971-1976, 2008.

[58] G. Borcia, C. A. Anderson, and N. M. D. Brown, "Dielectric barrier discharge for surface treatment: application to selected polymers in film and fibre form," *Plasma Sources Science & Technology*, vol. 12, pp. 335-344, 2003.

[59] G. Borcia, C. A. Anderson, and N. M. D. Brown, "Using a nitrogen dielectric barrier discharge for surface treatment," *Plasma Sources Science & Technology*, vol. 14, pp. 259-267, 2005.

[60] N. Y. Cui and N. M. D. Brown, "Modification of the surface properties of a polypropylene (PP) film using an air dielectric barrier discharge plasma," *Applied Surface Science*, vol. 189, pp. 31-38, 2002.

[61] N. Dumitrascu, C. Borcia, and G. Borcia, "Control of the Blood-Polymer Interface by Plasma Treatment," *Journal of Biomedical Materials Research Part B-Applied Biomaterials*, vol. 87B, pp. 364-373, 2008.

[62] G. T. Lewis and Y. Cohen, "Controlled Nitroxide-Mediated Styrene Surface Graft Polymerization with Atmospheric Plasma Surface Activation," *Langmuir*, vol. 24, pp. 13102-13112, 2008.

[63] M. Okubo, M. Tahara, N. Saeki, and T. Yamamoto, "Surface modification of fluorocarbon polymer films for improved adhesion using atmospheric-pressure nonthermal plasma graft-polymerization," *Thin Solid Films*, vol. 516, pp. 6592-6597, 2008.

[64] J. K. Park, W. T. Ju, K. H. Paek, Y. H. Kim, Y. H. Choi, J. H. Kim, and Y. S. Hwang, "Pre-treatments of polymers by atmospheric pressure ejected plasma for adhesion improvement," *Surface & Coatings Technology*, vol. 174, pp. 547-552, 2003.

[65] C. S. Ren, K. Wang, Q. Y. Nie, D. Z. Wang, and S. H. Guo, "Surface modification of PE film by DBD plasma in air," *Applied Surface Science*, vol. 255, pp. 3421-3425, 2008.

[66] A. Shashurin, M. Keidar, S. Bronnikov, R. A. Jurjus, and M. A. Stepp, "Living tissue under treatment of cold plasma atmospheric jet," *Applied Physics Letters*, vol. 93, 2008.

[67] E. Stoffels, ""Tissue processing" with atmospheric plasmas," *Contributions to Plasma Physics*, vol. 47, pp. 40-48, 2007.

[68] S. Yonson, S. Coulombe, V. Leveille, and R. L. Leask, "Cell treatment and surface functionalization using a miniature atmospheric pressure glow discharge plasma torch," *Journal of Physics D-Applied Physics*, vol. 39, pp. 3508-3513, 2006.

[69] E. K. Baksht, M. I. Lomaev, D. V. Rybka, and V. F. Tarasenko, "Afterglow emission from xenon, krypton, and argon dimers in nanosecond volume discharge at elevated pressures," *Technical Physics Letters*, vol. 32, pp. 847-849, 2006.

[70] E. K. Baksht, M. I. Lomaev, D. V. Rybka, and V. F. Tarasenko, "Study of emission of a volume nanosecond discharge plasma in xenon, krypton and argon at high pressures," *Quantum Electronics*, vol. 36, pp. 576-580, 2006.

[71] E. A. Bogdanov, A. A. Kudryavtsev, R. R. Arslanbekov, and V. I. Kolobov, "Simulation of pulsed dielectric barrier discharge xenon excimer lamp," *Journal of Physics D-Applied Physics*, vol. 37, pp. 2987-2995, 2004.

[72] B. Eliasson, M. Hirth, and U. Kogelschatz, "Ozone Synthesis from Oxygen in Dielectric Barrier Discharges," *Journal of Physics D-Applied Physics*, vol. 20, pp. 1421-1437, 1987.

[73] H. Ito, H. Kano, and M. Hori, "New Compact Continuous Spectrum Light Source Using Atmospheric Pressure Microplasma with High-Velocity Ar Gas Flow," *Applied Physics Express*, vol. 1, 2008.

[74] F. Massines, A. Rabehi, P. Decomps, R. B. Gadri, P. Segur, and C. Mayoux, "Experimental and theoretical study of a glow discharge at atmospheric pressure controlled by dielectric barrier," *Journal of Applied Physics*, vol. 83, pp. 2950-2957, 1998.

[75] F. Massines, P. Segur, N. Gherardi, C. Khamphan, and A. Ricard, "Physics and chemistry in a glow dielectric barrier discharge at atmospheric pressure: diagnostics and modelling," *Surface & Coatings Technology*, vol. 174, pp. 8-14, 2003.

[76] H. P. Li, G. Li, S. Wang, P. S. Le, and C. Y. Bao, "Radio-frequency glow discharges of different gases using bare metallic electrodes at atmospheric pressure," *Ieee Transactions on Plasma Science*, vol. 36, pp. 1418-1419, 2008.

[77] S. A. Zhdanok, "Nonequilibrium processes and their applications," *Applied Thermal Engineering*, vol. 28, pp. 254-260, 2008.

[78] L. Baars-Hibbe, P. Sichler, C. Schrader, N. Lucas, K. H. Gericke, and S. Buttgenbach, "High frequency glow discharges at atmospheric pressure with micro-structured electrode arrays," *Journal of Physics D-Applied Physics*, vol. 38, pp. 510-517, 2005.

[79] E. Stoffels, A. J. Flikweert, W. W. Stoffels, and G. M. W. Kroesen, "Plasma needle: a non-destructive atmospheric plasma source for fine surface treatment of (bio)materials," *Plasma Sources Science & Technology*, vol. 11, pp. 383-388, 2002.

[80] A. K. Srivastava and G. Prasad, "Spatio-temporal dynamics of plasma spots in helium surface barrier discharge," *Physics Letters A*, vol. 372, pp. 6101-6106, 2008.

[81] R. A. Siliprandi, H. E. Roman, R. Barni, and C. Riccardi, "Characterization of the streamer regime in dielectric barrier discharges," *Journal of Applied Physics*, vol. 104, 2008.

[82] X. X. Duan, F. He, and J. T. Ouyang, "Various plasma patterns in planar dielectric-barrier discharge," *Ieee Transactions on Plasma Science*, vol. 36, pp. 1332-1333, 2008.

[83] L. Stollenwerk, S. Amiranashvili, J. P. Boeuf, and H. G. Purwins, "Formation and stabilisation of single current filaments in planar dielectric barrier discharge," *European Physical Journal D*, vol. 44, pp. 133-139, 2007.

[84] Q. Y. Nie, C. S. Ren, D. Z. Wang, S. Z. Li, J. L. Zhang, and M. G. Kong, "Self-organized pattern formation of an atmospheric pressure plasma jet in a dielectric barrier discharge configuration," *Applied Physics Letters*, vol. 90, 2007.

[85] L. F. Dong, Z. Q. Yin, X. H. Li, Z. F. Chai, and Y. F. He, "Spatio-temporal patterns in dielectric barrier discharge in air/argon at atmospheric pressure," *Plasma Sources Science & Technology*, vol. 15, pp. 840-844, 2006.

[86] L. Stollenwerk, S. Amiranashvili, J. P. Boeuf, and H. G. Purwins, "Measurement and 3D simulation of self-organized filaments in a barrier discharge," *Physical Review Letters*, vol. 96, 2006.

[87] T. Shirafuji, T. Kitagawa, T. Wakai, and K. Tachibana, "Observation of self-organized filaments in a dielectric barrier discharge of Ar gas," *Applied Physics Letters*, vol. 83, pp. 2309-2311, 2003.

[88] L. F. Dong, X. C. Li, Z. Q. Yin, and L. Wang, "Pattern formation in dielectric barrier discharge in air at atmospheric pressure," *Acta Physica Sinica*, vol. 51, pp. 2296-2301, 2002.

[89] I. Muller, C. Punset, E. Ammelt, H. G. Purwins, and J. P. Boeuf, "Self-organized filaments in dielectric barrier glow discharges," *Ieee Transactions on Plasma Science*, vol. 27, pp. 20-21, 1999.

[90] B. Gellert and U. Kogelschatz, "Generation of Excimer Emission in Dielectric Barrier Discharges," *Applied Physics B-Photophysics and Laser Chemistry*, vol. 52, pp. 14-21, 1991.

[91] H. Ayan, G. Fridman, A. F. Gutsol, V. N. Vasilets, A. Fridman, and G. Friedman, "Nanosecond-pulsed uniform dielectric-barrier discharge," *Ieee Transactions on Plasma Science*, vol. 36, pp. 504-508, 2008.

[92] T. Shao, P. Yan, K. H. Long, and S. C. Zhang, "Dielectric-barrier discharge excitated by repetitive nanosecond pulses in air at atmospheric pressure," *Ieee Transactions on Plasma Science*, vol. 36, pp. 1358-1359, 2008.

[93] M. M. Kayes, F. J. Critzer, K. Kelly-Wintenberg, J. R. Roth, T. C. Montie, and D. A. Golden, "Inactivation of foodborne pathogens using a one atmosphere uniform glow discharge plasma," *Foodborne Pathogens and Disease*, vol. 4, pp. 50-59, 2007.

[94] Y. Maeda, N. Igura, M. Shimoda, and I. Hayakawa, "Inactivation of vegetative bacteria in a liquid medium by gas plasma under atmospheric pressure," *Journal of the Faculty of Agriculture Kyushu University*, vol. 48, pp. 159-166, 2003.

[95] E. Odic, A. Goldman, M. Goldman, S. Delaveau, and F. Le Hegarat, "Plasma sterilization technologies and processes," *High Temperature Material Processes*, vol. 6, pp. 385-396, 2002.

[96] P. R. Chalise, M. S. Rahman, H. Ghomi, Y. Hayashi, M. Watanabe, A. Okino, T. Ano, M. Shoda, and E. Hotta, "Bacterial inactivation using low-energy pulsed-electron beam," *Ieee Transactions on Plasma Science*, vol. 32, pp. 1532-1539, 2004.

[97] H. W. Herrmann, I. Henins, J. Park, and G. S. Selwyn, "Decontamination of chemical and biological warfare, (CBW) agents using an atmospheric pressure plasma jet (APPJ)," *Physics of Plasmas*, vol. 6, pp. 2284-2289, 1999.

[98] M. Laroussi, "Sterilization of contaminated matter with an atmospheric pressure plasma," *Ieee Transactions on Plasma Science*, vol. 24, pp. 1188-1191, 1996.

[99] J. R. Roth, Y. M. Ku, P. P. Tsai, L. C. Wadsworth, Q. Sun, T. C. Montie, and K. KellyWintenberg, "A study of the sterilization of nonwoven webs using one atmosphere glow discharge plasma," *1996 Nonwovens Conference*, pp. 225-230, 1996.

[100] M. Laroussi and F. Leipold, "Evaluation of the roles of reactive species, heat, and UV radiation in the inactivation of bacterial cells by air plasmas at atmospheric pressure," *International Journal of Mass Spectrometry*, vol. 233, pp. 81-86, 2004.

[101] D. A. Mendis, M. Rosenberg, and F. Azam, "A note on the possible electrostatic disruption of bacteria," *Ieee Transactions on Plasma Science*, vol. 28, pp. 1304-1306, 2000.

[102] M. Moisan, J. Barbeau, M. C. Crevier, J. Pelletier, N. Philip, and B. Saoudi, "Plasma sterilization. Methods mechanisms," *Pure and Applied Chemistry*, vol. 74, pp. 349-358, 2002.

[103] N. Abramzon, J. C. Joaquin, J. Bray, and G. Brelles-Marino, "Biofilm destruction by RF high-pressure cold plasma jet," *Ieee Transactions on Plasma Science*, vol. 34, pp. 1304-1309, 2006.

[104] C. Iliescu, B. T. Chen, J. S. Wei, and A. J. Pang, "Characterisation of silicon carbide films deposited by plasma-enhanced chemical vapour deposition," *Thin Solid Films*, vol. 516, pp. 5189-5193, 2008.

[105] J. P. Lim, H. S. Uhm, and S. Z. Li, "Influence of oxygen in atmospheric-pressure argon plasma jet on sterilization of Bacillus atrophaeous spores," *Physics of Plasmas*, vol. 14, 2007.

[106] F. A. Bettleheim and J. March, *Introduction to General, Organic, and Biochemistry*, 4th Edition ed: Saunders College Publishers, 1995.

[107] K. Yamashita, T. Miyoshi, T. Arai, N. Endo, H. Itoh, K. Makino, K. Mizugishi, T. Uchiyama, and M. Sasada, "Ozone production by amino acids contributes to killing of bacteria," *Proceedings of the National Academy of Sciences of the United States of America*, vol. 105, pp. 16912-16917, 2008.

[108] I. R. Grant, E. I. Hitchings, A. McCartney, F. Ferguson, and M. T. Rowe, "Effect of commercial-scale high-temperature, short-time pasteurization on the viability of Mycobacterium paratuberculosis in naturally infected cows' milk," *Applied and Environmental Microbiology*, vol. 68, pp. 602-607, 2002.

[109] R. A. Bezerra da Silva, M. R. Leonardo, L. H. Faccioli, A. I. Medeiros, and P. Nelson-Filho, "Effect of different methods of sterilization on the inactivation of bacterial endotoxin (LPS) in endodontic files," *Brazilian Journal of Microbiology*, vol. 38, pp. 270-272, 2007.

[110] K. M. Keener, "Private Communication," 2008.

[111] M. Madigan, J. M. Martinko, and J. Parker, *Brock Biology of Microorganisms*, 8th Edition ed. Englewoods Cliffs, NJ: Prentice-Hall, 1997.

[112] M. Laroussi, X. P. Lu, and C. M. Malott, "A non-equilibrium diffuse discharge in atmospheric pressure air," *Plasma Sources Science & Technology*, vol. 12, pp. 53-56, 2003.

[113] C. K. Jung, D. C. Lim, H. G. Jee, M. G. Park, S. J. Ku, K. S. Yu, B. Hong, S. B. Lee, and J. H. Boo, "Hydrogenated amorphous and crystalline SiC thin films grown by RF-PECVD and thermal MOCVD; comparative study of structural and optical properties," *Surface & Coatings Technology*, vol. 171, pp. 46-50, 2003.

[114] W. C. Wang, S. Wang, F. Liu, W. Zheng, and D. Z. Wang, "Optical study of OH radical in a wire-plate pulsed corona discharge," *Spectrochimica Acta Part a-Molecular and Biomolecular Spectroscopy*, vol. 63, pp. 477-482, 2006.

[115] T. Sakamoto, K. Naoi, H. Matsuura, and H. Akatsuka, "Experimental study of effect of rare gas admixture on temperatures of microwave-excited oxygen discharge plasma," *Japanese Journal of Applied Physics Part 1-Regular Papers Brief Communications & Review Papers*, vol. 45, pp. 243-246, 2006.

[116] K. Naoi, T. Sakamoto, H. Matsuura, and H. Akatsuka, "Experimental study on the effect of different noble gas admixtures on the gas temperature of oxygen plasma," *Journal of Advanced Oxidation Technologies*, vol. 8, pp. 25-32, 2005.

[117] H. Rabat and C. de Izarra, "Check of OH rotational temperature using an interferometric method," *Journal of Physics D-Applied Physics*, vol. 37, pp. 2371-2375, 2004.

[118] H. Nassar, S. Pellerin, K. Musiol, O. Martinie, N. Pellerin, and J. M. Cormier, "N-2(+)/N-2 ratio and temperature 2 measurements based on the first negative N-2(+) and second positive N-2 overlapped molecular emission spectra," *Journal of Physics D-Applied Physics*, vol. 37, pp. 1904-1916, 2004.

[119] M. Laroussi, J. P. Richardson, and F. C. Dobbs, "Effects of nonequilibrium atmospheric pressure plasmas on the heterotrophic pathways of bacteria and on their cell morphology," *Applied Physics Letters*, vol. 81, pp. 772-774, 2002.

[120] J. R. Hill and D. A. Mendis, "Electrostatic Disruption of a Charged Conducting Spheroid," *Canadian Journal of Physics*, vol. 59, pp. 897-901, 1981.

[121] M. Laroussi, G. S. Sayler, B. B. Glascock, B. McCurdy, M. E. Pearce, N. G. Bright, and C. M. Malott, "Images of biological samples undergoing sterilization by a glow discharge at atmospheric pressure," *Ieee Transactions on Plasma Science*, vol. 27, pp. 34-35, 1999.

[122] C. K. Goertz, *Dusty Plasmas in the Solar System*, vol. 27, 1989.

[123] J. L. Ingraham, O. Maaloe, and F. C. Neidhardt, *Physiology of the Bacterial Cell: A Molecular Approach*. Boston, MA: Sinauer Associates, 1983.

[124] M. Laroussi, D. A. Mendis, and M. Rosenberg, "Plasma interaction with microbes," *New Journal of Physics*, vol. 5, 2003.

[125] Y. Ralchenko, A. E. Kramida, J. Reader, and N. A. Team, "NIST Atomic Spectra Database (version 3.1.4)," 2008.

[126] L. F. Dong, Y. H. Li, W. J. Chen, and X. C. Li, "Measurement of N-2(+) rotational temperature in air dielectric barrier discharge," *Spectroscopy and Spectral Analysis*, vol. 27, pp. 2406-2408, 2007.

[127] Lofthus A. and K. P.H., "Reference Data," *Journal of Physical Chemistry*, vol. 6, 1977.

[128] R. W. B. Pearse and A. G. Gaydon, *The Identification of Molecular Spectra*. New York: John Wiley & Sons, 1963.

[129] B. Rapp, "Private Communication," 2008.

[130] G. Borcia, N. M. D. Brown, D. Dixon, and R. McIlhagger, "The effect of an air-dielectric barrier discharge on the surface properties and peel strength of medical packaging materials," *Surface & Coatings Technology*, vol. 179, pp. 70-77, 2004.

[131] C. H. Kruger, T. G. Owano, and C. O. Laux, "Experimental investigation of atmospheric pressure nonequilibrium plasma chemistry," *Ieee Transactions on Plasma Science*, vol. 25, pp. 1042-1051, 1997.

[132] R. B. Ye, T. Ishigaki, and T. Sakuta, "Controlled generation of pulse-modulated RF plasmas for materials processing," *Plasma Sources Science & Technology*, vol. 14, pp. 387-396, 2005.

[133] H. Yoshiki, K. Ikeda, A. Wakaki, S. Togashi, K. Taniguchi, and Y. Horiike, "Localized plasma processing of materials using atmospheric-pressure microplasma jets," *Japanese Journal of Applied Physics Part 1-Regular Papers Short Notes & Review Papers*, vol. 42, pp. 4000-4003, 2003.

[134] M. Laroussi and T. Akan, "Arc-free atmospheric pressure cold plasma jets: A review," *Plasma Processes and Polymers*, vol. 4, pp. 777-788, 2007.

[135] A. Chirokov, A. Gutsol, and A. Fridman, "Atmospheric pressure plasma of dielectric barrier discharges," *Pure and Applied Chemistry*, vol. 77, pp. 487-495, 2005.

[136] T. Nozaki and K. Okazaki, "Materials processing at atmospheric pressure: Nonequilibrium effects on nanotechnology and mega-industries," *Pure and Applied Chemistry*, vol. 78, pp. 1157-1172, 2006.

[137] L. Xu, H. Nonaka, H. Y. Zhou, A. Ogino, T. Nagata, S. Nanko, I. Kurawaki, and M. Nagatsu, "Characteristics of surface-wave plasma with air-simulated N-2-O-2 gas mixture for low-temperature sterilization," *Journal of Physics D-Applied Physics*, vol. 40, pp. 803-808, 2007.

[138] C. U. Bang, Y. C. Hong, and H. S. Uhm, "Synthesis and characterization of nano-sized nitride particles by using an atmospheric microwave plasma technique," *Surface & Coatings Technology*, vol. 201, pp. 5007-5011, 2007.

[139] J. Ehlbeck, A. Ohl, M. Maass, U. Krohmann, and T. Neumann, "Moving atmospheric microwave plasma for surface and volume treatment," *Surface & Coatings Technology*, vol. 174, pp. 493-497, 2003.

[140] Y. C. Hong and H. S. Uhm, "Production of carbon nanotubes by microwave plasma torch at atmospheric pressure," *Physics of Plasmas*, vol. 12, 2005.

[141] M. Jasinski, J. Mizeraczyk, and Z. Zakrzewski, "Microwave torch plasmas for decomposition of gaseous pollutants," *Journal of Advanced Oxidation Technologies*, vol. 7, pp. 51-58, 2004.

[142] A. Kono, J. Wang, and M. Aramaki, "Production and characterization of high-pressure microwave glow discharge in a microgap aiming at VUV light source," *Thin Solid Films*, vol. 506, pp. 444-448, 2006.

[143] T. Shimizu, B. Steffes, R. Pompl, F. Jamitzky, W. Bunk, K. Ramrath, M. Georgi, W. Stolz, H. U. Schmidt, T. Urayama, S. Fujii, and G. E. Morfill, "Characterization of microwave plasma torch for decontamination," *Plasma Processes and Polymers*, vol. 5, pp. 577-582, 2008.

[144] C. C. Ting, T. F. Young, and C. S. Jwo, "Fabrication of diamond nanopowder using microwave plasma torch technique," *International Journal of Advanced Manufacturing Technology*, vol. 34, pp. 316-322, 2007.

[145] T. Yuji, K. Fujioka, S. Fujii, and H. Akatsuka, "Basic characteristics of Ar/N-2 atmospheric pressure nonequilibrium microwave discharge plasma jets," *Ieej Transactions on Electrical and Electronic Engineering*, vol. 2, pp. 473-475, 2007.

[146] V. Karanassios, "Microplasmas for chemical analysis: analytical tools or research toys?," *Spectrochimica Acta Part B-Atomic Spectroscopy*, vol. 59, pp. 909-928, 2004.

[147] J. J. Shi, X. T. Deng, R. Hall, J. D. Punnett, and M. G. Kong, "Three modes in a radio frequency atmospheric pressure glow discharge," *Journal of Applied Physics*, vol. 94, pp. 6303-6310, 2003.

[148] H. Kakiuchi, H. Ohmi, M. Aketa, K. Yasutake, K. Yoshii, and Y. Mori, "Effect of hydrogen on the structure of high-rate deposited SiC on Si by atmospheric pressure plasma chemical vapor deposition using high-power-density condition," *Thin Solid Films*, vol. 496, pp. 259-265, 2006.

[149] J. Y. Kang and M. Sarmadi, "Textile plasma treatment review - Natural polymer-based textiles," *Aatcc Review*, vol. 4, pp. 28-32, 2004.

[150] E. E. Kunhardt, "Generation of large-volume, atmospheric-pressure, nonequilibrium plasmas," *Ieee Transactions on Plasma Science*, vol. 28, pp. 189-200, 2000.

[151] A. Ladwig, S. Babayan, M. Smith, M. Hester, W. Highland, R. Koch, and R. Hicks, "Atmospheric plasma deposition of glass coatings on aluminum," *Surface & Coatings Technology*, vol. 201, pp. 6460-6464, 2007.

[152] C. F. Chen and Y. W. Li, "The effects of hydrogen plasma treatment on the plasma-enhanced chemical vapor deposition a-SiC : H films," *Japanese Journal of Applied Physics Part 1-Regular Papers Short Notes & Review Papers*, vol. 43, pp. 5545-5549, 2004.

[153] S. Martin, F. Massines, N. Gherardi, and C. Jimenez, "Atmospheric pressure PE-CVD of silicon based coatings using a glow dielectric barrier discharge," *Surface & Coatings Technology*, vol. 177, pp. 693-698, 2004.

[154] P. Yancey and C. Lowery, "Developmental Designs For Producing a Solid State Tesla Coil Module," 2004.

[155] K. D. Skeldon, A. I. Grant, and S. A. Scott, "A high potential Tesla coil impulse generator for lecture demonstrations and science exhibitions," *American Journal of Physics*, vol. 65, pp. 744-754, 1997.

[156] X. H. Yuan and L. L. Raja, "Computational study of capacitively coupled high-pressure glow discharges in helium," *Ieee Transactions on Plasma Science*, vol. 31, pp. 495-503, 2003.

[157] Y. P. Raizer, M. N. Shneider, and N. A. Yatsenko, *Radio-Frequency Capacitive Discharges*. Boca Raton: CRC Press Inc., 1995.

[158] S. M. Rossnagel, W. D. Westwood, and J. J. Cuomo, *Handbook of Plasma Processing Technology: Fundamental Etching, Deposition and Surface Interactions*. Norwich: Noyes Publications, 1990.

[159] M. L. Hitchman and K. F. Jensen, *Chemical Vapor Deposition: Principles and Applications*. San Diego: Academic Press Limited, 1993.

[160] M. A. Lieberman and A. J. Lichtenberg, *Principles of Plasma Discharges and Materials Processing*: Wiley-Interscience, 2005.

[161] J. E. Crowell, "Chemical methods of thin film deposition: Chemical vapor deposition, atomic layer deposition, and related technologies," *Journal of Vacuum Science & Technology A*, vol. 21, pp. S88-S95, 2003.

[162] D. M. Dobkin and M. K. Zuraw, *Principles of Chemical Vapor Deposition*. Dordrecht: Kluwer Academic Publishers, 2003.

[163] S. E. Alexandrov and M. L. Hitchman, "Chemical vapor deposition enhanced by atmospheric pressure non-thermal non-equilibrium plasmas," *Chemical Vapor Deposition*, vol. 11, pp. 457-468, 2005.

[164] M. Ohring, *Materials Science of Thin Films*. New York: Academic Press, 2001.

[165] H. F. Winters, *Plasma Chemistry III*, vol. 94. New York: Springer-Verlag, 1980.

[166] D. W. Hess and D. B. Graves, "Plasma-Assisted Chemical Vapor Deposition (Chapter 7)," in *Chemical Vapor Deposition: Principles and Applications*, M. L. Hitchman and K. F. Jensen, Eds. San Diego: Academic Press Limited, 1993.

[167] X. Yang, M. Moravej, G. R. Nowling, S. E. Babayan, J. Panelon, J. P. Chang, and R. F. Hicks, "Comparison of an atmospheric pressure, radio-frequency discharge operating in the alpha and gamma modes," *Plasma Sources Science & Technology*, vol. 14, pp. 314-320, 2005.

[168] E. Brinley, K. S. Babu, and S. Seal, "The solution precursor plasma Spray processing of nanomaterials," *Jom*, vol. 59, pp. 54-59, 2007.

[169] J. Matejicek, P. Chraska, and J. Linke, "Thermal spray coatings for fusion applications - Review," *Journal of Thermal Spray Technology*, vol. 16, pp. 64-83, 2007.

[170] L. Pawlowski, "Finely grained nanometric and submicrometric coatings by thermal spraying: A review," *Surface & Coatings Technology*, vol. 202, pp. 4318-4328, 2008.

[171] H. Singh, B. S. Sidhu, D. Puri, and S. Prakash, "Use of plasma spray technology for deposition of high temperature oxidation/corrosion resistant coatings - a review," *Materials and Corrosion-Werkstoffe Und Korrosion*, vol. 58, pp. 92-102, 2007.

[172] G. Borcia and N. M. D. Brown, "Hydrophobic coatings on selected polymers in an atmospheric pressure dielectric barrier discharge," *Journal of Physics D-Applied Physics*, vol. 40, pp. 1927-1936, 2007.

[173] L. B. Di, X. S. Li, C. Shi, Y. Xu, D. Z. Zhao, and A. M. Zhu, "Atmospheric-pressure plasma CVD of TiO2 photocatalytic films using surface dielectric barrier discharge," *Journal of Physics D-Applied Physics*, vol. 42, 2009.

[174] J. L. Hodgkinson, D. W. Sheel, H. M. Yates, and M. E. Pemble, "Atmospheric pressure glow discharge CVD of Al2O3 thin films," *Plasma Processes and Polymers*, vol. 3, pp. 597-605, 2006.

[175] K. K. Mishra, R. K. Khardekar, R. Singh, and H. C. Pant, "Novel approach to produce polymerized hydrocarbon coatings using dielectric barrier controlled atmospheric pressure glow discharge plasma," *Review of Scientific Instruments*, vol. 73, pp. 3251-3257, 2002.

[176] K. Schmidt-Szalowski, Z. Rzanek-Boroch, J. Sentek, Z. Rymuza, Z. Kusznierewicz, and M. Misiak, "Thin films of silicon compounds deposited by PE-CVD at atmospheric pressure," *High Temperature Material Processes*, vol. 6, pp. 63-74, 2002.

[177] O. Goossens, E. Dekempeneer, D. Vangeneugden, R. Van de Leest, and C. Leys, "Application of atmospheric pressure dielectric barrier discharges in deposition, cleaning and activation," *Surface & Coatings Technology*, vol. 142, pp. 474-481, 2001.

[178] I. P. Vinogradov and A. Lunk, "Dependence of surface tension and deposition rate of fluorocarbon polymer films on plasma parameters in a dielectric barrier discharge (DBD)," *Surface & Coatings Technology*, vol. 200, pp. 695-699, 2005.

[179] J. Perez, J. Munoz-Dorado, T. De La Rubia, and J. Martinez, "Biodegradation and biological treatments of cellulose, hemicellulose, and lignin: An overview," *International Microbiology*, vol. 5, pp. 53-63, 2002.

[180] M. Tatoulian, F. Arefi-Khonsari, and J. P. Borra, "Deposition of organic coatings at atmospheric pressure from liquid precursors," *Plasma Processes and Polymers*, vol. 4, pp. 360-369, 2007.

[181] M. G. McCord, Y. J. Hwang, P. J. Hauser, Y. Qiu, J. J. Cuomo, O. E. Hankins, M. A. Bourham, and L. K. Canup, "Modifying nylon and polypropylene fabrics with atmospheric pressure plasmas," *Textile Research Journal*, vol. 72, pp. 491-498, 2002.

[182] P. L. Girard-Lauriault, F. Mwale, M. Iordanova, C. Demers, P. Desjardins, and M. R. Wertheimer, "Atmospheric pressure deposition of micropatterned nitrogen-rich plasma-polymer films for tissue engineering," *Plasma Processes and Polymers*, vol. 2, pp. 263-270, 2005.

[183] R. B. Bird, W. E. Steward, and E. N. Lightfoot, *Transport Phenomena*. New York, 1960.

[184] R. B. Timmons and A. J. Griggs, "Pulsed Plasma Polymerization (Chapter 6)," in *Plasma Polymer Films*
H. Biederman, Ed. London: Imperial College Press, 2004.

[185] D. Caputo, G. de Cesare, A. Nascetti, and R. Scipinotti, "Two-Color Sensor for Biomolecule Detection," *Sensor Letters*, vol. 6, pp. 542-547, 2008.

[186] K. Chirakawikul, T. Sujaridchai, B. Ratwises, D. Kruangam, S. Panyakeow, W. Boonkosum, T. Sugino, and J. Shirafuji, "Preparation of p-type poly-crystalline diamond films and their applications to hole injection layers in amorphous SiC : H thin film light emitting diodes," *Journal of Non-Crystalline Solids*, vol. 227, pp. 1156-1159, 1998.

[187] A. Tabata, Y. Komura, Y. Hoshide, T. Narita, and A. Kondo, "Properties of nanocrystalline cubic silicon carbide thin films prepared by hot-wire chemical vapor deposition using SiH4/CH4/H-2 at various substrate temperatures," *Japanese Journal of Applied Physics*, vol. 47, pp. 561-565, 2008.

[188] M. Vetter, C. Voz, R. Ferre, I. Martin, A. Orpella, J. Puigdollers, J. Andreu, and R. Alcubilla, "Electronic properties of intrinsic and doped amorphous silicon carbide films," *Thin Solid Films*, vol. 511, pp. 290-294, 2006.

[189] C. A. Zorman and R. J. Parro, "Micro- and nanomechanical structures for silicon carbide MEMS and NEMS," *Physica Status Solidi B-Basic Solid State Physics*, vol. 245, pp. 1404-1424, 2008.

[190] J. M. Lackner, W. Waldhauser, R. Ebner, A. Fian, G. Jakopic, G. Leising, and T. Schoberl, "Pulsed laser deposition of silicon containing carbon thin films," *Surface & Coatings Technology*, vol. 177, pp. 360-364, 2004.

[191] S. Boughaba, G. I. Sproule, J. P. McCaffrey, M. Islam, and M. J. Graham, "Synthesis of amorphous silicon carbonitride films by pulsed laser deposition," *Thin Solid Films*, vol. 402, pp. 99-110, 2002.

[192] M. D. Stamate, I. Lazar, and G. Lazar, "DC magnetron power dependence of a-SiC : H IR absorption properties," *Journal of Non-Crystalline Solids*, vol. 354, pp. 61-64, 2008.

[193] Z. Yao, A. Suzuki, D. Levchuk, and T. Terai, "Sic coating by rf sputtering as tritium permeation barrier for fusion blanket," *Fusion Science and Technology*, vol. 52, pp. 865-869, 2007.

[194] B. P. Swain, "The analysis of carbon bonding environment in HWCVD deposited a-SiC : H films by XPS and Raman spectroscopy," *Surface & Coatings Technology*, vol. 201, pp. 1589-1593, 2006.

[195] W. A. Nevin, H. Yamagishi, and Y. Tawada, "Wide Band-Gap Hydrogenated Amorphous-Silicon Carbide Prepared from a Liquid Aromatic Carbon Source," *Journal of Applied Physics*, vol. 72, pp. 4989-4991, 1992.

[196] M. L. Deoliveira, S. S. Camargo, and F. L. Freire, "On the Carbon Incorporation into a-Sic-H Films with Low-Carbon Content," *Journal of Applied Physics*, vol. 71, pp. 1531-1533, 1992.

[197] H. Kakiuchi, H. Ohmi, and K. Yasutake, "Formation of silicon carbide at low temperatures by chemical transport of silicon induced by atmospheric pressure H-2/CH4 plasma," *Thin Solid Films*, vol. 516, pp. 6580-6584, 2008.

[198] Y. Mori, H. Kakiuchi, K. Yoshii, K. Yasutake, and H. Ohmi, "Characterization of hydrogenated amorphous Si1-xCx films prepared at extremely high rates using very high frequency plasma at atmospheric pressure," *Journal of Physics D-Applied Physics*, vol. 36, pp. 3057-3063, 2003.

[199] H. Kakiuchi, H. Ohmi, R. Nakamura, M. Aketa, and K. Yasutake, "Structural characterization of polycrystalline 3C-SiC films prepared at high rates by atmospheric pressure plasma chemical vapor deposition using monomethylsilane," *Japanese Journal of Applied Physics Part 1-Regular Papers Brief Communications & Review Papers*, vol. 45, pp. 8381-8387, 2006.

[200] R. Peck, C. Olsen, and J. Devore, *Introduction to Statistics and Data Analysis*, First ed: Duxbury Press, 2000.

[201] C. Ye, J. N. Liu, F. Y. Ren, and N. Okafo, "Design of experiment and data analysis by JMP (R) (SAS institute) in analytical method validation," *Journal of Pharmaceutical and Biomedical Analysis*, vol. 23, pp. 581-589, 2000.

[202] G. E. B. Archer, A. Saltelli, and I. M. Sobol, "Sensitivity measures, ANOVA-like techniques and the use of bootstrap," *Journal of Statistical Computation and Simulation*, vol. 58, pp. 99-120, 1997.

[203] L. A. Carlini-Garcia, R. Vencovsky, and A. S. G. Coelho, "Factorial analysis of bootstrap variances of population genetic parameter estimates," *Genetics and Molecular Biology*, vol. 29, pp. 308-313, 2006.

[204] S. Xie, X. Liu, and G. Y. Meng, "A technical design and experiment of the chemical vapor deposition of AlN film," *Chemical Journal of Chinese Universities-Chinese*, vol. 17, pp. 838-842, 1996.

[205] *JMP Statistics and Graphics Guide, Release 7*: SAS, 2007.

[206] T. C. Wei and C. H. Liu, "Evaluation of plasma deposited fluorocarbon films using experimental design methodology," *Surface & Coatings Technology*, vol. 200, pp. 2214-2222, 2005.

[207] A. von Keudell and W. Jacob, "Growth and erosion of hydrocarbon films investigated by in situ ellipsometry," *Journal of Applied Physics*, vol. 79, pp. 1092, 1996.

[208] A. Vijayakumar, R. M. Todi, A. P. Warren, and K. B. Sundaram, "Influence of N-2/Ar gas mixture ratio and annealing on optical properties of SiCBN thin films prepared by rf sputtering," *Diamond and Related Materials*, vol. 17, pp. 944-948, 2008.

[209] F. Demichelis, C. F. Pirri, E. Tresso, H. Herremans, W. Grevendonk, G. J. Adriaenssens, G. Amato, and U. Coscia, "Investigation on Electronic Density-of-States in a-Sixc1-X-H Films," *Applied Surface Science*, vol. 70-1, pp. 664-668, 1993.

[210] Y. Y. Zhang, P. Y. Du, R. Zhang, G. R. Han, and W. J. Weng, "Structure and properties of hydrogenated amorphous silicon carbide thin films deposited by PECVD," *Journal of Non-Crystalline Solids*, vol. 354, pp. 1435-1439, 2008.

[211] Q. J. Cheng, S. Xu, J. D. Long, Z. H. Ni, A. E. Rider, and K. Ostrikov, "High-rate, low-temperature synthesis of composition controlled hydrogenated amorphous silicon carbide films in low-frequency inductively coupled plasmas," *Journal of Physics D-Applied Physics*, vol. 41, 2008.

[212] C. Onneby and C. G. Pantano, "Silicon oxycarbide formation on SiC surfaces and the SiC/SiO2 interface (vol A15, pg 1597, 1997)," *Journal of Vacuum Science & Technology a-Vacuum Surfaces and Films*, vol. 16, pp. 2742-2743, 1998.

[213] A. M. Wrobel, A. Walkiewicz-Pietrzykowska, M. Ahola, I. J. Vayrynen, F. J. Ferrer-Fernandez, and A. R. Gonzalez-Elipe, "Growth Mechanism and Chemical Structure of Amorphous Hydrogenated Silicon Carbide (a-SiC:H) Films Formed by Remote

Hydrogen Microwave Plasma CVD From a Triethylsilane Precursor: Part 1," *Chemical Vapor Deposition*, vol. 15, pp. 39-46, 2009.

[214] K. A. Gray, L. S. Zhao, and M. Emptage, "Bioethanol," *Current Opinion in Chemical Biology*, vol. 10, pp. 141-146, 2006.

[215] DOE, "Breaking the Biological Barriers to Cellulosic Ethanol: A Joint Research Agenda" December 7-9, 2005 Rockville, MD 2005.

[216] S. M. Starikovskaia, "Plasma assisted ignition and combustion," *Journal of Physics D-Applied Physics*, vol. 39, pp. R265-R299, 2006.

[217] K. Kiyokawa, H. Matsuoka, A. Itou, K. Hasegawa, and K. Sugiyama, "Decomposition of inorganic gases in an atmospheric pressure non-equilibrium plasma," *Surface & Coatings Technology*, vol. 112, pp. 25-28, 1999.

[218] Y. B. Guo and F. C. N. Hong, "Characteristics of large-area cold atmospheric discharges from radio-frequency microdischarge arrays," *Japanese Journal of Applied Physics Part 1-Regular Papers Short Notes & Review Papers*, vol. 42, pp. 6598-6604, 2003.

[219] M. Moravej, X. Yang, R. F. Hicks, J. Penelon, and S. E. Babayan, "A radio-frequency nonequilibrium atmospheric pressure plasma operating with argon and oxygen," *Journal of Applied Physics*, vol. 99, 2006.

[220] R. Prat, Y. J. Koh, Y. Babukutty, M. Kogoma, S. Okazaki, and M. Kodama, "Polymer deposition using atmospheric pressure plasma glow (APG) discharge," *Polymer*, vol. 41, pp. 7355-7360, 2000.

[221] R. Sanchez-Gonzalez, Y. Kim, L. A. Rosocha, and S. Abbate, "Methane and ethane decomposition in an atmospheric-pressure plasma jet," *Ieee Transactions on Plasma Science*, vol. 35, pp. 1669-1676, 2007.

[222] M. Laroussi and X. Lu, "Room-temperature atmospheric pressure plasma plume for biomedical applications," *Applied Physics Letters*, vol. 87, 2005.

[223] R. Rowell, *Handbook of Wood Chemistry and Wood Composites*. Boca Raton, FL: CRC Press, 2005.

[224] S. Y. Moon and W. Choe, "A comparative study of rotational temperatures using diatomic OH, O-2 and N-2(+) molecular spectra emitted from atmospheric plasmas," *Spectrochimica Acta Part B-Atomic Spectroscopy*, vol. 58, pp. 249-257, 2003.

[225] M. Pacheco, J. Pacheco, H. Moreno, A. Mercado, R. Valdivia, and A. Santana, "OES analysis in a nonthermal plasma used for toxic gas removal: Rotational and excitation temperature estimation," *Laser Physics*, vol. 18, pp. 303-307, 2008.

[226] L. Podgorski, B. Chevet, L. Onic, and A. Merlin, "Modification of wood wettability by plasma and corona treatments," *International Journal of Adhesion and Adhesives*, vol. 20, pp. 103-111, 2000.

[227] P. Rehn, A. Wolkenhauer, M. Bente, S. Forster, and W. Viol, "Wood surface modification in dielectric barrier discharges at atmospheric pressure," *Surface & Coatings Technology*, vol. 174, pp. 515-518, 2003.